

Vlad Cristea

# Storage Tank Concepts for Liquefied Hydrogen

Master's thesis in Energy and Environmental Engineering

Supervisor: Petter Nekså

March 2020

**NTNU**  
Norwegian University of Science and Technology  
Faculty of Information Technology and Electrical  
Engineering  
Department of Energy and Process Engineering



Norwegian University of  
Science and Technology



Vlad Cristea

# **Storage Tank Concepts for Liquefied Hydrogen**

Master's thesis in Energy and Environmental Engineering  
Supervisor: Petter Nekså  
March 2020

Norwegian University of Science and Technology  
Faculty of Information Technology and Electrical Engineering  
Department of Energy and Process Engineering





**MASTER WORK**

for

**Student Vlad Cristea**

Autumn 2019

**Storage tank concepts for liquefied hydrogen**

*Lagertank konsepter for flytende hydrogen*

**Background and objective**

There is an increasing concern related to climate change. This has led to the interest in using hydrogen as energy carrier and fuel for transportation, power production, industry and potentially other applications in order to avoid the end-use CO<sub>2</sub> emissions.

There are however several challenges related to the practical implementation of hydrogen as energy carrier. A suitable way of transporting larger amounts of hydrogen will be in liquid form at temperatures around -250 °C, as liquid hydrogen (LH<sub>2</sub>).

Even with well insulated storage tanks, a certain heat inleak will create boil-off gas (BOG). It is important to minimize the BOG with suitable tank insulation concepts. This task is quite analog with insulation of LNG tanks, but more challenging due to a higher temperature difference to the ambient and a lower heat of vaporization for LH<sub>2</sub>.

The overall goal should be to achieve BOG rates at the same level as for LNG, being lower than 0.2% per day. This will require thicker insulation and/or different insulation concepts, as today's concepts for cryogenic tanks based on vacuum insulation concepts.

The aim of this Master thesis work is to explore storage tank concepts for larger LH<sub>2</sub> storage tanks, primarily with respect to thermal aspects and low BOG rates, but also with respect to structural stress considerations.

**The following tasks are to be considered:**

1. Literature survey related to insulation and structural concepts for larger LNG and cryogenic storage tanks
2. Establish a model for thermal and structural evaluation of larger cryogenic storage tanks. As baseline storage tank concept shall be selected a double spherical tank with insulation in between. The tank is supported by a cylindrical skirt at equatorial position for the outer tank. The inner tank is hung up in an equatorial ring element supported to a corresponding ring

element of the outer tank through load bearing elements made of a material acting as a thermal breaker. The model should be able to consider insulation types and concepts currently used for LNG as well as concepts commonly used for cryogenic LH<sub>2</sub> storage tanks. For vacuum insulation concept, being non-loadbearing, the model should be able to evaluate required load supporting structures.

3. Utilize the developed model to consider designs to achieve acceptable BOG rates and quantify heat leak elements of the different parts of the construction
4. Validate the different parts of the model with information from literature and practical design considerations, including structural aspects.
5. Further develop the model to consider concepts of shield refrigeration or thermal break concepts for the thermally weak points of the construction, either by utilizing the BOG to perform a refrigeration duty or by utilizing auxiliary refrigeration concepts.
6. Make a draft scientific paper based on the work performed
7. Propose a plan for further work

-- “ --

Department for Energy and Process Engineering, September 1, 2019

---

Adjunct Prof. Petter Nekså  
Supervisor

Co-Supervisor(s):

Jostein Pettersen	Equinor ASA
Åsmund Ervik	SINTEF Energi AS

# Preface

The present master thesis was written at the Department of Energy and Process Engineering (EPT) at the Norwegian University of Science and Technology (NTNU). The thesis constitutes 30 ETCS and represents a final assignment of the MSc degree program in Energy and Environmental Engineering. The master thesis was written from September 2019 to March 2020, and was supervised by the chief scientist Petter Nekså (Sintef), research scientist Åsmund Ervik (Sintef) and senior technology advisor Jostein Pettersen (Equinor).

The topic of this thesis has proven to be the key which opened a door to a room full of scientific information, helping me to expand my knowledge in different engineering fields such as thermal engineering, mechanical engineering, material engineering and marine engineering.

I want to express my sincere gratitude to my supervisor, Petter Nekså for his invaluable time and support throughout the process of finalizing this thesis. I really appreciate all the feedback, professional advice and enthusiasm he contentiously offered.

I would also want to thank my co-supervisors Åsmund Ervik and Jostein Pettersen for their major contributions, and for sharing with me their irreplaceable knowledge, insight and time.

Trondheim, 2020.03.29



Vlad Cristea

# Abstract

With climate change representing an increasing problem in today's society, the need of transition to cleaner energy sources and carriers becomes more severe. This issue draws the attention towards hydrogen, as it is the most abundant element in the Universe and has great potential for being a suitable carbon-free energy carrier, especially when in liquid form.

The objective of this master thesis is to explore possible solutions for large scale liquid hydrogen storage tanks, which may result in evaporation losses as low as under 0.2 % per day, with respect to structural stress considerations and other thermal losses. Based on literature survey related to larger scale LNG and cryogenic storage tanks a preliminary design has been established and analysed, followed by two slightly changed alternative models, for validation of possible improvements. All three systems are of Type-B self-supported cryogenic vessels, having a double-walled spherical geometry, with the internal shell being placed on a skirt welded to the external tank. The capacity of the three tanks is of 40 000 m<sup>3</sup> given by an internal radius of 21.2 m. For the modeling part AutoCAD 2020 and Solidworks 2019 are used. The resulted designs are analysed, structurally and thermally, using the finite element method through ANSYS Mechanical APDL.

The outcome of the data showed that the preliminary design composed of 1.00 m thick evacuated bulk insulation layer with an apparent thermal conductivity of 1.003 mW/(m·K) is the most favourable option, showing a total boil-off rate of 0.059% per day and great structural resistance against different loading conditions.

The first alternative model, with a 0.3 m thick insulation layer of the same type and efficiency, resulted in an evaporation rate of 0.095% per day, with very high stresses on the internal support which resulted in structural failure of the system.

One major drawback with the apparent thermal conductivity value of 1.003 mW/(m·K) is that it is pure theoretical, probably achievable at a pressure level lower than 0.1 MPa. This high evacuation degree has, until now, been realized experimentally for small scale cryogenic containers, and may therefore present big challenges for industrial systems. Based on this aspect, the final alternative model is designed to represent the outcome of a closer to reality system, having the apparent thermal conductivity of the 0.4 m thick evacuated bulk insulation layer increased to 3.2 mW/(m·K), which accounts for possible uncertainties and higher pressure level. The tank is covered to 1.0 m thick polyurethane foam insulation to decrease the surface temperature on the external wall, resulting in a behaviour similar to that of shield refrigeration. The outcome of this model is a boil-off rate of 0.109 % per day, with maximum stress values close to the material's tensile limits.

Being critical of the results is of importance, since several uncertainties are present. However, the outcome depicts the behaviour of LH<sub>2</sub> storage tanks composed of different materials and subjected to different loading conditions.

Some engineering-challenges should first be solved, but results have shown that large scale LH<sub>2</sub> storage tank are feasible.



# Sammendrag

Med klimaendringene som representerer et økende problem i dagens samfunn, blir behovet for overgangen til renere energikilder og energibærere sterkere. Denne problematikken trekker oppmerksomheten mot hydrogen, da dette er elementet som forekommer mest av i universet og har et stort potensial for å være en passende karbon-fri energibærer, spesielt i væskeform.

Formålet med denne masteroppgaven er å undersøke mulige løsninger for design og utvikling av store tanker for lagring av flytende hydrogen med mindre enn 0.2 % avkok per dag, med betraktning av strukturell spenninger og termiske egenskaper. Basert på studie av eksisterende litteratur knyttet til lagring av LNG (flytende naturgass) og kryogene væsker i store lagringstanker. Et preliminært design har blitt utviklet og analysert, etterfulgt av to lett forandret alternative modeller, med formål om å undersøke mulige forbedringer. Alle tre systemer er av Type-B selvbærende kryogeniske tanker, bestående av en dobbeltvegget sfærisk geometri, der det innerste tanken er opplagret i et skjold mellom inner- og yttertank. Lagringskapasiteten til de tre tankene er 40 000 m<sup>3</sup> med en resulterende indre radius på 21.2 m. AutoCAD 2020, Solidworks 2019 og ANSYS Mechanical APDL brukes til design og analyse av de ulike konseptene.

Analysen viste at det preliminare designet bestående av 1.00 m tykt evakuert isolasjonslag med en tilsynelatende termisk konduktivitet på 1.003 mW/(m·K) er det mest foretrukne valget, med et totalt avkok gjennom fordamping på 0.059 % per dag og med strukturelle egenskaper i stand til å tillate forskjellige lagringsforhold.

Den første alternative modellen, med et 0.3 m tykt isolasjonslag av samme type og samme effektivitet, resulterte i en fordampning på 0.095 % per dag, men med uakseptabelt høye spenninger for den interne støtten, noe som resulterte i strukturell kollaps av systemet.

En stort tilbakefall med den tilsynelatende termiske konduktivitet på 1.003 mW/(m·K), er oppnåelig ved et trykknivå lavere enn 0.1 MPa. Denne høye evakueringsgraden har blitt oppnådd eksperimentelt for kryogeniske tanker av mindre skala. Det kan være utfordrende å oppnå dette for systemer av industriell størrelse. Det ble derfor utført en analyse hvor den tilsynelatende termiske konduktiviteten ble økt til 3.2 mW/(m·K), som illustrerer resultater av forhøyede trykknivåer. Tanken er dekket med 1.0 m tykt polyuretan isolasjonsskum for å minke overflatetemperaturen for den ytre tanken, som resulterte i en liknende oppførsel lik den for et kjøleskjold. Resultatet viste et avkok på 0.109 % per dag, med maksimale stressverdier nære materialets flytegrenser.

Å være kritisk til resultatene er viktig, siden ulike usikkerheter finnes. Allikevel, resultatene viser oppførselen til LH<sub>2</sub> lagringstanker sammensatte av forskjellige byggematerialer og utsatt for forskjellige lastingsforhold.

Noen ingeniørrelaterte utfordringer, må fortsatt løses, men resultatene har vist at lagringstanker for store mengder LH<sub>2</sub> er mulig å utvikle.

---

# Contents

<b>Preface</b>	<b>i</b>
<b>Abstract</b>	<b>ii</b>
<b>Sammendrag</b>	<b>iii</b>
<b>List of Figures</b>	<b>vii</b>
<b>List of Tables</b>	<b>x</b>
<b>Nomenclature</b>	<b>xi</b>
<b>1 Introduction</b>	<b>1</b>
1.1 Motivation for use of hydrogen as a future fuel . . . . .	1
1.2 Motivation for storing hydrogen in liquid form . . . . .	1
1.3 Motivation for designing a low-loss, high caring-capacity storage tank . . . . .	2
1.4 Objective and scope . . . . .	2
1.5 Thesis structure . . . . .	2
<b>2 Methodology and Theory behind the thesis</b>	<b>4</b>
2.1 Overall approach . . . . .	4
2.1.1 Software used . . . . .	4
2.1.2 Approach for structural analysis . . . . .	5
2.1.3 Approach for thermal analysis . . . . .	5
2.2 Theory behind the mechanical analysis . . . . .	5
2.2.1 Governing theoretical equations for the structural analysis . . . . .	6
2.2.2 Governing equations used by ANSYS Mechanical APDL in Static Structural . . . . .	8
2.3 Theory behind the thermal analysis . . . . .	9
2.3.1 Governing theoretical equations for the thermal analysis . . . . .	9
2.3.2 Governing equations used by ANSYS Mechanical APDL in Steady-State Thermal . . . . .	10
2.3.3 Boil-off gas rate . . . . .	12
<b>3 Insulation materials and concepts: general overview</b>	<b>13</b>
3.1 Foam insulation . . . . .	13
3.2 Bulk fill insulation . . . . .	13
3.3 MLI insulation . . . . .	14
3.4 Summary . . . . .	15
<b>4 LNG and cryogenic containment - background for LH<sub>2</sub> storage</b>	<b>17</b>
4.1 LNG storage vessels . . . . .	17
4.1.1 Self-supporting tank system . . . . .	18
4.1.2 Membrane tank system . . . . .	21
4.2 Storage vessels for other types of cryogenic liquids . . . . .	24
4.2.1 NASA Kennedy Space Center-LH <sub>2</sub> cryogenic vessel . . . . .	24
4.2.2 Kawasaki's LH <sub>2</sub> carrier . . . . .	25
4.2.3 Static LIN & LOX tank-design . . . . .	26
4.2.4 Linde cryogenic tanks . . . . .	26
4.3 LNG and other cryogenic liquids vs LH <sub>2</sub> - properties . . . . .	27

---

<b>5</b>	<b>LH<sub>2</sub> storage tank modelling approach - initial considerations</b>	<b>28</b>
5.1	Mechanical and geometrical design . . . . .	28
5.1.1	Internal shell . . . . .	29
5.1.2	External shell . . . . .	32
5.1.3	Support system of the inner shell . . . . .	33
5.1.4	Support system of the outer shell . . . . .	38
5.2	Thermal design . . . . .	39
5.2.1	Walls & insulation layer . . . . .	39
5.2.2	Support system of the internal spherical tank . . . . .	48
<b>6</b>	<b>Structural analysis of preliminary design</b>	<b>52</b>
6.1	Setup . . . . .	52
6.1.1	Design setup . . . . .	52
6.1.2	Mesh setup . . . . .	54
6.1.3	Material properties, and boundary conditions setup . . . . .	58
6.2	Verification analysis . . . . .	62
6.2.1	Simulation C1 . . . . .	63
6.2.2	Simulation C2 . . . . .	64
6.2.3	Simulation C3 . . . . .	65
6.2.4	Verification of skirt analysis . . . . .	66
6.3	Main analysis of the preliminary design . . . . .	67
6.3.1	Static failure . . . . .	67
6.3.2	Results . . . . .	68
<b>7</b>	<b>Thermal analysis of preliminary design</b>	<b>78</b>
7.1	Setup . . . . .	78
7.1.1	Design setup . . . . .	78
7.1.2	Mesh setup . . . . .	79
7.1.3	Material properties, and boundary conditions setup . . . . .	80
7.1.4	Verification simulations . . . . .	80
7.2	Results . . . . .	82
<b>8</b>	<b>Analysis of alternative designs</b>	<b>85</b>
8.1	Improvements considered . . . . .	85
8.2	Design and simulation setup . . . . .	86
8.2.1	A1 System . . . . .	86
8.2.2	A2 system . . . . .	89
8.3	Results . . . . .	94
8.3.1	Results of the A1 system analysis . . . . .	95
8.3.2	Results of the A2 system analysis . . . . .	97
<b>9</b>	<b>Discussion</b>	<b>101</b>
9.1	Comparison of the results . . . . .	101
9.1.1	Results from the steady-state thermal analyses . . . . .	102
9.1.2	Results from the steady-state structural analyses . . . . .	102
9.2	Possible uncertainties . . . . .	103
9.2.1	ANSYS and other technical issues . . . . .	103
9.2.2	Chosen loads and boundary conditions . . . . .	104
9.2.3	Chosen materials and their material properties . . . . .	104
9.2.4	Use of apparent thermal conductivity . . . . .	105
9.2.5	Simplicity of the model . . . . .	106
<b>10</b>	<b>Conclusion</b>	<b>107</b>
<b>11</b>	<b>Proposal for further work</b>	<b>109</b>
	<b>Bibliography</b>	<b>111</b>
	<b>Appendix A About cryogenic insulations</b>	<b>A-1</b>

---

<b>Appendix B LNG tank - scantlings</b>	<b>A-3</b>
<b>Appendix C Email from Moss Maritime AS</b>	<b>A-4</b>
<b>Appendix D Material Properties</b>	<b>A-5</b>
D.1 Low carbon steel . . . . .	A-5
D.2 AISI 316 . . . . .	A-6
D.3 Type of polyurethane foam used on the external insulation in design A2 . . . . .	A-8
D.4 Structural Steel . . . . .	A-9
<b>Appendix E Dimensions of the designs</b>	<b>A-10</b>
E.1 Preliminary design (P1) . . . . .	A-10
E.2 Alternative design (A1) . . . . .	A-11
E.3 Alternative design (A2) . . . . .	A-12
<b>Appendix F Results from validatory simulations</b>	<b>A-13</b>
F.1 Results from simulations with different mesh patterns and symmetry setups . . . . .	A-13
F.2 Results from Simulation C1 . . . . .	A-17
F.3 Results from Simulation C2 . . . . .	A-19
F.4 Results from Simulation C3 . . . . .	A-21
<b>Appendix G Resulted stresses from simulation of the preliminary design</b>	<b>A-23</b>
G.1 Results from PS1 . . . . .	A-23
G.2 Results from PS2 . . . . .	A-26
G.3 Results from PS3 . . . . .	A-29
<b>Appendix H Resulted stresses from simulation of the alternative designs</b>	<b>A-32</b>
H.1 Results from A1 . . . . .	A-32
H.2 Results from A2 . . . . .	A-35

# List of Figures

2.1	Flowchart depicting modelling and simulation procedure . . . . .	5
3.1	Radar diagram showing the performances of the three insulation types on a scale from 0 to 4 . . . . .	15
3.2	Thermal effectiveness of porous cryogenic insulations [68] . . . . .	16
4.1	Existing Fleet by Containment Type, end-2018 [32, p. 54] . . . . .	18
4.2	Self-supported tanks [78] . . . . .	19
4.3	Moss-type LNG carrier schematics [65] . . . . .	19
4.4	Cross-sectional view of MOSS-design [17, p. 231] . . . . .	20
4.5	Cross-sectional view of a SPB-tank [56] . . . . .	21
4.6	Structure of a membrane tank [50] . . . . .	21
4.7	Mark III structure [2] . . . . .	22
4.8	NO96 structure [3] . . . . .	23
4.9	Cross-sectional wall structure of a KC-1 LNG tank, with dimensions in [mm] [38] . . . . .	24
4.10	LH <sub>2</sub> storage sphere at KSC [44] . . . . .	25
4.11	Storage tank designed for the pilot concept as part of the HESC project [23, p. 20] . . . . .	25
4.12	Cluster tanks [48] . . . . .	26
5.1	Graphs of surface-area to volume for different geometrical shapes . . . . .	29
5.2	Scantling of Moss stretched tank [22, p.9] . . . . .	30
5.3	Base case design for support element of the inner spherical shell . . . . .	34
5.4	Deformation of different types of support systems under similar boundary conditions . . . . .	35
5.5	Dimensions of the suggested supportive system for the preliminary design . . . . .	37
5.6	Design of the external support . . . . .	39
5.7	Thermal circuit of a spherical cryogenic tank . . . . .	40
5.8	Schematic view of $k_a$ and the integral mean value between two temperatures [31] . . . . .	42
5.9	BOR-insulation thickness relationship of a spherical LH <sub>2</sub> storage vessel for different insulation types computed using Equation. 5.11 (own work) . . . . .	45
5.10	BOR-insulation thickness relationship of a spherical LH <sub>2</sub> storage vessel for (at 1.00 bar pressure) computed using Equation 5.11 (own work) . . . . .	46
5.11	Representation of the two spherical walls with a distance between them of 0.5 m, 1.0 m and 3.0 m . . . . .	47
5.12	BOR-insulation thickness relationship of a spherical LH <sub>2</sub> storage vessel ( $1.33 \cdot 10^{-6}$ bar) computed using Equation 5.11 (own work) . . . . .	48
5.13	BOR-insulation thickness relationship of a spherical LH <sub>2</sub> storage vessel (MLI at $1.33 \cdot 10^{-9}$ bar pressure) using Equation 5.11 (own work) . . . . .	48
5.14	Thermal circuit inside a skirt . . . . .	49
5.15	BOR-height relationship of a skirt used as a supportive system in LH <sub>2</sub> storage tanks . . . . .	50
6.1	Mesh for the spherical geometry of the containment system . . . . .	53
6.2	Method of binding the skirt to the spherical tank in a LNG Moss Rosenberg-design [1] . . . . .	54
6.3	Mesh for the spherical geometry of the containment system . . . . .	55
6.4	Comparison between a proposed and a personally made mesh of the skirt . . . . .	56
6.5	Mesh elements used in the Static Structural Analysis . . . . .	57
6.6	Sketch of the CONTA174 mesh element associated with Target surfaces [9] . . . . .	57
6.7	Weight distribution of insulation . . . . .	58
6.8	Representation of hydrostatic pressure resulting from movement of the tank on sea [61] . . . . .	60
6.9	Highlighted area where the fixed support is applied . . . . .	61

6.10	Geometries used for the verification analysis . . . . .	63
6.11	Deformation of P1 under loads existent for a motionless system . . . . .	69
6.12	Hydrostatic pressure distribution influenced by wave-induced accelerations [Pa] . .	71
6.13	Deformation of P1 under loads existent for a system in motion on sea . . . . .	72
6.14	Temperature profile based on the existent thermal loads . . . . .	74
6.15	Deformation in the solely presence of thermal loads [m] (x20) . . . . .	75
6.16	Deformation under thermal loads and loads existent for a motionless system (x20)	76
6.17	Highest stresses caused by thermal loads and loads present on a motionless system	76
6.18	Representation of the maximum von-Mises Stresses existent under themal and me- chanical loads of a motionless system . . . . .	77
7.1	Preliminary design with the insulation layer highlighted in orange . . . . .	79
7.2	Mesh setup for 3D Steady-State Thermal analysis . . . . .	79
7.3	Mesh elements used in the Steady-State Thermal Analysis . . . . .	80
7.4	3D-designs used in the thermal simulations conducted to verify the analysis . . . .	81
7.5	Temperature profile for the simulated cases . . . . .	83
7.6	Heat flux profile of Ideal and PUF insulation [ $W/m^2$ ] . . . . .	84
8.1	Design of A1 system with 0.3 m insulation thickness . . . . .	87
8.2	Mesh of A1 system . . . . .	88
8.3	Variation of k-value with CVP for three bulk insulation materials [1 millitor = 0.13 Pa] [24] . . . . .	90
8.4	Boil-off rate variation with different thicknesses of the external PUF insulation . .	91
8.5	Temperature on the outer tank surface varying with different thicknesses of the external PUF insulation . . . . .	92
8.6	Design of A2 system with 0.4 m thick internal insulation and 1.0 m thick external PUF insulation . . . . .	93
8.7	Mesh of A2 system . . . . .	94
8.8	Temperature profile from the thermal simulation of the A1 system [ $^{\circ}C$ ] . . . . .	95
8.9	Deformation [m] of the A1 design under mechanical loads (x19) . . . . .	96
8.10	A1 system: von-Mises and maximum shear stress probes . . . . .	97
8.11	Temperature profile from the thermal simulation of the A2 system [ $^{\circ}C$ ] . . . . .	98
8.12	Deformation [m] of the A2 design under mechanical loads (x19) . . . . .	99
9.1	Designs of the modeled and analysed tanks: P1 (left), A1 (center) & A2 (right) . .	101
11.1	Possible grid stiffened panels for the structural reinforcement of the external tank [14] . . . . .	109
11.2	A1 system: von-Mises and maximum shear stress probes . . . . .	110
E.1	Dimensions of the preliminary design P1 [m] . . . . .	A-10
E.2	Dimensions of the alternative design A1 [m] . . . . .	A-11
E.3	Dimensions of the alternative design A2 [m] . . . . .	A-12
F.1	Setup 1 (2D-axisymmetry): mesh representation and results . . . . .	A-13
F.2	Setup 2 (Cyclic-symmetry): mesh representation and results . . . . .	A-14
F.3	Setup 3 (High quality mesh): mesh representation and results . . . . .	A-15
F.4	Setup 4 (Most favourable option): mesh representation and results . . . . .	A-16
F.5	Results from Simulation C1 for 3D-design [Pa] . . . . .	A-17
F.6	Results from Simulation C1 for 3D-design [Pa] . . . . .	A-18
F.7	Results from Simulation C2 for 2D-design [Pa] . . . . .	A-19
F.8	Results from Simulation C2 for 3D-design [Pa] . . . . .	A-20
F.9	Results from Simulation C3 for 2D-design [Pa] . . . . .	A-21
F.10	Results from Simulation C3 for 3D-design [Pa] . . . . .	A-22
G.1	PS1: von-Mises Stress [Pa] . . . . .	A-23
G.2	PS1: Maximum Shear stress [Pa] . . . . .	A-24
G.3	PS1: Maximum Principal stress [Pa] . . . . .	A-25
G.4	PS2: von-Mises Stress [Pa] . . . . .	A-26

---

G.5	PS2: Maximum Shear stress [Pa]	A-27
G.6	PS2: Maximum Principal stress [Pa]	A-28
G.7	PS3: von-Mises Stress [Pa]	A-29
G.8	PS3: Maximum Shear stress [Pa]	A-30
G.9	PS3: Maximum Principal stress [Pa]	A-31
H.1	A1: von-Mises Stress [Pa]	A-32
H.2	A1: Maximum Shear stress [Pa]	A-33
H.3	A1: Maximum Principal stress [Pa]	A-34
H.4	A2: von-Mises Stress [Pa]	A-35
H.5	A2: Maximum Shear stress [Pa]	A-36
H.6	A2: Maximum Principal stress [Pa]	A-37

# List of Tables

1.1	Chapter overview . . . . .	3
4.1	Characteristics of Mark III systems [2] . . . . .	22
4.2	Characteristics of NO96 systems [3] . . . . .	23
4.3	Properties and minimum liquefaction work required for different gases . . . . .	27
5.1	Loads for the spherical tanks [15] . . . . .	28
5.2	Dimensions for the inner tank of the case study LH <sub>2</sub> cryogenic vessel . . . . .	29
5.3	Material properties for AISI 316, Al alloy 5083 and PA6 GF50 [52][51][26][25] . . . . .	31
5.4	Weight [tonnes] of inner tank + cargo for different cargo liquids and wall-materials . . . . .	31
5.5	Mechanical properties of AISI 304 and AISI 316 at ambient temperature [28] . . . . .	32
5.6	Material properties for low carbon steel (mild steel), NV-A grade type [16, p.16][34] . . . . .	33
5.7	Weight of the different containment system elements . . . . .	38
5.8	Gas-purged and evacuated insulations and their $k_{\text{eff}}$ [mW/(m·K)] [19, p.54] . . . . .	41
5.9	Commercial Multi-layer insulation types at $1.33 \cdot 10^{-9}$ bar [19, p.59] . . . . .	42
5.10	Summary of the constants of the empirical function for the treated insulation systems [31] . . . . .	43
5.11	Trade name and density of the three bulk-fill insulations [62] . . . . .	44
5.12	$k_a$ -values for bulk-fill insulation and pure vacuum at different evacuated levels [62] . . . . .	44
5.13	Thermal comparison of the three metals used in the skirts of the Moss Rosenberg-design . . . . .	50
6.1	Change in density of different segment on the geometry . . . . .	59
6.2	Loads acting on the designed-system . . . . .	59
6.3	Design accelerations in ULS conditions [64] . . . . .	61
6.4	von-Mises stresses caused by the internal and external overpressure [Pa] . . . . .	64
6.5	AAD [%] for the C1 Simulation . . . . .	64
6.6	von-Mises stresses on the internal tank caused by the internal pressure and self-weight forces [Pa] . . . . .	65
6.7	von-Mises stresses on the internal tank caused by the hydrostatic pressure, self-weight forces and internal overpressure [Pa] . . . . .	66
6.8	von-Mises stresses of the skirt for different symmetry and mesh designs . . . . .	67
6.9	Stress-limits before failure . . . . .	68
6.10	Maximum stresses obtained from PS1 . . . . .	70
6.11	Maximum stresses obtained from PS2 . . . . .	73
7.1	Variables necessary to calculate the desired heat flow . . . . .	81
7.2	Heat transfer rate Q[W] through the containment walls and the insulation layer . . . . .	82
7.3	Heat transfer rate through skirt . . . . .	82
7.4	Values of the temperature probes taken from the temperature profile [°C] . . . . .	83
7.5	Thermal analysis results of the preliminary design . . . . .	84
8.1	Vacuum range [71] . . . . .	89
8.2	Change in density of different segments on the geometry of the A2 system . . . . .	93
8.3	Temperature profile of A1 design . . . . .	95
8.4	Results from the thermal analysis of A1 design . . . . .	95
8.5	Maximum stresses obtained from simulation of A1 . . . . .	97
8.6	Results from the thermal analysis of A2 design . . . . .	98
8.7	Maximum stresses obtained from simulation of A2 . . . . .	99



9.1	Results from the thermal analysis of the three models . . . . .	102
9.2	Maximum deformation of the preliminary design under different loading conditions	102
9.3	Results from the structural analysis of the three models . . . . .	102

# Nomenclature

## Latin Symbols

$A$	Area	$m^2$
$C$	Circumference	m
$d$	Diameter	m
$E$	Young's modulus	-
$F$	View factor	-
$G''$	Weight force per unit area	$kN/m^2$
$H$	Latent Heat	$kJ/kg$
$h$	Height   Heat transfer coefficient	m   $W/(m^2 \cdot K)$
$k$	Thermal conductivity	$W/(m \cdot K)$
$n$	Integer number	-
$N'$	Internal force in a tank	$N/m$
$p$	Pressure	bar, Pa
$q$	Heat transfer rate	W
$q'$	Heat transfer rate per unit length	$W/m$
$q''$	Heat flux	$W/m^2$
$q'''$	Heat transfer rate per unit volume	$W/m^3$
$R$	Thermal resistance	$W/K$
$r$	Radius	m
$T$	Temperature	K, °C
$t$	Thickness	m
$u$	Deformation	m
$V$	Volume	$m^3$

---

## Greek Symbols

$\alpha$	Coefficient of thermal expansion	-
$\Delta$	Difference	-
$\gamma$	Specific weight of the liquid	kN/m <sup>3</sup>
$\nu$	Poisson's ratio	-
$\phi$	Circumferential angle	°
$\phi$	Meridional angle	°
$\rho$	Density	kg/m <sup>3</sup>
$\sigma$	Stress   Stefan Boltzmann constant (Thermal)	Pa   W/(m <sup>2</sup> ·K <sup>4</sup> )
$\tau$	Shear stress	Pa

## Subscripts and Superscripts

$\phi$	Meridional
$\theta$	Circumferential
a	Apparent
b	Bottom
cond	Conduction
conv	Convection
eff	Effective
g	Gas or gravitational
i/in	Inner, Internal
ins	Insulation
LH <sub>2</sub>	Liquid hydrogen
LNG	Liquid natural gas
m	Middle
o/out	Outer, External
rad	Radiation
ref	Reference
s	Surface
sim	Simulation
sk	Skirt
t	Top

---

tot	Total
vap	Vaporization

## Abbreviations

A	Alternative design	
AAD	Absolute Average Deviation	
ALS	Accident limit state	
APDL	Ansys Parametric Design Language	
BOR	Boil-off rate	%/day
C	Verification/check	
CO <sub>2</sub>	Carbon dioxide	
FLS	Fatigue limit state	
H <sub>2</sub>	Hydrogen gas	
L	Load	
LAR	Liquid Argon	
LCH <sub>4</sub>	Liquid methane	
LCO <sub>2</sub>	Liquid carbon dioxide	
LH <sub>2</sub>	Liquid hydrogen gas	
LIN	Liquid nitrogen	
LN <sub>2</sub> O	Liquid nitrous oxide	
LNG	Liquid natural gas	
LOX	Liquid oxygen	
MLI	Multi-layer insulation	
NBP	Normal boiling point	
P	Preliminary design	
PS	Simulation of the preliminary design	
PUF	Polyurethane foam	
ULS	Ultimate limit state	
UNFCCC	United Nations Framework Convention on Climate Change	

Observation: Some symbols listed here may differ from what is defined in some equations, but a clear explanation should be given inside the text.

---

# Chapter 1

## Introduction

### 1.1 Motivation for use of hydrogen as a future fuel

Based on the 2019 reports of UNFCCC secretariat<sup>1</sup>, the amount of global annual emission by the end of 2030 should be less than 42.51 Gt CO<sub>2</sub> eq<sup>2</sup>, in order to achieve the objective of limiting the global warming to 2°C. It implies that the emissions must achieve a peak in the nearest future, and the levels of greenhouse gasses emitted must be 16.4 %<sup>3</sup> less in 2030 than in 2016 [63]. This indicates the necessity for clean and CO<sub>2</sub>-free sources, carriers and storages of energy, trending away from the carbon based ones towards greener ones. An example is hydrogen. The depletion of fossil fuels and global warming are two of humanity's current problems that require a long-lasting resolve. Hydrogen is an energy vector which can solve both issues, due to its abundance and its carbon-free products, water and electrical energy, which result from the combustion process. To sum it up, the reasons why hydrogen is considered a fuel of the future are as followed:

- Hydrogen is bountiful in supply and therefore undepletable; may as well be considered a renewable energy carrier.
- Hydrogen is clean and non-toxic since it doesn't negatively affect the environment, nor the human health.
- Due to its great gravimetric energy density, it is possible to produce greater amounts of energy from hydrogen than from any other know fuels of similar mass quantities. Hydrogen produces between 120 to 142 MJ of energy per kg of burnt fuel, while diesel produces only 45.3 MJ. [27, p. 12-15]

### 1.2 Motivation for storing hydrogen in liquid form

Despite all the positive aspects, the use of hydrogen as a fuel has also some disadvantages. The major drawback, besides high extraction costs and other safety issues, is the very low volumetric energy density in comparison to other fuels. At atmospheric temperature and pressure, hydrogen gas contains an energy amount of only 9.89 MJ/m<sup>3</sup>. As for diesel at similar conditions, the value is of 36 800 MJ/m<sup>3</sup>. [29, p. 6] Hence, for a sustainable hydrogen industry, improving the volumetric energy density of stored hydrogen while maintaining its gravimetric energy density is subject to substantial research.

A promising solution to solving this matter has proven to be storing pure hydrogen in its liquid state. At NBP<sup>4</sup> conditions, liquid hydrogen contains around 8 600 MJ/m<sup>3</sup> which is roughly 860 times higher than the energy amount of hydrogen gas at atmospheric conditions and circa three times higher than compressed H<sub>2</sub>(g) at 350 bar, containing 2 800 MJ/m<sup>3</sup> [29, p. 6]. Being able to operate at atmospheric pressure is an advantage since large scale pressure vessels require very thick walls. Liquid hydrogen has another positive quality. Since hydrogen's atomic weight in pure form is the lowest among all elements, LH<sub>2</sub> is a satisfactory solution for the low-weight demand.

---

<sup>1</sup>Secretariat of the United Nations Framework Convention on Climate Change

<sup>2</sup>Range of uncertainty 36.28–43.63 Gt CO<sub>2</sub>

<sup>3</sup>Range of uncertainty: 14.1–28.6 %

<sup>4</sup>Normal boiling point: defined as the temperature at which a liquid boil at 1.00 atmosphere of pressure [30]

This requirement exists not only in the industrial sector, but in the transportation sector as well.

### 1.3 Motivation for designing a low-loss, high carrying-capacity storage tank

With today's technology, storing and transporting industrial quantities of liquid hydrogen is challenging; the cause being two essential hydrogen properties. It has a normal boiling point temperature of 20.3 K, value above which the phase of H<sub>2</sub> becomes gaseous. This, together with the low volumetric heat of vaporisation<sup>5</sup> of 31.6 MJ/m<sup>3</sup> are the factors that affect the boil-off rate caused by heat leakage. Both production and liquefaction processes are highly demanding in terms of power resources. Approximately a third of the the energy amount of hydrogen is necessary for liquefying the gas. Since the boil-off gas must be released or re-liquefied to maintain a constant pressure inside the containment system, the evaporated amount is considered cargo loss. Hence, the idea behind an effective storage system is reducing the boil-off rate as much as possible. For specific quantities of stored liquid, the variable that can be changed to reduce BOR is the heat flow into the cryogenic tank. This can be achieved by using high quality insulation concepts and suitable structural designs.

### 1.4 Objective and scope

An acceptable boil-off rate is considered to be lower than 0.2 % per day, a value analog to that of existing LNG storage systems. With the objective of achieving this goal, a model using different insulation types and concepts is to be established and analysed, both structurally and thermally.

The starting point of the modeling approach is based on research on conventional containment concepts of LNG and cryogenic liquids, as well as a baseline LH<sub>2</sub> storage tank design. The predefined model is a double-walled spherical tank with insulation in between. The outer wall is supported by a cylindrical skirt at equatorial area of the tank, while the inner vessel is suspended by an equatorial ring through load bearing elements made of a material which acts as a thermal breaker.

Upon the results from simulations of the preliminary design, alternative models considered from a more practical approach are to be further investigated. With regards to validation of the results with literature and practical design considerations, a proposed plan for further work is to be included.

Reference is made to the prior specialized project work entitled "Solution for transport and storage of liquefied hydrogen" [23], setting the groundwork of the topic of storage tank concepts for LH<sub>2</sub>. In dialog with the supervisor, considering the complexity of the study, some topics receive less attention or are omitted. Such topics are the possible development of the model by evaluating shield refrigeration, and the execution of a draft scientific paper based on the work performed; which is entirely excluded.

### 1.5 Thesis structure

The thesis is structured into three parts. Chapters 2, 3, 4 includes basic and general information on which the evaluations and analysis are based on. The aforementioned chapters also facilitates the understanding of some terminologies used in the thesis. Chapters 5, 6 and 7 covers the concept of a preliminary design used as a start-point for the analysis of an improved design. Chapters 8, 9, 10 and 11 handles the analysis of the main design by presenting and discussing the results, followed by some proposed ideas for a future work. Table 1.1 describes each chapter in a detailed manner.

---

<sup>5</sup>Value calculated from the LH<sub>2</sub>'s latent heat of vaporization of 446.1 kJ/kg and density of 70.8 kg/m<sup>3</sup>.

Table 1.1: Chapter overview

Chapter	Title & Description
2	<b><u>Methodology and Theory behind the thesis</u></b>
	The chapter is divided into three sections. The first section gives a general overview of the approach used to conduct mechanical and thermal analysis of several design concepts of the storage tank. The last two sections list the governing theoretical equations required in this study, as well as the governing equations used by the simulation software. These sections cover the mechanical and the thermal analysis respectively.
3	<b><u>Insulation materials and concepts</u></b>
	Briefly highlights the three main existing types of insulation materials, followed by a short summary with an attached Appendix which enumerates the advantages and disadvantages of the specific materials used for thermally isolating cryogenic storage systems.
4	<b><u>LNG and cryogenict containment - background for LH<sub>2</sub></u></b>
	Is divided into three sections: two main sections describing several existing concepts for larger LNG and cryogenic storage tanks respectively, and a third section comparing hydrogen with other cryogenic liquids, especially with LNG. The description includes the geometry, materials which different components are made of, and the achieved boil off gas rates.
5	<b><u>LH<sub>2</sub> tank modelling approach - initial considerations</u></b>
	Sets the basis for an analysis of a preliminary LH <sub>2</sub> storage tank design by evaluating and describing possible geometries, properties and dimensions for several components which form the structure. The two main sections of Chapter 5 cover the aforementioned attributes from a mechanical and a thermal perspective, individually.
6	<b><u>Structural analysis of preliminary design</u></b>
	The chapter covers the structural analysis of the preliminary tank design. It is divided into three sections. The first section includes a description of the several setup considerations existing in the analysis, such as the designed geometry and dimensions, designed mesh, materials assigned and boundary conditions. The second section outlines three check-up simulations which are conducted with the purpose of validating the aforementioned analysis setup. The third section present the final results gathered after a simulation of a complete setup of the preliminary tank design.
7	<b><u>Thermal analysis of preliminary design</u></b>
	Resembles Chapter 6, but covers the thermal analysis and evaluates the heat leakage from the ambient into the containment system.
8	<b><u>Analysis of alternative designs</u></b>
	Based on the results from the analyses of the preliminary design, two alternative models are structurally and thermally analysed. The purpose is to compensate for some uncertainties and validate possible improvements.
9	<b><u>Discussion</u></b>
	The chapter is divided into two parts. The first part summarises the overall obtained results and the second part discusses possible uncertainties with regard to the values obtained.
10	<b><u>Conclusion</u></b>
	Concludes the key findings of the present study.
11	<b><u>Proposal for further work</u></b>
	A plan for further work is necessary as the theme of the preset study is relatively challenging. Chapter 11 enumerates some topics which can be further investigated and elaborated.

---

## Chapter 2

# Methodology and Theory behind the thesis

This study is based on a combination between theoretical analyses and computer simulations. This chapter includes a briefly description of the approach and programs used for the simulations as well as some basic theory applied throughout the process of completing the thesis.

### 2.1 Overall approach

The results evaluated are produced by using the finite element method. Considering the design described in the task-list given beforehand, a preliminary and simple model of the cryogenic container is first decided. The tank is then simulated in terms of structural strength and heat flow to determine its boil off rate. Based on the results, new adjustments are evaluated for more feasible models. With respect to the results of the alternative tanks, a final conclusion is drawn based on which a further work is proposed.

Regarding the literature survey, as defined by Bonnie J. M. Swoger [66], the following types of documentation are studied and used throughout the thesis:

- Primary research articles which are published in peer reviewed journals.
- Technical reports produced by companies, government agencies and NGO's.
- Books containing theoretical and general information or data on subjects different fields of study.

Other types of literature such as conference proceedings and online publications are also used, but in a smaller degree.

#### 2.1.1 Software used

The finite element analysis has been conducted with the help of ANSYS Mechanical APDL solver in combination with AutoCAD 2020, Solidworks 2019 and ANSYS Meshing in order to obtain the geometrical design and meshing. Figure 2.1 is a self-made diagram, inspired by a flowchart created by Arun Tamilarasn in one of his works [67], which depicts the step-by-step procedure adopted to achieve reliable simulated data.



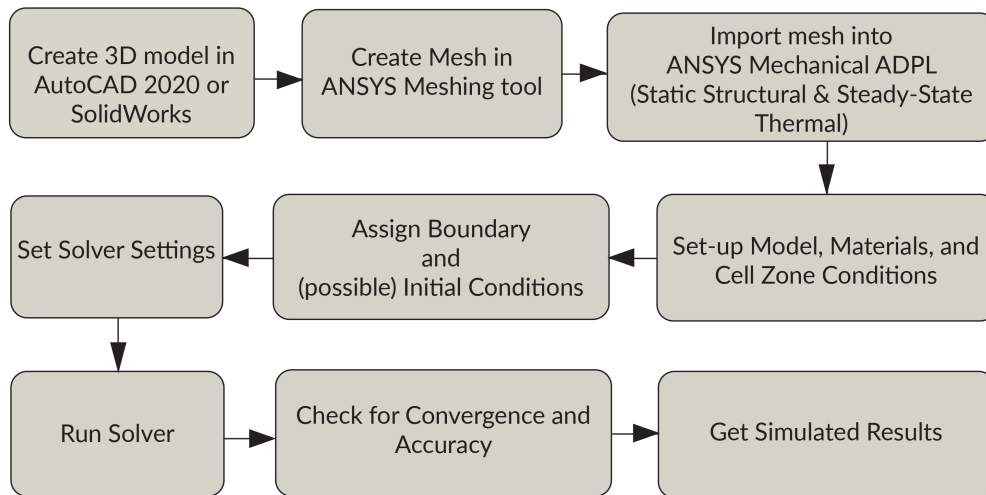


**Figure 2.1:** Flowchart depicting modelling and simulation procedure

The reason why AutoCAD is used is due to the personal existing knowledge in using this software as a modelling program, making it easier to create a new design from scratch. The use of Solidworks is justified by two different reasons:

- It is easier to resize different dimensions, and set different constrains.
- The ambition of learning to work with a new design software.

### 2.1.2 Approach for structural analysis

For the structural simulation the analysis is restricted to homogeneous, isotropic, static structural analysis. Initial dimensions, and geometries as well as material types are considered based on the literature survey on LNG and other cryogenic storage tanks. These data result in a simplified design which is gradually subjected to several mechanical and thermal loads so that a real-case scenario can be simulated. Several types of stresses and the total deformation is analyzed using the finite element method. Depending on the outcome of the simulation, redimensioning and geometrical reconstruction occur for the proposition of alternative designs.

In order to validate the simulated results, different loads are incorporated one by one while comparing the outcome, gradually, with theoretically obtained values.

### 2.1.3 Approach for thermal analysis

The thermal analysis is based on simple steady-state thermal simulations. Several materials and thicknesses for the insulation layer are firstly evaluated and compared with respect to the practical application and the performance of minimizing the heat ingress. Three different insulation materials are added one by one to the preliminary design analysed structurally beforehand, and the resulted heat flow and boil off rates are compared between each other. The three simulations represent the worst case, the ideal case and a case in-between. For the alternative desings, the case in-between is further used, containing possible adjustments.

The validation of the simulated results is done firstly by simulating the heat ingress through the insulation layer and the supportive element separately. The outcome is compared with values obtained from theoretical equations.

## 2.2 Theory behind the mechanical analysis

The theory presented in this section is theory strictly necessary for computational purposes to validate the simulated results, and to offer a better understanding on how ANSYS Mechanical APDL uses input data to calculate output. Thus, the equations to follow are just highlighted and

do not have the theoretical background thoroughly explained. Most of the equations are designed for 1D analysis, but in some cases equations for 3D analysis are also formulated. However, it is well known that the theoretical background is much more detailed for such a complex structure, but the most important equations are represented in this report.

### 2.2.1 Governing theoretical equations for the structural analysis

This subsection refers to the theory explained in [40] for Equations 2.1 to 2.6 and [58] for the Equations 2.7 to 2.16. The remaining equations of the subsection are taken from [15, p.36] and [21, p. 304].

The force equilibrium inside a thin-walled spherical object requires that:

$$\pi(r_o^2 - r_i^2)\sigma_t - \pi r_i^2 p_i = 0 \quad (2.1)$$

where  $r_o = r_i + t$  [m] is the radius from the center of the sphere to its exterior,  $r_i$  [m] is the inner radius,  $p_i$  [Pa] is the internal pressure,  $t$  [m] is the thickness of the spherical wall and  $\sigma_t$  [Pa] is the circumferential, or tangential, or hoop stress at any location and in any tangential orientation, which are similar due to symmetry. The shear stresses are equal to zero. This gives:

$$\sigma_t = \frac{r_i^2 p_i}{2r_i + t^2} \quad (2.2)$$

which can be simplified to

$$\sigma_t = \frac{p_i r_i}{2t} \quad (2.3)$$

because  $t^2 \ll 2r_i t$

The stress caused by the external pressure comes from

$$-r_o^2 p_o \int_0^\pi \sin^2 \theta d\theta \int_0^\pi \sin \phi d\phi - \pi(r_o^2 - r_i^2)\sigma_t + \pi r_i^2 p_i = 0 \quad (2.4)$$

and is equal to

$$\sigma_t = \frac{r_i^2 p_i - r_o^2 p_o}{(r_o + r_i)t} \quad (2.5)$$

which can be simplified to

$$\sigma_t \approx \frac{(p_i - p_o)r_i}{2t} \quad (2.6)$$

with  $r$  being the radius of interest, assuming  $r_o \approx r_i = r$ .

The gravity and other types of motion accelerations creates gravitational and acceleration/inertial loads which are weight dependent.

For a spherical tank, the internal forces created by the tank's self-weight for the upper hemisphere:

$$N'_{\phi,w} = -\frac{G''r}{1 + \cos \phi} \quad (2.7)$$

$$N'_{\theta,w} = -G''r \cdot \left( \cos \phi - \frac{1}{1 + \cos \phi} \right) \quad (2.8)$$

Internal forces created by the tank's self-weight for the lower hemisphere:

$$N'_{\phi,w} = -\frac{G''r}{1 - \cos \phi} \quad (2.9)$$

$$N'_{\theta,w} = -G''r \cdot \left( \cos \phi - \frac{1}{1 - \cos \phi} \right) \quad (2.10)$$

In both cases,  $N'_{\phi,w}$  [N/m] is the meridional force produced by the weight of the tank,  $N'_{\theta,w}$  [N/m] is the circumferential force produced by the weight of the tank,  $G''$  [kN/m<sup>2</sup>] is the weight per unit area,  $r$  [m] is the radius of the spherical tank and  $\phi$  [°] is the angle along the meridional line.

Internal forces created by the hydrostatic pressure and internal ambient pressure inside the upper hemisphere:

$$N'_{\phi,l} = \frac{\gamma r^2}{6} \left(1 - \frac{2 \cos^2 \phi}{1 + \cos \phi}\right) + \frac{r p_g}{2} \quad (2.11)$$

$$N'_{\theta,l} = \frac{\gamma r^2}{6} \left(5 - 6 \cos \phi + \frac{2 \cos^2 \phi}{1 + \cos \phi}\right) + \frac{r p_g}{2} \quad (2.12)$$

Internal forces created by the hydrostatic pressure and internal ambient pressure inside the lower hemisphere:

$$N'_{\phi,l} = \frac{\gamma r^2}{6} \left(5 + \frac{2 \cos^2 \phi}{1 - \cos \phi}\right) + \frac{r p_g}{2} \quad (2.13)$$

$$N'_{\theta,l} = \frac{\gamma r^2}{6} \left(1 - 6 \cos \phi - \frac{2 \cos^2 \phi}{1 - \cos \phi}\right) + \frac{r p_g}{2} \quad (2.14)$$

In both cases, the  $N'_{\phi,l}$  [N/m] is the meridional force produced by the hydrostatic pressure and the gas pressure,  $N'_{\theta,l}$  [N/m] is the circumferential force produced by the same pressures,  $\gamma$  [kN/m<sup>3</sup>] is the specific weight of the liquid,  $p_g$  [Pa] is the uniform ambient pressure or the gas pressure.

All the aforementioned forces create meridional and circumferential stresses expressed by:

$$\sigma_{\phi} = \frac{N'_{\phi}}{t} \quad (2.15)$$

$$\sigma_{\theta} = \frac{N'_{\theta}}{t} \quad (2.16)$$

where  $\sigma_{\phi}$  [Pa] and  $\sigma_{\theta}$  [Pa] are the meridional and circumferential stresses,  $N'_{\phi}$  [N/m] and  $N'_{\theta}$  [N/m] are the sum of the forces produced by the weight of the cargo plus the self-weight of the tank, and  $t$  [m] being is the thickness of the spherical wall.

It should be noted that the source [58] refers to the  $N'_{\phi}$  and  $N'_{\theta}$  as internal forces ( $N_{\phi}$  &  $N_{\theta}$ ) which should have the SI unit [N]. The units are neither stated in the reference paper. By verifying the equations it seems as the meridional and circumferential forces are acting per unit length, resulting in [N/m] as unit for the two, ergo the peculiar notation  $N'$  used in this thesis.

### Equivalent and thermal stress

The von-Mises stress<sup>1</sup> equation which is one of the formulas used to find out if a structure resists against different loads causing deformation is expressed in case of a sphere as:

$$\sqrt{\sigma_{\phi}^2 + \sigma_{\theta}^2 - \sigma_{\phi} \sigma_{\theta} + 3\tau^2} \quad (2.17)$$

where  $\sigma_{\phi}$  [Pa] is the meridional normal stress,  $\sigma_{\theta}$  [Pa] is the circumferential normal stress and  $\tau$  [Pa] is the shear stress.

Since in the present study a relatively high temperature difference exists, the thermal deformation must be considered. The equation for thermal strain is as follows:

$$\varepsilon_o = \alpha \Delta T \quad (2.18)$$

where  $\alpha$  is the coefficient of thermal expansion and  $\Delta T$  is the change of temperature.

From the total strain can be therefore written as

$$\varepsilon = \varepsilon_e + \varepsilon_o = E^{-1} \sigma + \alpha \Delta T \quad (2.19)$$

where  $\varepsilon_e$  is the elastic strain due to mechanical loads with  $E$  being the Young's modulus which measures the stiffness of a solid material.

By inverting the Equation 2.19, the stress is then given by

$$\sigma = E(\varepsilon - \varepsilon_o) \quad (2.20)$$

---

<sup>1</sup>Also know as the equivalent stress

### 2.2.2 Governing equations used by ANSYS Mechanical APDL in Static Structural

The governing equations used by the software are taken directly from ANSYS Workbench Help - Theory Reference with focus on Structural Fundamentals [12] as it is the most reliable source for this topic. However, a secondary source is used, which is the book entitled Finite Element Simulations with ANSYS Workbench 12 by Huei-Huang Lee [46, p. 24-30].

The scope of the structural analysis is to find the responses of a structural system to environmental conditions. These responses are characterized by displacements, stresses or strains.

The displacement field  $\{u\}$ , also known as the deformation, is a vector expressed in terms of three components which are functions of position.

$$\{u\} = \{u_x u_y u_z\} \quad (2.21)$$

The stress state at a certain point is described by the following tensor:

$$\sigma = \begin{bmatrix} \sigma_x & \tau_{xy} & \tau_{xz} \\ \tau_{yx} & \sigma_y & \tau_{yz} \\ \tau_{zx} & \tau_{zy} & \sigma_z \end{bmatrix} \quad (2.22)$$

which, being symmetric has six independent components, dependent on the position. The strain state can be written in a similar form as Equation 2.22:

$$\varepsilon = \begin{bmatrix} \varepsilon_x & \gamma_{xy} & \gamma_{xz} \\ \gamma_{yx} & \varepsilon_y & \gamma_{yz} \\ \gamma_{zx} & \gamma_{zy} & \varepsilon_z \end{bmatrix} \quad (2.23)$$

This represents also a symmetric tensor with six independent components described as functions of position.

The quantities expressed in 2.21, 2.22, 2.23 are not independent of each other and they can be solved by 15 different equations which are used by ANSYS Mechanical APDL in the structural analysis as governing equations. There are three equilibrium equations, six equations describing the strain-displacement relation and six equations describing the stress-strain relation, also known as the Hooke's law

The equilibrium equations can either be inside the structural body or on the boundary surface. In the inside, the equations are expressed as:

$$\begin{aligned} \frac{\partial \sigma_x}{\partial x} + \frac{\partial \tau_{xy}}{\partial y} + \frac{\partial \tau_{xz}}{\partial z} + b_x &= 0 \\ \frac{\partial \tau_{yx}}{\partial x} + \frac{\partial \sigma_y}{\partial y} + \frac{\partial \tau_{yz}}{\partial z} + b_y &= 0 \\ \frac{\partial \tau_{zx}}{\partial x} + \frac{\partial \tau_{zy}}{\partial y} + \frac{\partial \sigma_z}{\partial z} + b_z &= 0 \end{aligned} \quad (2.24)$$

On the boundary surface, the equilibrium equations are:

$$\begin{aligned} \sigma_x n_x + \tau_{xy} n_y + \tau_{xz} n_z + s_x &= 0 \\ \tau_{yx} n_x + \sigma_y n_y + \tau_{yz} n_z + s_y &= 0 \\ \tau_{zx} n_x + \tau_{zy} n_y + \sigma_z n_z + s_z &= 0 \end{aligned} \quad (2.25)$$

The strain-displacement relation is described by:

$$\begin{aligned}
 \varepsilon_x &= \frac{\partial u_x}{\partial x}, \varepsilon_y = \frac{\partial u_y}{\partial y}, \varepsilon_z = \frac{\partial u_z}{\partial z} \\
 \gamma_{xy} &= \frac{\partial u_x}{\partial y} + \frac{\partial u_y}{\partial x} \\
 \gamma_{yz} &= \frac{\partial u_y}{\partial z} + \frac{\partial u_z}{\partial y} \\
 \gamma_{zx} &= \frac{\partial u_z}{\partial x} + \frac{\partial u_x}{\partial z}
 \end{aligned} \tag{2.26}$$

The Hooke's law, also called material model is expressed as:

$$\begin{aligned}
 \varepsilon_x &= \frac{\sigma_x}{E} - \nu \frac{\sigma_y}{E} - \nu \frac{\sigma_z}{E} \\
 \varepsilon_y &= \frac{\sigma_y}{E} - \nu \frac{\sigma_x}{E} - \nu \frac{\sigma_z}{E} \\
 \varepsilon_z &= \frac{\sigma_z}{E} - \nu \frac{\sigma_x}{E} - \nu \frac{\sigma_y}{E} \\
 \gamma_{xy} &= \frac{\tau_{xy}}{G}, \gamma_{yz} = \frac{\tau_{yz}}{G}, \gamma_{zx} = \frac{\tau_{zx}}{G}
 \end{aligned} \tag{2.27}$$

where  $G = \frac{E}{2(1+\nu)}$ ,  $E$  is the Young's modulus and  $\nu$  is the Poisson's ratio. Both  $E$  and  $\nu$  are material parameters.

The von Mises stress equation used by ANSYS Mechanical APDL in structural analysis to evaluate fracture is written as

$$\sigma = \sqrt{\frac{1}{2}[(\sigma_x - \sigma_y)^2 + (\sigma_y - \sigma_z)^2 + (\sigma_z - \sigma_x)^2]} \tag{2.28}$$

where  $\sigma_e$  is the von-Mises stress, also know as equivalent stress in ANSYS, and the other stresses come from the stress state matrix highlighted by Equation 2.22.

## 2.3 Theory behind the thermal analysis

Similar to Section 2.2 the theory and governing equations are explained in a straightforward and understandable manner, focusing on the 1D analysis and highlighting the most important equations needed for the thermal analysis. Equations necessary for the 3D analysis are also represented in some cases for better understanding.

### 2.3.1 Governing theoretical equations for the thermal analysis

All the information included in this subsection refers to "Incropera's Principles of Heat and Mass Transfer" [36].

From the analogy that heat flows like current, and that the temperature difference drives the heat flow the same way as voltage drives the electrical current, the heat flow equation can be written as follow:

$$q_{tot} = \frac{\Delta T}{\sum R_{tot}} \tag{2.29}$$

where  $q_{tot}$  [W] is the total heat flow rate of the system,  $\Delta T$  [K] is the temperature difference between two mediums, and  $R_{tot}$  [W/K] is the total thermal resistance of the system.

The resistances can either be connected in series or in parallel. The total resistance connected in series is expressed by

$$R_{tot} = R_1 + R_2 + R_3 + \dots + R_n \tag{2.30}$$

and for resistance connected in parallel, the total resistance equals to

$$R_{tot} = \left( \frac{1}{R_1} + \frac{1}{R_2} + \frac{1}{R_3} + \dots + \frac{1}{R_n} \right)^{-1} \tag{2.31}$$

The heat from one object to another can be transferred in three different ways

- By conduction through a solid
- By convection due to the movement of a gas or a liquid
- By thermal radiation.

This implies that in a composite system, there can be three different types of thermal resistance which can be combined in parallel or in series. The conductive resistance formula is:

$$R_{cond} = \frac{\Delta x}{kA} \quad (2.32)$$

where  $k$  [W/(m·K)] is the conductivity, and  $A$  [m<sup>2</sup>] is the cross-sectional area of the heat flow traveling a distance of  $\Delta x$  [m].

For a spherical geometry, the conductive resistance is expressed as:

$$R_{cond} = \frac{1}{4\pi k} \left( \frac{1}{r_{in}} - \frac{1}{r_{out}} \right) = \frac{r_{out} - r_{in}}{4\pi r_{in} r_{out} k} \quad (2.33)$$

$r_{in}$  [m] and  $r_{out}$  [m] are the inner and outer radius of a spherical shell.

The convective resistance on a spherical shaped surface is:

$$R_{conv} = \frac{1}{hA} = \frac{1}{h4\pi r^2} \quad (2.34)$$

with  $h$  [W/(m<sup>2</sup>·K)] being the heat transfer coefficient of the gas or liquid and  $r$  [m] being the radius.

Since thermal radiation is always present in objects whose temperature is different from absolute zero (0 K), the radiation resistance must also be considered. The equation is as follow:

$$R_{rad} = \frac{1}{h_{rad} A_i} = \frac{1}{\frac{\sigma \varepsilon (T_i^2 + T_j^2)(T_i + T_j)}{\frac{1}{\varepsilon_i} + \frac{A_i}{A_j} \left( \frac{1}{\varepsilon_j} - 1 \right)} A_i \varphi} \quad (2.35)$$

where  $\sigma$  is the Stefan Boltzmann constant 5.675<sup>-8</sup> W/(m<sup>2</sup>·K<sup>4</sup>),  $\varphi$  is the radiation angle coefficient 1, and  $\varepsilon$  is the surface emissivity.

### 2.3.2 Governing equations used by ANSYS Mechanical APDL in Steady-State Thermal

The purpose of conducting a thermal analysis is to have a better understanding of the behaviour and response of a structural system with thermal boundary conditions. The temperature, thermal gradient, and heat flux distribution are thermal quantities that can be obtained from the two types of thermal analysis, steady-state and transient. The steady-state thermal analysis results in temperature or heat flux distribution in a structure when a thermal equilibrium is reached. The transient thermal analysis focuses on the type of changes different thermal quantities suffer over time. However, since it is not conducted in the present study, mostly the steady-state thermal governing equations are highlighted. Similar to Subsection 2.2.2 the source of the equations to follow is the ANSYS Workbench Help -Theory Reference with focus on Heat Flow Fundamentals [35].

The Fourier's law for 1D and 3D space is:

$$q_x'' = -k \frac{\partial T}{\partial x} \quad (2.36)$$

and

$$\begin{Bmatrix} q_x'' \\ q_y'' \\ q_z'' \end{Bmatrix} = -\mathbf{K} \begin{Bmatrix} \frac{\partial T}{\partial x} \\ \frac{\partial T}{\partial y} \\ \frac{\partial T}{\partial z} \end{Bmatrix}$$

where  $q''$  is the heat flux per unit area in the specific direction  $x$ ,  $y$  or  $z$ ,  $T = T(x, t)$  is the temperature field and  $k$  is the thermal conductivity for 1D, and for 3D there is the conductivity matrix which in the case of isotropic materials is:

$$\mathbf{K} = \begin{bmatrix} k & 0 & 0 \\ 0 & k & 0 \\ 0 & 0 & k \end{bmatrix}$$

Based on the Fourier's law and the first law of thermodynamics, the heat flow equation is given by

$$-\left[\frac{\partial q''_x}{\partial x} + \frac{\partial q''_y}{\partial y} + \frac{\partial q''_z}{\partial z}\right] + q''' = c\rho \frac{\partial T}{\partial t} \quad (2.37)$$

where  $q'''$  is the rate of internal heat generation per unit volume of the medium,  $c$  is the specific heat capacity and  $\rho$  is the mass density.

For spherical coordinates Equation 2.37 is represented by

$$\frac{1}{r^2} \frac{\partial}{\partial r} \left( k \cdot r^2 \frac{\partial T}{\partial r} \right) + \frac{1}{r^2 \sin^2 \theta} \frac{\partial}{\partial \phi} \left( k \frac{\partial T}{\partial \phi} \right) + \left( \frac{1}{r^2 \sin \theta} \frac{\partial}{\partial \theta} \right) \left( k \cdot \sin \theta \frac{\partial T}{\partial \theta} \right) + q''' = \rho c \frac{\partial T}{\partial t} \quad (2.38)$$

where  $r$  is the radius,  $\phi$  is the meridional angle or direction, and  $\theta$  is the circumferential angle or direction.

In the case of steady-state where  $\frac{\partial T}{\partial t} = 0$  and isotropic materials, the following Poisson equation results, and must be solved under given boundary conditions:

$$k \nabla^2 T = -q''' \quad (2.39)$$

There are three types boundary conditions considered:

1. Specified temperatures acting on surface  $S_1$ :

$$T = T^* \quad (2.40)$$

with  $T^*$  being the specified temperature.

2. Specified heat flows acting over surface  $S_2$

$$q_{cond} = -k \frac{\partial T}{\partial n} = q^*_{cond} \quad (2.41)$$

with  $n$  being the unit outward normal element and  $q^*$  the specified heat flow.

3. Specified convection surfaces acting over surface  $S_3$

$$q^*_{conv} = h_f (T_s - T_b) \quad (2.42)$$

with  $h_f$  is the film coefficient evaluated at  $(T_b + T_s)/2$  otherwise specified for the element,  $T_b$  is the bulk temperature of the adjacent fluid and  $T_s$  is the temperature at the surface of the model.

Based on 2.39 the Finite Element equation for heat conduction Problems can be written as:

$$\mathbf{K}_T \mathbf{T} = \mathbf{q} \quad (2.43)$$

where  $\mathbf{K}$  is the conductivity matrix,  $\mathbf{T}$  is the vector of nodal temperature and  $\mathbf{q}$  is the vector of thermal loads.

For thermal radiation ANSYS Mechanical APDL uses the Stefan-Boltzmann law for a system of  $N$  enclosures, where the energy balance for each surface in the enclosure for a gray diffuse body is written as:

$$\sum_{i=1}^N \left( \frac{\delta_{ji}}{\varepsilon_i} - F_{ji} \frac{1 - \varepsilon_i}{\varepsilon_i} \right) \frac{1}{A_i} Q_i = \sum_{i=1}^N (\delta_{ji} - F_{ji}) \sigma T_i^4 \quad (2.44)$$

with  $N$  = number of radiating surfaces,  $\delta_{ji}$  = Kronecker delta,  $\varepsilon_i$  = the effective emissivity,  $F_{ji}$  = the radiation view factor,  $A_i$  = area of surface  $i$ ,  $Q_i$  = energy loss of surface  $i$ ,  $\sigma$  = the Stefan-Boltzmann constant and  $T_i$  = the absolute temperature of surface  $i$ .

When two surfaces radiate to each other, Equation 2.44 can be simplified to:

$$q_i = \frac{1}{\frac{1-\varepsilon_i}{A_i\varepsilon_i} + \frac{1}{A_iF_{ij}} + \frac{1-\varepsilon_j}{A_j\varepsilon_j}} \cdot \sigma(T_i^4 - T_j^4) \quad (2.45)$$

The view factor between two surfaces is defined as:

$$F_{ij} = \frac{1}{A_i} \int_{A_i} \int_{A_j} \frac{\cos\theta_i \cos\theta_j}{\pi r^2} d(A_j) d(A_i) \quad (2.46)$$

where  $A_i$  and  $A_j$  are the area of the two surfaces,  $r$  is the distance between the surfaces, and  $\theta_i$  and  $\theta_j$  are the angles between the normal lines on different elements on the two surfaces and the radius lines.

### 2.3.3 Boil-off gas rate

The amount in % of a liquid's evaporated mass per day, with respect to the initial loaded liquid cargo is called boil off gas rate; in short BOR. The heat flow  $q$  [W] coming from the ambient into the stored liquid is translated into BOR by the following formula:

$$BOR = \frac{q \cdot 24 \cdot 3600 \cdot 10^{-3}}{V \cdot \rho \cdot H_{vap}} \cdot 100\% \quad (2.47)$$

where  $V$  is the volume in [m<sup>3</sup>] of the stored liquid,  $H_{vap}$  is its heat of vaporisation in [kJ/kg] and  $\rho$  is the liquid's density in [kg/m<sup>3</sup>].

With the aforementioned equation, BOR can either be calculated for an entire carrier or for each tank individually, using the respective heat flow and volume values.



---

## Chapter 3

# Insulation materials and concepts: general overview

Heat transfer is the mechanism which leads to heating a liquid to its boiling point, and then evaporating it. Besides heat transfer within the fluid, the thermal influx from the ambient through the structural system of the cryogenic container plays the major role. Therefore a very effective cryogenic tank must be designed to be able to store a cryogenic liquid such as  $\text{LH}_2$ . The one component which can drastically reduce the heat leak is the cryogenic thermal insulation system. The choice of a suitable material and its configuration is governed by the ability to reduce the heat leakage, cost of fabrication and maintenance, and density or mass. The insulation materials are typically divided into three primary compositions which can either be evacuated (i.e held at low pressure) at different levels or not. These are: foam, bulk fill or multi-layer.

Under a temperature difference, the performance of an insulation material is given by the apparent thermal conductivity, expressed as watt per meter-kelvin. This k-value defines the effects of all three processes of heat transfer. The apparent thermal conductivity is considered based on the understanding of the warm and cold boundary temperature, vacuum level, installed thickness and residual gas composition.

The subsections to follow are predominantly based on distilling the information given by K.D. Timmerhaus and R.P. Reed in their book called "Cryogenic Engineering: Fifty Years of Progress" [69].

### 3.1 Foam insulation

The foam insulation is a gas-expanded organic or inorganic material. Examples of such are polyurethane and polystyrene. The mixture of solid and gas produces a low-density structure with many void spaces. Hence, the heat transfer method which is drastically reduced in this type of insulation is the solid thermal conduction. Nonetheless, its cellular structure has a continuous pathway, making it more thermally conductive than the other material-types. The absence of convection and negligible amount of thermal radiation, makes the thermal conduction through the interstitial gas the most influential heat transfer mechanism in foam insulation [69, p. 125].

Foam insulation is a relatively low-cost material, easy to fabricate and it has a self-supporting structure. A great disadvantage, besides higher thermal conductivity, is the large thermal expansion which may cause fractures into the material. The open pathways caused by these cracks increases the thermal conductivity of the insulation, due to air and water vapour penetration. The close gas-filled cells makes foam insulation very difficult to evacuate.

### 3.2 Bulk fill insulation

Bulk fill insulation usually comes in form of powder, beads, bubbles and microspheres. They are characterized by low thermal conductivity and low density and are shock and vibration reducers. Examples of such materials are expanded perlite, silica aerogel, diatomaceous earth, phenolic

spheres and lampblack.

The small gas voids within the non-evacuated powder minimizes the convective heat transfer, and the presence of the solid particles reduces the thermal radiation. Solid and gas conduction, therefore, are predominant. In most of the cases, the apparent thermal conductivity of non-evacuated powders may approach the thermal conductivity of the residual gas.

A great quality of bulk fill insulation materials is that they can be evacuated, minimizing the gaseous thermal conduction. With respect to the evacuation of residual gas of the bulk fill, for pressures between  $1.3 \cdot 10^{-2}$  and  $1.3 \cdot 10^{-5}$  bar, the overall apparent thermal conductivity shows a significant decrease to a value possibly lower than that of pure vacuum. The reason is that between ambient and liquid nitrogen temperatures, the thermal leakage by radiation is higher than that by solid conduction [69, p.123].

Adding copper or aluminium flakes to evacuated bulk fill insulation reduces the radiant heat transfer even more. However, the process is expensive and over time the gravity pulls down the metal flakes increasing the solid conduction in the lower part of the cryogenic tank [69, p.124].

One down-side of the non-evacuated powder insulation is the need of a vapor barrier to avoid diffusion of air and water and a nonreactive fill-gas. Another disadvantage is the tendency to pack due to thermal contraction at cryogenic temperatures, leaving insulation voids in some areas and increasing the solid conduction in other areas. This is quite common for perlite powder; a solution can be the microspheres insulation<sup>1</sup>.

A special type of insulation under evacuated bulk fill insulation category are the microspheres, creating a special type of insulation which can compete with MLI both in terms of apparent thermal conductivity and lightweight. Hollow glass is the most common type of microsphere insulation.

Glass microspheres have shown impressive results in terms of thermal performance. In a paper entitled "Advances in microsphere insulation systems" [5] a type of glass microspheres named 3M Type K1<sup>2</sup> has been tested and results had shown that the thermal performance has been concluded to be 7.0 times worse than that of multilayer insulation, 3.3 times better than of perlite, and 1.5 times better than that of polyurethane; for different vacuum levels depending on the possibility of evacuation. A downside of glass microspheres is that they are expensive in comparison to other bulk-fill insulation materials.

### 3.3 MLI insulation

The idea behind the multi-layer insulation system is to minimize all three mechanisms of heat transfer. Radically reducing thermal radiation, requires a close alignment of 30 to 80 of low-emittance radiation shield, which are either crinkled, embossed or separated by spacers for minimal solid thermal conductivity [69, p.126]. The system must be highly evacuated to minimize the gaseous thermal conductivity and possible convection. Material used for spacers are coarse nylon, silk net, low-density foam or glass-fiber mat. As for the radiation shields, aluminium foils or Mylar coated with aluminium particles is usually used.

The predominant heat transfer mechanisms in a highly evacuated MLI system, with a pressure value of  $1.3 \cdot 10^{-9}$  bar, are heat radiation and solid conduction, as gas conduction and convection are reduced to a minimum [69, p.127]. The radiant heat transfer is indirectly proportional with the number of shields, meaning that the higher the amount the better. However, more radiation shields mean less space between them for a given insulation thickness, which increases the solid conduction. Therefore, an equilibrium between the two must exist.

---

<sup>1</sup> Usually consists of hollow glass bubbles, have high crush strength, low density, are noncombustible, and perform well in soft vacuum.

<sup>2</sup> Microspheres manufactured from soda-lime-borosilicate glass. Inside the spheres there is SO<sub>2</sub> and O<sub>2</sub> at a third of the atmospheric pressure

The apparent thermal conductivity is dependable on several factors: layer number, layer density, perforation coefficient and installation method. The installation method can be by tape, button or shingle. Compressive external loads, and gas penetration also have a chronological, negative effect on the system's efficiency, as the solid and gas conductivity increases with time.

Despite being an optimal solution for small tanks, considering all the aforementioned factors, the complexity of MLI increases the difficulty of application methods and also makes it highly expensive for larger tanks.

### 3.4 Summary

Each type of insulation systems has advantages and disadvantages, based on which the right material choice for specific applications may be decided. Based on collected information about different types of insulation materials, a radar diagram represented by Figure 3.1 has been created for this study. It shows a general comparison of the three insulation groups mentioned in the prior section, based on six main aspects that are considered in the choice of a fitting insulation material.

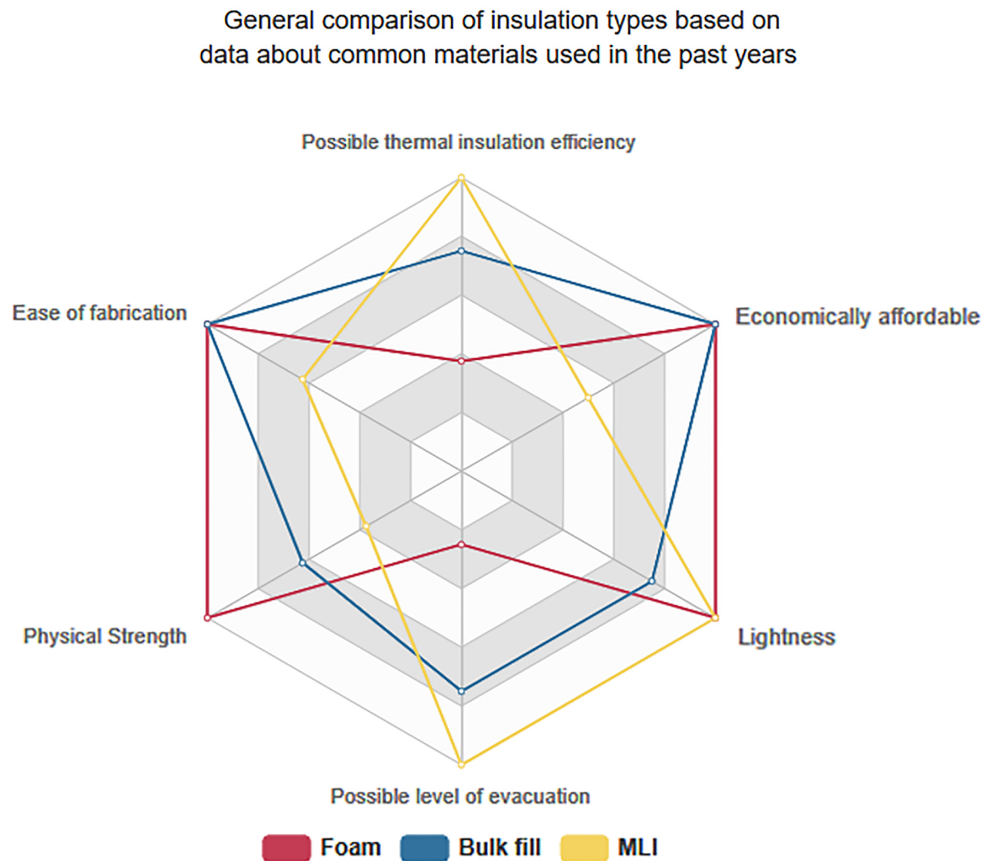


**Figure 3.1:** Radar diagram showing the performances of the three insulation types on a scale from 0 to 4

From the an article written by C.L. Tien and G.R. Cunnington on glass microspheres insulations [68], a diagram comparing different types of insulation materials based on their thermal effectiveness is extracted in Figure 3.2.

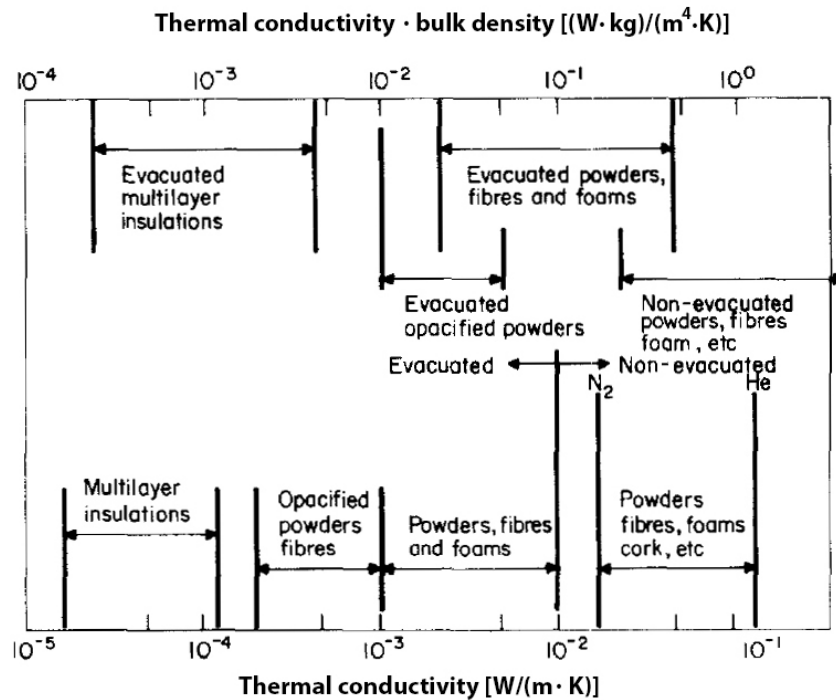


Figure 3.2: Thermal effectiveness of porous cryogenic insulations [68]

From the authors point of view thermal effectiveness is defined by a product of thermal conductivity and bulk density, or thermal conductivity alone. The lower the property values of the different insulation materials are, the greater the thermal effectiveness.

The primary focus when choosing the correct material is based on thermal resistance efficiency, density and overall costs. The use of specific insulation systems must, however, be achievable for different scales and at different surrounding conditions. Hence, other characteristics may be equally important. An elaborated list highlighting several pros and cons of specific insulation materials can be studied in Appendix A.

---

## Chapter 4

# LNG and cryogenic containment - background for LH<sub>2</sub> storage

In the middle of the 20<sup>th</sup> century, the LNG technology, in terms of carrier designs, met the same issues as the LH<sub>2</sub> today. Thermal contractions, material properties at low temperature conditions, minimum heat leakage of the cargo, and protection of hull structure of the ship against low temperatures, are all features related to the high temperature difference between the cargo and the ambient. This is considered to be the most important design issue besides safety, costs and difficulty of manufacturing. Since 1959, when the first carrier delivered LNG from Lake Charles, LA to the United Kingdom, the design of the containment system has been undergoing serious changes and improvements. The majority of the present LNG carriers have a cargo capacity between 125 000 m<sup>3</sup> and 175 000 m<sup>3</sup>, and a boil-off rate of around 0.15 % per day [33, p. 9]

For gases with a NBP lower than that of LNG, the storage systems are lacking the technology that supports the idea of under 0.5 % BOR for volume capacity per tank of over 40 000 m<sup>3</sup>, even though cryogenic containers of smaller sizes are already available for industrial and astronomical projects.

Based on the already existing technology, improvements to the LH<sub>2</sub> storage system that may result in a sustainable hydrogen economy, can be evaluated and considered.

### 4.1 LNG storage vessels

According to the IGU, on a global level, the LNG fleet was composed of 525 vessels by the end of 2018 [32, p. 7]. One can classify the most common designs of LNG containment vessels into two main tank systems; the membrane tanks and the self-supporting tanks. This aspect is depicted by Figure 4.1, showing that by the end of 2018, 33 % of the active fleet had self-supported tank systems while the rest of 67 % had the membrane system design.

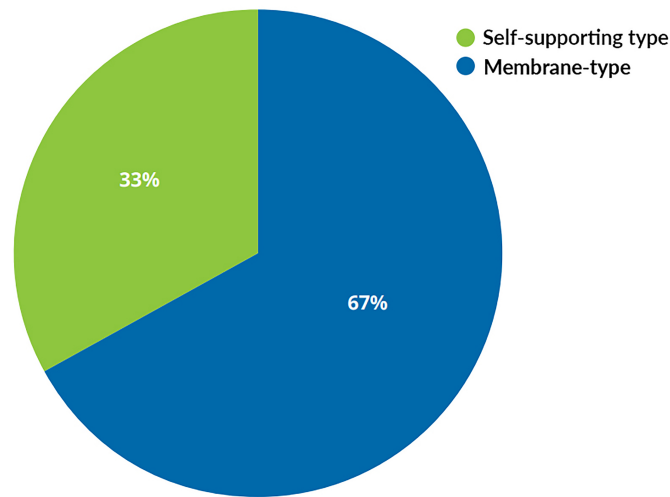


**Figure 4.1:** Existing Fleet by Containment Type, end-2018 [32, p. 54]

To minimize the evaporation of the cargo, the two designs rely on high-quality and high-cost insulation which keeps LNG cold during transit. The main factor which determines the boil-off gas rate is the insulation of the LNG carrier, which in turn, differs with the type of the containment system.

#### 4.1.1 Self-supporting tank system

The self-supporting containment systems can, alone, sustain the internal pressure of the cargo as well as possible over-pressure, aspects which makes them independent from the ship's hull [45].

Out of all IMO types<sup>1</sup>, IMO type-B tanks are used for transporting liquefied natural gas. The reason is that this type has a well defined fatigue strength to prevent crack penetration throughout its operational life, and it has minimal cargo leakage in case of fatigue defects occur [41].

In LNG industry, the Moss Rosenberg spherical tank predominates in terms of self-supporting systems. There is also the self-supporting prismatic IMO-type B LNG tank (SPB), developed by Ishikawajima-Harima Heavy Industries; therefore the name IHI containment system. The two concepts can be seen in Figure 4.2.

<sup>1</sup>There are three self-supporting tank designs defined by IMO; the non-pressurized IMO Type A and Type B, and the pressurized IMO Type C. Type A has a full secondary barrier, while Type B has partial secondary barrier, due to higher strength against fatigue and destruction failure.

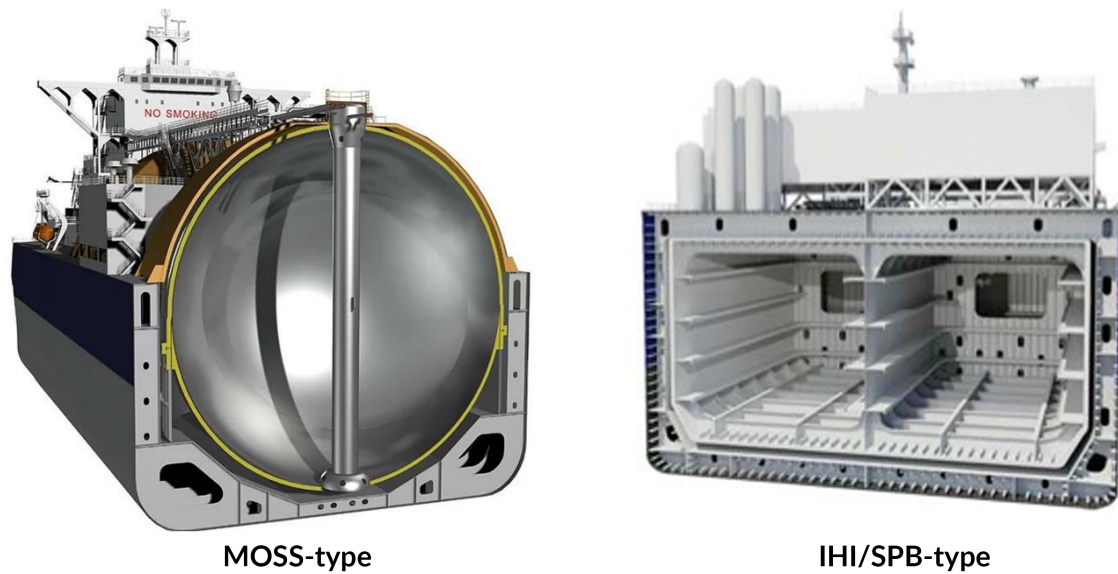


Figure 4.2: Self-supported tanks [78]

### Moss Rosenberg design

The spherical IMO-type B design is the property of the Norwegian company Moss Maritime, therefore the name. The carrier, depicted as in Figure 4.3 has a total capacity ranging from 147 000 to 270 000 m<sup>3</sup> divided among 4 or 5 spherical tanks.

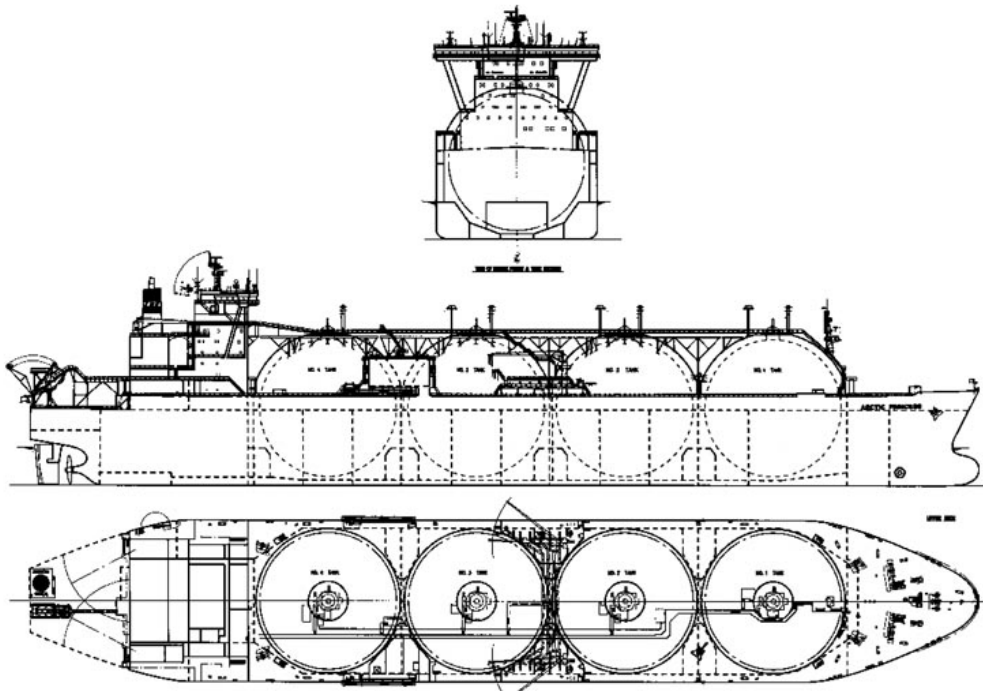


Figure 4.3: Moss-type LNG carrier schematics [65]

The structure of the Moss cryogenic vessel follows the "leak before failure" principle, which implies that in case of cracks and leakages in the system, it will have little to no sudden consequences at all. The spherical container, made of aluminium 5083-0 or 9 % Ni-steel allow, is designed to withstand the weight of the LNG at cryogenic temperature and atmospheric pressure [70]. Around the circumference of the tank, there is an equatorial ring<sup>2</sup> which connects the vessel to a circular

<sup>2</sup>Structural transition joint which also has the role of a thermal break between steel and aluminium.

skirt made of both steel (lower half) and aluminium (upper half). This skirt takes the weight of the tank to the bottom of the ship's lower hull, and ensures a safe thermal deformation<sup>3</sup> of the tank during the cool-down and warm-up operations. The spherical vessel is insulated with approximately 220 mm nitrogen purged polystyrene foam, which is then covered by a layer of tin foil to keep the insulation layer dry. On top of the entire aforementioned system there is a half spherical steel tank cover for protection against different weather conditions [20]. The entire MOSS-tank structure can be seen in Figure 4.4.

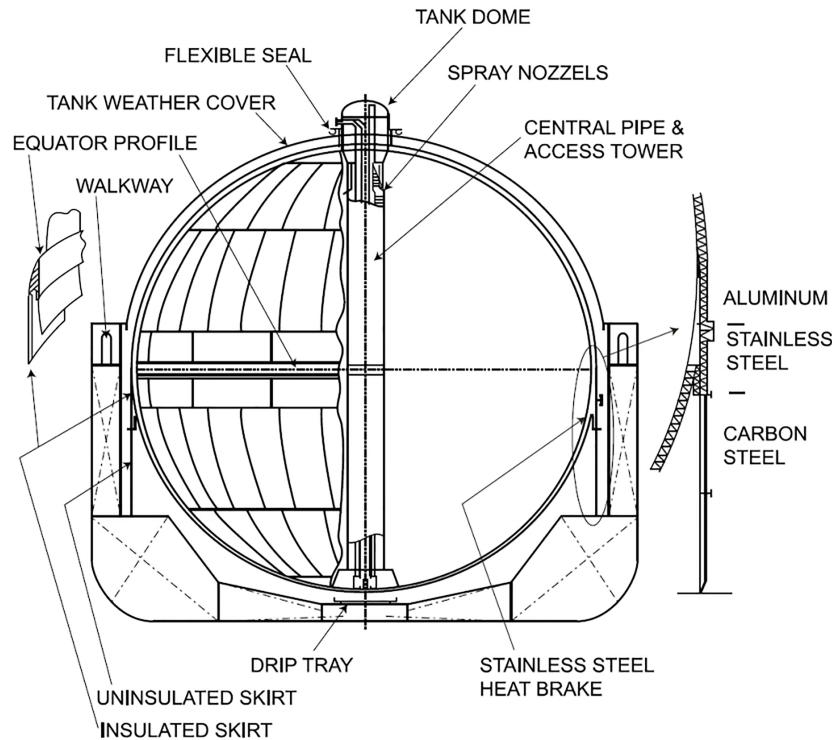


Figure 4.4: Cross-sectional view of MOSS-design [17, p. 231]

There are also other important aspects regarding the Moss-tank design, and are listed based on distilled information given by [49][74][13]:

- The ship has a double hull. The space between the two hulls is used for ballast and it protects the LNG vessels in case of grounding or collision.
- Due to thermal deformation, the inlet of all piping into the tank is at the top.
- The filling ration of the tank can vary since the spherical tank is highly resistive against internal sloshing of the cargo. However, the maximum allowed filling level according to the IGC Code, is of 98 - 99 % to prevent spilling and to account for some accumulation of the boil-off gas [60].
- Gravitational forces accumulates any LNG leakage in the lower hemisphere of the tank, into a partial secondary barrier beneath the sphere, known as a drip tray.
- The wall of the spherical shell is divided into sections of different height, thickness and weight to withstand the varying magnitudes of the mechanical loads acting on the specific areas of the storage tank.

### IHI (SPB) design

The number of existing LNG ships using the SPB-system is in the single-digit amount. By 2016 there were only two LNG carriers using this design, both having a volume capacity of 87 500 m<sup>3</sup> [55]. The geometrical structure of the system is very similar to IMO Type-A, but classifies

<sup>3</sup>The cargo vessel of a Moss-tank can contract or expand up to approximately 0.6 m due to temperature changes during the unloading and loading of the LNG cargo.



as a IMO Type-B tank due to its high strength and reliability over long periods of time; a full secondary barrier is not required. The materials used for the inner layer is Alloy-5083 (aluminium-4.5 % magnesium) or 9 % Ni-steel [18, p. 56]. The tank is covered by polyurethane foam insulation panels, with cushion joints in-between which absorb possible movement between the insulation and the tank; thus eliminating the thermal stress in the PUF [54]. The prismatic shape makes it easy for the container to fit into the ship's hull. The subdivision of the tank by the center-line bulkhead and a swash bulkhead, as depicted in Figure 4.5, reduces effects of sloshing and enables partial loading.

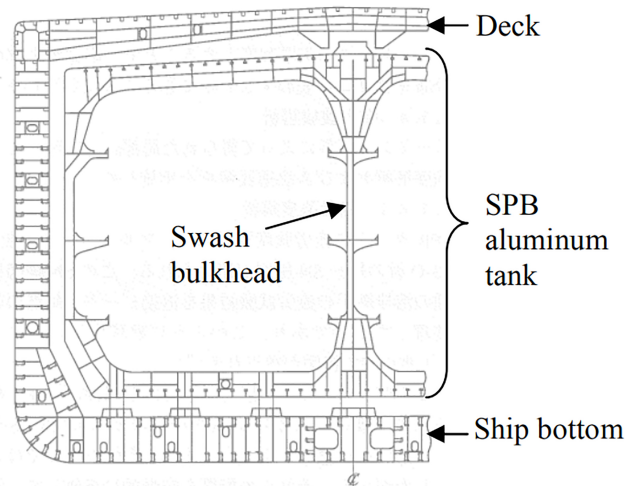


**Figure 4.5:** Cross-sectional view of a SPB-tank [56]

#### 4.1.2 Membrane tank system

Membrane tanks are characterized by its dependence on the hull of the ship, in terms of supporting strength. As the membrane-layers are very thin, the pressure of the internal liquid is delivered through the insulation which is closely connected with the hull. A visual representation of this system can be observed in Figure 4.6.

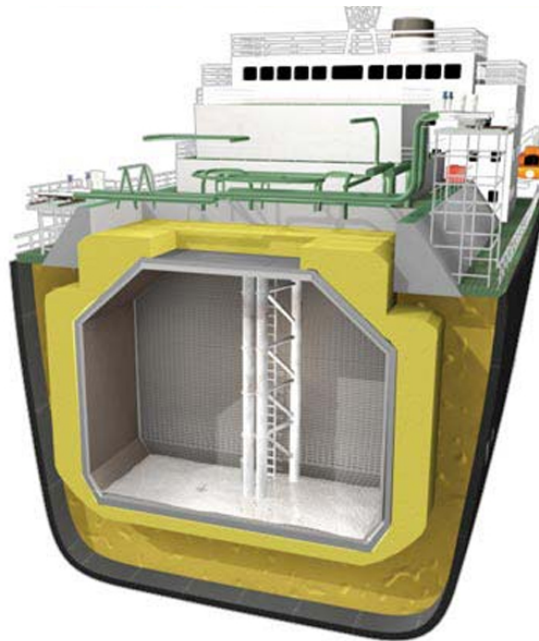


**Figure 4.6:** Structure of a membrane tank [50]

Gaztransport and Technigaz, also known as GTT, is the primary designer of the most common

membrane-tank systems. Mark III- and NO96-systems are the two basic concepts which GTT is responsible for. These two systems are also the ones that are mostly used in the today's membrane-type LNG fleet.

### Mark III-design

The basic Mark III membrane system has a BOR varying from 0.15 to 0.125 % per day. The entire containment and insulation system is supported directly by hull structure of the ship. The primary membrane is made of corrugated, low-temperature stainless steel and has a thickness of 1.2 mm. Due to the high dilatation coefficient of the steel, the well-defined membrane has joints which contribute to a two dimensional movement under light loads. The membrane is positioned on top of a prefabricated insulation panel made of polyurethane foam which in turn may be reinforced with fiberglass. This layer is glued to a secondary membrane made of composite material, called triplex<sup>4</sup> [2]. A structural image is shown in Figure 4.7.

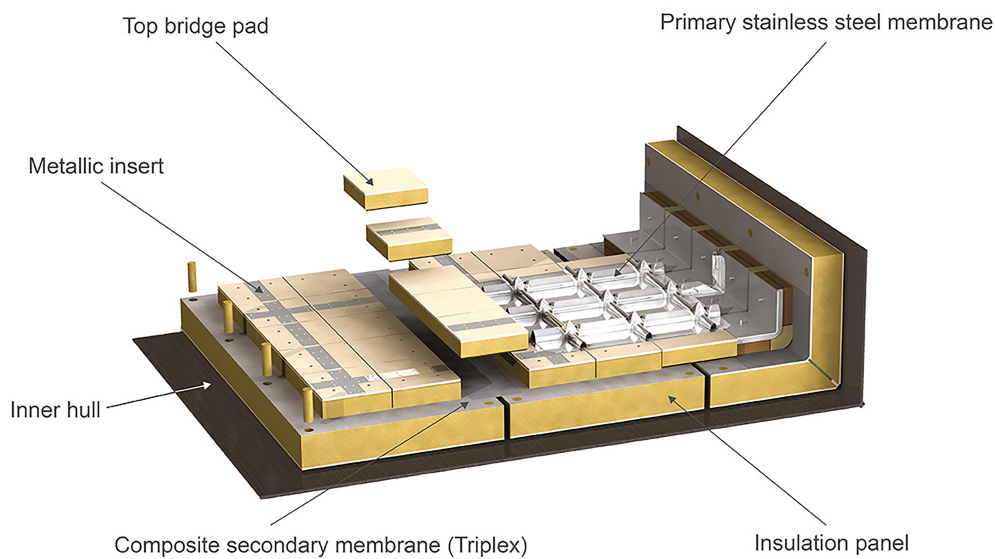


**Figure 4.7:** Mark III structure [2]

Throughout the years, this type of containment system has been improved in terms of thermal and structural efficiency, decreasing its guaranteed boil-off rate to 0.07 % per day; the main reason being the increase of the insulation thickness. Table 4.1 depicts the evolution and composition of the Mark III system.

**Table 4.1:** Characteristics of Mark III systems [2]

	Mark III	Mark III Flex	Mark III Flex+
<b>Boil-off Rate</b> (170.000 m <sup>3</sup> vessel)	From 0.15 to 0.125 %	From 0.10 to 0.085 %	0.07 %
<b>Date to market</b>	1969	2011	2017
<b>Insulation</b>	Foam 130 kg/m <sup>3</sup>		
<b>Membranes</b>	Primary: Stainless steel 304L - 1.2 mm Secondary: composite material		
<b>Support</b>	Primary and secondary panel: foam and plywood		
<b>Thickness Primary</b> <b>+ Secondary panel</b>	270 mm = 100 + 170	400 mm = 100 + 300	480 mm = 100 + 300

<sup>4</sup>A metal foil put in-between glass-wool layers and compressed together.

### NO96-design

The NO96 concept has two membranes, both made of a 0.7 mm thick alloy called Invar. This material contains 36 % nickel and 64 % steel, a mixture which has negligible thermal contraction. The primary membrane is used to contain the liquid cargo, and the secondary one has the role of suppressing the LNG in case of a possible leakage. The membranes are then supported by a primary and secondary insulation, respectively. The material used for these layers is originally made of plywood filled with expanded perlite, a treated volcanic rock based compound with high insulation characteristics which do not diminish over time [3]. Figure 4.8 depicts the structure of a NO96 system.

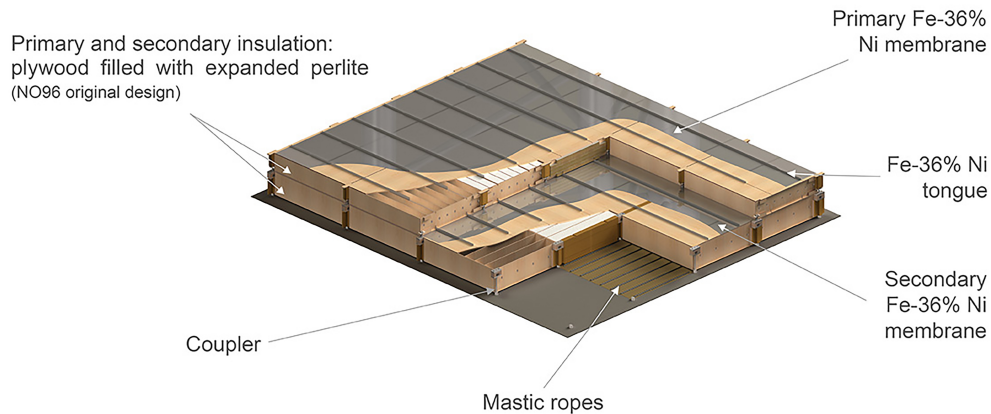


Figure 4.8: NO96 structure [3]

However, newer NO96 concepts have replaced the perlite with foam or glass-wool for better insulation properties, and their properties are tabulated in Table 4.2.

Table 4.2: Characteristics of NO96 systems [3]

	NO96	NO96 GW	NO96 LO3	NO96 LO3+
<b>Boil-off Rate (170.000 m<sup>3</sup> vessel)</b>	0.15 %	0.125 %	0.11 %	0.10 %
<b>Main insulating material</b>	Perlite	Glass-wool	Glass-wool and foam 130 kg/m <sup>3</sup>	
<b>Membranes</b>	Invar 0.7 mm			
<b>Support</b>	<b>Boxes with bulkheads:</b> plywood	<b>Boxes primary and top secondary with bulkheads:</b> plywood	<b>Boxes primary and top secondary with bulkheads:</b> plywood	<b>Boxes with bulkheads:</b> plywood <b>Panels:</b> foam and plywood
<b>Thickness</b>	<b>530 mm</b> (primary box: 230 mm + secondary box: 300 mm)			

The reinforced boxes in the NO96 LO3 and NO96 LO3+ have the role of sustaining higher loads.

### KC-1 design

In the World LNG report of 2019, IGU states that KOGAS has developed a new membrane-tank design called KC-1. SK Shipping has ordered two vessels with this system [32].

Compared to the aforementioned membrane designs, Mark III and NO96, KC-1 has a single insulation layer. It is made of a high density polyurethane foam (H-PUF), with a blowing agent in its

cells. This structure, which has the same performance as a double insulation system, simplifies the geometry of the tank and facilitates its construction and maintenance. The H-PUF layer is sandwiched between two plywood plates, and the gap between the inner hull and the bottom plywood layer is supported by a mastic/air layer made of fiberglass or G10 epoxy. The inner surface of the tank is composed of two 1.5 mm thick stainless-steel membrane layers, having an inter barrier spacer in-between. This double membrane accounts for thermal deformation and also enhances the safety in case of LNG leakage through the primary membrane [38]. The cross-sectional schematic view of the KC-1's wall structure is shown in Figure 4.9.

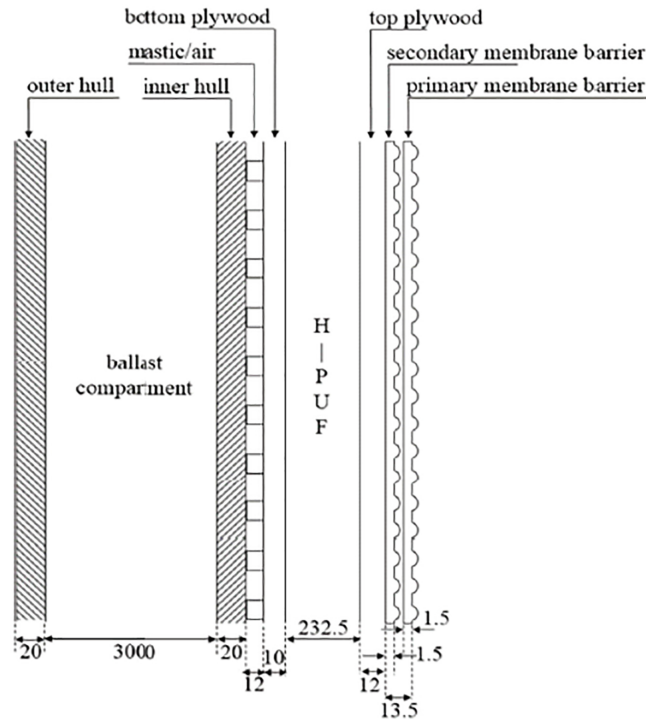


Figure 4.9: Cross-sectional wall structure of a KC-1 LNG tank, with dimensions in [mm] [38]

## 4.2 Storage vessels for other types of cryogenic liquids

The general configuration of a cryogenic liquid vessel is a cylindrical or spherical double-walled structure with an evacuated insulation layer in the annular space. Most of them are working at high pressures of 18 bar and higher, but there are also open, non-pressurized systems called dewars.

### 4.2.1 NASA Kennedy Space Center-LH<sub>2</sub> cryogenic vessel

To support the Apollo Program, two 3 218 m<sup>3</sup> Liquid Hydrogen storage spheres were built at the Kennedy Space Center in 1965. The stainless steel inner vessel with a diameter of 18.7 m is suspended on supports inside a 21.6 m diameter outer sphere made of carbon steel. The 1642.4 m<sup>3</sup> annular space is filled with perlite powder insulation which is evacuated to  $1.3 \cdot 10^{-5}$  bar. The BOR specified in the design specification should not exceed 0.075 %/day of the capacity [44]. This has been achieved on the sphere at Pad A, however the BOR for the Pad B sphere increased to 0.12 %/day. That was due to failure inside the insulation system. Therefore, it has been decommissioned in 2009, but put in use again after a perlite top-off operation which significantly reduced the boil-off per day afterwards. Figure 4.10 shows one of the liquid hydrogen storage tanks at the Kennedy Space Center.



Figure 4.10: LH<sub>2</sub> storage sphere at KSC [44]

#### 4.2.2 Kawasaki's LH<sub>2</sub> carrier

As part of the Hydrogen Energy Supply Chain (HESC) project, Kawasaki Heavy industries, Ltd. and Shell have designed a pilot ship carrying two 1 250 m<sup>3</sup> IMO Type C tanks as depicted in Figure 4.11.

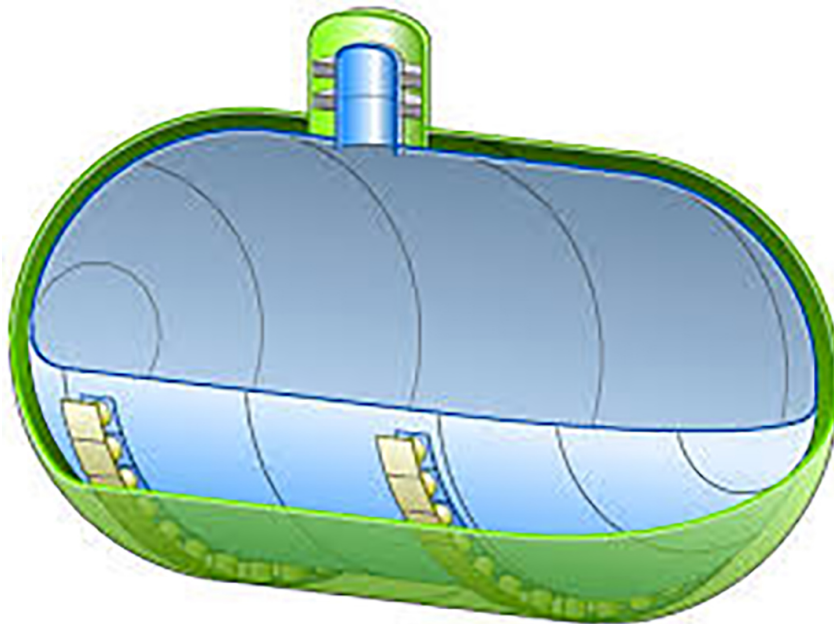


Figure 4.11: Storage tank designed for the pilot concept as part of the HESC project [23, p. 20]

The insulation system is composed of an evacuated multi-layer insulation material, supplemented by an original Kawasaki Panel Insulation. The inner cylinder is placed on several Glass-Fiber Reinforced Plastic support pillars [23, p. 19].

Based on a similar design and technology, a large-scale ship having a capacity of 160 000 m<sup>3</sup> and a boil-off of 0.18 %/day, is under development. The design concept of this carrier would be similar

to that of an LNG ship where the aforementioned volume is divided between four spherical storage vessels.

### 4.2.3 Static LIN & LOX tank-design

The most common used large-scale vessels for storing liquid nitrogen and liquid oxygen are vertical cylindrical shape tanks with a capacity of 1142 to 1720 m<sup>3</sup>. They can either have a dustbin or a cluster configuration.

The dustbin-type is described as a double-walled container having a 13 m high inner vessel with a diameter of 13 m. The 0.5 m thick insulation layer is composed of perlite powder and can be sufficient to achieve a boil-off rate of 0.5 %/day. The flat base of the tank has an extra 0.7 m load bearing insulation made of foam glass [19, p. 138].

The cluster configuration is a multi-cylinder design composed of several 13 m high vessels with a diameter of 4 m, inside an outer tank of 14 m diameter. The 0.5 m thick, nitrogen gas purged, perlite powder insulation layer separates each inner container from each other as well as from the external wall. The boil off rate of this geometry can be reduced to 0.3 %/day [19, p. 138].

Larger sizes have been built for both types, however with a higher boil-off rate, depending on the size of the tank and on the cargo stored. Figure 4.12 shows a real-life example of cluster-type cryogenic vessels.



Figure 4.12: Cluster tanks [48]

### 4.2.4 Linde cryogenic tanks

According to Linde Engineering, the company has delivered around 20 000 high quality cryogenic tanks for liquefied gases since 1960. With a wide range of capacity between 3 and 100 m<sup>3</sup>, the different cryogenic tanks operate at pressures of 18, 22 and 36 bar and are capable of storing LIN, LAR, LOX, LH<sub>2</sub>, LNG, LCO<sub>2</sub> and LN<sub>2</sub>O [47].

The fundamental design is a double-walled cryogenic container with an inner vessel made of stainless steel, which is covered by an evacuated perlite insulation system. The external shell is coated for extra protection.

### 4.3 LNG and other cryogenic liquids vs LH<sub>2</sub> - properties

Understanding the differences of thermo-physical properties between natural gas and hydrogen is a key factor in adapting and fitting the well known storage technology of LNG to LH<sub>2</sub>; aspect available also for other cryogenic liquids such. Table 4.3 gives an overview of the properties of hydrogen, methane, nitrogen and helium as well as the required minimum liquefaction work. This facilitates the understanding of the aspects which must be improved and considered when designing a cryogenic storage vessel for liquid hydrogen.

**Table 4.3:** Properties and minimum liquefaction work required for different gases

Liquids	Normal Boiling point [K]	Density at NBP [kg/m <sup>3</sup> ]	Heat of vaporization [MJ/kg]	Total minimum liquefaction work [kWh/kg]	Lower heating value [MJ/kg]
Hydrogen	20.27	70.8	0.446	3.91	119.96
Methane	111.2	423	0.510	0.31	50.02
Nitrogen	77.34	810	0.201	0.21	-
Helium	4.216	125	0.0209	2.32	-

NOTE: The table includes chosen values from several sources: [73][4][42][39, p. 14]

The weak van der Waals forces between the molecules are the reason why hydrogen meets so many difficulties in terms of keeping the fuel in liquid state. This intermolecular attraction affects the normal boiling point temperature, its density, and also its enthalpy of vaporization. One of the reasons of why hydrogen requires more energy to be liquefied than helium is caused by the ortho-para<sup>5</sup> conversion of the H<sub>2</sub>-molecules.

Compared to LNG(LCH<sub>4</sub>) with a normal boiling point of 111 K, LH<sub>2</sub> has a normal boiling point of only 20.3 K. Safety concerns regarding the liquefaction of the air are presents when it comes to hydrogen, since the condensation of air components such as N<sub>2</sub> and O<sub>2</sub> takes place at temperatures of 77.3 K and 90.2 K, respectively.

LH<sub>2</sub> is also considered a low-density fluid. At normal boiling point and atmospheric pressure, liquid hydrogen has a density of 70.8 kg/m<sup>3</sup> while liquid methane has a density of 423 kg/m<sup>3</sup> and ordinary water has one of ca. 1000 kg/m<sup>3</sup>. For the same amount of stored energy, hydrogen in liquid state weights only 0.38 times the mass of LNG, however having a volume 2.4 times greater [42].

As for the latent heat of vaporization, the value of energy per unit mass for LH<sub>2</sub> seems relatively high compared to the other cryogenic liquids. However, per unit volume the value is 31.6 MJ/m<sup>3</sup>. Compared to the volumetric latent heat of vaporization of LCH<sub>4</sub> which is equal to 216.4 MJ/m<sup>3</sup>, the value is approximately 7 times lower, which results in much less thermal energy needed to evaporate LH<sub>2</sub> than the amount required to evaporate LCH<sub>4</sub> [42].

<sup>5</sup>The hydrogen molecule has two forms, ortho- and parahydrogen caused by the spinning orientation between two hydrogen molecules [23, p. 4]

---

## Chapter 5

# LH<sub>2</sub> storage tank modelling approach - initial considerations

In terms of designing a cryogenic storage vessel, there are several constraints, assumptions and specific modules to be discussed. Base on the resulting criteria, preliminary dimensioning and choice of materials can be established, upon which more precise and other technical aspects can be decided; one of these being the arrangement of the components comprising the cryogenic vessel. The initial considered structure is based on available options and restrictions observed from mechanical, geometrical and thermal perspectives.

### 5.1 Mechanical and geometrical design

Establishing fitting dimensions and geometry of the cryogenic container is founded on the consideration of the area per volume ratio, properties of the used materials, together with several loads acting upon the tank. There are other deciding criteria to be taken into account, but considering the general approach of this study, they are less important.

The aforementioned loads can be divided into three main groups, which are tabulated in Table 5.1. They are equally applicable for the LH<sub>2</sub> storage tanks as they are for the LNG Moss Rosenberg design, with some of them acting on a different degree, due to the thermo-physical properties of the cargo.

**Table 5.1:** Loads for the spherical tanks [15]

Static loads	Dynamic loads	Thermal loads
<ul style="list-style-type: none"><li>• Cargo weight</li><li>• Tank system self-weight<ul style="list-style-type: none"><li>- spheres and skirts/supports</li><li>- Insulation</li><li>- Tower and dome*</li></ul></li><li>• Internal and external overpressure</li><li>• Still water interaction forces*</li></ul>	<ul style="list-style-type: none"><li>• Vertical, transverse and longitudinal accelerations acting on the system</li><li>• Dynamic interaction forces from wave loads*</li><li>• Sloshing loads*</li></ul>	<ul style="list-style-type: none"><li>• Stationary temperature distribution</li><li>• Transient temperature distribution of initial cool down*</li></ul>

\* The loads are not considered further in the modelling approach due to the complexity of the information needed for the numerical and simulation procedure.

Similar to the LNG industry, the tabulated loads may be used to evaluate how suitable the structure is with respect to three limit state conditions:

- ULS: Ultimate limit state design conditions constituting of plastic deformation and buckling.
- FLS: Fatigue limit state design conditions constituting of fatigue failure and crack propagation analysis.
- ALS: Accident limit state design conditions constituting of plastic deformation and buckling.

From a structural analysis perspective, this study only focuses on ULS constituting solely of plastic deformation.



### 5.1.1 Internal shell

#### General dimensions

Considering the area per volume ratio to reduce the heat transfer rate and the structural strength for high capacity cryogenic tanks, the proposed spherical geometry is definitely the most promising solution when storing LH<sub>2</sub>. Figure 5.1 together with some examples given in Chapter 4 where the spherical design is used in the LNG industry, as well as in other projects, support the choice of this study. Figure 5.1 depicts the necessary surface area at different volumes for several geometrical shapes, and it shows how the area decreases for rounder shapes. It can also be observed that by increasing the volume, the area-to-volume ratio decreases.

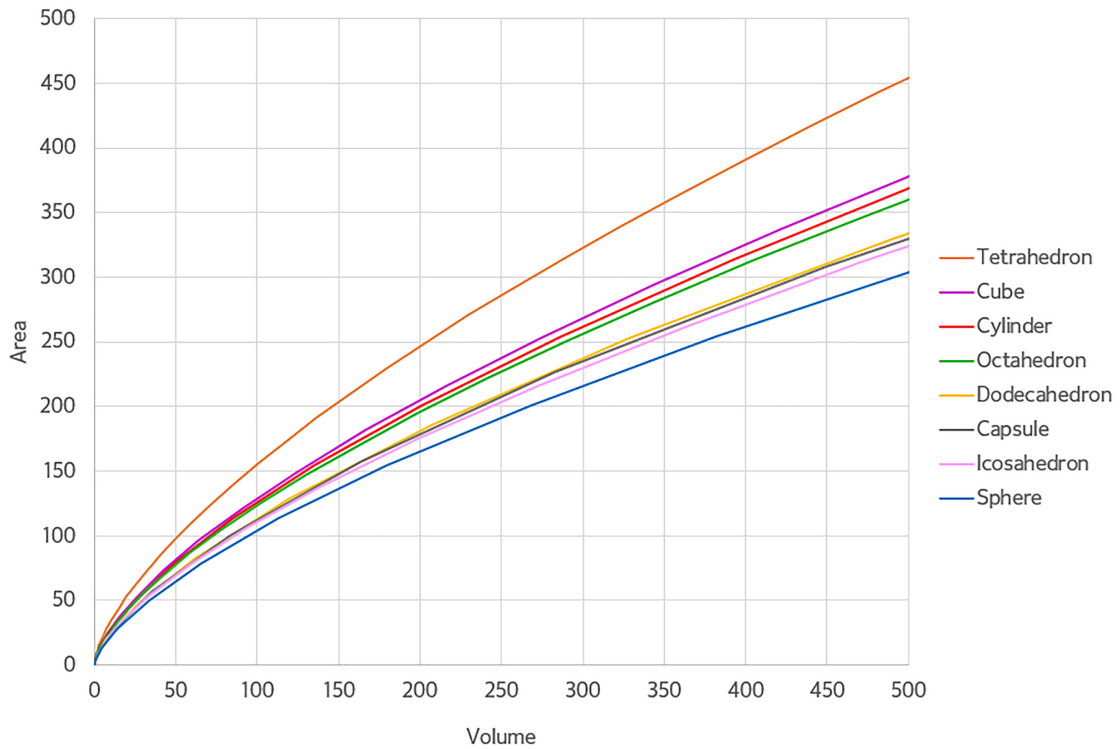


**Figure 5.1:** Graphs of surface-area to volume for different geometrical shapes

Figure 5.1 is a self-made representation inspired from Wikipedia [76].

Using the geometrical formulas of a sphere, for a volume of 40 000 m<sup>3</sup>, the inside of the inner container will have the dimensions as tabulated in Table 5.2.

**Table 5.2:** Dimensions for the inner tank of the case study LH<sub>2</sub> cryogenic vessel

Name	Value
Diameter, $d$ [m]	42.4
Circumference, $C$ [m]	133.0
Area, $A$ [m <sup>2</sup> ]	5 660

#### Wall thickness

Different components of the spherical-tank design are individually subjected to particular loads specified in Table 5.1. The forces acting on the wall of the inner vessel are caused by internal overpressure, self-weight, insulation weight, cargo weight, sloshing and thermal deformation. These loads are acting differently on different areas of the spherical shell. For a reliable structure, as depicted in Figure 5.2, a realistic design of this type of tank is divided into zones of different height and thickness.

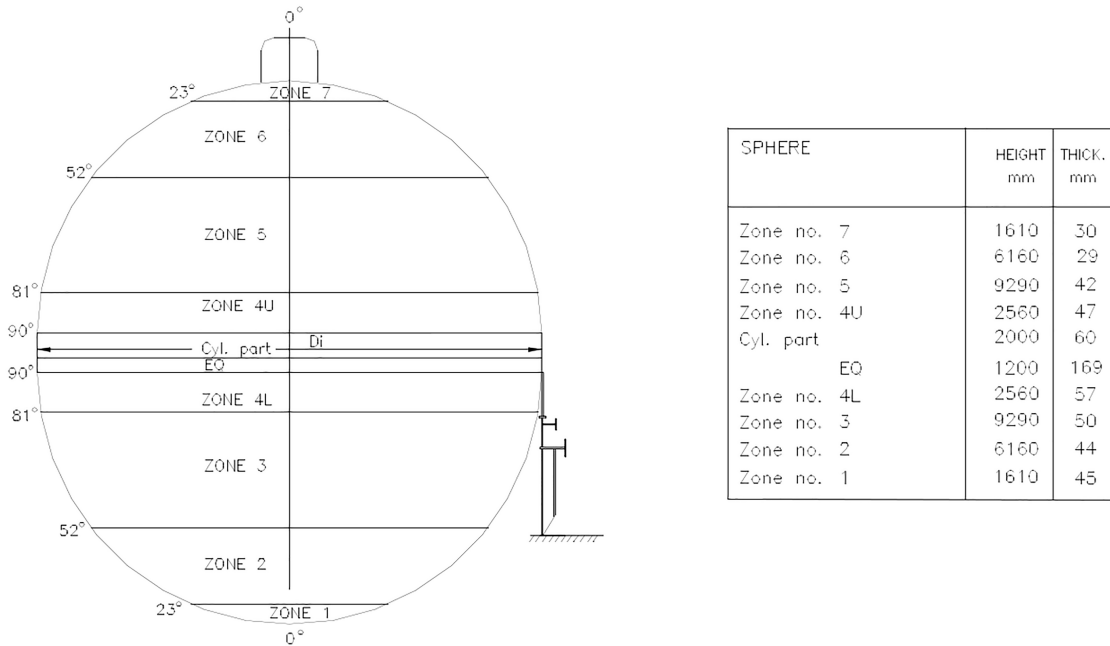


Figure 5.2: Scantling of Moss stretched tank [22, p.9]

To avoid overloading, the equatorial segment is the thickest since the entire weight is transferred through that area into the component that supports the inner container. The reason why the lower hemisphere has thicker zones than the upper one is because they are exposed to higher hydrostatic pressure.

For a LNG Moss spherical containment system, DNV GL specifies that to ensure enough strength against a net external overpressure of 0.02 MPa, the minimum thickness of the shell is expressed by the following equations [15, p.149]:

- Steel as a material used

$$\frac{r}{t} \leq 1300 \quad (5.1)$$

- Aluminium as a material used

$$\frac{r}{t} \leq 750 \quad (5.2)$$

With a radius of 21.2 m, Equation 5.1 will result in a minimum thickness of approximately 0.016 m and Equation 5.2 will result in a value of 0.028 m respectively. These values can be considered when adjusting the design, depending on the existing overpressure in the case of LH<sub>2</sub> transportation.

However, based on the height and thickness values given by Christiansen [22] in Figure 5.2, an average thickness is calculated. To facilitate the preliminary design simulated in this study, the resulted value of 0.048 m is decided to be uniformly applied as the wall-thickness for the inner tank.

### Wall material

Permeation and hydrogen embrittlement are two important aspects to consider when choosing a fitting material for creating the tank in which liquid hydrogen is to be stored. The very small size of the hydrogen molecules, makes permeation an issue which may become negligible by using metallic tanks, as hydrogen has a higher tendency to permeate nonmetallic materials rather than the metallic ones. However, some metals may become brittle<sup>1</sup> when in contact with hydrogen, causing physical failure at stress levels bellow the yield stress value and even without significant deterioration. Materials sensitive to hydrogen embrittlement are nickel and its high nickel alloys as well as titanium and its alloys [59][72].

<sup>1</sup>A type of material deterioration causing a material to break in the presence of insignificant deformation and little energy absorbed

Other aspects to be considered are from a mechanical and thermal perspective. The material must have sufficient tensile and compression strength at given temperatures, however it must have low thermal conductivity so that the passive heat ingress through the wall can be reduced as much as possible.

Stainless steel and aluminium alloys are some materials used for handling LNG, but also for other cryogenic liquids, as described in the previous Chapter. Precisely, aluminium alloy type 5083 is especially used for applications regarding the spherical or prismatic storage tanks for ship transportation of LNG, while AISI 304L stainless steel has been used in the NASA storage containers. Therefore, these two materials may both be suitable to be used for the inner tank, in this study. Table 5.3 contains the mechanical and physical properties of the two metals, as well as a 50 % Glass Fiber reinforced Polyamide 6 (PA6 GF50). The plastic nylon is similar to the one used for the Kawasaki LH<sub>2</sub> carrier described in Subsection 4.2.2, and is tabulated just for comparison.

**Table 5.3:** Material properties for AISI 316, Al alloy 5083 and PA6 GF50 [52][51][26][25]

Material type	Temperature [K]	Density [kg/m <sup>3</sup> ]	Thermal Conductivity [W/(mK)]	Yield Strength [MPa]	Tensile Strength [MPa]
AISI 304L	297	7900	13.4 - 15.1	193	586
	77.5	-	9	241	1340
	19	-	-	233	1516
Al alloy 5083	297	2660	117	140	290
	77.5	-	-	157	442
	19	-	-	-	-
PA6 GF50	297	1 560	0.28	240	880

The table has been established by using the information extracted from different cross-references registered on totalmaterial.com [52][51], for the two metals. For the glass fiber reinforced nylon, Table 5.3 includes information from matmach.com and a scientific paper written by Amandine Gay et. al. [26][25]. PA6 GF50 may probably be the best solution for LH<sub>2</sub> storage as it has the lowest thermal conductivity and density among the three, and highest structural strength. However, since collecting information about this material has presented to be challenging, it is not further used.

In terms of density, and temperature dependency, aluminium is superior compared to stainless steel as it is lighter and shows little change in value of the mechanical properties at different temperatures. The thermal dependency is an important aspect to be considered for AISI 304L, but the density on the other hand does not necessarily represent an issue as it can be concluded from Table 5.4 which tabulates the following:

- The weight of a 0.048m thick empty spherical tank built from AISI 304L and Al alloy 5083, individually, in BLUE color.
- The masses of 40 000 m<sup>3</sup>-volume of LNG and LH<sub>2</sub>, in GREEN color.
- The summed up weights, when the tanks made out of each metal is filled 100 % with each liquid separately, in RED color.

Liquid cargo	Tank-shell material	None	AISI 304L	Al alloy 5083
	None	-	2 340	789
LH <sub>2</sub>		2 830	5 180	3 620
LNG		16 900	19 200	17 700

**Table 5.4:** Weight [tonnes] of inner tank + cargo for different cargo liquids and wall-materials

Since liquid hydrogen is significantly lighter than LNG, the total weight of the LNG filled storage tank made of Al alloy 5083 is greater than the total weight of the LH<sub>2</sub> filled tank made of AISI

304L. The great difference in weight between the two liquids facilitates the choice of material used for the tank-wall since the risk of an heavier structure does not represent an issue if the weight of the cargo is considered. Choosing a more dense material may however make the construction process more difficult and complex. According to Konecranes [43, p.6], they have delivered over 50 Goliath Gantry Cranes with a lifting height of ca. 100 m, a rail span of ca. 207 m, and a lifting capacity of approximately 1 500 tonnes. Assuming that such a crane is used to construct a liquid hydrogen carrier, the inner tank made out of AISI 304L has to be mounted on the ship into two different pieces since the crane does not have the strength to lift up an entire container; which on the other hand is possible if Al alloy 5083 is used. There are, however, stronger cranes such as Taisun, but this specific topic is to be further evaluated in another study.

The stainless steel has thermal conductivity which is approximately ten times lower than that of Al alloy 5083. Not only that, but the yield and tensile strength are also greater for AISI 304L. As a preliminary choice, stainless steel is therefore the most favourable option to be used in this study.

There are several types of stainless steel which may be suited for the containment of LH<sub>2</sub>. According to a study performed by Le Thanh Hung Nguyen et al. on hydrogen exposed 316L stainless steel, this type of material is considered one of the most attractive material candidates for LH<sub>2</sub> storage vessels [53]. It is because of his high resistance to hydrogen embrittlement and because it has good mechanical properties at low temperatures. If the environment is salty or acidic, AISI 316-type is especially recommended due to the existence of molybdenum in the material mixture, which helps in a corrosive environment. In the paper entitled "Hydrogen Embrittlement of Stainless Steel" [59] it is mentioned that AISI 316 suffers three times less losses due to H<sub>2</sub>-embrittlement compared to AISI 304. Based on the information on materialgrades.com [28], some mechanical properties of AISI 304 and 316 are as tabulated in Table 5.5.

**Table 5.5:** Mechanical properties of AISI 304 and AISI 316 at ambient temperature [28]

AISI type	Tensile Strength [MPa]	Yield Strength [MPa]	Hardness [HB]	Elongation [%]
AISI 304	535	215	200	40
AISI 316	545	275	220	50

Simultaneously, each type of stainless steel is divided into smaller categories as well. For the two metals AISI 304 and AISI 304L from Tables 5.3, 5.5, the properties are not similar. This is because the composition is different; The letter "L" stands for low carbon. This is also applied in the case of AISI 316 and AISI 316L. However, an observation regarding the values gathered and tabulated the aforementioned tables and similar tables to follow, is that the values may vary depending on the source of information.

Based on the literature studied on stainless steel, it is decided that for the preliminary design, AISI 316 is the most suitable type in terms of material properties and composition.

## 5.1.2 External shell

### General dimensions and wall thickness

Since the proposed containment system has a double-walled design, an external shell is necessary. The reason is justified by the fact that the insulation layer applied may be evacuated to obtain favourable results in terms of BOR.

The geometry and wall thickness of the outer tank is initially decided to be similar to the inner shell. However, the loads acting on the external wall are different from the ones acting on the internal tank, and may probably have a greater impact. For example, the outer shell is exposed to the weight of the entire system. Also a spherical vessel shows greater resistance against internal pressures compared to external pressures. It must therefore be considered that the wall thickness as well as the geometry will turn out to be slightly different from that of the inner tank.

Other general dimensions are dependable on the thickness of the insulation layer. Assuming that the thickness will be of 1.00 m, the inner radius of the outer shell will be of 22.248 m.

### Wall material

The decision regarding the material used is based on the information gathered about the design of the tank cover used in the Moss Rosenberg design for LNG. As both of them are exposed to similar surrounding conditions, it can be concluded that the same material may be used. However, the tank cover does not play any role in sustaining the weight of the cryogenic vessel as it does in the specific case of this thesis. Consequently, the mechanical properties must be proven satisfactory for the demand of withstanding the existing loads, aspect which is determined by the simulations.

According to the email response from Appendix C, Moss Maritime says that normal shipbuilding low carbon steel, NV-A grade is usually used to construct the aforementioned tank covers. As it can be observed in Table 5.6, this type of material has relatively high mechanical and physical properties, and therefore offers good quality toughness, ductility and strength.

**Table 5.6:** Material properties for low carbon steel (mild steel), NV-A grade type [16, p.16][34]

Property name	Value
Chemical composition	C: 0.18 %-0.28 %, Mn: min 2.5·C, P: 0.035 %, S: 0.035 %
Density $\rho$ [kg/m <sup>3</sup> ]	7858
Thermal conductivity $k$ [W/(m·K)]	51.9
Tensile strength $R_m$ [MPa]	400-490
Yield stress $R_eH$ minimum [MPa]	235
Poisson's ratio	0.27-0.30
Elongation at break	15 %-20 %

Based on the tabulated information and since it is such a general material in shipbuilding, it seems reasonable to attribute low carbon steel, NV-A grade to the shell of the external tank.

### 5.1.3 Support system of the inner shell

#### General design

In the baseline design, the system which supports the internal vessel is described as an equatorial ring element supported to a corresponding ring element of the outer tank. Assuming that this concept is similar to the one depicted in Figure 5.3a, it can easily be concluded that there are possibly better solutions; one of which is an internal cylindrical skirt as depicted in Figure 5.3b. In both cases the support-elements are designed with similar thicknesses of different sections and relatively similar attaching-areas to the inner sphere.

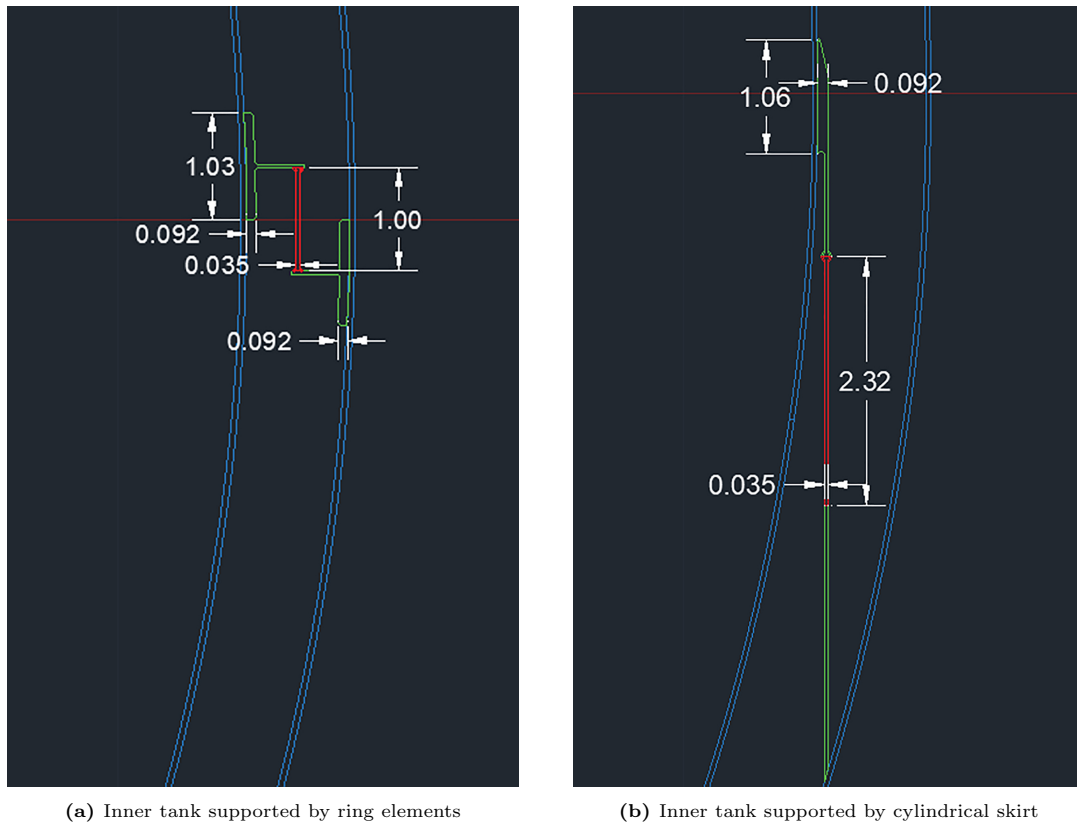


**Figure 5.3:** Base case design for support element of the inner spherical shell

By logically evaluating the two concepts, the cylindrical skirt shows signs of improvement from a structural and a thermal perspective as well. The horizontal distance from the point of application of the force<sup>2</sup> to the point of attachment between the support-element with the outer sphere is greater in Figure 5.3a than in Figure 5.3b. The torque is therefore higher in the case of the ring-support. By observing and comparing the two systems, it is clearly that there are higher chances for the ring elements to deform and probably fail. To support this conclusion, a quick simulation has been conducted in ANSYS Static Structural. With similar materials and forces applied on the two designs, the deformations can be observed in the sub-figures of Figure 5.4.

<sup>2</sup>Force acting on the support system produced by the weight of the inner shell and the weight of the cargo

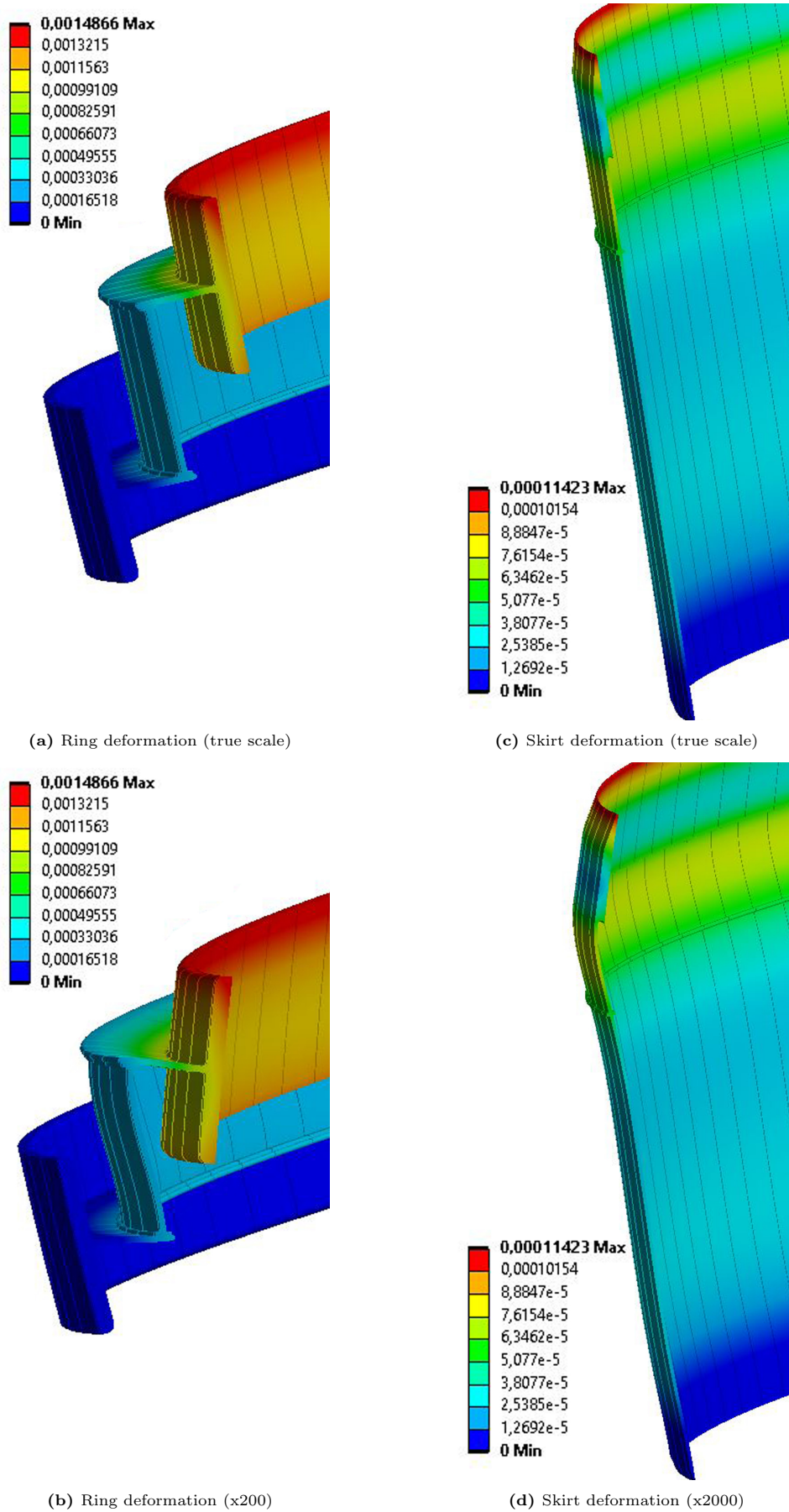


Figure 5.4: Deformation of different types of support systems under similar boundary conditions

Structural steel<sup>3</sup> is used as material for the entire geometry, and a force of 10 000 N is acting vertically, downwards, on the surface where the inner tank is attached to the support. Gravitational acceleration is also placed on, both, the ring and the skirt to represent a natural behaviour of the tested elements. Since the boundary conditions are similar, the only variable remains the geometry which confirms the aforementioned theory. The maximum deformation of the ring-support is 1.47 millimeters, and for the skirt is 0.11 millimeters.

Buckling may represent a bigger problem with the skirt component than with the ring element, but as only plastic deformation is simulated in this study, the statement cannot be proven.

As from a thermal perspective, it is well known that the heat transfer rate is dependable on the distance between the two temperatures. Longer distance results in higher the thermal resistance which results in lower heat transfer rate. This aspect is detailed in Subsection 5.2.2. Based on this, using a skirt instead of an equatorial ring reduces the BOR.

### General Dimensions

A cross sectional area of a cylindrical skirt used in the LNG Moss Rosenberg design is illustrated and dimensioned in Appendix B.

As highlighted in Table 5.4, the weight which the cylindrical skirt must sustain is three to four times lighter than in the case of LNG, for a 100 % filled tank. Therefore the dimensions are slightly adjusted, but without knowing exactly the behaviour of the skirt in the two cases, the dimensions are arbitrarily chosen. After a preliminary analysis is conducted, possible modifications may be considered based on the results gathered.

The dimensions are shown in Figure 5.5. Considered dimensions are represented in the same manner as in Appendix B, using the same sketch of the skirt. In the upper-left corner of the figure, a suggested design of supportive system is depicted.

---

<sup>3</sup>The default solid material used by ANSYS Mechanical APDL taken from its database with the material properties attached in Appendix D, Section D.4



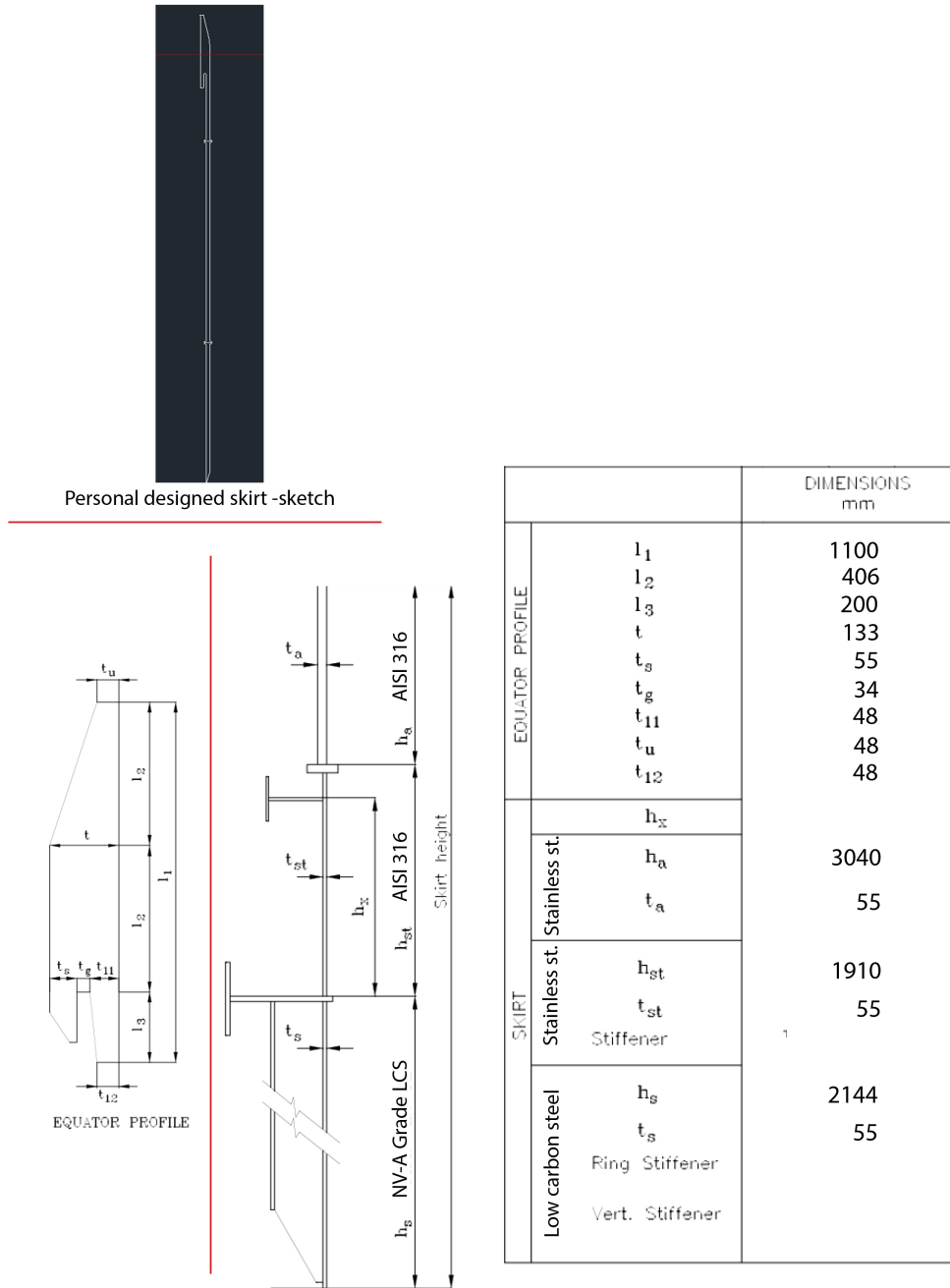


Figure 5.5: Dimensions of the suggested supportive system for the preliminary design

### Materials

From the sketch in Appendix B and conversation with Moss Maritime AS in Appendix C results that the skirt in the LNG Moss Rosenberg-design is divided into three segments composed of different materials. The bottom segment as well as the top segment are made of the same material type as the components they come in contact with. The lowest part which is welded to the bottom of the ship is made of high strength carbon steel which is able to sustain the weight of the entire system. The top segment is made of Al-alloy 5083 considering that it must have the same bending behaviour under the different mechanical and thermal loads as the container wall. The middle segment is made of Stainless Steel 304 and serves as a thermal breaker considering the low thermal conductivity of the material.

In the proposed preliminary design, the skirt is also divided into three segments following similar attributes. Similar to the external tank shell, the bottom segment of the skirt is made of carbon steel for support purposes. The middle segment is made of Stainless Steel 316 having the function

of a thermal breaker. Based on the choice of material for the internal container, in the case of LH<sub>2</sub>, AISI 316 is used for the top segment of the skirt as well. This can result in a design composed of two parts, carbon steel and stainless steel. However, considering the possibility of using another material as a thermal breaker in a later design, assuming the geometry is acceptable, the division into three parts is used, being considered a general model of the skirt.

Similar to the Kawasaki's LH<sub>2</sub> carrier, glass fiber reinforced plastic may be used as a thermal breaker material. If the case were to account for the use of PA6 GF50, it probably would have not been suitable for the concept of skirt as a supportive system of the inner tank, and the design had to be therefore reconsidered.

#### 5.1.4 Support system of the outer shell

A secondary cylindrical skirt, on which the external tank is fixed has the role of supporting the entire weight of the cryogenic storage system. A rough estimation of the total weight, based on the decisions made in the previous Subsections of this Chapter, is made and tabulated in Table 5.7

**Table 5.7:** Weight of the different containment system elements

Element Name	Weight [tonnes]
Cargo (LH <sub>2</sub> )	2 830
Internal spherical tank	2 110
Internal skirt	482
Insulation layer*	1 320
External spherical tank	2 350
Total system	9 100

The mass of the insulation layer is estimated based on an arbitrarily thickness of 1.00 m and the density of 225 kg/m<sup>3</sup>, corresponding with that of a specific type of micro glass spheres 3M type B37/2000 quality.

As it can be observed, the assumed weight of the system is slightly over a, what can be considered, half the value of 40 000 m<sup>3</sup> stored LNG in an uninsulated aluminium tank. Accordingly, it means that the thickness of the external skirt can be significantly reduced.

In terms of geometry, dimension and material, this particular segment has little limitation. As it has negligible influence on the heat ingress, the spherical system may as well be placed directly on the ship's hull; assuming the direct contact between the system and the environment has no negative outcome. The general aspect which may be evaluated when it comes to the external supportive system is its position and ability of sustaining the entire weight of the system without deteriorating it.

As a first consideration, the most logic idea is to position it on the exterior of the external tank, in the exact same area where the bottom of the inner skirt touches the internal side of the same tank. This layout may reduce the deformation caused on the system and may show signs of a more stable construction, as the loads are absorbed directly into the external supportive system which is directly connected to the hull of the ship.

Based on the aforementioned reflection, a support element made of NV-A grade carbon steel is designed as depicted in Figure 5.6.

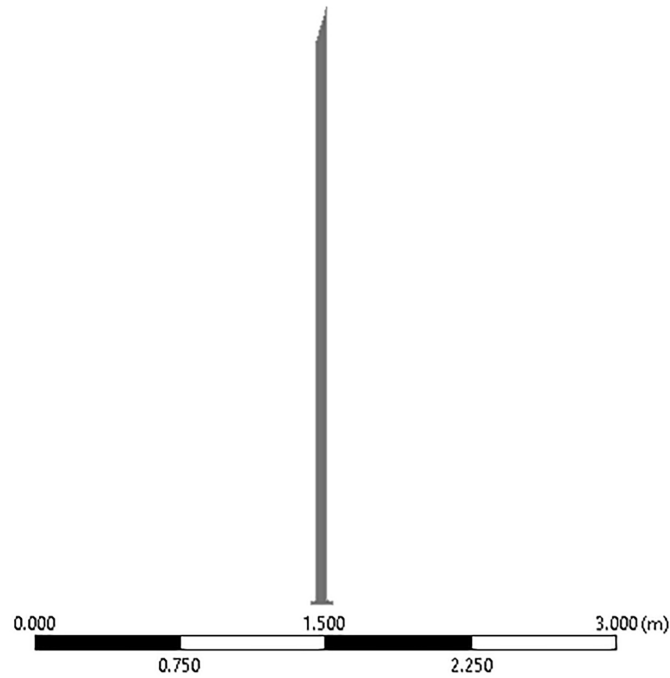


**Figure 5.6:** Design of the external support

## 5.2 Thermal design

The heat inflow into a relatively well-insulated cryogenic cargo container is highly dependable on the mixture between thermal radiation, conduction and convection; especially the heat transfer that takes place via the insulation space and the support system of the internal tank.

To reduce the heat transfer rate, ergo the boil-off rate, the insulation layer and the structural support can be manipulated throughout several methods which are evaluated and discussed in the sections of this chapter.

### 5.2.1 Walls & insulation layer

In the specific case of this project, the heat may be transferred from the ambient to the surface of the external wall by convection and radiation, and then through the entire structure depending on the type of the material used. Through the walls of the internal and external containers, the heat is transferred entirely through conduction. Since the insulation material usually has cellular empty spaces which can be evacuated or filled with fluid, all processes of heat transfer may be present in a relatively equal degree. Then, the heat may flow from the inner surface of the internal container into the liquid cargo by convection or radiation.

Assuming that the inside and the outside surface temperatures of the containment system are equal to the ambient temperature and  $\text{LH}_2$  respectively, an approximate thermal circuit of a system containing the insulation layer between two spherical walls is simplified in a self-made Figure 5.7.

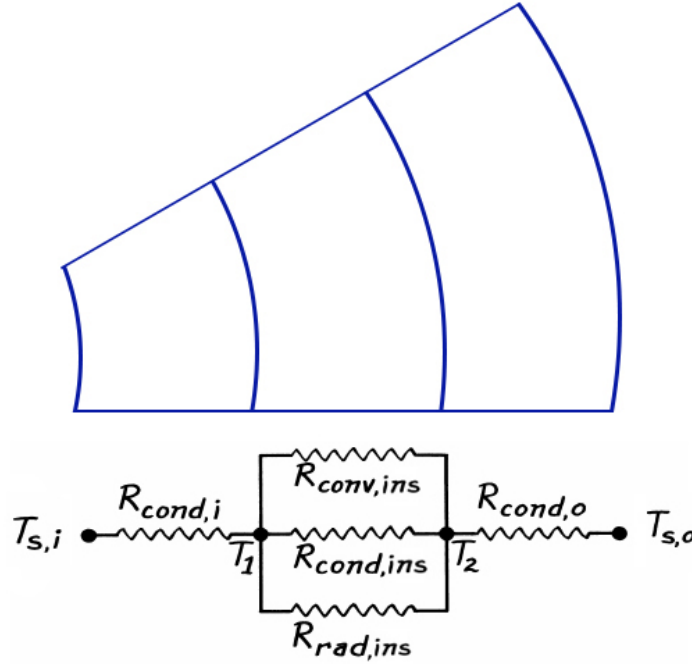


**Figure 5.7:** Thermal circuit of a spherical cryogenic tank

Adapting equation 2.29 results in:

$$Q = \frac{T_{s,o} - T_{s,i}}{R_{cond,o} + R_{tot,ins} + R_{cond,i}} \quad (5.3)$$

where

$$R_{tot,ins} = \left( \frac{1}{R_{cond,ins}} + \frac{1}{R_{conv,ins}} + \frac{1}{R_{rad,ins}} \right)^{-1} \quad (5.4)$$

Considering the fact that the system has the geometry of a sphere, the corresponding equations for calculating the different resistances are applied which are Equations 2.33, 2.34 and 2.35.

To have as little as possible heat leakage, the different thermal resistances from Equation 5.4 in the structure must be as high as possible. Changing  $R_{tot,ins}$  has the greatest impact on the thermal heat transfer. The resistance can be increased by changing the material type, the cross-sectional area, and the thickness of the insulation.

### Insulation material

Every process of heat transfer can be reduced based on the type of insulating material used. Throughout the years scientists and engineers have developed and used different methods to calculate the ability of such materials to conduct and radiate heat. For theoretical calculations, the most practical way is to determine an apparent thermal conductivity value of a material, which includes all the existing heat transfer methods. To theoretically establish these k-value one can either use simplified calculations for approximate results or can use more complicated formulas for more precise ones. Depending on the case, one method may be more suited than the other.

#### K-value based on the predominant heat transfer mechanism

For some of the insulation materials, the fluid motion and infra-red radiation within the layer can be significantly reduced so that, compared to the amount of heat transfer through conduction, the convective and radiation heat transfer may become negligible. In this case, the heat leakage via the insulation will be simplified to heat conduction and expressed as:

$$Q = \frac{\Delta T}{\frac{1}{4\pi k_{eff}} \left( \frac{1}{r_{in}} - \frac{1}{r_{out}} \right)} \quad (5.5)$$

where  $k_{eff}$  is the effective thermal conductivity<sup>4</sup>, which may only be used for comparison of performances between different insulators, and not as a definer of an average property of the composite material.

Insulation materials following this model are low thermal conductivity materials such as solid fibers, powders and foam walls. The convection heat transfer can be reduced or eliminated by creating mediums which have microscopically small gas cells within their structure, and the thermal radiation is relatively low because of the existence of solid particles. The most common materials of the forenamed type, used in the cryogenic industry, are tabulated in Table 5.8 showing their effective thermal conductivity.

**Table 5.8:** Gas-purged and evacuated insulations and their  $k_{eff}$  [mW/(m·K)] [19, p.54]

	Pressure 1 bar nitrogen	Evacuated to $1.33 \cdot 10^{-6}$ bar
Expanded perlite	26-44	1.0
Silica aerogel	19	1.6
Fiber glass	25	1.7
Foam glass	35-52	-
Expanded polystyrene	24-33	-
Polyurethane foam (PUF)	25-33	-

For heat transfer through multi-layer reflective insulation materials, all three processes of thermal exchange must be accounted for. With the decrease of temperature, the radiative heat transfer goes with as the forth power of the temperature, while the relationship between conductive heat transfer and temperature drop is linear. The importance and sensitivity of conductivity can be considered dominant, but it is however poorly defined in the literature. For acceptable apparent thermal conductivity values methods such as the Layer-by-layer method<sup>5</sup> presented by McIntosh, or the Lockheed method<sup>6</sup> are available. However, both procedures are highly demanding in terms of material properties data. As these methods are too complex for preliminary calculations, other solutions may be considered.

As mentioned in Chapter 3, radiation heat flow dominates over the gas conduction heat flow, because the multi-layer reflective insulations operate at very low pressures. In this specific case, an effective thermal conductivity for reflective insulants in a MLI can be defined, such that Equation 5.5 may be used accordingly. With reference to theory detailed on Page 58, in the book called "Low-Loss Storage and Handling of Cryogenic Liquids" [19] the  $k_a$ -value for MLI is determined as follow:

By combining the radiation heat transfer equation for n thermally floating reflecting parallel surfaces,

$$\frac{Q}{A} = \frac{\varepsilon\sigma(T_o^4 - T_i^4)}{2(n+1)} \quad (5.6)$$

with the standard conductivity equation

$$\frac{Q}{A} = \frac{k_a(T_o - T_i)}{\Delta x} \quad (5.7)$$

results:

$$k_a^{MLI} = \frac{\varepsilon\sigma(T_o^4 - T_i^4)\Delta x}{2(n+1)(T_o - T_i)} \quad (5.8)$$

<sup>4</sup>The effective thermal conductivity  $k_{eff}$  applies for saturated porous mediums and it is dependable on the porosity or the volume of fluid relative to the total volume. It is mainly a combination between fluid and solid conductivity. However, for more precise results, it may also be defined by residual heat flow from the other thermal transfer processes [36, p. 107-109].

<sup>5</sup>A method where the temperature and heat transfer is calculated for each reflective layer in a MLI.

<sup>6</sup>A method which uses an experimental based semi-empirical formula to calculate the overall heat flux through the insulation layer.

where  $\varepsilon$  is the emissivity of the reflecting surfaces,  $\sigma$  is the Stefan Boltzmann constant,  $T_o$  is the ambient temperature,  $T_c$  is the cargo temperature, and  $\Delta x$  is the thickness of the insulation [19, p. 58].

Equation 5.8 gives a theoretical minimum  $k_a^{MLI}$  of reflective insulants. However in practice, the value is higher since heat flow via solid conduction, molecular desorption between the reflecting layers and possibly residual gas conduction may be present.

The most common MLI used in the cryogenic industry are tabulated in Table 5.9.

**Table 5.9:** Commercial Multi-layer insulation types at  $1.33 \cdot 10^{-9}$  bar [19, p.59]

	Layers/cm	$k_{\text{eff}}$ [mW/(m·K)]
0.01 mm aluminium foil + Dexter paper	20	0.052
0.01mm aluminised Mylar + Dexter paper	9	0.2
0.006 mm aluminium foil + nylon net	11	0.034
NRC2 crinkled aluminised Mylar film	20	0.028
0.01 mm aluminium foil + carbon-loaded fiberglass paper	30	0.008-0.019
0.01 mm aluminised Mylar + carbon-loaded fiberglass paper	30	0.026-0.036

#### K-value based on empirical formulas

Excluding some heat transfer mechanisms and not taking into account the temperature dependency of the apparent thermal conductivity may, in the particular case of storing liquid hydrogen, give inaccurate results.

Based on measured values, A. Hofmann managed to approximate, in one of his studies [31], different empirical formulas to determine the thermal conductivity of several materials at different vacuum levels as a function of temperature.

The suggested function is

$$k_a = a + bT^c \quad (5.9)$$

which results in a schematic view of the equation similar to Figure 5.8.

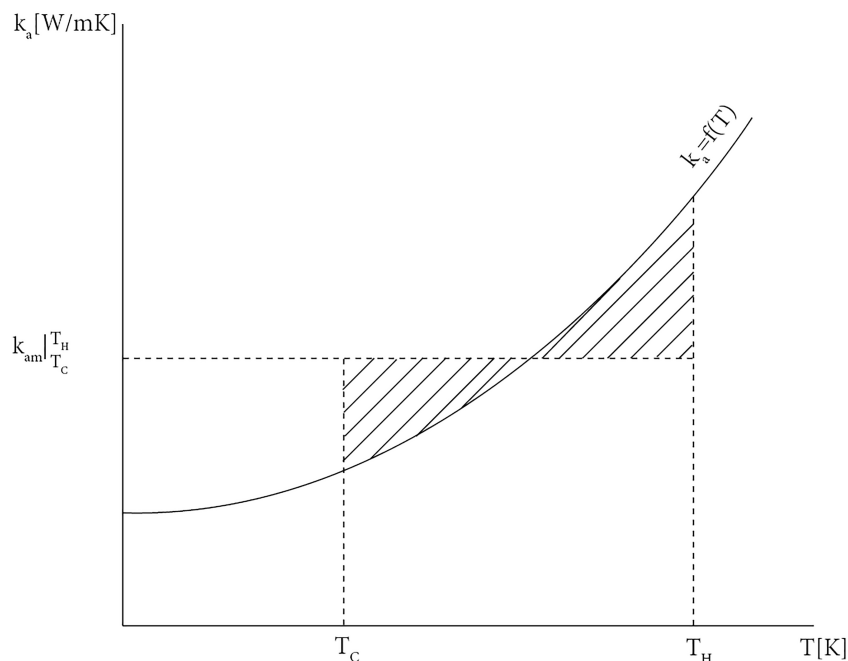


**Figure 5.8:** Schematic view of  $k_a$  and the integral mean value between two temperatures [31]

By integrating Equation 5.9 between the hot and cold temperature, and equating the areas depicted

in Figure 5.8, results in:

$$k_a|_{T_C}^{T_H} = a + \frac{b}{c+1} \left( \frac{T_H^{c+1} - T_C^{c+1}}{T_H - T_C} \right) \quad (5.10)$$

where  $a, b$  and  $c$  are constants which are determined through a minimum of three measurements<sup>7</sup> for each insulation material.

In Hofmann's study [31] it has been concluded that, for insulation materials at atmospheric pressure the apparent thermal conductivity has a linear behaviour, with  $c$  having a value of 1. The reason is that the dominant heat transfer mechanism is the heat conduction of the interstitial gas, while radiation heat has a negligible value.

Since, under vacuum conditions, the conduction of the interstitial gas is of negligible order compared to radiation and conduction over the bulk material, the  $c$  value becomes greater than 1. Hofmann managed to calculate the three different constants for evacuated perlite, microglass spheres of the 3M type B37/2000 quality, and fiberglass. These empirical formula constants are tabulated in Table 5.10 together with the values for other materials as well.

In a real multi-layer insulation arrangement, the heat conduction through the rarefied gas and through the spacer between the reflectors, as well as the heat radiation contribute to the total heat transfer. The numerical procedure to determine  $a, b$  and  $c$  has been somehow more complicated<sup>8</sup>, but manageable. A. Hofmann came up with values for 40-layers MLI Linde-system which can be seen in Table 5.10.

**Table 5.10:** Summary of the constants of the empirical function for the treated insulation systems [31]

Insulation system	Constants for the Empirical Functions 5.9 and 5.10
N <sup>2</sup> $p = 1$ bar	$a = -3.4085 \cdot 10^{-3}; b = 0.4210 \cdot 10^{-3}; c = 0.7433$
Perlite in air $\rho = 64$ kg/m <sup>3</sup> $d_m = 0.5$ mm $p = 1$ bar	$a = 8.2500 \cdot 10^{-3}; b = 1.1650 \cdot 10^{-4}; c = 1.0000$
Perlite-vacuum $\rho = 50$ kg/m <sup>3</sup> $d_m = 0.5$ mm $p \leq 1 \cdot 10^{-6}$ bar	$a = 1.9112 \cdot 10^{-4}; b = 3.4757 \cdot 10^{-12}; c = 3.6783$
Microglass spheres-vacuum $\rho = 225$ kg/m <sup>3</sup> $d_m = 0.1$ mm $p \leq 1 \cdot 10^{-6}$ bar	$a = 3.7037 \cdot 10^{-4}; b = 7.4041 \cdot 10^{-11}; c = 3.0158$
Fiberglass-vacuum $\rho = 240$ kg/m <sup>3</sup> $d_m = 1.143$ $\mu$ m $p \leq 1 \cdot 10^{-6}$ bar	$a = 2.7074 \cdot 10^{-4}; b = 3.0830 \cdot 10^{-11}; c = 3.0$
Multilayer insulation (Linde-system) $N = 40$ $L = 0.040$ m $p \leq 1 \cdot 10^{-7}$ bar	$a = 1.6918 \cdot 10^{-5}; b = 1.2268 \cdot 10^{-13}; c = 3.6457$
Ideally arranged reflectors $N = 40$ $L = 0.5$ m $p \leq 1 \cdot 10^{-9}$ bar	$a = 1.1176 \cdot 10^{-7}; b = 2.4220 \cdot 10^{-14}; c = 3.8642$

It is important to mention that the maximum pressure limit chosen for the evacuated materials, besides MLI, is at the point where the heat conduction through the interstitial gas becomes negli-

<sup>7</sup>Measurements where at least one of the boundary temperatures has to be changed while all the other parameters are constant.

<sup>8</sup>More information can be found in the reference

gibly small compared to the other heat transfer mechanisms based on the characteristic diameter of the insulation material. As for the MLI, the conditions were randomly chosen for the representative measurement.

*K-value based on experimental data specific for bulk-fill insulation materials*

B.E. Scholtens et al. [62] has conducted a detailed experiment using a Cryostat-100<sup>9</sup> test apparatus to establish the apparent thermal conductivity under actual-use conditions of several bulk-fill insulation materials. The data provided by this experiment is of high interest for the present study as bulk-fill insulation may be the best option for large scale LH<sub>2</sub> storage. Glass bubbles, perlite powder and aerogel beads have been subjected to 83 tests conducted over a period of 500 hours and under different vacuum conditions. The material density as well as its trade name are tabulated in Table 5.11.

**Table 5.11:** Trade name and density of the three bulk-fill insulations [62]

Material	Trade name	Tap density [kg/m <sup>3</sup> ]
Glass Bubbles	3M Scotchlite Type K1	80
Perlite Powder	Ryolex grade no. 39	166
Aerogel Beads	Nanogel	86

B.E. Scholtens et al. conclude that the glass bubbles have the best thermal performance under evacuated, but aerogel beads may perform better under normal pressure conditions. The results are shown in Table 5.12.

**Table 5.12:** k<sub>a</sub>-values for bulk-fill insulation and pure vacuum at different evacuated levels [62]

Pressure, [bar]	k-value [mW/(m·K)]			
	Glass Bubbles	Perlite Powder	Aerogel Beads	Vacuum Only
1.33·10 <sup>-8</sup>	0.70	0.94	1.71	10.14
1.33·10 <sup>-7</sup>	0.70	0.95	1.73	10.66
1.33·10 <sup>-6</sup>	0.71	1.00	1.83	12.54
1.33·10 <sup>-5</sup>	0.83	1.31	1.83	18.16
1.33·10 <sup>-4</sup>	1.70	3.83	4.33	22.44
1.33·10 <sup>-3</sup>	7.76	13.99	7.44	-
1.33·10 <sup>-2</sup>	19.58	27.85	8.89	-
1.33·10 <sup>-1</sup>	25.13	33.60	10.29	-
1.00	26.12	34.85	14.34	-

In the research paper [62] experiments with pure vacuum as insulation is also conducted, data which may be used as reference in this study. It is also mention that the apparent thermal conductivity is a total of solid conduction, gas conduction and convection, as well as radiation heat transfer, and that the temperature ranges from 78 K to 293 K with nitrogen as the residual gas.

### Insulation thickness

The type of insulation material is not the only method to reduce the boil-off gas rate. From Equation 2.32 it can be observed that higher the  $\Delta x$ , in this case the thickness of the insulation, the higher the conductive resistance. Hence, from Equations 5.5 and 2.47, it results that the BOR decreases if the thickness of the insulation layer increases.

To avoid underestimated values of the heat transfer rate through the insulation system, the presence of the inner tank must be considered, due to increase of the insulation's inner and outer radius; hence increase of the overall cross-sectional area. Since the thickness of the inner tank is included, the thickness of the outer tank will be included as well. Both of the thicknesses are uniformly

<sup>9</sup>A cylindrical liquid nitrogen evaporation calorimeter from which absolute apparent thermal conductivity values can be obtained



distributed on the spheres and are equal to 0.048 m as mentioned in the aforementioned subsection. Considering this particular case, we get:

$$Q = \frac{T_{s,o} - T_{s,i}}{\frac{r_{ins} - r_{w_i}}{4\pi k_{w_i} r_{w_i} r_{ins}} + \frac{r_{w_o} - r_{ins}}{4\pi k_a^{ins} r_{ins} r_{w_o}} + \frac{r_s - r_{w_o}}{4\pi k_{w_o} r_{w_o} r_s}} \quad (5.11)$$

where:

$T_{s,i} = 20.3K$  is the internal surface temperature of the primary tank

$T_{s,o} = 313K^{10}$  is the external surface temperature of the secondary tank

$r_{w_i} = 21.2m$  is the radius to the primary tank

$r_{ins} = r_{w_i} + 0.048m$  is the radius to the insulation layer

$r_{w_o} = r_{ins} + \Delta x$  is the radius to the secondary wall, with  $\Delta x[m]$  being the thickness of the insulation layer

$r_s = r_{w_o} + 0.048m$  is the radius to the external surface

$k_{w_i}$  is the thermal conductivity of the primary tank

$k_a^{ins}$  is the apparent thermal conductivity of the insulation layer

$k_{w_o}$  is the thermal conductivity of the secondary tank

With the results of Equation 5.11, depending on the thickness of the insulation, different preliminary BOR values have been calculated for different insulation materials, and are depicted in Figure 5.9 in a Log BOR-thickness diagram.

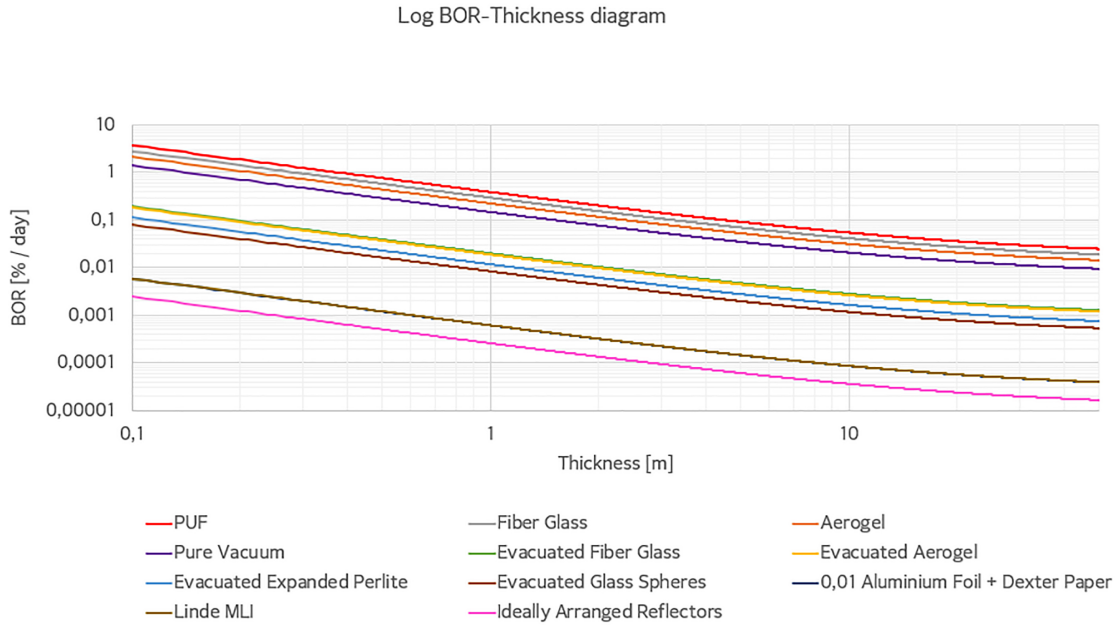


**Figure 5.9:** BOR-insulation thickness relationship of a spherical LH<sub>2</sub> storage vessel for different insulation types computed using Equation. 5.11 (own work)

In their paper entitled "Design and safety considerations for large-sea-borne hydrogen transport" U. Petersen, G. Würsig and R. Krapp show that the heat transfer coefficient ratio between LNG and LH<sub>2</sub> storage is approximately equal to 10 for similar boil-off rates, filling levels and identical geometries. [57] It translates that the thermal resistance for liquid hydrogen storage systems should be 10 times greater to achieve a similar performance as the liquid natural gas storage tank, in terms of BOR. Considering this statement and observing the diagram from Figure 5.10, it can be concluded that the two may validate each other. Figure 5.10 shows how the boil-off rate varies with  $\Delta x$  for non-evacuated insulation systems.

<sup>10</sup>According to DNV GL [17], the upper design temperatures for normal services are 305 K in the sea and 318 K in the air, thus resulting an overall estimated value of 313 K for easier calculations.

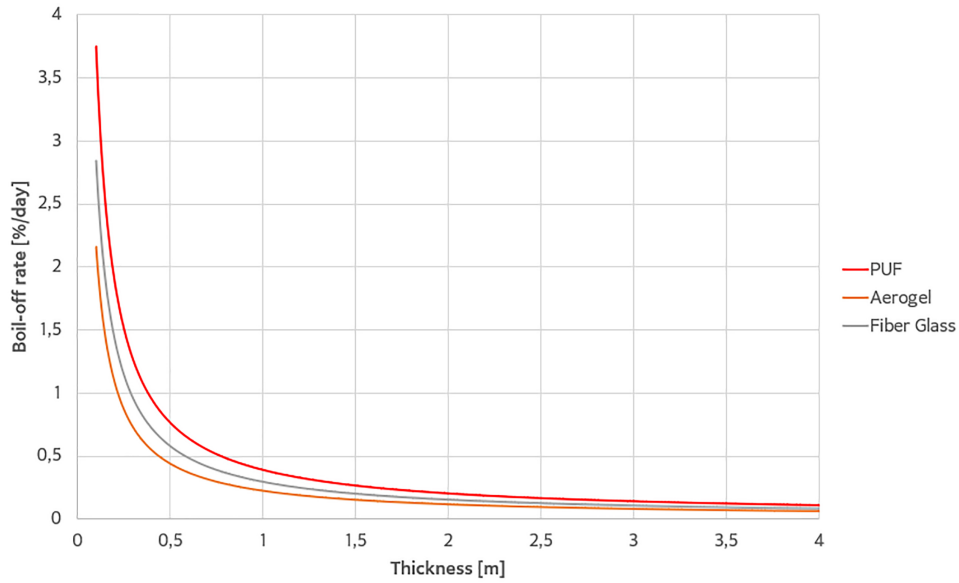


**Figure 5.10:** BOR-insulation thickness relationship of a spherical LH<sub>2</sub> storage vessel for (at 1.00 bar pressure) computed using Equation 5.11 (own work)

In a LNG Moss Rosenberg design, the thickness of the insulation system is of approximately 0.22 m having a boil off rate of 0.15 % per day. For the same insulation thickness, the boil off rate of liquid hydrogen is of 1.5 % per day, under similar conditions, which is 10 times greater. To achieve a BOR of 0.15 % the insulation layer for LH<sub>2</sub> storage system, as shown in Figure 5.10, must be approximately 2.20 m. If the supportive system is included as well, a general conclusion based on the diagram is that a thickness greater than 2.00 m is required to end up with a boil-off rate of under 0.2 % per day.

Figure 5.11 (own work) sketches the proportion between different insulation thicknesses and the radius of the inner wall, for an understanding of a real case scenario.

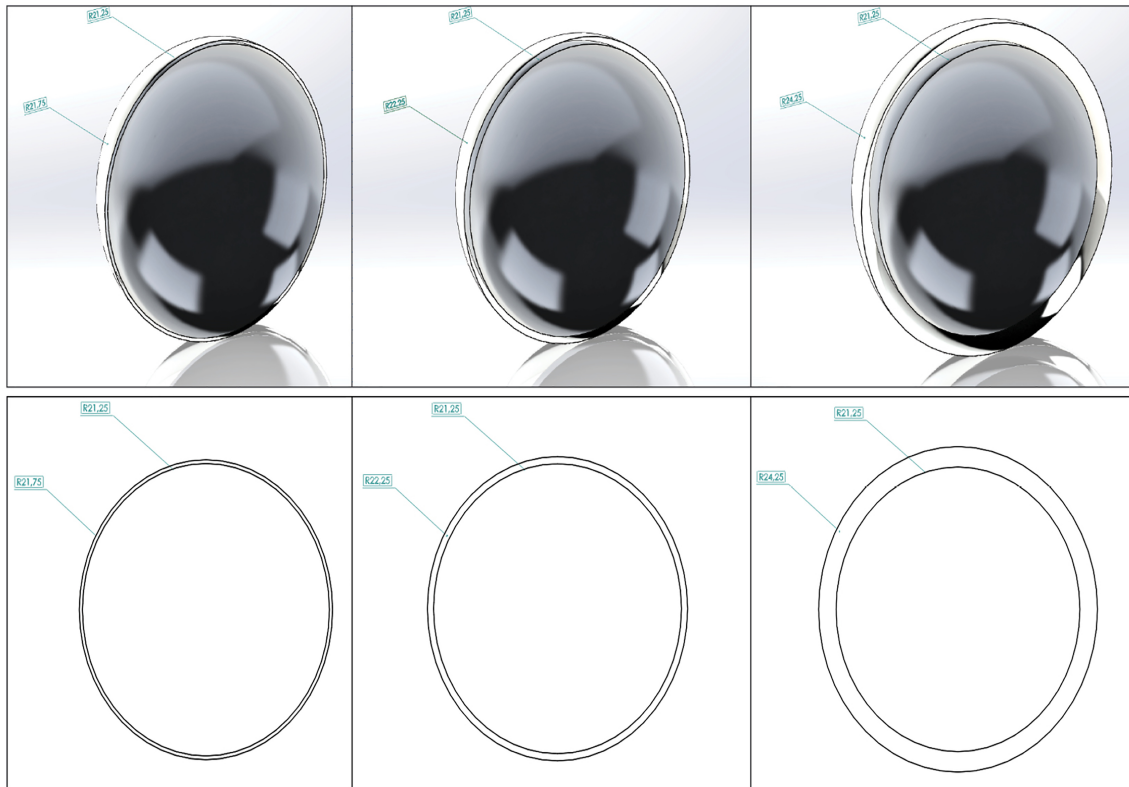


**Figure 5.11:** Representation of the two spherical walls with a distance between them of 0.5 m, 1.0 m and 3.0 m

Based on the aspect-ratio and considering the costs of the materials of the system as well as the difficulty of fabrication and maintenance, the use of a 2.00 m thick insulation layer, or greater seems questionable due to the great dimensions of the structure. On the other hand, the thickness of 1.00 m or less seems reasonable.

Better suited options are depicted in Figure 5.12 showing the BOR variation for different thicknesses of evacuated insulations. With a layer between 0.4 and 0.6 m thick, using evacuated perlite, for example, may be a suitable solution to achieve the goal of under 0.2 % BOR. The fact that NASA also uses this type of material in storing liquid hydrogen may support the idea of using evacuated powders or similar evacuated materials.

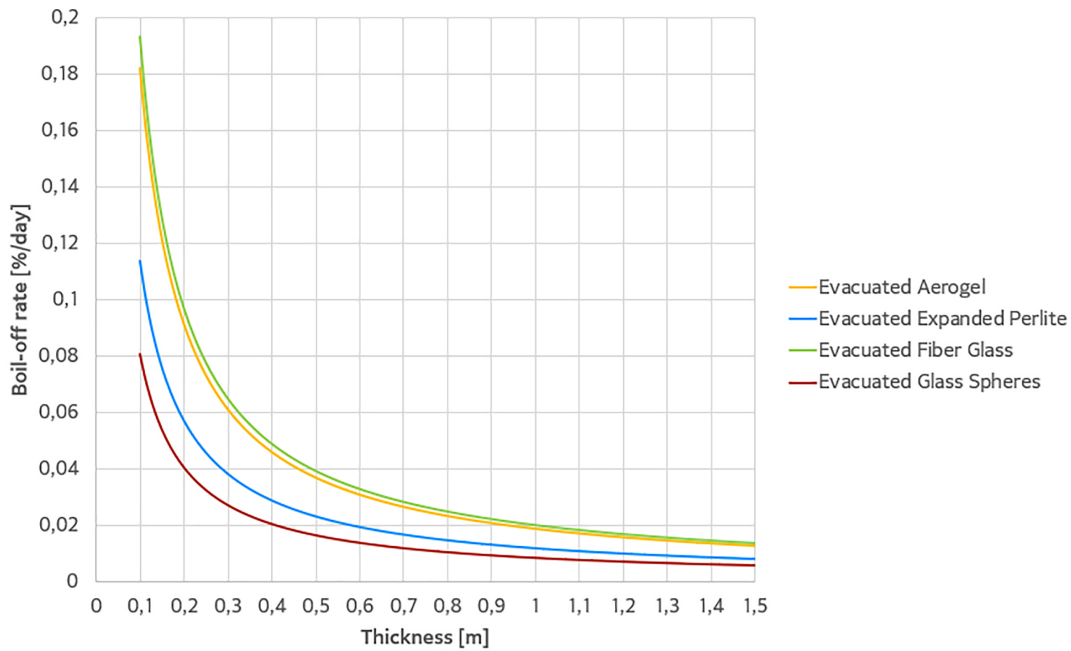


**Figure 5.12:** BOR-insulation thickness relationship of a spherical LH<sub>2</sub> storage vessel ( $1.33 \cdot 10^{-6}$  bar) computed using Equation 5.11 (own work)

As for multi-layer insulation materials, Figure 5.13 shows a boil-off rate close to 0 % which may be ideal. Nevertheless, using MLI may probably be difficult to realize for very large scale storage systems such as the one in the present case, due to poor physical strength and higher evacuation levels.

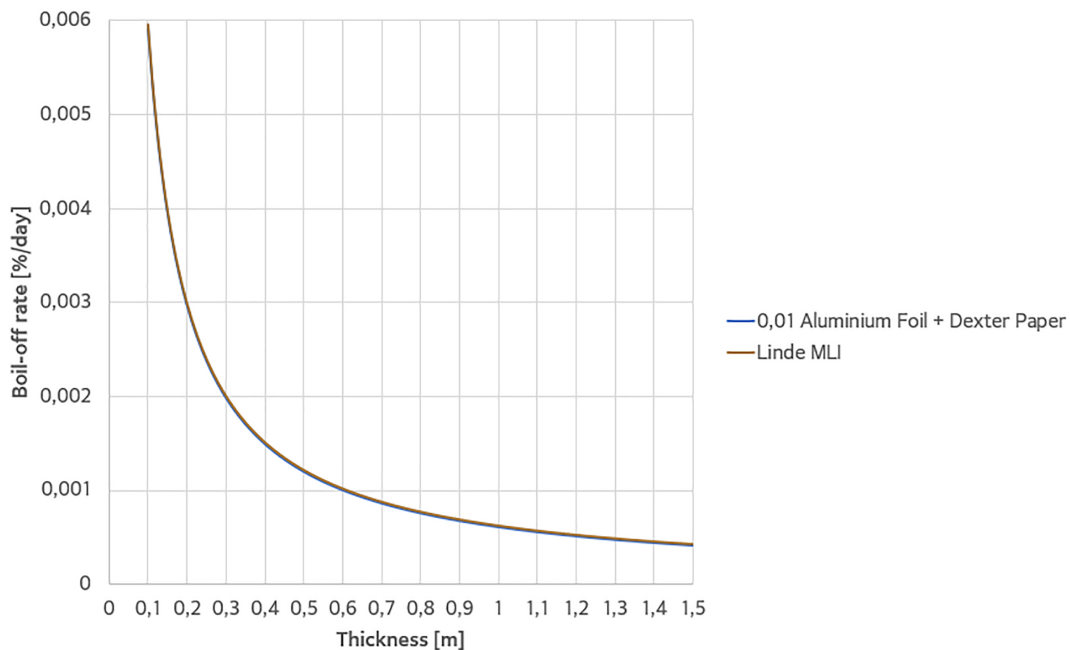


**Figure 5.13:** BOR-insulation thickness relationship of a spherical LH<sub>2</sub> storage vessel (MLI at  $1.33 \cdot 10^{-9}$  bar pressure) using Equation 5.11 (own work)

### 5.2.2 Support system of the internal spherical tank

The system that bears the weight of the cargo and spherical inner tank is of equally importance as the insulation system in terms of heat leakage. The main mechanism of thermal transfer is by conduction through the structure as it is made of solid materials that can support the mechanical loads. The materials applied have high apparent thermal conductivities compared with the ones

used for the insulation layer. This results in a significant amount of heat ingress.

Using segments of different materials which may act as thermal breakers is a common procedure. Similar to the sandwiched insulation layer between two spherical walls, the support can also be characterised by a specific thermal circuit. A simplified depiction of how the thermal heat transfer can be theoretically analysed is represented in the self-made Figure 5.14 with the resulting Equation 5.12.

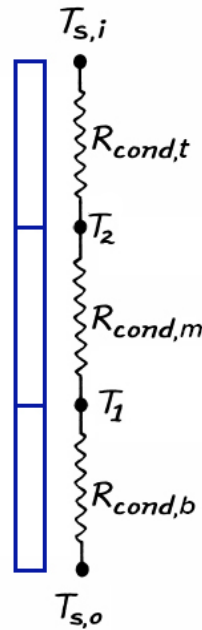


Figure 5.14: Thermal circuit inside a skirt

$$Q = \frac{T_{s,o} - T_{s,i}}{R_{cond,b} + R_{cond,m} + R_{cond,t}} \quad (5.12)$$

The aforementioned image and the resulted equation are used to evaluate the heat flow inside a skirt similar to the one discussed in the Subsection 5.1.3. The sketch is based on major simplifications which only concludes in values that can be used as references for the simulation results. The different resistances are expressed by the Equation 2.32 with the specific variables for each segment. The segmentation into three pieces is typical for the skirts used in the LNG industry, but can however vary depending on the case.

Similar to the case described in the previous section the thermal resistance must be increased as much as possible to reduce the heat leakage. This is done by either increasing the distance travelled by the heat or choosing suitable materials.

### Support system material

To highlight the importance of the material applied, a simple comparison is done between three metals which are highly used in the LNG industry is done. In Moss Rosenberg designs, stainless steel is chosen to act as a thermal breaker between the bottom section and top section of the skirt which are made of carbon steel and aluminium alloy respectively. The reason is the low thermal conductivity of the material. Table 5.13 shows the thermal conductivity of the three metals and resulting heat transfer from 40 to -253 °C through a 0.5 m thick plate with a cross section area of 1.00 m<sup>2</sup>. The heat flow is calculated by using the following equation:

$$q = \frac{\Delta T}{\frac{t}{kA}} \quad (5.13)$$

Metal	$k_a$ -value [W/(m·K)]	Heat flow $q$ [W]
N-VA Grade C-steel	52.0	$30.4 \cdot 10^3$
AISI 304/316	13.4	$7.84 \cdot 10^3$
Al-alloy 5083	117	$68.5 \cdot 10^3$

**Table 5.13:** Thermal comparison of the three metals used in the skirts of the Moss Rosenberg-design

The ratio between the resulted heat transfer rates are equal to the ratio between the thermal conductivity values as all the other variables are equal. As it can be observed, stainless steel conducts approximately nine times less heat than aluminium alloy, which is the reason why this material is used as a thermal breaker material for skirts in the LNG industry.

### Support system length

In Subsection 5.1.3 when comparing the two support systems, it has been specified that the greater the distance between the two temperatures the lower the heat leakage. Figure 5.15 shows how the BOR may vary with the  $q$  obtained from using Equation 5.14 for different lengths of the middle section of the skirt depicted in Figure 5.14.

$$Q = \frac{T_{s,o} - T_{s,i}}{\frac{h_b}{k_b t_{sk} 2\pi r_{sk}} + \frac{h_m}{k_m t_{sk} 2\pi r_{sk}} + \frac{h_t}{k_t t_{sk} 2\pi r_{sk}}} \quad (5.14)$$

where:

$T_{s,i} = 20.3K$  is the internal surface temperature of the primary tank

$T_{s,o} = 313K$  is the external surface temperature of the secondary tank

$t_{sk} = 0.05m$  the thickness of the skirt

$r_{sk} = 21.248m$  is the radius of the cylindrical

$h_b = 1.00m$  is the height of the bottom segment of the skirt

$h_m = \Delta x$  is the height of the middle segment of the skirt, also known as the thermal breaker, where  $\Delta x[m]$  is the distance between the top part of the bottom segment and the bottom part of the top segment

$h_t = 1.00m$  is the height of the top segment of the skirt

$k_b = 52W/(m \cdot K)$  is the thermal conductivity of the bottom segment of the skirt

$k_m = 13.4W/(m \cdot K)$  is the thermal conductivity of the middle segment of the skirt.

$k_t = 117W/(m \cdot K)$  is the thermal conductivity of the top segment of the skirt.

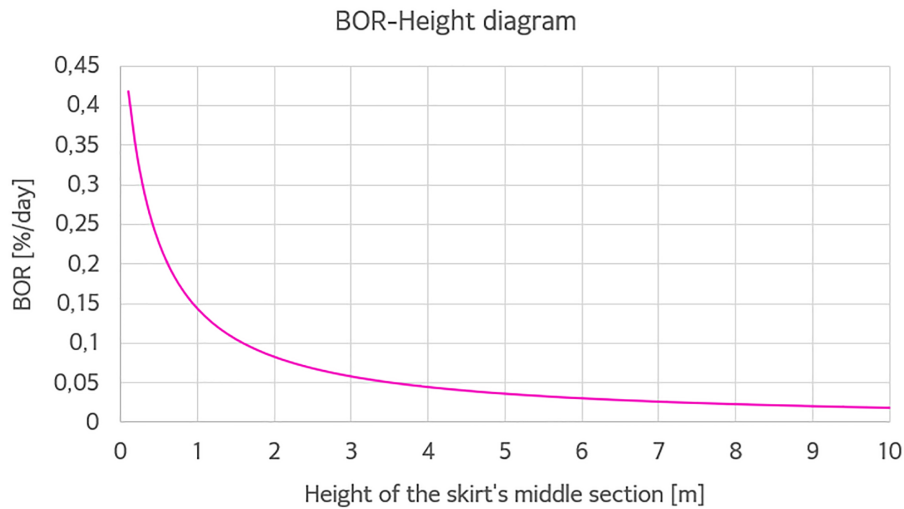


**Figure 5.15:** BOR-height relationship of a skirt used as a supportive system in LH<sub>2</sub> storage tanks

The thermal conductivity values come from the materials usually used for the skirt in the LNG Moss Rosenberg design, carbon structural steel, stainless steel and aluminum alloy. The two lengths of the bottom and top segments of the skirt are lengths which are given arbitrary values, but can also

vary similar to the middle skirt section. The reason that only the middle part varies is simply to easily highlight the dependency on length of the heat flow while following the segmented geometry from Figure 5.14.

---

## Chapter 6

# Structural analysis of preliminary design

There are two fundamental analysis that must be conducted to be able to accomplish the objective of this study; the thermal and mechanical analysis. The application of an insulation material that can be used to achieve the desired boil-off rate requires a fitting structural geometry that can sustain real-case scenario loads. The mechanical strength of the structure must be thoroughly evaluated to see if the proposed preliminary design is suited for the task.

### 6.1 Setup

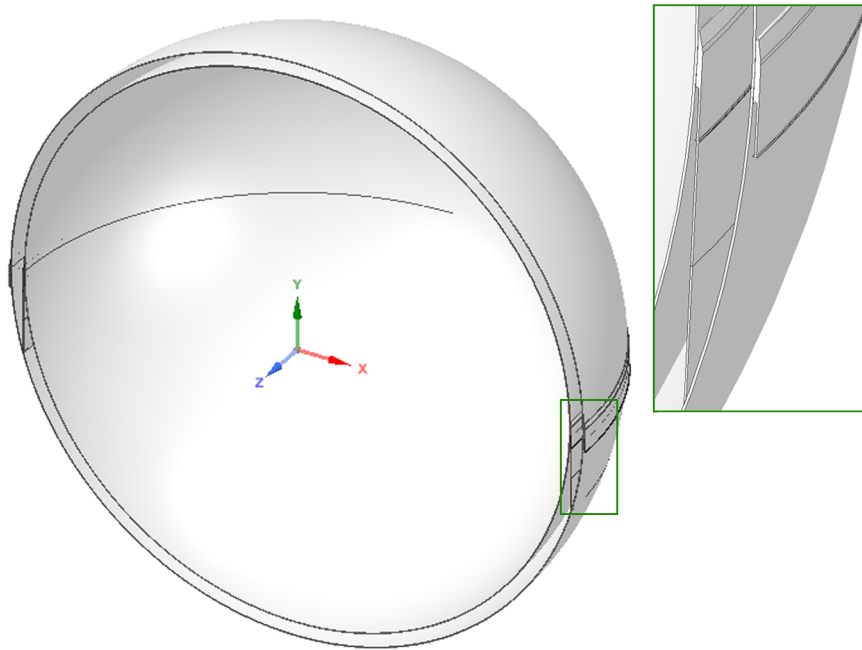
The structural analysis is achieved by conducting several static-structural simulations from which the total deformation and Von-Mises, Maximum Principle, and Maximum Shear stress are evaluated.

Due to limited computer resources an entire 3D-geometry with a fitting and detailed mesh is impossible to simulate within this thesis work. For a correct mesh, the low thickness of the model requires small elements resulting in an extremely high number of nodes which demands great computer resources. This issue is solved with the help of the symmetry that is either implemented on a quarter or a half of the entire system, depending on the behaviour of the applied loads and boundary conditions. If their behaviour is axisymmetric, for example, even a 2D cross-sectional model of the geometry can be simulated resulting in equally relevant values as for an entire 3D-model at lesser costs in terms of computational time and computer resources. A detailed description about what type of symmetry can be used based on the existing loads is given in Subsection 6.1.3.

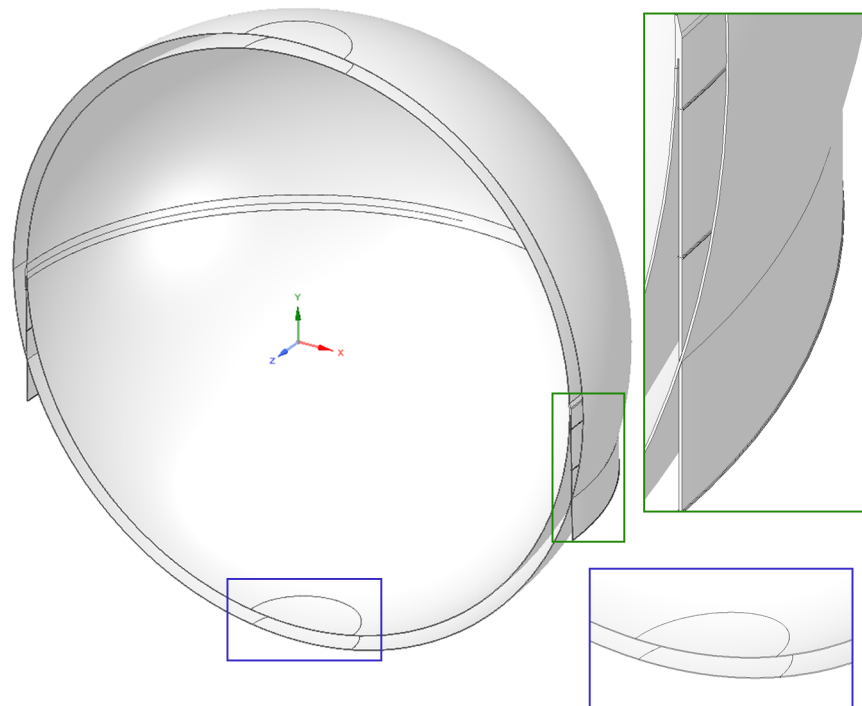
#### 6.1.1 Design setup

In the preliminary design, named P1, the initial idea was to model two whole spherical shaped figures which would then be attached to the to the inner side of the separated skirt-elements as seen in Figure 6.1a. By analysing the design more carefully, it has been concluded that it is better to divide the spherical wall into segments as depicted in Figure 6.1b.





(a) Preliminary design (initial setup)



(b) Preliminary design (final setup)

**Figure 6.1:** Mesh for the spherical geometry of the containment system

The lid-shaped segments at the poles serve the purpose of facilitating the creation of the desired mesh, discussed in Subchapter 6.1.2. By making this segmentation, one can avoid having a large number of elements meeting in a singular point at the poles, probably causing the effect of a singularity in a region where this is not the case.

The idea of designing an equatorial ring welded between the two hemispheres of the dome shells

serves two purposes. The first one is to follow the concept of the LNG Moss Rosenberg-design as much as possible since using a skirt as a support system is inspired from this design. All the sketches in the researched literature follow such a concept; examples being Figure 6.2 and the design in Appendix B.

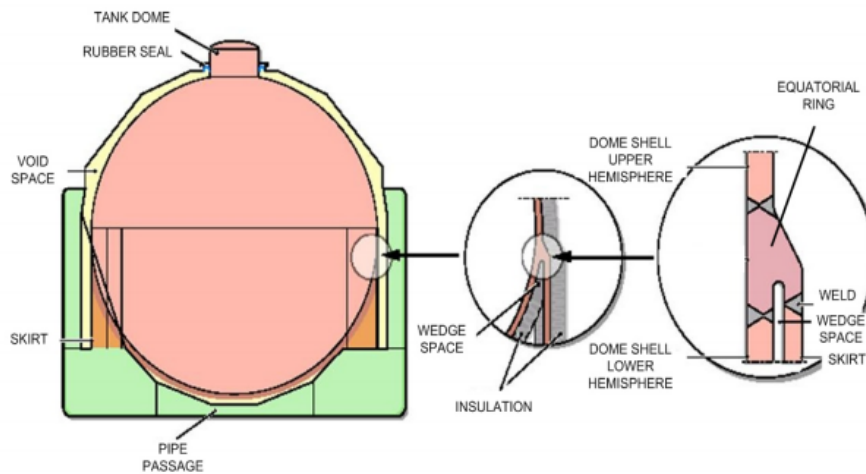


**Figure 6.2:** Method of binding the skirt to the spherical tank in a LNG Moss Rosenberg-design [1]

The second purpose is to facilitate the weight distribution of the insulation layer. The insulation material is not visually represented in design, but its weight is however considered as a load and is applied on different segments of the spherical tanks. The distribution of the insulation mass is detailed in Subchapter 6.1.3. The reason why the insulation layer is not designed in the structural analysis is because the intended insulation material, either bulk-fill or MLI, is not self-supportive and therefore the impact of its structural resistance can be neglected.

The exterior skirt has negligible effect on the quantity of heat ingress as it is not in direct contact with the inner tank. Its geometry and material properties can be more or less ignored in this study, and it can be concluded that its shape can be freely chosen. Therefore only the superior segment of the skirt has been designed, serving the sole purpose of being used as a fixed support when conducting the structural analysis.

For a more understandable overview, Figure E.1 in Appendix E depicts the most important dimensions used to create the geometry, especially around the supportive system.

### 6.1.2 Mesh setup

The mesh setup description given by DNV GL in the class guideline "DNVGL-CG-0134" [15, p.55] has been considered for the designed geometry. Given that the ratio between the diameter and the wall-thickness is approximately 1000, a combination of 8- and 6-node shell elements on the hemispheres and 20-node solid elements at the equatorial line is recommended by DNV GL. A mesh size of  $\frac{1}{30}$  of the tank's diameter should satisfy the number of elements required to correctly represent the stiffness of the model. Figure 6.3a depicts this arrangement. An attempt on following a similar mesh-pattern is firstly created for an unsegmented spherical geometry as shown in Figure 6.3b, where the element size is smaller and the particular arrangement around the equatorial ring is absent. This arrangement is then modified to fit the actual geometry used in the simulations, as seen in Figure 6.3c

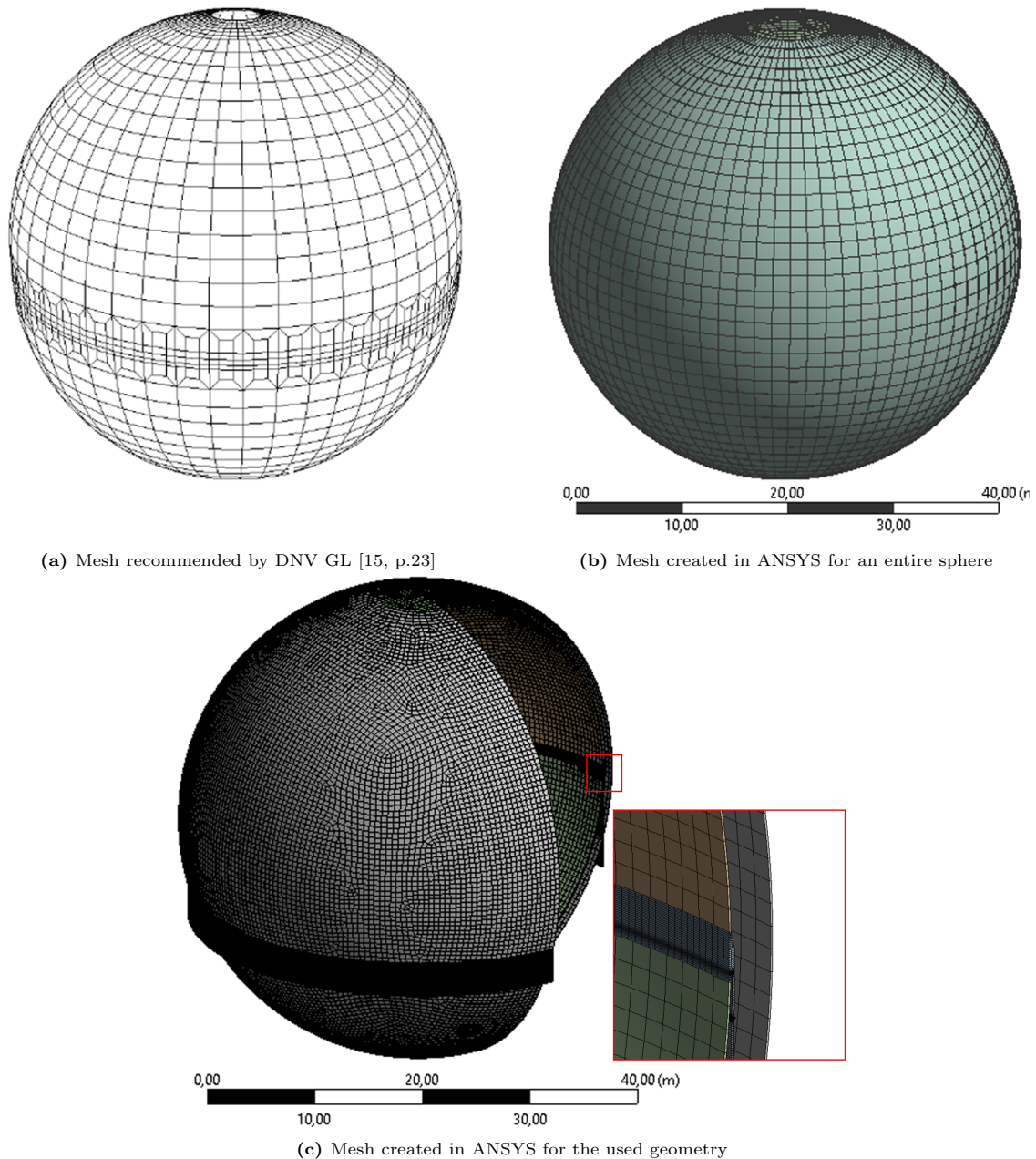
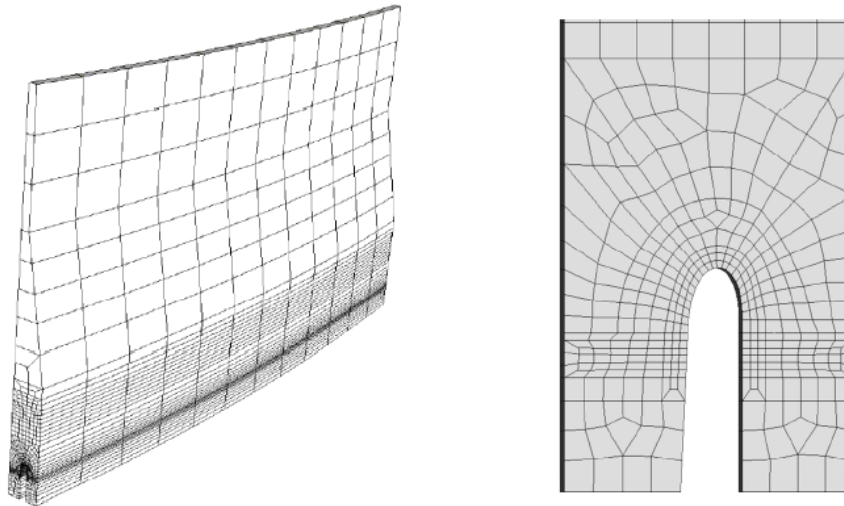


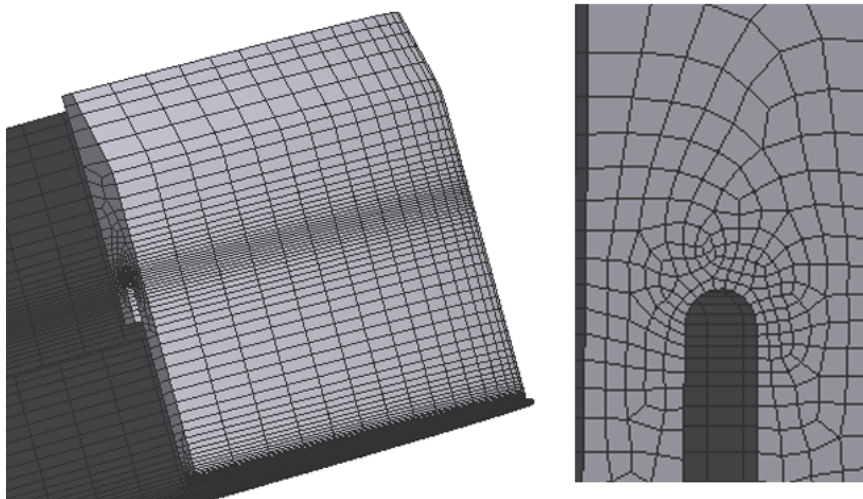
**Figure 6.3:** Mesh for the spherical geometry of the containment system

The increase in the element numbers is due to the, shrinking of the element size to achieve better results and to avoid unrealistic results caused by singularities. The initial element size used to create the mesh in Figure 6.3b resulted in exaggerated values in some specific points on the geometry, a problem which has been fixed by reducing the element size even more, as shown in Figure 6.3c.

A complex description on how to correctly mesh the skirt is given by DNV GL in "DNVGL-CG-0134" [15, p.23]. However, since the designed skirt of this study is not as elaborated as in a real case scenario, only the idea of following the correct mesh density as depicted in Figure 6.4a has been applied.



(a) Illustration of typical mesh density for skirt-element by DNV GL [15, p.58]



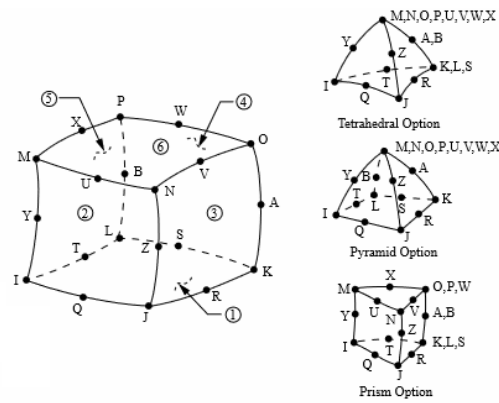
(b) Illustration of personal made mesh of the skirt

**Figure 6.4:** Comparison between a proposed and a personally made mesh of the skirt

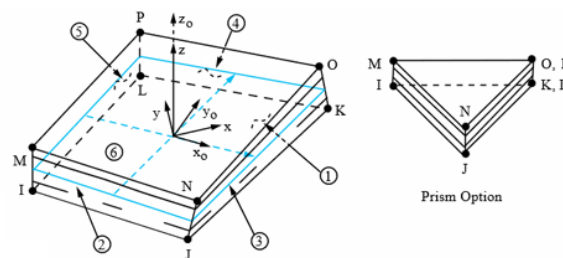
The final mesh is created for a  $\frac{1}{4}$  of an entire geometry by using a combination of MultiZone and Sweep methods, and it is composed of a total number of 141 580 elements and 670 046 nodes. For the Static Structural analysis the mesh is mostly a combination of SOLID186, SOLSH190 elements which are described, in ANSYS Element Library as follow:

The SOLID186 are higher order 3D 20-node solid elements that exhibit quadratic displacement behaviour. This type of element has 20 nodes with three degrees of freedom per node, as depicted in Figure 6.5a. SOLID186 is especially useful when simulating deformations of fully incompressible hyperelastic materials, and nearly incompressible elastoplastic materials, as it supports plasticity, hyperelasticity, creep, stress stiffening, large deflection, and large strain capabilities [6].

The SOLSH190 combine the best of both solid and shell elements and are used to simulate shell structures with a wide range of thickness. It includes the continuum solid element topology and features 8-node connectivity with three degrees of freedom per node, as depicted in Figure 6.5b. They are more fitting than shell elements, as initially described by DNV-GL since this type is compatible with 3D constitutive relations and can be connected directly with other continuum elements. SOLSH190 can simulate deformations for nearly incompressible elastoplastic and fully incompressible hyperelastic materials, and supports similar capabilities as SOLID186 [8].



(a) Sketch of the SOLID189 mesh element [6]

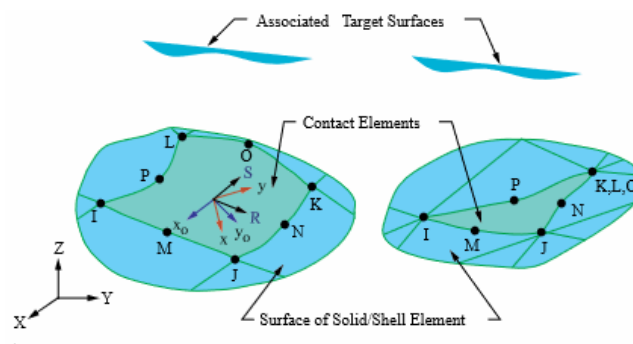


(b) Sketch of the SOLSH190 mesh element [8]

**Figure 6.5:** Mesh elements used in the Static Structural Analysis

In the solution information, Ansys Mechanical APDL also shows the presence of two element types which work in pair. These are CONTA174 and TARGE170 and are used to analyse the contact mechanisms of two bodies, with the surface of one body as a contact surface and the surface of the other body as the target surface.

CONTA174 is intended for general flexible-flexible and rigid-flexible analysis, having 8-nodes as depicted in Figure 6.6. Due to the existence of both solids and solid-shells, the elements are automatically created and simulate the forces existent at the contact between the two; Such forces can be coulomb friction and shear stress friction [9].

**Figure 6.6:** Sketch of the CONTA174 mesh element associated with Target surfaces [9]

The TARGE170 on the other hand is used to represent the 3D "target" surfaces for the associated contact elements. On these elements translational or rotational displacement, temperature, voltage, magnetic potential, pore pressure, concentration, as well as forces and moments can be imposed [10].

### 6.1.3 Material properties, and boundary conditions setup

Besides creating and implementing new materials into the program, ANSYS Workbench gives access to several material databases which mostly includes the materials used for the design of the structure evaluated in this study. There is the main Ansys Material Database and the Ansys GRANTA Material Data. The second database has a slightly wider variety of materials, most of which have temperature dependent properties, something which is highly relevant for this study. To facilitate the work, all the materials needed for the structural analysis have been directly taken from the Ansys GRANTA Material database and modified if needed.

Both stainless steel 316 and NV-A Grade low carbon steel are found in the aforementioned database, and by comparing the registered values of the material properties of AISI 316 with the ones tabulated in Table 5.5, the values are consistent. The material properties of both metals can be found in Appendix D, Sections D.1 and D.2.

The two materials are attributed to the specific components of the design, as follows:

- AISI 316: All the segments of the internal sphere and the top and middle segment of the inner skirt.
- Low Carbon Steel: All the segments of the external sphere, the bottom segment of the skirt, and the external supportive system.

Two additional materials are created to approximately represent the weight of the insulation layer. Assuming there is no wave induced movement, a gravitational load exists and acts vertically on the structure. This load is weight-dependent, and therefore the weight of the insulation layer and is considered. This is achieved by increasing the density of the metal used for the structural segments on which the weights is acting. The weight of the insulation material is vertically acting on the exterior of the top hemisphere of the internal tank, and the inside of the external tank's lower hemisphere, as highlighted in Figure 6.7.

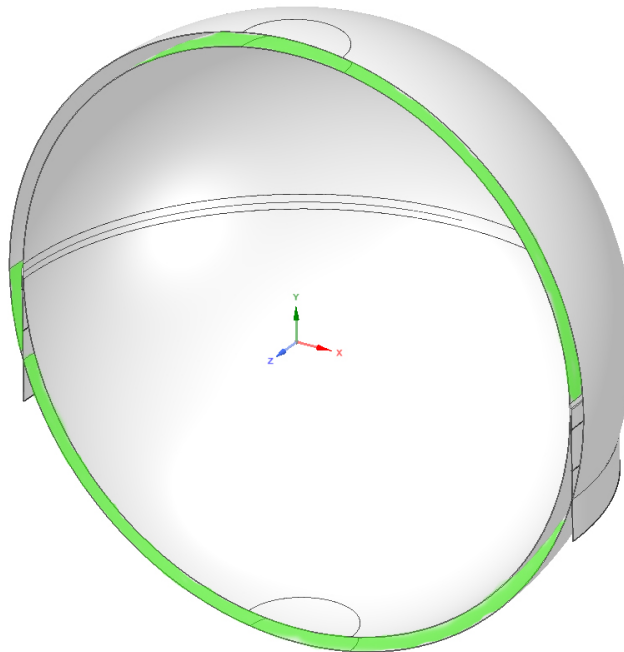


**Figure 6.7:** Weight distribution of insulation

The procedure to find out the value of the added weight per cubic meter of metal is as follows:

- Step 1: Find the total weight value of the insulation layer by multiplying the density with the total volume supported by the specific tank segment.
- Step 2: Divide the resulted value by the surface area on which the weight acts as a load.

- Step 3: Divide the result with the thickness of the tank wall, and then add the resulted density to the density of the respective metal.

The total weight of the insulation system made of micro-glass spheres with a density of 225 kg/m<sup>3</sup> filling the space between the tanks of 5 945 m<sup>3</sup> is ca. 1 338 tonnes. The value is overestimated because the presence of the skirt is absent in the calculation. Considering this weight and the surface areas extracted from ANSYS DesignModeler for each segment of the geometry created, the aforementioned procedure gives the following results:

**Table 6.1:** Change in density of different segment on the geometry

Segment	Surface	Initial density [kg/m <sup>3</sup> ]	Added density from weight-load [kg/m <sup>3</sup> ]	New density [kg/m <sup>3</sup> ]
Inner tank: higher hemisphere	Exterior	7 969	5 035	13 004
External tank: lower hemisphere	Interior	7 850	4 480	12 330

It is important to mention that this procedure is a trivial approximation that fits the created geometry. It is expected that in a real case scenario, the distribution of the weight may differ in a minor degree.

Based on the classification represented in Table 5.1 of the loads considered in this study, Table 6.2 gives an overview of their numerical value and their application area on the system inside Ansys Mechanical APDL.

**Table 6.2:** Loads acting on the designed-system

ID	Type	Value	Area of application
Loads for a motionless system			
L1	Static external atmospheric pressure, $p_{a_o}$ [Pa]	$1.01 \cdot 10^5$	External wall of outer shell
L2	Static internal ambient pressure, $p_{a_i}$ [Pa]	$1.01 \cdot 10^5$	Internal wall of inner shell
L3	Hydrostatic pressure of LH <sub>2</sub> (100 % fill), $p_{LH_2}$ [Pa]	$0.0 - 2.95 \cdot 10^4$	Internal wall of inner shell
L4	Gravitational acceleration, $a_g$ [m/s <sup>2</sup> ]	9.81	All components
Additional loads when the system is in motion			
L5	Hydrostatic pressure of LH <sub>2</sub> from a sloped liquid surface (x % fill), $p_{LH_2}$ [Pa]	-	Internal wall of inner shell
L6	Wave-induced longitudinal acceleration, $a_x$ [m/s <sup>2</sup> ]	1.94	All components
L7	Wave-induced vertical acceleration, $a_y$ [m/s <sup>2</sup> ]	3.58	All components
L8	**Wave-induced transverse acceleration, $a_z$ [m/s <sup>2</sup> ]	5.96	All components
Extra load			
L9	Thermal loading because of the temperature difference from 313K to 20.3 K	-	Applied respective temperature on the external shell and inside the inner shell

In case of a system in motion and partially filled, L5 replaces L3 as it takes into account the movement of the liquid as well as sloshing forces. L6, L7 and L8 are added as extra loads. The

procedure to obtain the values of the loads from L5 to L8 are described in the paragraphs to follow.

### Sloshing load

For large scale cryogenic liquid storage and transportation, sloshing is a mechanical load that must be considered when analysing the strength of a containment vessel.

Sloshing takes place in partially filled tanks and is considered a dynamic load as it is dependable on the movement of the system. The procedure described by DNV GL [15, p. 50] makes it however possible to analyse sloshing as a static load, by calculating an acceleration of the liquid which may be used to account for the sloshing forces in the tank. This acceleration is used to calculate the hydrostatic pressure due to the slope liquid surface as follow:

$$p = \rho \cdot a_R \cdot h \quad (6.1)$$

with  $h$  [m] being the filling level of the cargo in a normal direction to the liquid surface,  $a_R$  [ $\text{m/s}^2$ ] is the acceleration of the liquid produced by the slope/sloshing, and  $\rho$  [ $\text{kg/m}^3$ ] is the density of the liquid.

A visual representation of how the process works is represented in Figure 6.8.

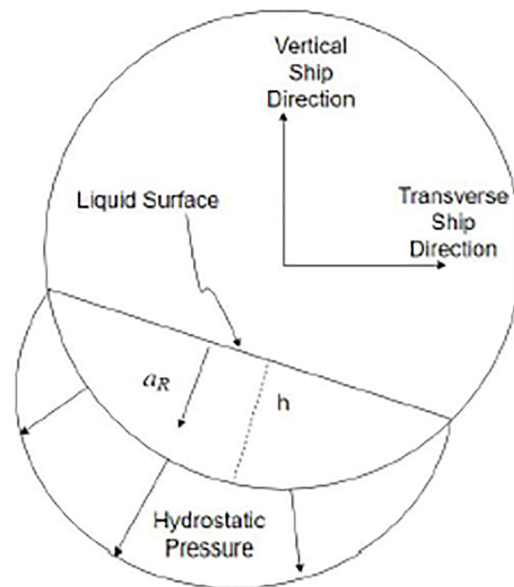


**Figure 6.8:** Representation of hydrostatic pressure resulting from movement of the tank on sea [61]

The first point of the procedure of finding the acceleration  $a_R$  is to find the transverse acceleration on a reference ship which is used to calculate the respective transverse weight force acting on the tank. This is then used to calculate the forces on the actual tank model based on which a transverse acceleration that includes sloshing is composed. The new transverse acceleration is used together with the vertical acceleration to compute  $a_R$ . A more detailed explanation of the process can be found on Pages 50 to 53 in the "DNVGL-CG-0134 Liquefied gas carriers with spherical tanks of type B" [15].

The hydrostatic pressure coming from a tank in sloped position is to be verified. However, as the tank is 100% filled in the analysis of this study, sloshing is not accounted for. Nonetheless may probably represent a negligible issue since the density of  $\text{LH}_2$  is low compared to that of LNG, where sloshing is a mandatory aspect to be analysed.

### Wave induced acceleration

Besides the gravitational acceleration, the wave induced movement of the ship causes additional



accelerations in vertical, transverse and longitudinal directions. Based on these values, a general acceleration can be defined which can be applied on the entire simulated geometry so that the wave motion can be accounted for.

Sang-Hoon Shin tabulates the design accelerations used in the actual structural analysis [64]. They are represented as static loads since they are based on particular ship design specifications. The accelerations are defined in Table 6.3

**Table 6.3:** Design accelerations in ULS conditions [64]

Acceleration	Tank no. 2-4	Tank no. 1
Vertical, $a_y$	0.465g	0.732g
Transverse, $a_z$	0.608g	0.628g
Longitudinal, $a_x$	0.198g	0.201g

As it can be observed the tank is accelerated according to its position on the ship, where the first tank is accelerated the most while Tanks 2 to 4 are equally accelerated. In the case of this study, the values for Tanks 2 to 4 are used.

### Fixed support and thermal loads

The boundary conditions applied to the the system is the fixed support at the bottom of the external support as depicted in Figure 6.9 which fixes all the nodes in all six degrees of freedom.

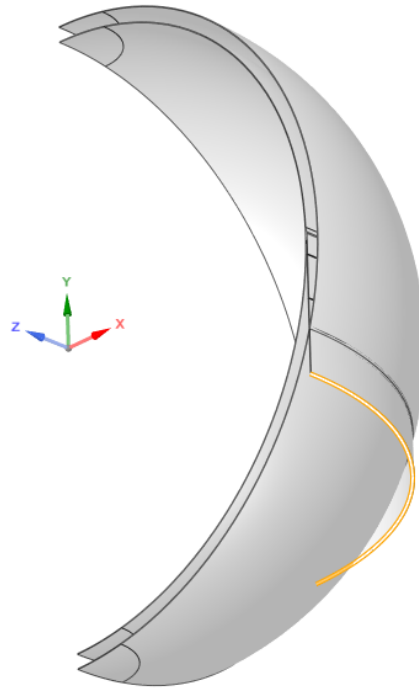


**Figure 6.9:** Highlighted area where the fixed support is applied

The thermal loads are the two temperature limits: the ambient temperature of  $313K$  and the liquid hydrogen temperature of  $20.3K$ . These are applied on the surfaces which comes in direct contact with the outside air and the cargo, respectively. Precisely, to all the exterior surfaces of the outer tank and the surfaces of the external support are attributed the temperature of  $313K$ , and to all the inner surfaces of the internal tank and the inner surface of the top segment of the skirt is attributed the other temperature.

### Symmetry

Considering the fact that an entire storage system cannot be simulated due to the low amount

of computer resources, pieces with specific symmetries and applied loads are simulated. The possibilities are as followed:

- 2D-axisymmetry: This type of symmetry is applied on the 2D cross section of the design, subjected to the loads which have a symmetric behaviour. From the loads tabulated in Table 6.2 these are the loads from L1 to L4, and the thermal loads L9. L7 may also be applied considering that an acceleration in the Y direction is symmetric around the Y-axis.
- Cyclic symmetry: This type of symmetry may be applied to represent the the symmetry around the Y-axis. It has a similar behaviour with the 2D-axisymmetry, but it is applied on a 3D-segment of the design, which can be an arbitrary fraction of the design; for example  $\frac{1}{3}$  or  $\frac{1}{8}$ .
- Region symmetry normal to X and Z axis: It is applied on a quarter of the containment system. The behaviour and range of application is similar to the 2D-axisymmetry. It may be used when loads which are symmetric around the Y-axis are present. In this case the loads present on a motionless storage system, the thermal loads and the wave induced acceleration in vertical direction. The symmetry is done by defining as scope the edges on which the specific directions, X and Z, are normal to.
- Region symmetry normal to Z axis: This type can be used on a half of the system. The symmetry can be used if the system is in a sloped position, inclined in the direction of the X axis. In this case, some wave induced loads may be applied. From Table 6.2 these may be L6 and L7 as well as L5. Considering that L8 has a higher magnitude than L6, these two may be switched assuming that the longitudinal direction is along the Z-axis.

## 6.2 Verification analysis

To confirm the accuracy of the analysis methodology and to easily keep track of, and validate the main results, three simplified check-up simulations on both 2D cross-sectional geometry and 3D quarter-sphere geometry are conducted. These simulations can be described as built-up simulations for the main analysis. In each simulation static loads are added, one by one. The geometries can be seen in Figure 6.10. The simulated results are compared with the theoretical results obtained from using the formulas described in Subsection 2.2.1.

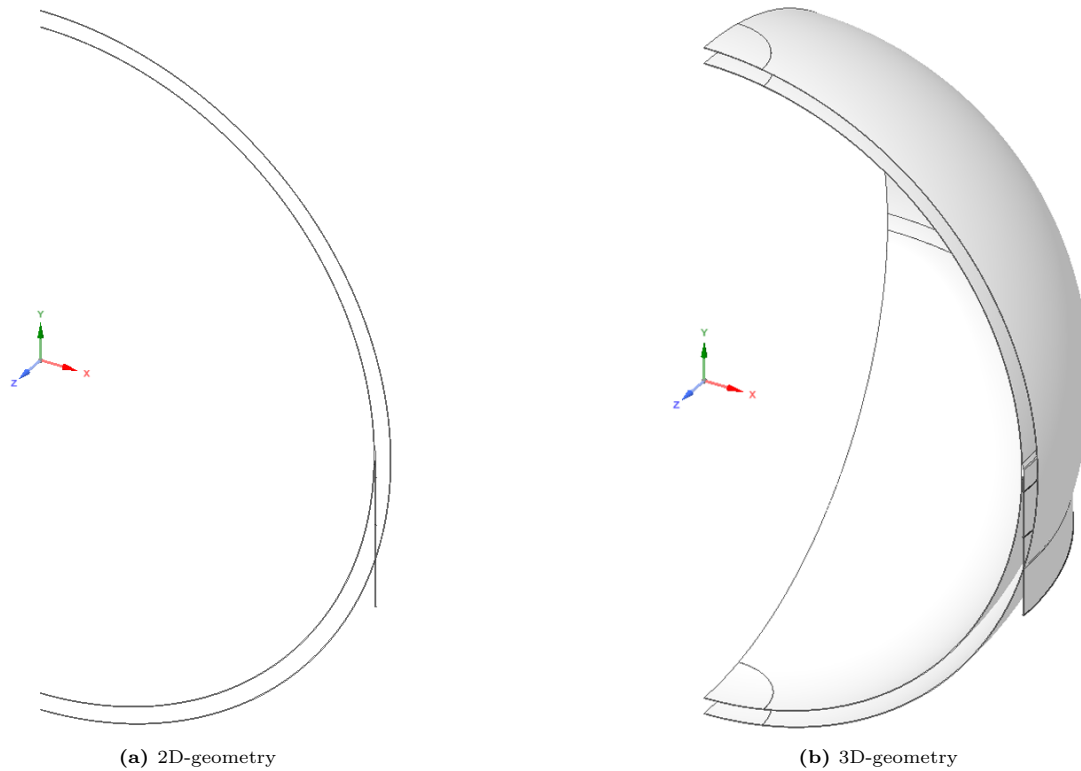


**Figure 6.10:** Geometries used for the verification analysis

It is possible to only conduct the analysis on the 3D-model, but due to its simplicity, the 2D-model is also included in the entire verification analysis as an extra procedure to strengthen as much as possible the validity of the overall used simulation method.

The default material set by ANSYS, which is structural steel, is used for the entire geometry under the verification analysis. Since the purpose of these simulations is to compare the results of different setups under similar conditions, the need of changing the material for different segments of the design is unnecessary. Another reason why the material is not changed in these simulations is to verify and confirm that the change in material is correctly applied when the main preliminary analysis is conducted. This is done by comparing the results of one of the verification simulations with the results of the main analysis under similar setup and load conditions, but with different materials.

For an easier reference in the rest of this report, the ID-name of the three simulations are C1, C2, and C3. Each analysis is detailed in the subsections to follow.

### 6.2.1 Simulation C1

In this simulation the applied loads are the atmospheric pressures, L1 and L2. Theoretically, the uniformly distributed atmospheric pressure should result in a single von-Mises stress value independent of the position on the sphere and the material used. By applying numerical values in Equations 2.3 and 2.6, it results in a meridional and circumferential stress of:

$$\sigma_{\phi} = \sigma_{\theta} = \frac{1.01325 \cdot 10^5 Pa \cdot 21.2m}{2 \cdot 0.048m} = 2.2376 \cdot 10^7 Pa \quad (6.2)$$

for the internal tank and a meridional and circumferential stress :

$$\sigma_{\phi} = \sigma_{\theta} = \frac{1.01325 \cdot 10^5 Pa \cdot 22.296m}{2 \cdot 0.048m} = 2.3533 \cdot 10^7 Pa \quad (6.3)$$

for the external spherical container.

By including these two stresses into Equation 2.17 we get a Von-Mises stress value of  $2.2376 \cdot 10^7$  Pa, and  $2.3533 \cdot 10^7$  Pa respectively. Comparing the two results with the values of arbitrarily taken probes tabulated in Table 6.4, we can see that the results are relatively similar.

**Table 6.4:** von-Mises stresses caused by the internal and external overpressure [Pa]

Probe	2D-geometry		3D-geometry	
	von-Mises stress on internal tank	von-Mises stress on external tank	von-Mises stress on internal tank	von-Mises stress on external tank
1	$2.2462 \cdot 10^7$	$2.3456 \cdot 10^7$	$2.2394 \cdot 10^7$	$2.3416 \cdot 10^7$
2	$2.2455 \cdot 10^7$	$2.3483 \cdot 10^7$	$2.2370 \cdot 10^7$	$2.3452 \cdot 10^7$
3	$2.2404 \cdot 10^7$	$2.3582 \cdot 10^7$	$2.2332 \cdot 10^7$	$2.3525 \cdot 10^7$
4	$2.2354 \cdot 10^7$	$2.3444 \cdot 10^7$	$2.2382 \cdot 10^7$	$2.3542 \cdot 10^7$
5	$2.2422 \cdot 10^7$	$2.3548 \cdot 10^7$	$2.2368 \cdot 10^7$	$2.3483 \cdot 10^7$
6	$2.2390 \cdot 10^7$	$2.3450 \cdot 10^7$	$2.2445 \cdot 10^7$	$2.3500 \cdot 10^7$
7	$2.2450 \cdot 10^7$	$2.3432 \cdot 10^7$	$2.2363 \cdot 10^7$	$2.3573 \cdot 10^7$
8	$2.2410 \cdot 10^7$	$2.3506 \cdot 10^7$	$2.2322 \cdot 10^7$	$2.3540 \cdot 10^7$
9	$2.2464 \cdot 10^7$	$2.35440 \cdot 10^7$	$2.2419 \cdot 10^7$	$2.3563 \cdot 10^7$
10	$2.2476 \cdot 10^7$	$2.3545 \cdot 10^7$	$2.2381 \cdot 10^7$	$2.3526 \cdot 10^7$

In the Section F.2 of Appendix F the tabulated results of the simulation are shown as probe-values taken directly from the geometry. The amount of digits represented exceed the accepted number of significant figures, to highlight the variation of each probe and the difference between measured values and the theoretical ones. Rounding the numbers to three significant digits, the results will present similar values with very few exceptions, which in this case the outcome is satisfactory and leads to a positive conclusion.

Using the formula for absolute average deviation, where the reference values are the theoretical values:

$$AAD\% = \frac{1}{N} \sum_{i=1}^N |val_{sim} - val_{ref}| \cdot 100\% \quad (6.4)$$

Results in the absolute average deviation values as tabulated in Table 6.5.

**Table 6.5:** AAD [%] for the C1 Simulation

2D-geometry		3D-geometry	
von-Mises stress on internal tank	von-Mises stress on external tank	von-Mises stress on internal tank	von-Mises stress on external tank
2.261	0.52	0.266	0.382

Besides the values of von-Mises stress on the internal tank for the 2D-geometry, the deviation is concluded to be reasonable.

## 6.2.2 Simulation C2

Simulation C2 is conducted by also having the gravitational acceleration, L4 in addition to L1 and L2. In the presence of gravity, the von-Mises stresses on a spherical object are both material and position depended. The dependency on the material is caused by its density which defines the weight of the object. The defined density of the structural steel in Ansys is of  $7850 \text{ kg/m}^3$ . Focusing solely on the inner tank, Equations 2.7 and 2.8 are used to calculate the internal forces caused by the container's self-weight for the upper hemisphere, and Equations 2.9 and 2.10 are used to calculate the same forces for the lower hemisphere. To the obtained results, the value of the force caused by internal pressure obtained in Simulation C1, Equation 6.2 is added. The obtained stresses caused by the meridional and circumferential forces are used in Equation 2.17 to calculate the equivalent stress. The theoretical values are compared with the outcome of the analysis of the 2D- and 3D-geometries.

In Table 6.6 all the results are tabulated, and the simulated values are depicted in Appendix F, Section F.3 as well. The only variable for the different results is the zenith angle on the sphere at which the stress is measured. All the other values remain unchanged.

**Table 6.6:** von-Mises stresses on the internal tank caused by the internal pressure and self-weight forces [Pa]

Angle $\phi$	Theoretical von-Mises stress	Simulated von-Mises Stress from the 2D geometry	Simulated von-Mises stress from the 3D-geometry
0	$2.156 \cdot 10^7$	$2.160 \cdot 10^7$	$2.167 \cdot 10^7$
10	$2.157 \cdot 10^7$	$2.166 \cdot 10^7$	$2.163 \cdot 10^7$
20	$2.161 \cdot 10^7$	$2.161 \cdot 10^7$	$2.162 \cdot 10^7$
30	$2.167 \cdot 10^7$	$2.167 \cdot 10^7$	$2.174 \cdot 10^7$
40	$2.175 \cdot 10^7$	$2.179 \cdot 10^7$	$2.184 \cdot 10^7$
50	$2.186 \cdot 10^7$	$2.195 \cdot 10^7$	$2.194 \cdot 10^7$
60	$2.200 \cdot 10^7$	$2.217 \cdot 10^7$	$2.211 \cdot 10^7$
70	$2.216 \cdot 10^7$	$2.223 \cdot 10^7$	$2.226 \cdot 10^7$
80	$2.234 \cdot 10^7$	$2.281 \cdot 10^7$	$2.241 \cdot 10^7$
90	-	-	-
100	$2.267 \cdot 10^7$	$2.262 \cdot 10^7$	$2.269 \cdot 10^7$
110	$2.280 \cdot 10^7$	$2.276 \cdot 10^7$	$2.283 \cdot 10^7$
120	$2.293 \cdot 10^7$	$2.284 \cdot 10^7$	$2.294 \cdot 10^7$
130	$2.305 \cdot 10^7$	$2.294 \cdot 10^7$	$2.303 \cdot 10^7$
140	$2.316 \cdot 10^7$	$2.302 \cdot 10^7$	$2.313 \cdot 10^7$
150	$2.325 \cdot 10^7$	$2.312 \cdot 10^7$	$2.318 \cdot 10^7$
160	$2.331 \cdot 10^7$	$2.315 \cdot 10^7$	$2.334 \cdot 10^7$
170	$2.335 \cdot 10^7$	$2.320 \cdot 10^7$	$2.334 \cdot 10^7$
180	$2.337 \cdot 10^7$	$2.322 \cdot 10^7$	$2.337 \cdot 10^7$

The results follow the same pattern with relatively similar values at the specific angles. Using Equation 6.4 to calculate the absolute average derivation, it results in a derivation of 1.1 % for the calculation of the stresses in the 2D-geometry and in 0.51 % for the 3D-geometry respectively. This concludes that simulating on a 3D-model may be more accurate.

### 6.2.3 Simulation C3

In Simulation C3, the hydrostatic pressure of the liquid (L3) is also added, leading to a simulation where all the major mechanical loads acting on a motionless system are present. From a theoretical point of view, the results from Equation 2.11, Equation 2.12, Equation 2.13 and Equation 2.14 are used to determine the stresses caused by internal pressure loading. These values are added to the stresses caused by the self-weight loading, results which are then used to calculate the von-Mises stresses at different angles on the internal spherical tank. These values are compared with the extracted values from the simulations, at approximately the exact same angles.

Table 6.7 shows the theoretical values and the simulated values from both geometries.

**Table 6.7:** von-Mises stresses on the internal tank caused by the hydrostatic pressure, self-weight forces and internal overpressure [Pa]

Angle $\phi$	Theoretical von-Mises stress	Simulated von-Mises Stress from the 2D geometry	Simulated von-Mises stress from the 3D-geometry
0	$2.156 \cdot 10^7$	$2.157 \cdot 10^7$	$2.144 \cdot 10^7$
10	$2.162 \cdot 10^7$	$2.167 \cdot 10^7$	$2.160 \cdot 10^7$
20	$2.180 \cdot 10^7$	$2.188 \cdot 10^7$	$2.183 \cdot 10^7$
30	$2.211 \cdot 10^7$	$2.213 \cdot 10^7$	$2.215 \cdot 10^7$
40	$2.254 \cdot 10^7$	$2.252 \cdot 10^7$	$2.266 \cdot 10^7$
50	$2.309 \cdot 10^7$	$2.301 \cdot 10^7$	$2.324 \cdot 10^7$
60	$2.375 \cdot 10^7$	$2.385 \cdot 10^7$	$2.390 \cdot 10^7$
70	$2.453 \cdot 10^7$	$2.461 \cdot 10^7$	$2.472 \cdot 10^7$
80	$2.543 \cdot 10^7$	$2.574 \cdot 10^7$	$2.545 \cdot 10^7$
90	-	-	-
100	$2.639 \cdot 10^7$	$2.689 \cdot 10^7$	$2.664 \cdot 10^7$
110	$2.722 \cdot 10^7$	$2.745 \cdot 10^7$	$2.735 \cdot 10^7$
120	$2.807 \cdot 10^7$	$2.784 \cdot 10^7$	$2.783 \cdot 10^7$
130	$2.890 \cdot 10^7$	$2.834 \cdot 10^7$	$2.834 \cdot 10^7$
140	$2.964 \cdot 10^7$	$2.876 \cdot 10^7$	$2.877 \cdot 10^7$
150	$3.027 \cdot 10^7$	$2.914 \cdot 10^7$	$2.915 \cdot 10^7$
160	$3.075 \cdot 10^7$	$2.946 \cdot 10^7$	$2.937 \cdot 10^7$
170	$3.104 \cdot 10^7$	$2.959 \cdot 10^7$	$3.030 \cdot 10^7$
180	$3.114 \cdot 10^7$	$2.975 \cdot 10^7$	$2.968 \cdot 10^7$

The stresses tabulated take place on the surface of the inner spherical tank, but other areas on the system have been checked as well against calculated values, following the same pattern of similarity as the ones represented in Table 6.7.

The ADD values obtained from Equation 6.4 for the C3 simulations are 4.5 % for the 2D model and 4.04 % for the 3D-design.

#### 6.2.4 Verification of skirt analysis

Due to the relatively complex shape of the top segment of the support system, a theoretical equation which can be used to calculate the stresses inside the skirt has proven challenging to obtain. However, another method to verify and validate the results is considered. The results from four different types of simulation setup under similar loads and boundary condition as in Simulation C2, are compared. This is based on two facts/considerations: The first one is that the results may vary with the quality and design of the mesh, and the second one is based on the need of symmetry since the entire system cannot be simulated due to the low computer resources. The four setup methods are as follow:

- Setup 1: 2D-design of the cross-section of the system, with 2D-axisymmetry applied, having a mesh of 253 940 nodes and 74 833 elements.
- Setup 2: 3D-design of a quarter of the system, with cyclic symmetry applied, having a mesh of 277 558 nodes and 219 978 elements.
- Setup 3: 3D-design of a quarter of the system, with two symmetry regions normal on the X- and Z-axis, having a mesh of 2 356 434 nodes and 513 170 elements.
- Setup 4: 3D-design of a quarter of the system, with two symmetry regions normal on the X- and Z-axis, having a mesh of 670 046 nodes and 141 580 elements.

In Table 6.8, some probes taken from the approximately same regions on the top segment of the skirt are tabulated. The mesh representation and the results are depicted in the four Figures which can be found in Appendix F, Section F.1.

**Table 6.8:** von-Mises stresses of the skirt for different symmetry and mesh designs

Probe no.	Setup 1	Setup 2	Setup 3	Setup 4
1	$2.2462 \cdot 10^7$	$2.3456 \cdot 10^7$	$1.815 \cdot 10^7$	$1.821 \cdot 10^7$
2	$2.2455 \cdot 10^7$	$2.3483 \cdot 10^7$	$2.272 \cdot 10^7$	$2.262 \cdot 10^7$
3	$2.2404 \cdot 10^7$	$2.3582 \cdot 10^7$	$1.121 \cdot 10^7$	$1.244 \cdot 10^7$
4	-	$2.3444 \cdot 10^7$	$2.043 \cdot 10^7$	$2.684 \cdot 10^7$
5	$2.2422 \cdot 10^7$	$2.3548 \cdot 10^7$	$1.0364 \cdot 10^7$	$1.070 \cdot 10^7$
6	$2.2422 \cdot 10^7$	$2.3548 \cdot 10^7$	$1.710 \cdot 10^7$	$1.623 \cdot 10^7$

The pattern as well as the tabulated values have a relatively high degree of similarity. This observation, together with the validation obtained from Simulation C2 where Setup 4 is used, concludes that all the setups may be equally reliable. However, Setup 4 is decided to be furtherly used in the main analyses of this study due to the following reasons:

1. A 3-Dimensional representation gives a finer and more understandable picture of how the system reacts under different loads and boundary conditions. Therefore a 3D-design is more favourable than a 2D-geometry. The 2D-axisymmetry is also available just for loads which have an axisymmetric behaviour as described in Subsection 6.1.3, making it unfitting for a simulation of a containment system in motion.
2. Applying the hydrostatic load is not possible when using cyclic symmetry. Therefore Setup 2 does not satisfy all the requirements to obtain the wanted results.
3. A high quality mesh as the one applied in Setup 3 is not able to be conducted on the personal PC. The one conducted simulation used for this comparison and validation has been done from another PC with limited time access for this simulation only.

## 6.3 Main analysis of the preliminary design

With the validation obtained from the results evaluated in Section 6.2, the main analysis of the preliminary design can be conducted according to the setup described in Section 6.1.

To know what type of data must be extracted from the simulations, the concept of failure must be understood. Therefore static failure is firstly described based on which results are extracted and evaluated.

### 6.3.1 Static failure

There are two existing types of material failures that can occur from static loading. These are ductile failure and brittle failure. According to Xiaolin Chen and Yijun Liu in "Finite Element Modeling and Simulation with ANSYS Workbench", the difference between the two lies in the quantity of plastic deformation a material can experience before fracture. [21, p. 419] Ductile materials can sustain a high degree of plastic deformation, compared to brittle materials which can be fractured without experiencing any apparent plastic deformation.

There are three theories which can be used to analyse static failure; two for ductile failure, and one for brittle failure. They are described in reference to the aforementioned source, [21, p. 419-420].

The first two are the maximum shear stress theory, known as Tresca Criterion and the distortion energy theory, known as von Mises Criterion. Based on the Tresca Criterion, failure can occur if the maximum shear stress exceeds one half of the material yield strength. According to the von Mises Criterion, one can experience failure when the maximum von Mises stress or the equivalent stress is higher than the material yield strength.

The last theory is called the maximum normal stress theory and states that brittle failure exists when the maximum principal stress is greater than the ultimate tensile/compressive strength of the

material.

As mentioned, the two materials used to construct the structure of the system, excluding the insulation layer are AISI 316 and Low Carbon Steel, both defined by Granta Desing in Ansys. The limits which cannot be exceeded for the two materials are tabulated in Table 6.9.

**Table 6.9:** Stress-limits before failure

Material	Tensile Yield Strength [Pa]	$\frac{1}{2}$ Tensile Yield Strength [Pa]	Tensile Ultimate Strength [Pa]
AISI 316	$2.521 \cdot 10^8$	$1.261 \cdot 10^8$	$5.651 \cdot 10^8$
Low CS	$2.330 \cdot 10^8$	$1.165 \cdot 10^8$	$3.650 \cdot 10^8$

### 6.3.2 Results

For the main analysis the preliminary design is gradually simulated under three different conditions, ergo for three different cases entitled PS1, PS2, PS3.

1. In the PS1 all the mechanical loads of a motionless structure are applied.
2. The PS2 simulation includes all the wave induced loads for a representation of the system on moving ship.
3. In the PS3 the ambient and cargo temperatures are set accordingly in addition to the wave-induced loads to evaluate the effect of the thermal loads on the system as well.

To evaluate the strength and failure degree of the system, from all the cases the following data is collected:

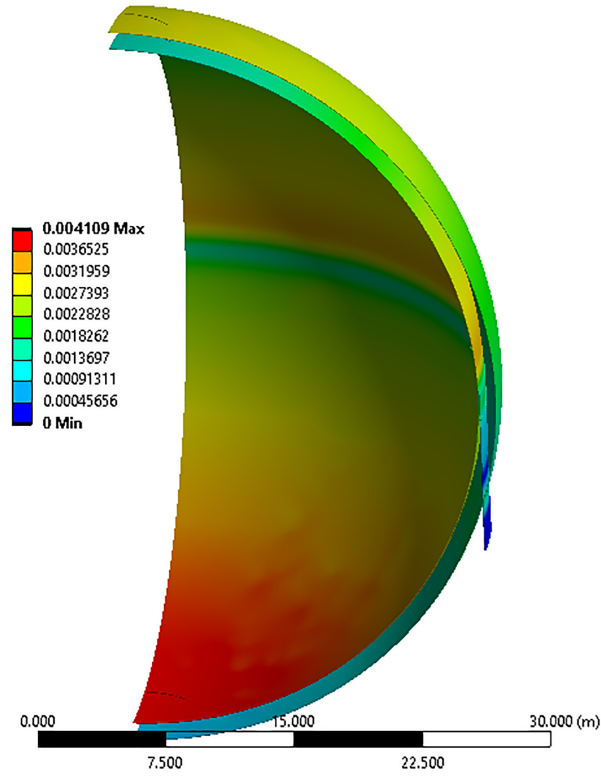
- Total deformation
- von-Mises (Equivalent) Stress
- Maximum Shear Stress
- Maximum Principal Stress

#### Deformation caused by loads present on a motionless system

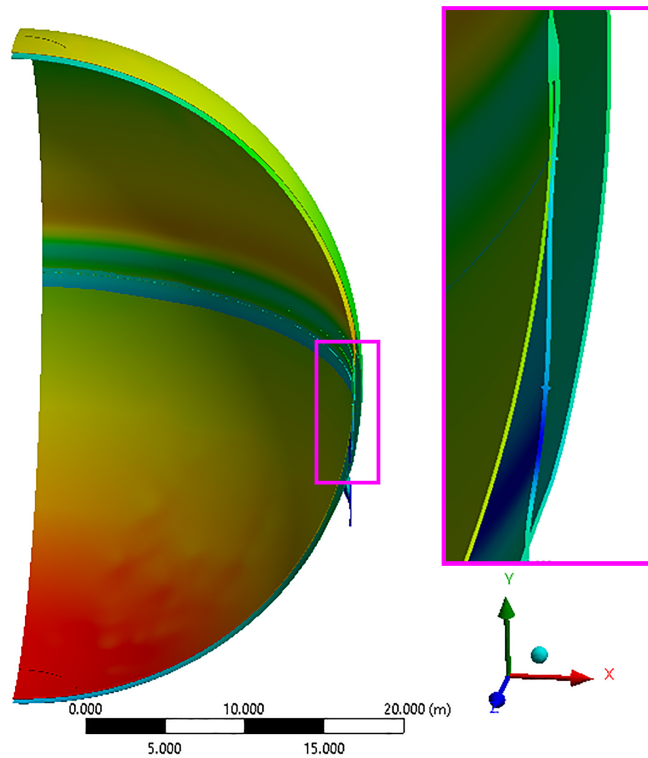
With a fixed support on the bottom surface of the external support, the containment system is subjected to gravitation, hydrostatic pressure of the cargo and external and internal pressure. Based on Table 6.2 in Subsection 6.1.3, the loads present are the loads ID-ed from L1 to L4 with the corresponding magnitudes.

The deformation obtained can be observed in Figure 6.11a in true scale and in Figure 6.11b in a exaggerated representation with 560 times greater magnitude.





(a) Deformation under loads existent for a motionless system [m] (True Scale)



(b) Deformation under loads existent for a motionless system [m] (x100)

**Figure 6.11:** Deformation of P1 under loads existent for a motionless system

The pattern of the total deformation of the system has an expected behaviour. From the ex-

aggregated representation of Figure 6.11b it can be observed how the the external tank tends to compress due to the ambient pressure, and how its south pole has a smaller deformation compared to its north pole due to directions of the gravitational and pressure forces. On top, both forces are acting in the same direction, while at the bottom they are acting in opposite directions. The deformation of the internal tank, on the other hand, has a contrasting behaviour. The bottom is more deformed than the top, and it tends to expand because of the inner overpressure. Because of the great amount of cargo fluid, the system presents its maximum of 4.11 mm at the bottom of the inner tank. This is to be expected as the material used, stainless steel 316 and low carbon steel, have great structural strength.

The obtained equivalent, maximum principal and maximum shear stress-distributions are depicted in Appendix G, Section G.1. The highest values of the different stresses are tabulated in Table 6.10.

**Table 6.10:** Maximum stresses obtained from PSI

Stress Type	Value [Pa]	Max. value - Max. limit ratio
von-Mises Stress [Pa]	$4.203 \cdot 10^7$	5.998
Maximum Shear Stress [Pa]	$2.269 \cdot 10^7$	5.558
Maximum Principal Stress [Pa]	$4.333 \cdot 10^7$	24.91

The maximum limits of all stresses exist on the elements made of AISI 316. Therefore the ratios tabulated are the ratios between the limits of the stainless steel and the obtained maximum values. Looking at the pattern on the Figures in Appendix G, Section G.1, there is a high chance that the maximum values are caused by singularity points due to poor mesh in that specific area, which results in values that may not be reliable. However, as long as the maximum values do not exceed or are close to the limits, it can be concluded that the system does not fail under the loads present on the preliminary designed LH<sub>2</sub> storage system. This conclusion may be applied even if other important components which are part of a real cryogenic storage system are present.

#### Deformation caused by wave-induced loads

To represent the static loads acting on a system in motion on sea as much as possible, at least a half of a system is needed which result in maximum one symmetric region. The reason is that wave induced loads do not have a symmetric behaviour. For a system in a sloped position, the hydrostatic pressure of a 100 % filled tank may be represented as in Figure 6.12.

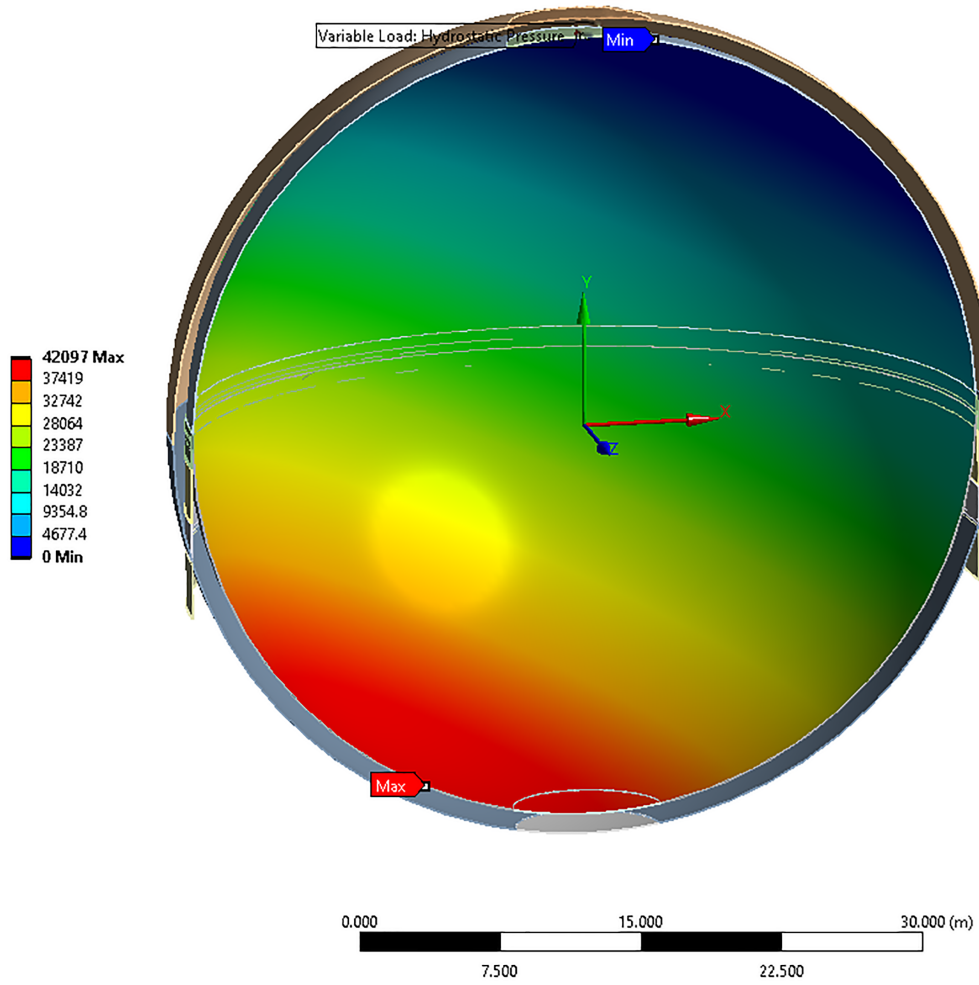
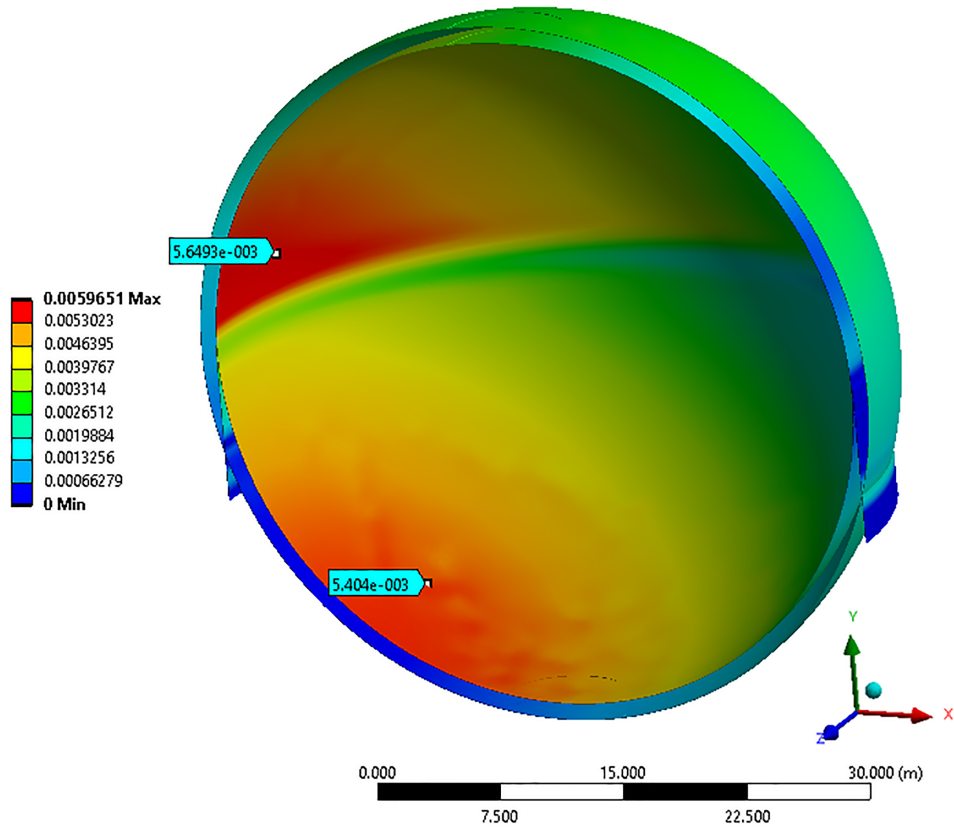
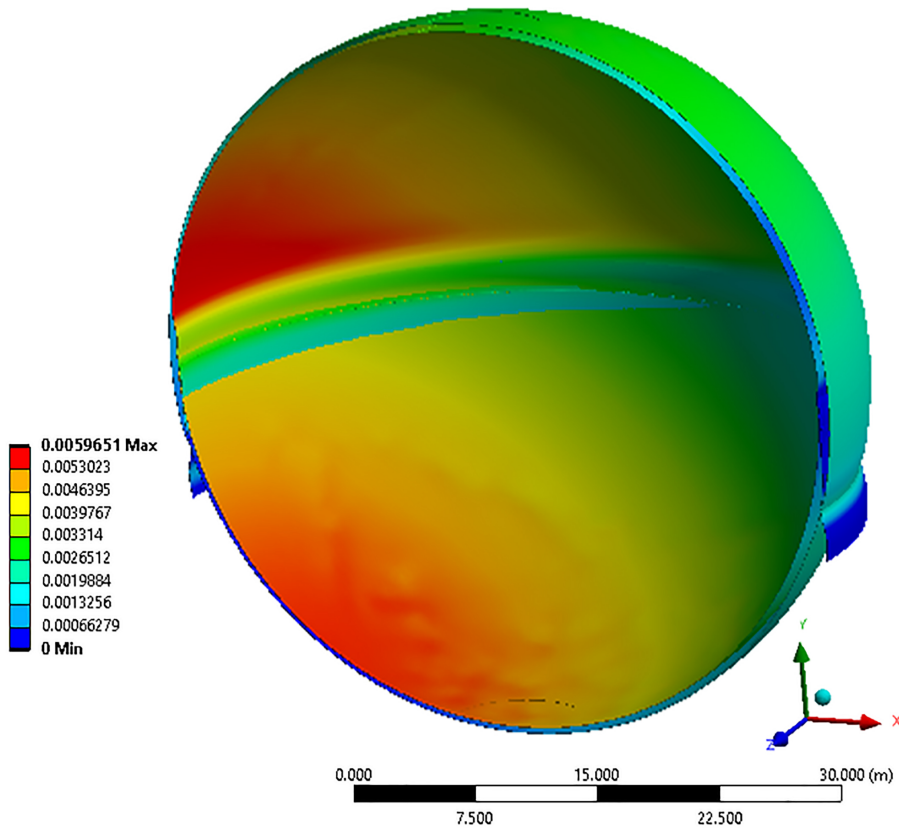


**Figure 6.12:** Hydrostatic pressure distribution influenced by wave-induced accelerations [Pa]

The increase in value is caused by the existence of the additional presence of the waved induced accelerations, L7 and L8, which are tabulated in Table 6.2. These loads are added to the already existed ones for a motionless system, from L1 to L4. The resulted deformation is as depicted in Figure 6.13



(a) Deformation under loads existent for a system in motion on sea [m] (True Scale)



(b) Deformation under loads existent for a system in motion on sea [m] (x120)

**Figure 6.13:** Deformation of P1 under loads existent for a system in motion on sea

Since the tank is 100 % filled in the simulated case, the forces caused by sloshing are not present. The deformation follows the pattern created by the slope, considering that the system is accelerated in the Y- and X-direction with a total value of  $13.4 \text{ m/s}^2$  and  $5.96 \text{ m/s}^2$  respectively. While the value of 5.40 mm at the bottom of the inner tank is relatively correct, the value 5.65 mm above the skirt may show a slightly overestimated value caused by the way of distributing the the weight of the insulation layer as shown in Figure 6.7 from Subsection 6.1.3. On the other hand, a higher degree of deformation is expected in that specific area which is caused by the sloped hydrostatic pressure with values between 1.9 kPa and 2.5 kPa.

Similar to the case of the motionless system, PS1, the maximum obtained values of the different stresses do not exceed the limits of failure. Table 6.11 and the Figures from Section G.2, Appendix G highlights this aspect.

**Table 6.11:** Maximum stresses obtained from PS2

Stress Type	Value [Pa]	Max. value - Max. limit ratio
von-Mises Stress [Pa]	$1.365 \cdot 10^8$	1.847
Maximum Shear Stress [Pa]	$7.824 \cdot 10^7$	1.616
Maximum Principal Stress [Pa]	$8.386 \cdot 10^7$	6.739

Figure G.4 from Section G.2 in the Appendix, zooms in on the area where the von-Mises stress is at his maximum. The other stresses have their maximum in the exact same area. Considering the pattern, it is highly possible that the value is caused by singularities due to poor mesh, especially in this particular case where the mesh of the top segment of the skirt has been changed as the MultiZone method could not be applied. However, assuming that this is a correct value, and that the area of contact between the top and the middle segment of the skirt is highly stressed by the deformation, the system may still be strong enough to resist against the wave-induced loads. Considering that sloshing is not included, that the accelerations may be greater due to a greater magnitude of the loads, and also taking fatigue into account, the small ratio between the maximum values obtained and the failure limit must not be neglected and therefore must be taken into consideration when building a new design.

#### Deformation caused by thermal loads

Stainless steel is a material whose mechanical properties vary with the change temperature. When filling the tank with liquid hydrogen, the cryogenic temperature may have a great impact on the tank's structure and must therefore be evaluated. For results based on a correctly distributed temperature profile, the static structural analysis is connected to a static thermal simulation which results in a temperature profile based on accurately applied ambient and cargo temperatures; namely on the surfaces of the system which are in direct contact with the ambient and cargo respectively. Figure 6.14 shows the temperature profile and how the skirt acts as a thermal bridge, which is correct considering that the insulation layer is not present.

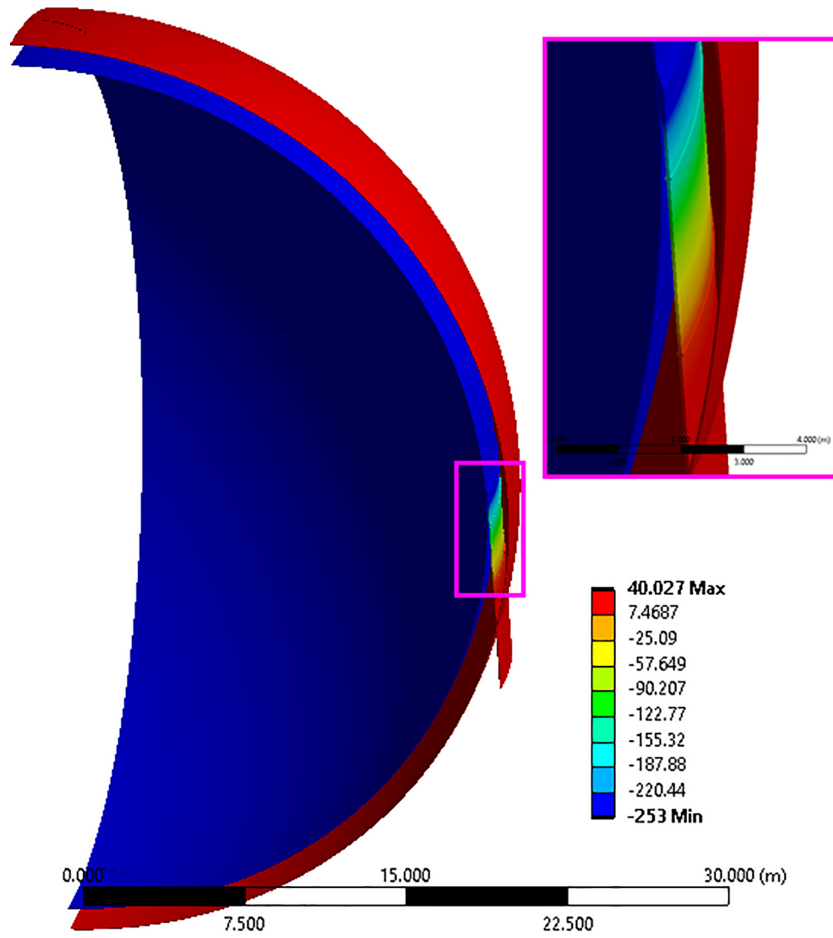


Figure 6.14: Temperature profile based on the existent thermal loads

The resulted deformation at equilibrium based solely on the presence of thermal loads, after filling the tank with liquid hydrogen, is depicted in 6.15.

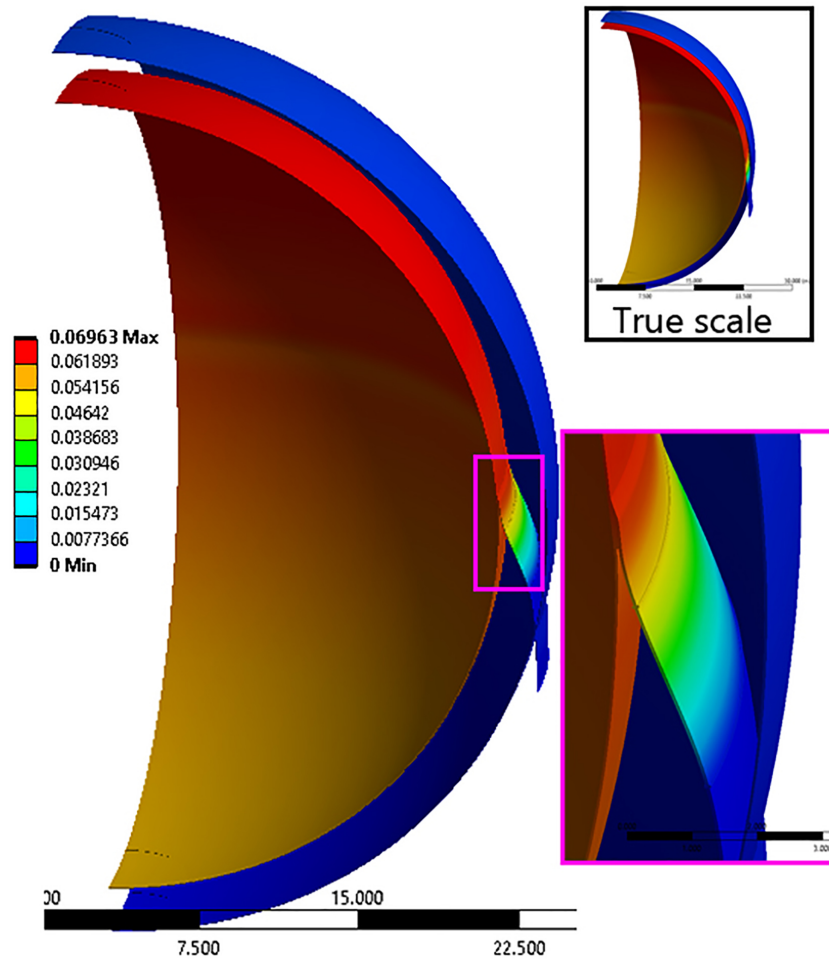


Figure 6.15: Deformation in the solely presence of thermal loads [m] (x20)

The maximum value of 0.0696 m is similar to the theoretical value of 0.0701 m coming from the linear expansion equation:

$$\Delta L = \alpha L_0 \Delta T \quad (6.5)$$

where, in this case

$\Delta L$  [m] is the deformed distance

$\alpha \approx 1.13 \cdot 10^{-5} \frac{1}{K}$  is the thermal coefficient of expansion for AISI 316, according to Granta Design at the temperature of 20.3 K

$L_0 = R_i = 21.2m$  is the inner radius of the tank

$\Delta T = 313 - 20.3 = 292.7K$  is the temperature difference

With the result validated, a simulation where the mechanical forces from the PS1 analysis are also present is conducted. Simulating the thermal loads on the half-system from PS2 has resulted in very long computational time, and several errors caused by the insufficient physical memory of the PC. Therefore the present loads applied are from L1 to L4 which are the loads for a motionless system, and L9 being the two existing temperatures of 313 K and 20.3 K. The resulted deformation of the system can be observed in Figure 6.16

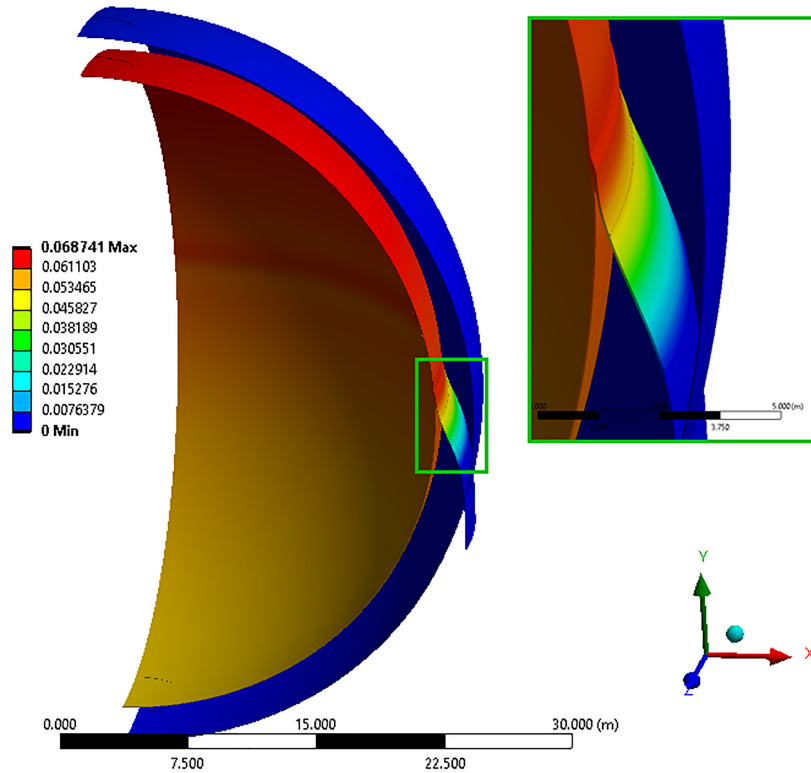


**Figure 6.16:** Deformation under thermal loads and loads existent for a motionless system (x20)

The maximum deformation is 0.195 mm lower than the one where only the thermal loads are present due to the inner overpressure which presses against the direction of the thermal contraction.

The aforementioned amount of deformation caused by the thermal compression results in highest stress values, at equilibrium as seen in Figure 6.17.

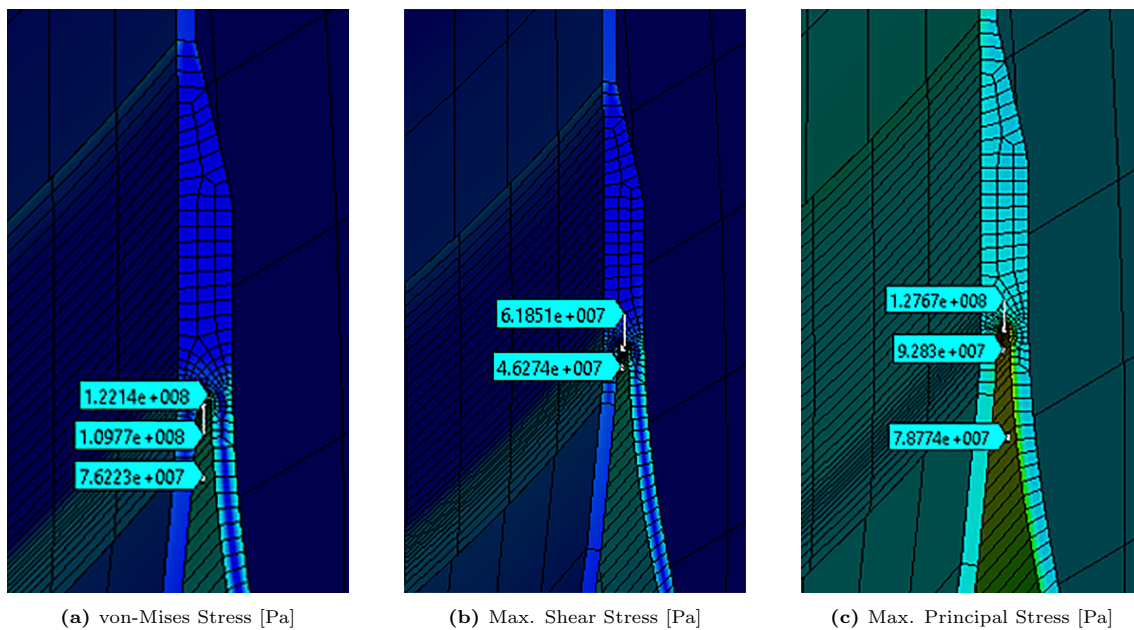


**Figure 6.17:** Highest stresses caused by thermal loads and loads present on a motionless system

Also in this particular case the stresses do not exceed the limits, and with respect to the tensile strengths of AISI 316, results that the system can sustain approximately twice as much stress.



The maximum values from the colormap depicted in the figures of Appendix G, Section G.3 are values of little importance as they are present in the area where the external supportive element has the boundary condition of a fixed support. However, it is reminded that this element can be freely constructed as it has a negligible effect on the heat leakage. Looking closely at the pattern similar (for all the cases) to the one given in Figure 6.18, the maximum values are also concluded to be caused by possible singularities.

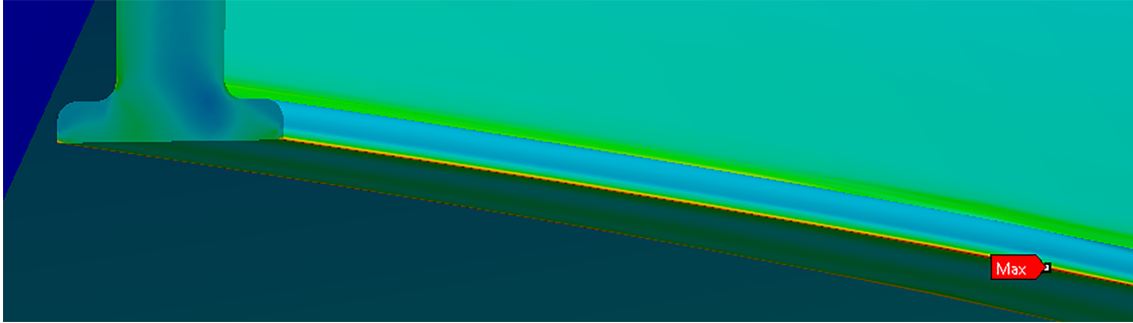


**Figure 6.18:** Representation of the maximum von-Mises Stresses existent under themal and mechanical loads of a motionless system

---

## Chapter 7

# Thermal analysis of preliminary design

As a preliminary design of a liquid hydrogen containment system is established, the thermal analysis is necessary to verify if the heat ingress is low enough to achieve a boil off gas rate of less than 0.2 % per day; which is the overall goal of this study. Based on the results of this analysis together with the results gathered from the structural simulation in Chapter 6, one can more easily evaluate the necessary improvements needed to obtain a satisfactory system.

### 7.1 Setup

A steady-state thermal analysis is conducted, where the temperature profile, the heat flux and the heat flow rate are verified for three different cases. The first one represents the ideal case, where the insulation layer has zero capability of conducting heat, ergo perfect vacuum without radiation. The second one represents the worst case, where the insulation material used has the highest apparent thermal conductivity between the materials discussed in Subsection 5.2.1; namely polyurethane foam. Finally, in the third case, an insulation material, which has a relatively low apparent thermal conductivity and may easily be applied in a real-life large scale system, is used. This is one of the evacuated bulk insulations.

The thermal boundary conditions which are the ambient temperature and liquid hydrogen temperature have an axisymmetric behaviour, resulting in the fact that a 2D-axisymmetric analysis is enough to obtain the wanted results. However, for a more accurate outcome and for validation purposes, a 3D-model of a quarter of a system is also conducted.

#### 7.1.1 Design setup

The geometry to simulate the steady-state thermal analysis of the preliminary design is as depicted in Subsection 6.1.1, but the void space between the two spherical shells is filled with solid geometries to which the specific material properties are given based on the insulation material desired.

The geometry is as depicted in Figure 7.1, with the thickness of the insulation material of 1.00 m which is equal to the void space from the Figure E.1 represented in Appendix E.

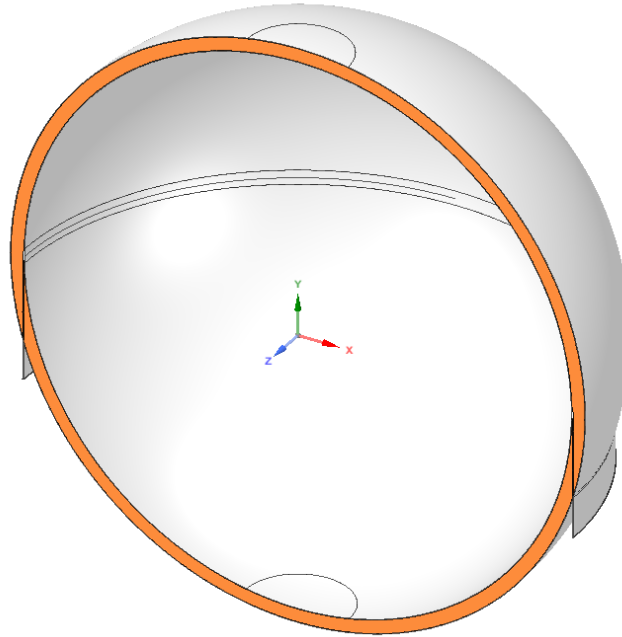


**Figure 7.1:** Preliminary design with the insulation layer highlighted in orange

### 7.1.2 Mesh setup

For the structural components of the cryogenic storage system, the same mesh setup described in Subsection 6.1.2 is also applicable in the 3D steady-state thermal analysis. The only difference is when the insulation layer is added. The total number of elements and nodes become 635 005 and 1 389 151, and the mesh design is as depicted in Figure 7.2.

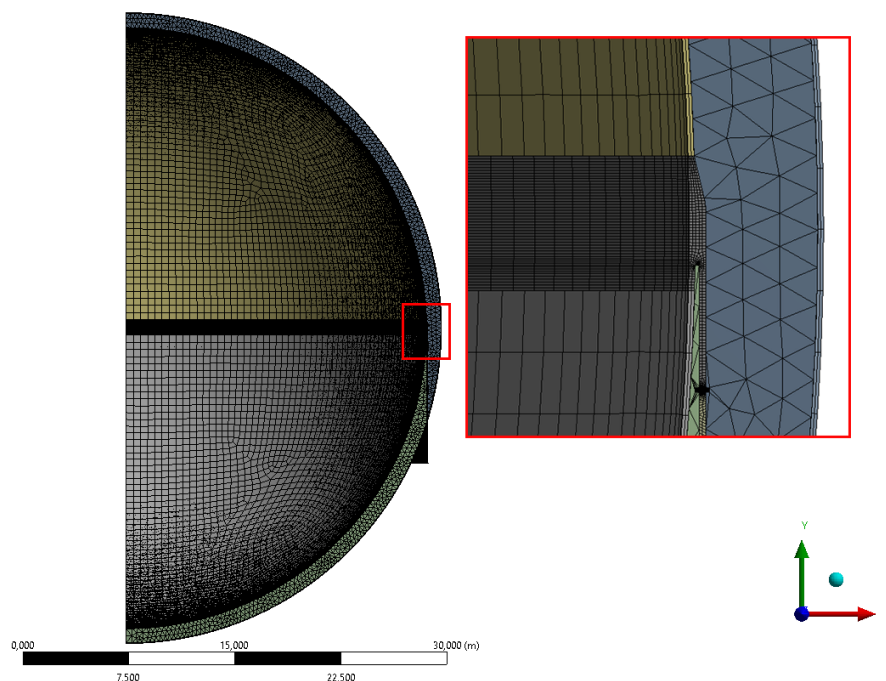


**Figure 7.2:** Mesh setup for 3D Steady-State Thermal analysis

In terms of element type, for the 3D steady-state thermal analysis, the SOLID186 and SOLSH190 used to conduct the Static Structural analysis are entirely replaced with SOLID70 and SOLID90. These are 3D thermal solid elements with 8-nodes and 20-nodes respectively, as depicted in Figures

7.3a and 7.3b. Both types have 3D thermal conduction capability and are applicable to steady-state and transient thermal analysis. Therefore using the apparent thermal conductivity value which includes all the heat transfer mechanisms is suited for these types of analysis. The elements have a single degree of freedom at each node which is the temperature. The elements can also compensate for mass transport heat flow from a constant velocity field [11]. The only difference between SOLID70 and SOLID90 is that SOLID90 have compatible temperature shapes and are well suited to model curved boundaries [8].

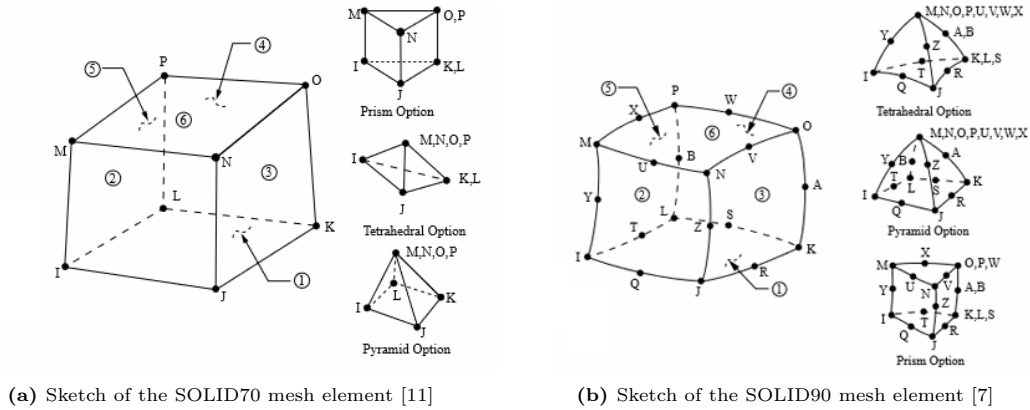


Figure 7.3: Mesh elements used in the Steady-State Thermal Analysis

### 7.1.3 Material properties, and boundary conditions setup

The materials used for the supportive structure of the containment system remain unchanged. The properties of Stainless Steel 316 collected by ANSYS GRANTA is attributed to the middle and superior part of the skirt as well as the internal tank segments. The rest of the structure has the low carbon steel as attributed material. The low carbon steel has a constant thermal conductivity of 52 W/(m·K) while the thermal conductivity of AISI 316 varies with temperature and is tabulated accordingly. For the ideal case, the insulation layer is suppressed, as it represents perfect vacuum without radiation, but for the other two cases polyurethane foam and 3M type B37/2000 evacuated micro-glass spheres are used. The properties of PUF are taken from ANSYS GRANTA as it is already defined there, regardless the fact that the thermal conductivity given is 26.5 mW/(m·K) instead of the maximum existing apparent thermal conductivity of 33.0 mW/(m·K), value obtained from the literature and presented in Table 5.8. The evacuated micro-glass spheres on the other hand do not exist in the material database and therefore the material is manually created, having an apparent thermal conductivity of 1.03 mW/(m·K), value obtained from the empirical Equation 5.10 with the constants tabulated in Table 5.10.

The boundary conditions set are the ambient temperatures of 313 K and cargo temperature of 20.3 K. The high temperature is set on the external surface of the outer tank, and the external support element, and the low temperature is set on the internal surfaces of the inner tank. Briefly said, to all the surfaces that come in direct contact with the cargo and the ambient air are attributed the respective temperatures.

### 7.1.4 Verification simulations

To validate the results, 2D-axisymmetric and 3D analysis of  $\frac{1}{4}$  of the design are conducted on different components individually. The first simulation verifies the heat transfer rate that only takes place through the walls and the insulation layer, while the second simulation verifies the heat transfer rate through the skirt that supports the internal tank. The two geometries are depicted in Figure 7.4.

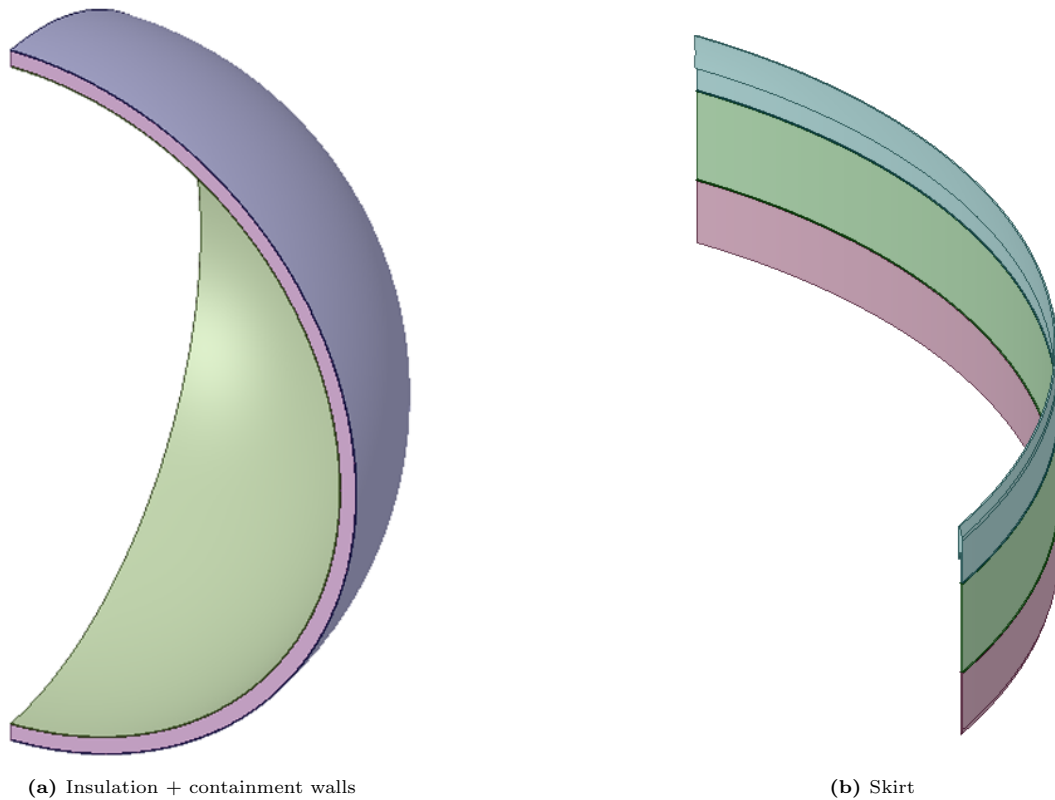


**Figure 7.4:** 3D-designs used in the thermal simulations conducted to verify the analysis

In these simulations the corresponding material are attributed to each component. The spherical shells and skirt elements are composed of low carbon steel and AISI 316 respectively, having the corresponding apparent thermal conductivity mentioned in the previous section. The insulation material used to verify the results is the rigid polyurethane foam defined by Granta Design, having an isotropic thermal conductivity of  $2.65 \text{ mW}/(\text{m}\cdot\text{K})$ . The other components are made of the same materials used in Chapter 6 to simulate the structural resistance.

The results are compared with the theoretical results obtained from using Equation 5.11 for the sandwiched wall system and Equation 5.14 for the skirt. The values used for each variable are given in Table 7.1.

**Table 7.1:** Variables necessary to calculate the desired heat flow

Component	Segment	$k_a$ value [ $\text{W}/(\text{m}\cdot\text{K})$ ]	$\Delta x$ [m]
Walls & insulation	Inner wall	7.00	0.048
	Insulation layer	0.0265	1.00
	External wall	52.00	0.048
Skirt	Top section	7.00	1.0074
	Middle section	11.00	3.04
	Bottom section	52.00	2.1442

Regardless using AISI 316 for the top and middle part of the skirt, the apparent thermal conductivity of the two components vary because the properties of the material are temperature dependent. Since the top segment is at a lower temperature than the middle segment, the  $k_a$ -value follows. The cross sectional areas are calculated as described in Section 5.2 using the corresponding variables from Figure E.1 in Appendix E. The tabulated values do not account for significant figures since the purpose is to compare the theoretical results with the simulated ones as precise as possible.

Results of thermal heat transfer through the containment walls and insulation layer are tabulated as follows:

**Table 7.2:** Heat transfer rate Q[W] through the containment walls and the insulation layer

Theoretical Q [W]	2D-simulated Q[W]	3D-simulated Q[W]
46 054	46 096	46 088

The simulated values have an error of less than 0.1 % when compared with the theoretical results, which is acceptable. Since the 3D-simulation is done on a  $\frac{1}{4}$  of the system, the tabulated value in Table 7.2 is 4 times the result obtained from ANSYS, which is equal to  $11.522 \cdot 10^3$  W. The 2D-axisymmetry simulation on the other hand gives the exact tabulated value. The same applies for the simulation of the skirt as well.

Results of thermal heat transfer through the skirt:

**Table 7.3:** Heat transfer rate through skirt

Theoretical Q [W]	2D-simulated Q[W]	3D-simulated Q[W]
4 674	4 872	4 872

From the tabulated values in Table 7.3 it can be concluded that results obtained are acceptable since the theoretical computation is based on a simplified geometry.

Considering the outcome of the two analysis, it may be acceptable to conclude that the decided simulation setup also results in relatively reliable values.

## 7.2 Results

The heat temperature profile of the steady-state thermal analysis is depicted as in Figure 7.5. This profile is relatively similar between the three cases simulated, but by taking some probes in some specific areas, small differences can be observed. Table 7.4 shows the values of these particular probes for the three different insulation systems; ideal, evacuated spheres 3M Type B37/2000 and Polyurethane foam.

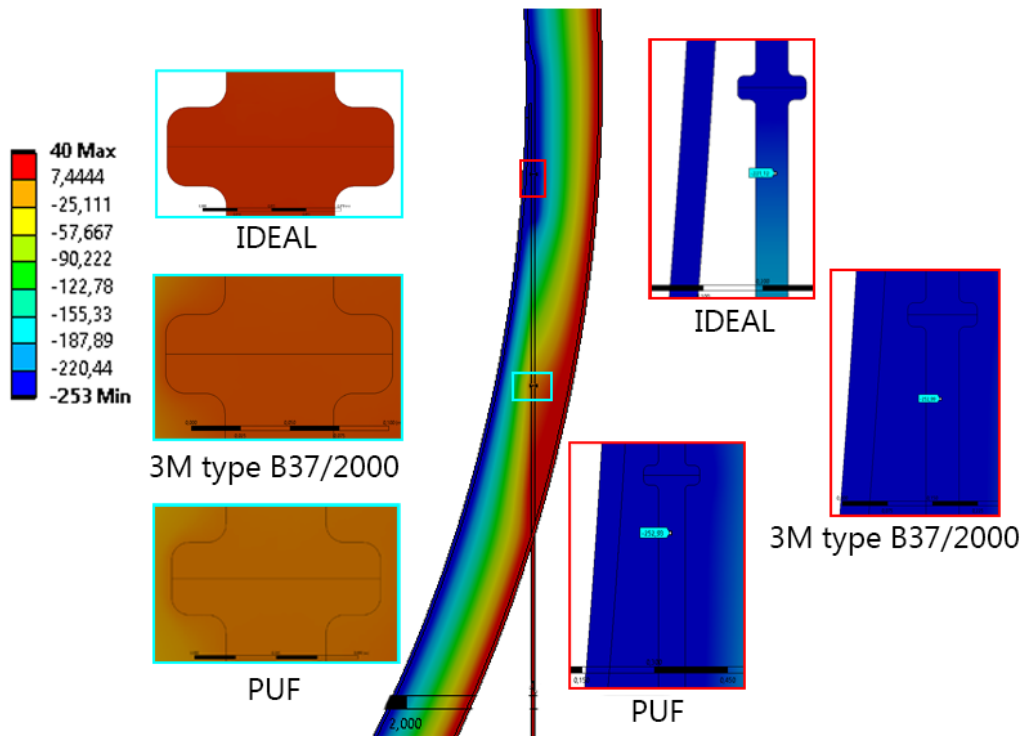


Figure 7.5: Temperature profile for the simulated cases

The geometry depicted in Figure 7.5 is a 2D geometry for a clearer representation. For a 3D geometry, the pattern is similar.

Table 7.4: Values of the temperature probes taken from the temperature profile [°C]

Area of probe	Ideal insulation	3M type B37/2000 evacuated spheres	Polyurethane foam
Middle-bottom skirt connection	12.75	6.484	-2.146
Middle skirt segment	-221.12	-252.99	-252.93

As it can be observed, the higher the apparent thermal conductivity of the insulation system, the smaller the temperature in the particular areas when it reaches equilibrium. This may be caused by the fact that the closer the  $k_a$ -values of the skirt and insulation are to each other, the more evenly the heat is dispersed. For instance, with an ideal insulation system, the heat flows only through the supportive system, and does not go into the insulation since there is no heat transfer mechanism. Therefore the temperature is greater in that specific point compared to the case in which polyurethane foam is used. However, this is just a statement based on logic and evaluation of the resulted heat flux depicted in Figure 7.6. It is not proven in more detail throughout the present study.

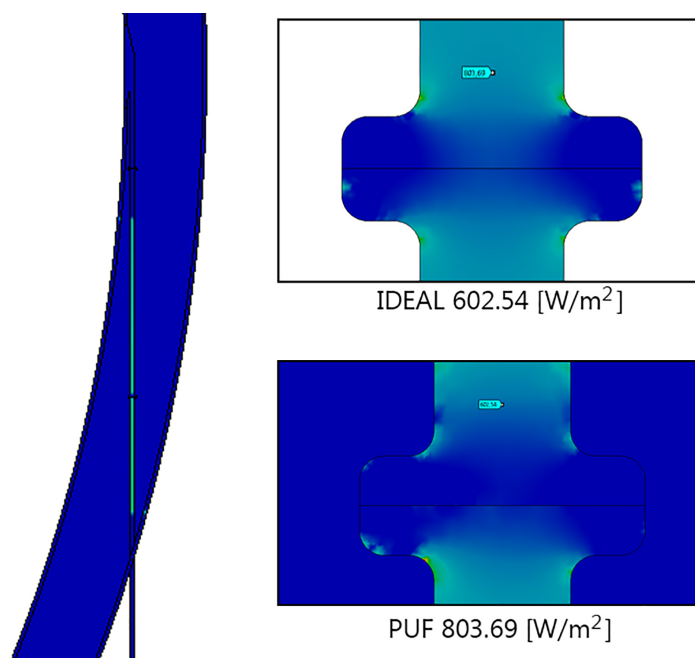


**Figure 7.6:** Heat flux profile of Ideal and PUF insulation [W/m<sup>2</sup>]

The heat flux probes taken show how the value is higher in the case of ideal insulation compared to the value taken for PUF, in approximately same point. This can probably explain the aforementioned described temperature profile.

A second observation regarding Figure 7.6 is that the highest amount of heat flow per unit area is as expected through the supportive area. The reason being the higher apparent thermal conductivity.

The most important results from the thermal analysis are the heat flow rates. These values which are used to compute the boil off rate are tabulated in Table 7.5 together with the calculated BOR.

**Table 7.5:** Thermal analysis results of the preliminary design

Case	2D-geometry		3D-geometry	
	Heat flow rate [W]	Boil-off rate [%/day]	Heat flow rate [W]	Boil-off rate [%/day]
Ideal insulation	$4.973 \cdot 10^3$	0.0339	$4.868 \cdot 10^3$	0.0332
3M type B37/2000	$8.627 \cdot 10^3$	0.0589	$8.388 \cdot 10^3$	0.0573
PUF insulation	$54.930 \cdot 10^3$	0.375	$54.600 \cdot 10^3$	0.373

As anticipated, for the case with an ideal insulation, the heat transfer rate has a value close to the one resulting from the supportive system alone. On the other hand, the resulted heat transfer rate for the case where PUF is used as insulation, is ca. 10 % higher compared to the sum of the results in the verification analysis, which are the separated heat flow rates of the skirt and insulation tabulated in Tables 7.2 and 7.3. One reason may be that the relatively rough geometry can affect the results due to unwanted additional interaction between the insulation layer and the supportive system despite the manual setup of the connective surfaces in ANSYS.

This issue aside, the higher result may conduct to positive outcomes if a similar system is to be constructed. Firstly other components are present in a real-life system which are not represented in this design. Thus, the heat leakage may increase. Such components are the tank dome and the vertical tubular support for piping and access. In a real-life scenario, obtaining a boil-off rate lower than the one actually simulated may be beneficial.



---

## Chapter 8

# Analysis of alternative designs

Both the structural and thermal simulations of the primary chosen design show favourable outcomes. However, due to including as many variables as possible to represent a real-case scenario, the analysis may result in slightly underestimated values. There are several reasons which can be considered, but most of them are linked to the simplified geometry, choices of properties and parameters, as well as other technical aspects regarding the use of the simulation software. The aspect of uncertainties in assumptions and model is elaborated in Chapter 9.

On the other hand, there is also the matter of costs and difficulty when it comes to building and maintaining such a system. Many of the considered aspects in the preliminary design focus solely on the efficiency of the storage system in obtaining a BOR as low as possible. It is therefore questionable if such a system can be easily created in real life.

Considering that there is a possibility of unfavorable results, and taking into account economical and building issues as well, alternatives of the preliminary design must be evaluated.

### 8.1 Improvements considered

With regard to the overall picture concluded from the results obtained in Chapters 6 and 7, adjusting the insulation layer may cover a wide range of possible improvements. The thermal analysis of the previous design shows that having an evacuated insulation layer made of bulk insulation, 3M type B37/2000 glass microspheres in particular, gives a boil-off rate of 0.057 % per day. The amount is approximately three times lower than the objective of 0.15 - 0.2 % BOR per day, which gives room for improvements in terms of costs, facilitating the construction procedure, and structural reinforcement. This is done at the possible expense of extra evaporation of the cargo, however well under the aforementioned objective.

Evacuating a volume of ca. 5 900 m<sup>3</sup> to a pressure lower than 0.10 Pa is energy demanding and may be difficult to achieve. On top of that, the prices for the glass microspheres is relatively high, and filling the 1.00 m thick insulation layer with the calculated value of 1 338 tonnes of material may not be convenient.

One solution to solve both issues is to reduce the insulation thickness to a more achievable size while maintaining a favourable evaporation rate. Taking into account the considered simplicity of the design and other factors which result in underestimated values of heat transfer, a BOR between 0.10 and 0.12 % is evaluated as being an acceptable maximum limit.

Assuming that evacuated glass microspheres are used as material for the insulation, the thickness of the layer can be chosen based on the data given in Figure 5.12 of Subsection 5.2.1, The greatest depletion rate of BOR is observed to take place until it reaches a thickness of 0.3 m<sup>1</sup>. This seem a reasonable value as it gives a boil-off rate, from the insulation alone, of only 0.025 % per day higher than when using a 1.00 m thick insulation. Having a 0.3 m thick insulation layer reduces

---

<sup>1</sup>The value can be relative as the depletion rate may seem satisfactory until it reaches 0.4 m or 0.5 m

the weight of the insulation needed to 390 tonnes<sup>2</sup> as well. Compared to the previous weight of the insulation, this value is more than 3 times lower.

With lower insulation thickness there is also a reduction in the skirt's height, which increases the heat ingress. This downside may be compensated with a change in material or reduction in thickness if possible. For example, as both stainless steel and low carbon steel has been used for the inner-support system of the preliminary design, the one which has the lowest apparent thermal conductivity between the two, can be used for the entire supportive system.

To further adjust the system, the idea of adding an external layer of polyurethane foam insulation on the surface of the outer tank while having the thickness of internal insulation layer reduced, may present greater benefits, both structural and thermal.

From one perspective additional insulation results in the reduction of the boil-off rate. From another perspective, if evacuating the bulk-fill insulation to 0.10 Pa is challenging to achieve for even a 0.3 m thick layer, the presence of an external PUF layer may compensate for the increase of the apparent thermal conductivity of the internal insulation due to a lower evacuation degree. Simultaneously by decreasing the degree of evacuation the forces caused by the overpressure pressing against the spherical walls towards the insulation are also reduced.

One additional benefit of using an external layer of PUF is the avoidance of condensed air on the metal surface<sup>3</sup> when in contact with low temperatures.

## 8.2 Design and simulation setup

Two different designs are evaluated on which the aforementioned possible improvements are established using as a reference point the preliminary design. The first design is not so much an improvement in terms of efficiency as an improvement in terms of amount of material-use. It has similar volumes, wall dimensions and skirt thicknesses as the model tested beforehand. The only difference is the reduced insulation space between the tanks which also reduces the height of the skirts. The purpose of it is to simply verify if a less demanding system can achieve the objective of less than 0.2 % BOR. To facilitate the method of referring to this system, it's identification code is entitled "A1", which stands for the first alternative design.

The second design serves the purpose of depicting a closer-to-reality scenario, where there is the possibility that the  $k_a$  of the insulation layer is slightly increased due to either lower evacuation degree or poorer thermal insulation efficiency. It has a similar design with a reduced inner insulation thickness, but it also includes an extra layer of polyurethane foam on the exterior. The identification code of this system is "A2", referring to the second alternative design.

### 8.2.1 A1 System

The geometry is similar to the preliminary design, with the space between the tanks of 0.3 m and a 3.99 m high internal skirt composed of only one segment made of AISI 316. Since only one material type is used, the segmentation is not required. The aspect and other dimensions besides the height of this component are the same as the top part of the internal skirt used in the preliminary design. The design is represented in Figure 8.1, with the dimensions highlighted by Figure E.2 from Appendix E, Section E.2 .

---

<sup>2</sup>Weight for the entire volume between the tanks, 100 % filled with insulation in the absence of the skirt.

<sup>3</sup>External tank and external supportive system

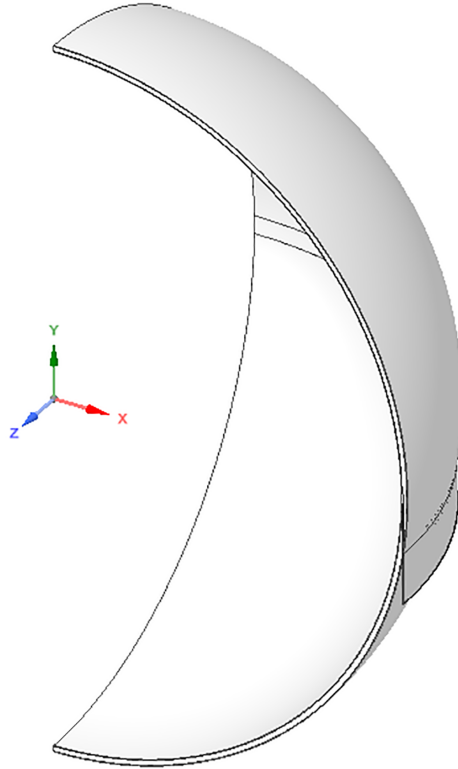


**Figure 8.1:** Design of A1 system with 0.3 m insulation thickness

The insulation material filling the 0.3 m space is chosen to be 3M type B37/2000 glass microspheres with a  $k_a$ -value of 1.003 mW/(m-K). Low carbon steel is attributed to the external support and the external wall, resulting in the fact that all the materials used are similar to previous simulated system; with the physical and thermal properties attached as appendices. The reason of choosing the exact materials is based on the favorable results obtained in Chapter 6 and Chapter 7.

Similar to the P1 design, the insulation layer is suppressed in the structural analysis. To successfully conduct such an analysis, other material properties for the insulation layer are required and finding them has proven challenging. Therefore, the weight of the insulation is represented by adding it to the density of 1 586 kg/m<sup>3</sup> to the material used for the top hemisphere of the internal tank, and 1249 kg/m<sup>3</sup> to the material used for the bottom hemisphere of the external tank. The two values are calculated as described in Subsection 6.1.3.

The mesh is depicted in Figure 8.2 and follows an equal pattern as in P1. The MultiZone method is applied on the skirts, the Sweep method is applied on the walls resulting in solid-shell elements, and for the insulation layer the Hex Dominant is used to avoid tetrahedrone-shaped elements. The mesh elements are the same as described in Subsections 6.1.2 and 7.1.2 for the structural analysis and the thermal analysis respectively. The total number of nodes and elements are of 673 842 and 1 449 827, including the insulation system.

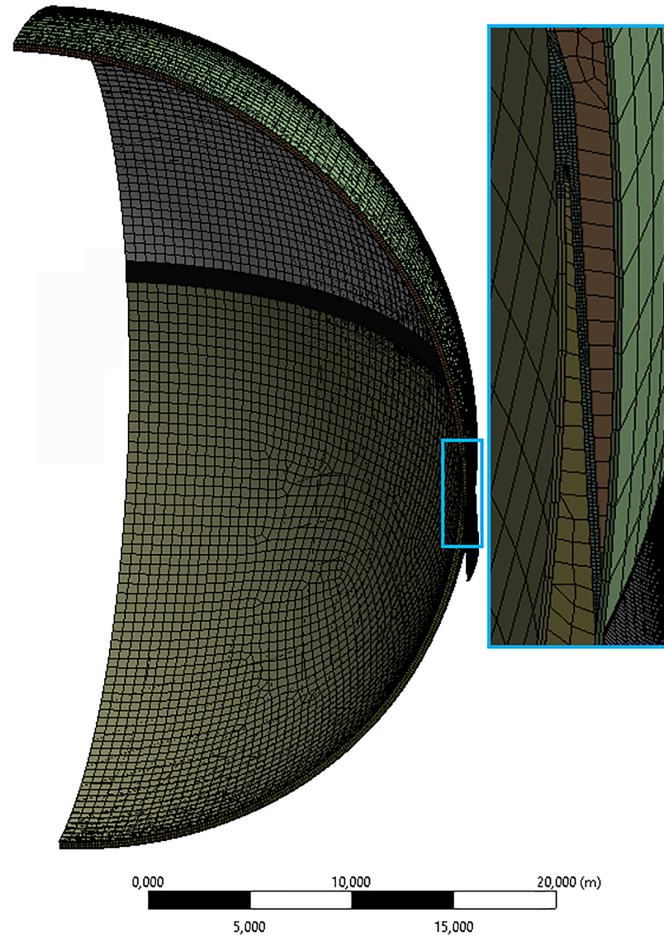


**Figure 8.2:** Mesh of A1 system

The applied loads considered for this design are as follow, with the values tabulated in Table 6.2.:

- L1 - Static external pressure applied on the exterior surface of the external tank
- L2 - Static internal pressure applied on the interior surface of the internal tank
- L3 - Hydrostatic pressure of LH<sub>2</sub> for 100 % filled tank applied on the interior surface of the internal tank
- L4 - Gravitational acceleration applied on the entire system
- L7 - Wave-induced vertical acceleration applied on the entire system
- L9 - Thermal loading because of the temperature difference with the specific temperatures applied on the surfaces which are in direct contact with the ambient and cargo.

Considering the new design and the results highlighted in Chapter 6, the only wave-induced acceleration used is the vertical acceleration. The reason of excluding the longitudinal and transverse accelerations is that the reduced height of the skirt is expected to react better under accelerated loads due to less torque when the system is in a sloped position. However, the insufficient computer resources makes it possible to simulate only a  $\frac{1}{4}$  of the 3D-system or the 2D-axisymmetric design. Most of the wave-induced loads do not have a symmetric behaviour around the Y-axis and cannot be applied on these geometries.

As for the symmetry and other boundary conditions, they follow the exact same pattern as in the preliminary design. There are two symmetry regions normal on the X- and Z-axis, the fixed support is set on the face at the bottom of the external support, and the two temperatures are set accordingly on the surfaces which are in direct contact with the cargo and the ambient.

### 8.2.2 A2 system

The choices taken in terms of dimensioning the thickness of the external PUF layer and the change in apparent thermal conductivity of the evacuated glass microspheres insulation is based on a background evaluation which is described as follow.

#### Background evaluation

There are several levels of vacuum, but the most relevant in the present case are medium and high level vacuum. Based on the data of Table 8.1 taken form the Engineering ToolBox [71], the border between the two is at 0.1 Pa. B.E. Scholtens et al. [62] and many other sources state that this is the pressure at which bulk insulations such as glass microspheres and perlite have an apparent thermal conductivity of 0.001 W/(m·K) or lower.

**Table 8.1:** Vacuum range [71]

Vacuum type	Pressure range [Pa]
Low vacuum	$1 \cdot 10^5 - 3 \cdot 10^3$
Medium vacuum	$3 \cdot 10^3 - 1 \cdot 10^{-1}$
High vacuum	$1 \cdot 10^{-1} - 1 \cdot 10^{-7}$
Ultra high vacuum	$1 \cdot 10^{-7} - 1 \cdot 10^{-10}$
Extremely high vacuum	$1 \cdot 10^{-10}$
Perfect vacuum	0

Achieving a pressure of over 1.0 Pa may be possible with simple systems and less expensive pumps, such as positive displacement pumps<sup>4</sup>, but to achieve a pressure of under 0.1 Pa requires larger pump systems and different types of pumps such as a turbomolecular pump<sup>5</sup>.

The presence of a large system represents a great challenge when it comes to obtaining a high degree of vacuum inside the insulation layer, and therefore other  $k_a$  values for the bulk fill insulation must be considered.

In their paper entitled "Thermal Performance testing of glass microspheres under cryogenic vacuum conditions" the two NASA researchers J.E. Fesmire and S.D. Augustynowicz, have a well defined diagram which shows how the apparent thermal conductivity for glass bubbles, perlite powder and aerogel beads vary with the magnitude of vacuum pressure. The boundary temperatures in the research are 293 K and 77 K, and the residual gas is nitrogen [24]. The diagram is shown in Figure 8.3.

<sup>4</sup>Wikipedia definition: A positive displacement pump makes a fluid move by trapping a fixed amount and forcing (displacing) that trapped volume into the discharge pipe" [75]

<sup>5</sup>Wikipedia definition: A turbomolecular pump is a type of vacuum pump, superficially similar to a turbopump, used to obtain and maintain high vacuum. [77]

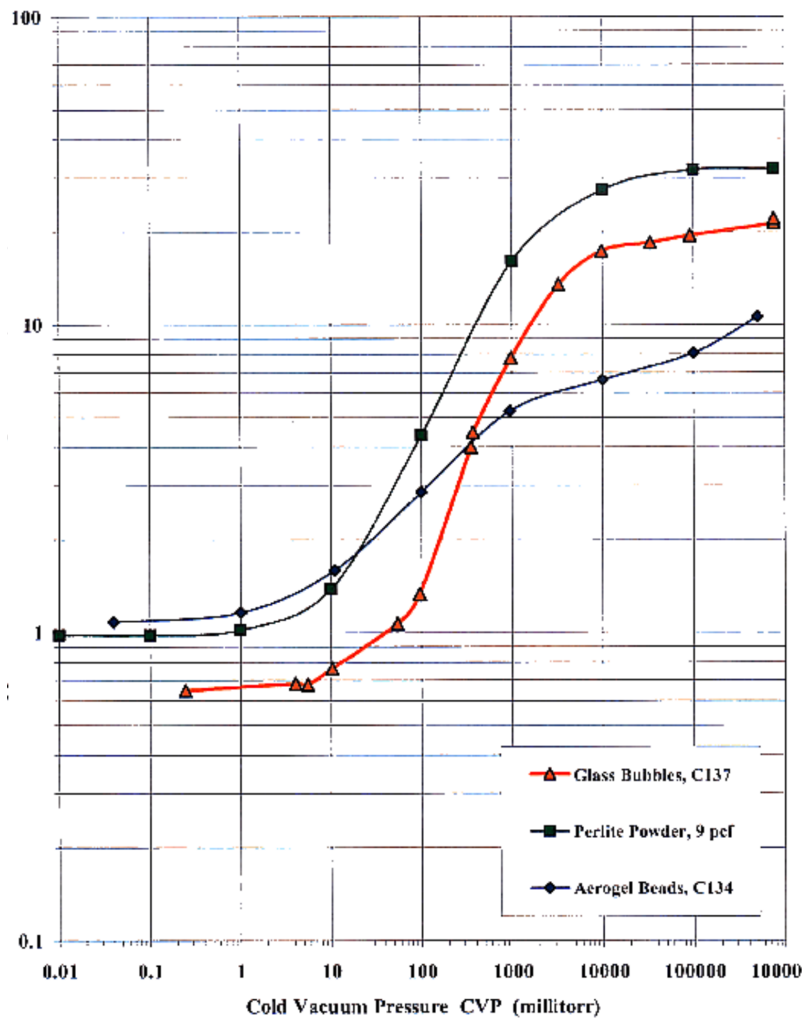


**Figure 8.3:** Variation of k-value with CVP for three bulk insulation materials [1 millitorr = 0.13 Pa] [24]

Assuming all the uncoated glass microspheres have the same behaviour as the tested bulk insulation, a value of 3.0-3.5 mW/(m·K) obtained at a vacuum pressure of 7-10 Pa is chosen to be used in the analysis of the A2 system. This consideration is based on two aspects.

1. Approximately after 1.3 Pa the  $k_a$ -value of all the tested materials steeply increases. For the glass bubbles the steepness of the graph becomes even greater after 13 Pa. Therefore choosing an apparent thermal conductivity at a pressure between 1.3 and 13 Pa is presumably acceptable.
2. A small degree of uncertainty based on common sense is also considered. The perlite with the greatest apparent thermal conductivity at the pressure of ca. 10 Pa, has a value of approximately 3.0 mW/(m·K). It is assumed that for a large scale system this value is greater for perlite. Since the tested glass bubbles show a slightly improved insulation efficiency, and considering that most of the glass microspheres have the same behaviour, a  $k_a$ -value between 3.0 and 3.5 mW/(m·K) is a reasonable choice.

For verification purposes Equations 5.11 and 2.47 are used to calculate the boil-off rate of a tank with a 0.3 meters thick insulation layer made of an insulation material with an apparent thermal conductivity of 3.2 mW/(m·K). It results in 0.123 %/day. This value does not satisfy the aforementioned maximum limit of 0.1 - 0.12 % per day, plus that the heat leakage from the skirt is not considered in this calculation. With the scope of having a lower evacuation level and using as

little as possible glass microspheres, a solution to reduce the evaporation rate is to add external polyurethane foam.

With one additional layer of insulation added, the heat transfer rate equation through a container without the supporting system is written as follow:

$$Q = \frac{T_{s,o} - T_{s,i}}{\frac{r_{ins_i} - r_{w_i}}{4\pi k_{w_i} r_{w_i} r_{ins_i}} + \frac{r_{w_o} - r_{ins_i}}{4\pi k_a^{ins_i} r_{ins_i} r_{w_o}} + \frac{r_{ins_o} - r_{w_o}}{4\pi k_{w_o} r_{w_o} r_{ins_o}} + \frac{r_s - r_{ins_o}}{4\pi k_a^{ins_o} r_{ins_o} r_s}} \quad (8.1)$$

where:

$T_{s,i} = 20.3K$  is the internal surface temperature of the primary tank

$T_{s,o} = 313K^6$  is the external surface temperature of the system

$r_{w_i} = 21.2m$  is the radius to the primary tank

$r_{ins_i} = r_{w_i} + 0.048m$  is the radius to the internal insulation layer

$r_{w_o} = r_{ins_i} + \Delta x_i$  is the radius to the secondary wall, with  $\Delta x_i[m]$  being the thickness of the internal insulation layer

$r_{ins_o} = r_{w_o} + 0.048m$  is the radius to the external PUF insulation layer

$r_s = r_{ins_o} + \Delta x_o$  is the radius to the surface of the system, with  $\Delta x_o[m]$  being the thickness of the external PUF insulation layer

$k_{w_i} = 3.00W/(m \cdot K)$  is the thermal conductivity at 20.3 K of the primary tank made of AISI 316

$k_a^{ins_i} = 0.0032W/(m \cdot K)$  is the chosen apparent thermal conductivity of the inner insulation layer made of glass microspheres

$k_{w_o} = 52.0W/(m \cdot K)$  is the thermal conductivity of the secondary tank made of low carbon steel

$k_a^{ins_o} = 0.03W/(m \cdot K)$  is the apparent thermal conductivity of the external PUF insulation layer

Based on Equation 8.1 with the respective values, Figure 8.4 represents a graph depicting the boil off rate as a function of varying external PUF insulation thickness for a system with a 0.3 m thick inner insulation and without the supportive elements.

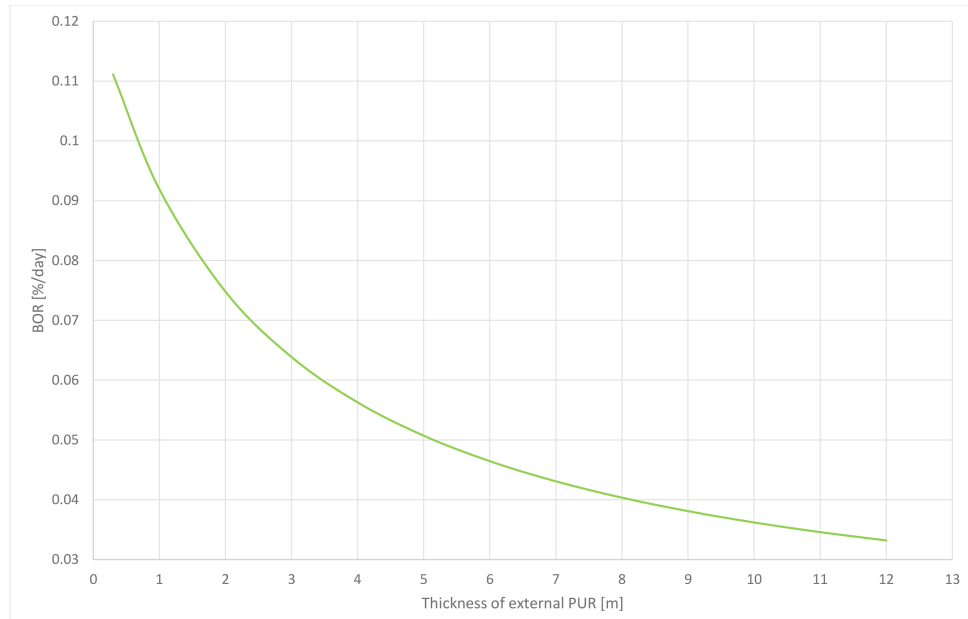


**Figure 8.4:** Boil-off rate variation with different thicknesses of the external PUF insulation

From the energy balance  $\dot{E}_{in} - \dot{E}_{out}$  due to the conservation of the energy, the surface temperature on the external tank is expressed as:

$$T_{s,w_e} = \frac{T_{s,o} R_{syst} + T_{s,i} R_{ins_o}}{R_{ins_o} + R_{syst}} \quad (8.2)$$

<sup>6</sup>According to DNV GL [17], the upper design temperatures for normal services are 305 K in the sea and 318 K in the air, thus resulting an overall estimated value of 313 K for easier calculations.

where:

$T_{s,w_o}$  is the unknown temperature on the surface of the secondary tank which is in contact with the polyurethane foam insulation

$T_{s,o} = 313K$  is the external surface temperature of the system

$T_{s,i} = 20.3K$  is the internal surface temperature of the primary tank  $R_{syst}$  is the total thermal resistance of the system from inside the containment system to the external surface of the outer tank  $R_{ins_o}$  is the thermal resistance inside the external PUF insulation layer

Using Equation 8.2 with the respective resistance and values from Equation 8.1 a graph, is computed and depicted in Figure 8.5 . It highlights how the temperature on the surface of external tank varies with the thickness of the polyurethane insulation layer is computed.

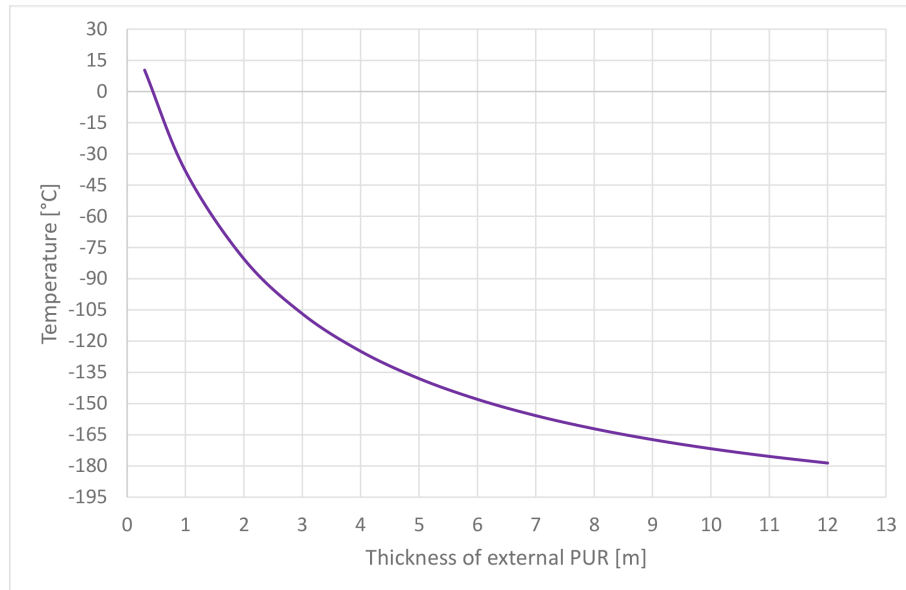


**Figure 8.5:** Temperature on the outer tank surface varying with different thicknesses of the external PUF insulation

With the scope of reducing the surface temperature of the outer tank to a value between  $-20\text{ }^{\circ}\text{C}$  and  $-50\text{ }^{\circ}\text{C}$ , having a PUF thickness of 1.00 m is a reasonable initial choice for the designed model. The surface temperature at this thickness is reduced to approximately  $-30\text{ }^{\circ}\text{C}$ , from the initial temperature of  $40\text{ }^{\circ}\text{C}$ .

However, the BOR value resulting from the heat transfer through the insulation at the specific PUF thickness of 1.00 m is of ca. 0.092 % per day which is relatively high considering that the heat leakage through the internal skirt is not included. To achieve a lower BOR the thickness of one of the two insulations present in the system must be increased. The most efficient option is to increase the evacuated micro sphere layer to possibly 0.4 m as it has a high decrease of  $k_a$ -value between 0.3 and 0.4 m and the skirt height also increases along with it; which reduces the BOR even more. The resulting BOR from using Equation 8.1 for a system with 0.4 m thick evacuated insulation and 1.00 m PUF is of 0.074 % per day; value which may be acceptable.

### Design description

Found on the background evaluation, the containment system created for the simulations is designed as shown in Figure 8.6.



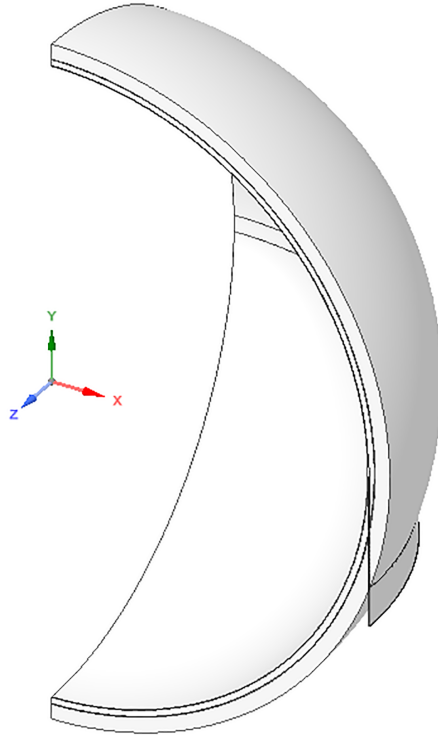


**Figure 8.6:** Design of A2 system with 0.4 m thick internal insulation and 1.0 m thick external PUF insulation

The design has a 0.4 m thick inner insulation made of the same type of glass microspheres, 3M type B37/2000, but with an applied apparent thermal conductivity of  $3.20 \text{ mW}/(\text{m}\cdot\text{K})$ . The value is based on the aforementioned evaluation and may cover a wide range of microspheres, but a detailed argument on why this specific type of glass microspheres is chosen is discussed in Chapter 9. The external polyurethane foam layer is chosen to be 1.00 m high with the material properties tabulated in Appendix D, Section D.3. The supportive elements and tank walls are made of the exact same materials as in A1. AISI 316 is used for the internal skirt and tank and low carbon steel for the external ones. The properties of the materials are shown in Appendix D, Sections D.4 and D.2. Similar to the previous designs, to represent the weight of the existent insulations, as the layers are suppressed in the structural analysis, the densities of the materials used for the components on which the weight of the insulations works as a load, are changed. Besides the internal microsphere insulation with a density of  $225 \text{ kg}/\text{m}^3$ , an external PUF insulation layer exists with the density of ca.  $40 \text{ kg}/\text{m}^3$ . Following the same procedure as described in Subsection 6.1.3, the densities of three components are changed as tabulated in Table 8.2.

**Table 8.2:** Change in density of different segments on the geometry of the A2 system

Segment	Surface	Initial density [ $\text{kg}/\text{m}^3$ ]	Added density from weight-load [ $\text{kg}/\text{m}^3$ ]	New density [ $\text{kg}/\text{m}^3$ ]
Inner tank: upper hemisphere	Exterior	7 969	2 173	19 42
External tank: lower hemisphere	Interior + Exterior	7 850	1 624 + 555	10 029
External tank: upper hemisphere	Exterior	7 850	555	8 405

The thicknesses of the walls remain unchanged, with a value of 0.048 m. The inner skirt is composed of one segment having a height of 4.42 m. The external supportive structure is composed of two different segments and has a total height of 6.35 m. The top segment crossing the polyurethane foam is 3.80 m high. Figure E.3 from Appendix E, Section E.3 shows all the dimensions of the design.

The mesh of the 3D-model is as depicted in Figure 8.7, with 825 445 elements and 1 926 749 nodes, of similar types as for the previously described systems.

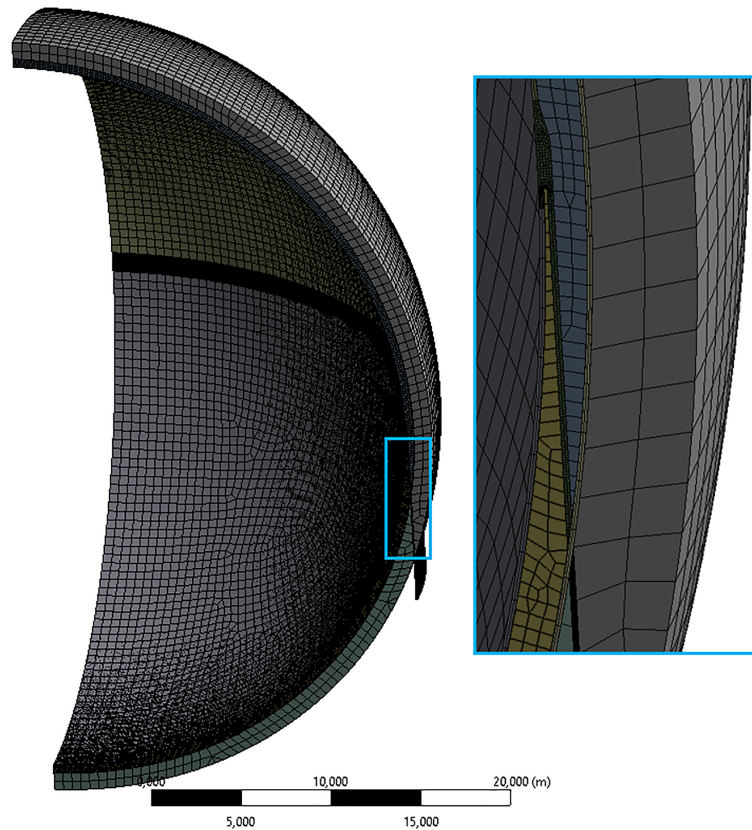


**Figure 8.7:** Mesh of A2 system

The exact same loads, symmetry and boundary conditions applied for the A1 design, which are detailed in Subsection 8.2.1, are applied for the A2 design as well. Concerning the external and internal pressure loads, they are applied as there is pure vacuum inside the evacuated insulation layer. This is because the amount of pressure inside the layer is unknown and the results from a worst case scenario are of interest.

## 8.3 Results

For both alternative designs composed of the aforementioned materials, steady-state structural and thermal analysis are conducted. In the steady state structural analysis, the two systems are subjected to the loads and boundary conditions described in the previous Section. The deformation and the specific stresses for verifying failure, as described in Subsection 6.3.1, are evaluated.

From the steady state thermal analysis, the extracted data are the temperature profile and the heat transfer rate given by the two boundary temperatures.

### 8.3.1 Results of the A1 system analysis

The temperature profile resulting from the thermal simulation is as depicted in Figure 8.8. The probes taken are tabulated in Table 8.3, representing the values from top to bottom.

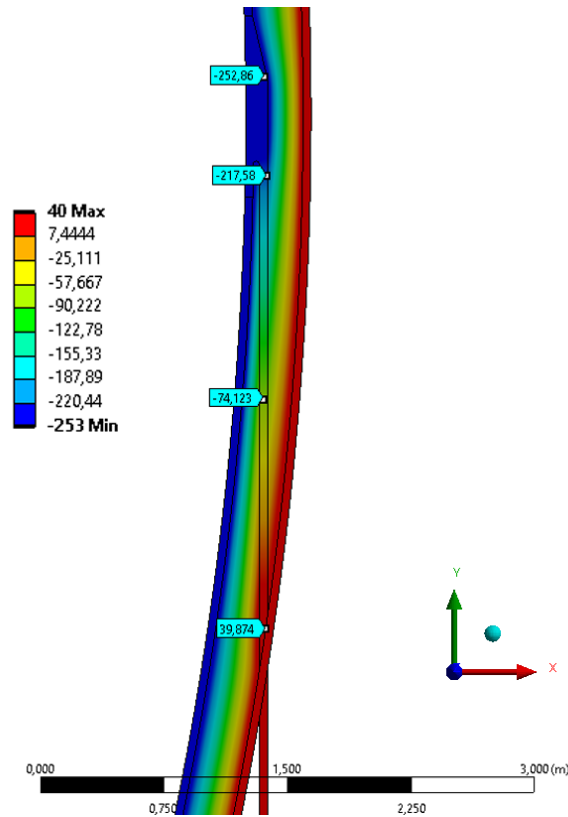


**Figure 8.8:** Temperature profile from the thermal simulation of the A1 system [°C]

The image depicted is a 2D representation for a better understanding.

**Table 8.3:** Temperature profile of A1 design

Probe no.	Temperature [° C]
1	-252.86
2	-217.58
3	-74.123
4	39.874

The obtained heat flow of from the entire system is compared to a theoretical value calculated by adding together the heat flows from the insulation system and the skirt, resulted from using Equations 5.11 and 5.12. The values are highlighted in Table 8.4 together with the evaporation rate obtained from the simulated thermal ingress.

**Table 8.4:** Results from the thermal analysis of A1 design

Theoretical heat flow rate [W]	Simulated heat flow rate [W]	Boil-off rate [%/day]
12 112	13 734	0.095

The variables used to calculate the theoretical heat flow of the system are similar to the respective dimensions and apparent thermal conductivity of the different components forming the system. The difference between the two results, of 13 % is probably caused by the simplified heat flow

calculation through the skirt. The Equation 5.12 is used to calculate the heat flow through a plate. The thicker segment which causes additional heat leakage is therefore not included. Other factors causing the difference are probably the amount of significant figures used in the calculations and using a constant  $k_a$ -value for AISI 316 instead of a temperature dependent thermal conductivity as used in the simulation.

The total BOR resulted is under the limit of 0.1 % per day. Assuming that a low  $k_a$ -value of 0.001003 W/(m·K) is achievable for a large scale cryogenic storage system, the design satisfies the thermal issues.

From the structural point of view, under the influence of the mechanical loads, the system resulted in a deformation as depicted in Figure 8.9.

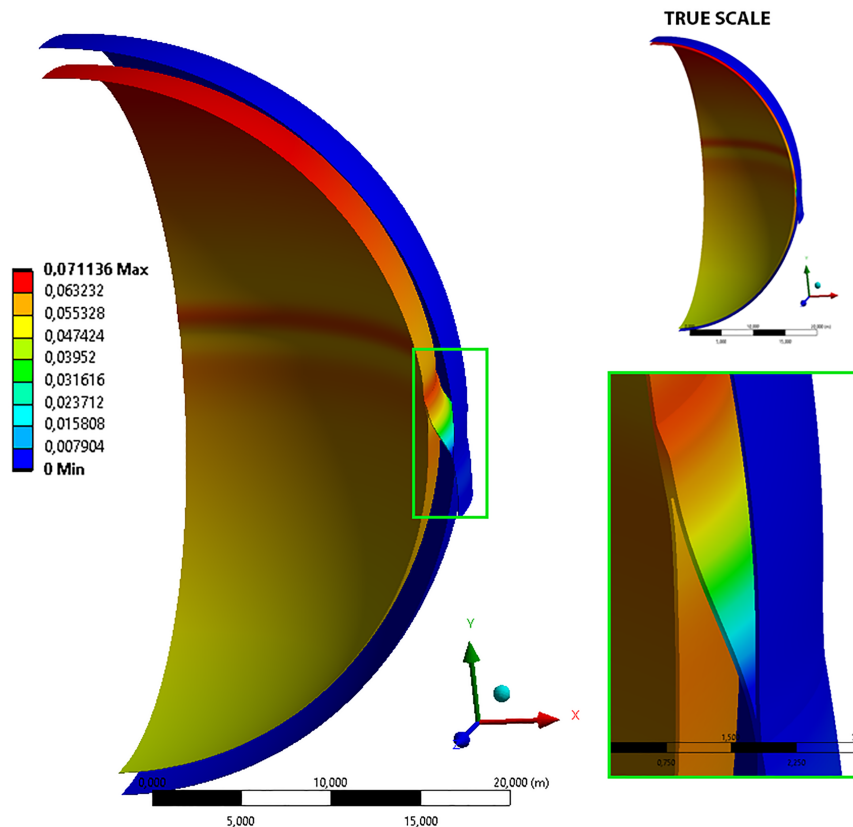


**Figure 8.9:** Deformation [m] of the A1 design under mechanical loads (x19)

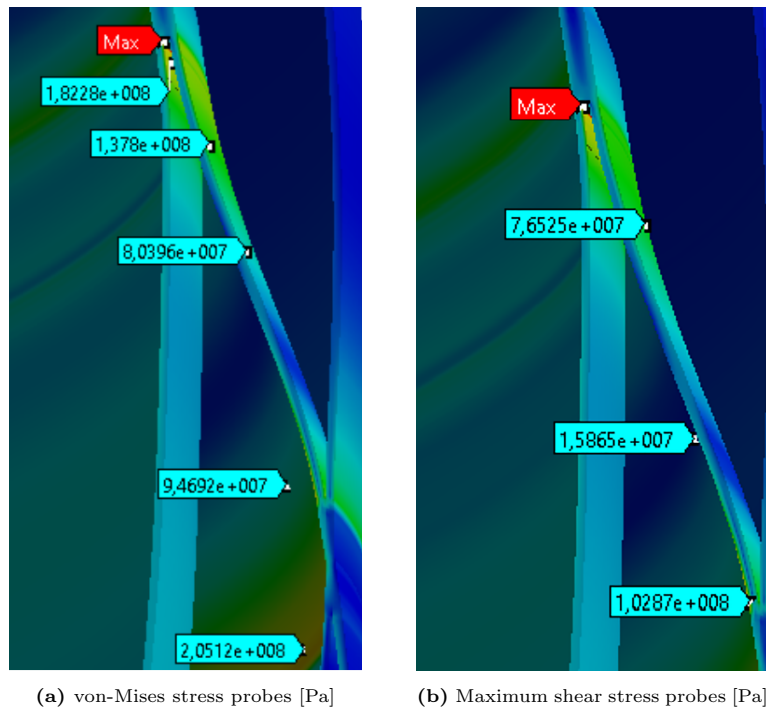
The figure depicts an accentuated deformation which is 19 times greater than the one shown in true scale. This is to provide a better understanding of how the storage tank is deformed. The system shows a maximum deformation of 0.071 m at the top of the internal sphere which is mostly caused by the thermal compression. At the top of the skirt segment, the deformation is approximately 0.065 m. This is slightly smaller due to the internal hydrostatic pressure force which presses against the compressive force. At the bottom of the internal tank the deformation has a value of ca. 0.042 m because of the gravity, vertical wave-induced acceleration and the internal hydrostatic pressure. The three forces are acting in the opposite direction compared to the thermal compression and therefore cancel each other.

In terms of failure the representations of the von-Mises, Maximum Principal, and Maximum shear stress are depicted in the Figures H.1, H.2, H.3 from Appendix H, Section H.1. The maximum values obtained are tabulated in Table 8.5 together with the maximum strength limits of AISI 316, since the skirt is the component subjected to maximum stresses.

**Table 8.5:** Maximum stresses obtained from simulation of A1

Stress Type	Value [Pa]	Maximum limit [Pa]
von-Mises Stress [Pa]	$2.755 \cdot 10^8$	$2.512 \cdot 10^8$
Maximum Shear Stress [Pa]	$1.585 \cdot 10^8$	$1.261 \cdot 10^8$
Maximum Principal Stress [Pa]	$3.191 \cdot 10^7$	$5.651 \cdot 10^8$

The von-Mises stress and maximum shear stress obtained exceed the strength limits of AISI 316. The pattern of the colormap may again indicate exaggerated values due to singularity regions caused by the mesh. However, considering the positions of the highest values, as depicted in Figures 8.10a and 8.10b it is probably safe to assume that the skirt element is likely to fail. A solution would be to replace the stainless steel with a metal which has a higher yield strength.

**Figure 8.10:** A1 system: von-Mises and maximum shear stress probes

### 8.3.2 Results of the A2 system analysis

With a cryogenic tank covered in a 1.00 m thick polyurethane layer, the steady state temperature profile shows interesting results around the components which come in direct contact with the insulation; the external tank and external skirt. Figure 8.11 depicts how the temperature is distributed throughout the storage system.

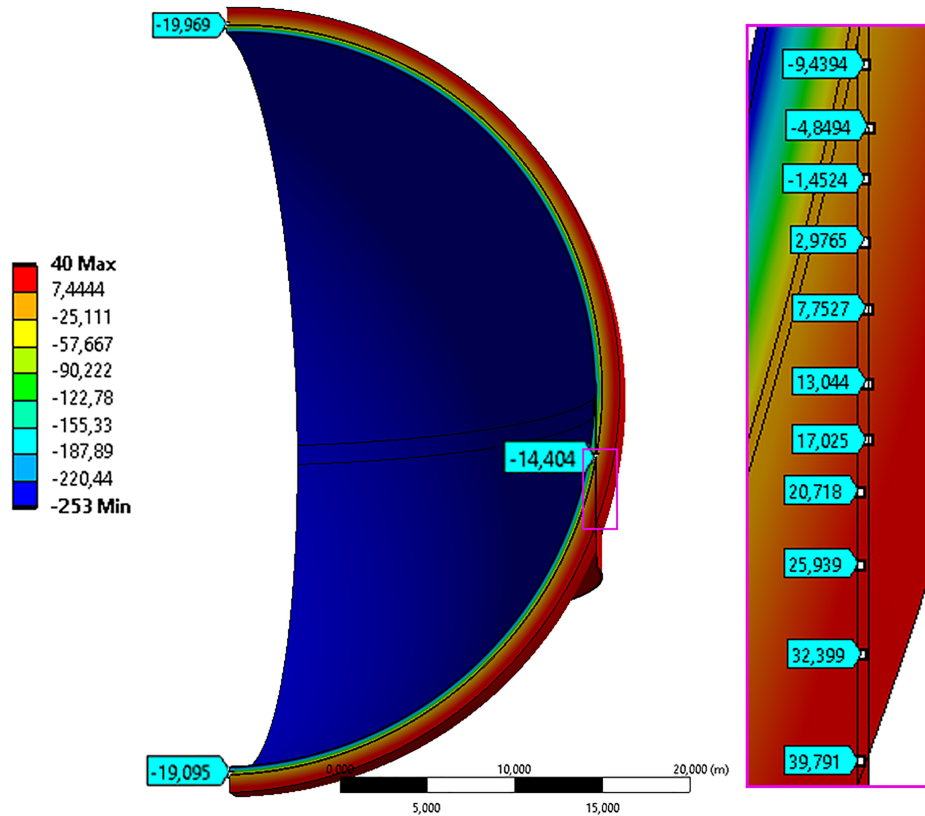


Figure 8.11: Temperature profile from the thermal simulation of the A2 system [°C]

Using Equation 8.2 the surface temperature at the top and bottom of the outer sphere is calculated to be  $-19.99\text{ }^{\circ}\text{C}$ , with the same dimensions and material properties as in the simulation. The two probes taken have relatively similar values, of  $-19.97\text{ }^{\circ}\text{C}$  and  $-19.10\text{ }^{\circ}\text{C}$ . The variation is caused by how accurate the point of the probe is set on the model.

The temperature of the external skirt when it reaches the tank wall is of  $-9.44\text{ }^{\circ}\text{C}$  due to the thermal conductivity through the support, and probably due to the fact that some of the heat inside it is also dispersed into the PUF insulation layer.

The simulated and theoretical heat transfer rate and its resulting BOR is tabulated in Table 8.6. The calculated heat leakage is done by combining the results of Equation 8.1 and a slightly adjusted form of 5.12. The adjustment is based on the idea of combining the inner skirt and the top segment of the outer skirt into one bigger support and calculating the total heat transfer through it.

Table 8.6: Results from the thermal analysis of A2 design

Theoretical heat flow rate [W]	Simulated heat flow rate [W]	Boil-off rate [%/day]
15 649	15 998	0.109

The difference of 2.2 % between the theoretical and simulated heat transfer rate is caused by the same factors as described in Subsection 8.3.1.

The increased BOR of this design is mainly caused by the increase in the apparent thermal conductivity of the inner insulation layer. However the evaporation rate presents a value under the set limit of 0.12 % per day which is set to consider the presence of more heat leakage due to other factors, as discussed in Section 8.1.

The structural deformation caused by the different pressures, gravitation, wave-induced vertical acceleration and the boundary temperatures is depicted in Figure 8.12.

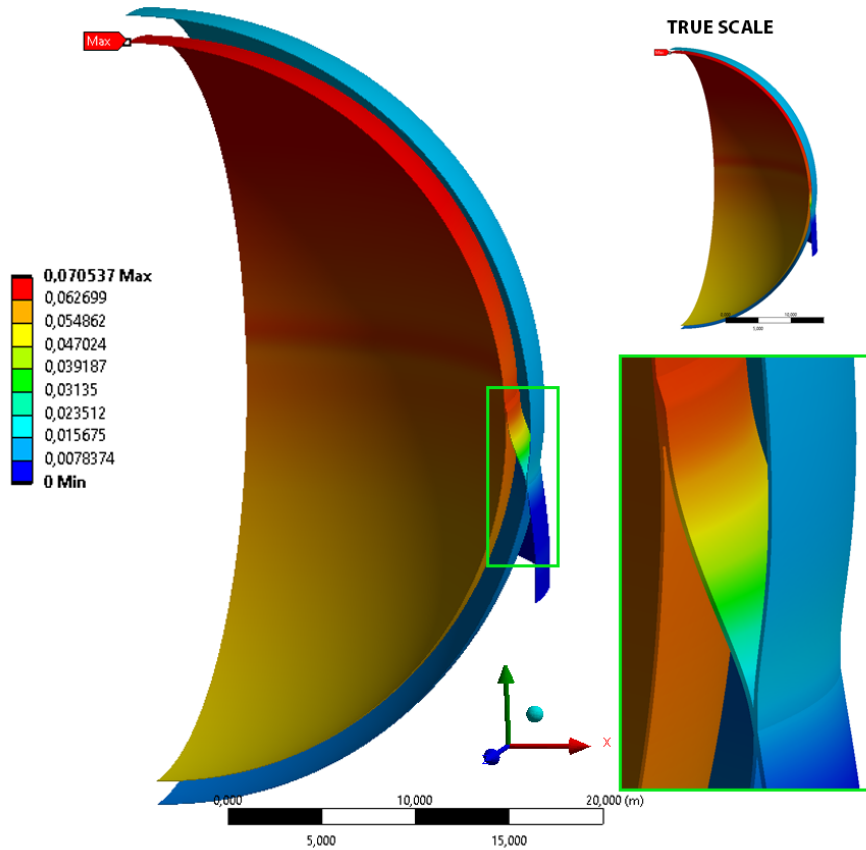


**Figure 8.12:** Deformation [m] of the A2 design under mechanical loads (x19)

The deformation pattern follows a similar one to the one obtained for the A1 system. This is because the exact same loads are applied on the two designs. Despite the greater density of the top hemisphere caused by the weight of the slightly thicker insulation layer, the A2 design shows a lower maximum deformation compared to the A1 design. The reason may be it is from the smaller temperature difference between the two tanks resulting from the existence of the outer polyurethane foam.

The resulting stresses which may cause structural failure to the storage tank are depicted in Appendix H, Section H.2 and tabulated in Table 8.7.

**Table 8.7:** Maximum stresses obtained from simulation of A2

Stress Type	Value [Pa]	Maximum limit [Pa]
von-Mises Stress [Pa]	$2.004 \cdot 10^8$	$2.512 \cdot 10^8$
Maximum Shear Stress [Pa]	$1.150 \cdot 10^8$	$1.261 \cdot 10^8$
Maximum Principal Stress [Pa]	$1.424 \cdot 10^7$	$5.651 \cdot 10^8$

The maximum values obtained for the von-Mises and maximum shear stress almost as high as the yield limits, with differences of 2.02 % and 0.09 % respectively. The possibility of unrealistic maximum values due to singularity is not excluded. Nonetheless considering that the results are reliable, the values are very close to the strength limits of AISI 316 and a positive conclusion cannot be extracted. Applying the other absent elements to the structure, such as the tank dome and pipe tower, and considering that the loads acting on the container are higher than the ones used in the simulation, will cause the structural system to fail.

One the other hand, one positive observation is that the values are more favourable than in the case of the A1 design. One reason is probably the same which causes the less maximum deformation,

namely the lower temperature difference between the two walls of the tank. Another reason may be the height of the skirt, meaning that higher the skirt, better the structural strength; excluding possible buckling as an analysis is not conducted.



---

## Chapter 9

# Discussion

With the background on large LNG and cryogenic storage tanks, a preliminary 40 000 m<sup>3</sup> LH<sub>2</sub> storage tank is modeled and evaluated. The types of conducted simulations are steady state thermal and steady state structural analysis. Upon the resulted values, two other alternative designs with simple changes of the insulation system are analysed in a similar manner. The three different designs are depicted in Figure 9.1. 8.12.

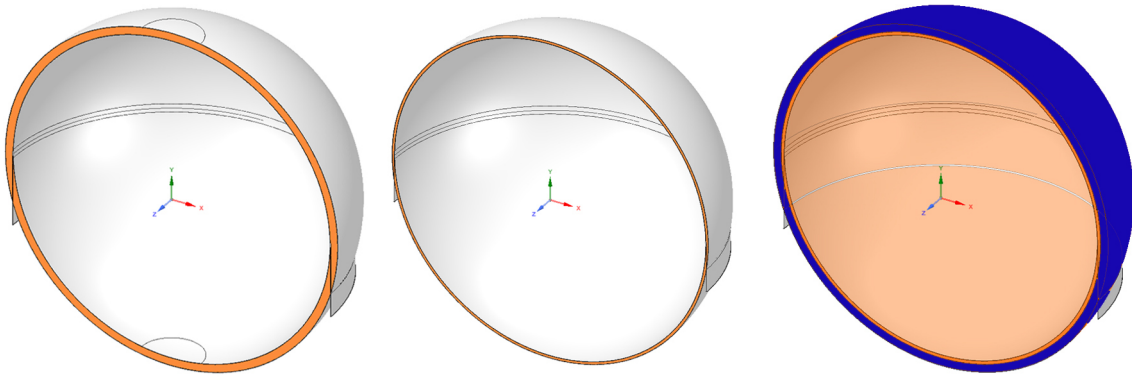


**Figure 9.1:** Designs of the modeled and analysed tanks: P1 (left), A1 (center) & A2 (right)

The orange coloured regions represent the insulation layers which vary in thickness and slightly in numbers. The P1-model has a 1.00 m evacuated insulation layer and an inner skirt divided into three segments. The A1-model has a 0.3 m evacuated insulation layer and an inner one-part skirt. The A2-model has a 0.4 m evacuated insulation layer, an inner one-part skirt and is covered in a 1.00 m thick PUF insulation layer. The exact dimensions of the three models and a 2D close-up on the skirt segments can be seen in the Figures of Appendix E.

The discussion topics to follow are mainly based on the resulted data of the three models, and on the general information gathered.

### 9.1 Comparison of the results

To facilitate the validity and tracking of the results, the preliminary design underwent a series of analyses under different conditions. The variable in the steady state thermal analysis for the P1-model has been the insulation material having different apparent thermal conductivity values. For the structural analysis the system has been subjected to different loads and boundary conditions which were applied step by step under each simulation. An elaborated description is included in Sections 6.3 and 7.2.

As detailed in Subsection 8.2.1 and 8.2.2, the alternative models have been simulated once for each type of steady state analysis, based on the concluded evaluation of the previous simulations.

### 9.1.1 Results from the steady-state thermal analyses

The most important results obtained from the steady state thermal analysis are the heat ingress of the three models and the resulting boil-off rates of the liquid hydrogen cargo. These results are summed up in Table 9.1.

**Table 9.1:** Results from the thermal analysis of the three models

ID of the design	Simulated heat flow rate [W]	Boil-off rate [%/day]
P1	8 627	0.059
A1	13 734	0.095
A2	15 998	0.109

From the tabulated results, and considering the differences between the three designs it is clear that the dimensions and materials of the main components, insulation and support of the inner tank, are highly important for resulted losses of the cargo. Despite the fact that all three systems show promising results to achieve the goal of under 0.2 %/day BOR, the decrease in the amount of the insulation material and its quality at the cost of more evaporated LH<sub>2</sub> rises the question of what is worth compromising. There is also the question of what can physically be achieved with today's technology.

### 9.1.2 Results from the steady-state structural analyses

The mechanical deformation, von-Mises stress, maximum shear stress and maximum principal stress, under mechanical and thermal loading conditions, are the results extracted from the steady state structural analyses. The most important are the values obtained when the two different temperatures are also applied. The reason is that in the simulations of the preliminary design, the deformation is approximately 12 times greater than in the case when they are absent. The stresses acting on the system also increases with the deformation and therefore not including the thermal loads is of little interest. Table 9.2 shows the maximum deformations obtained for each simulation, with the reference to Table 6.2 for the explanation of the IDs of the loads.

**Table 9.2:** Maximum deformation of the preliminary design under different loading conditions

Types of loading conditions	Max. deformation [m]
On a motionless system (L1, L2, L3, L4)	0.00411
On a system in motion (L1, L2, L4, L5, L7, L8)	0.00597
Thermal loading added (L1, L2, L4, L5, L7, L9)	0.0694

Table 9.3 compares the maximum/highest<sup>1</sup> results extracted from the steady state structural simulation of the three models.

**Table 9.3:** Results from the structural analysis of the three models

ID of the design	Deformation [m]	von-Mises stress [Pa]	Max. shear stress [Pa]	Max. principal stress [Pa]
P1	0.0694	$1.221 \cdot 10^8$	$6.185 \cdot 10^7$	$1.277 \cdot 10^8$
A1	0.0711	$2.755 \cdot 10^8$	$1.585 \cdot 10^8$	$3.191 \cdot 10^8$
A2	0.0705	$2.004 \cdot 10^8$	$1.150 \cdot 10^8$	$5.651 \cdot 10^8$

As depicted in Figure 6.17 and all the sections of the Appendix H, the maximum values are present on the top segment of the skirt. From a mechanical perspective, the two variables which may cause the difference in the stress values between the three designs are the weight of the insulation and the

<sup>1</sup>This is a reminder that the von-Mises and shear stresses for the preliminary design show the maximum value at the bottom of the external skirt which is caused by singularity. The highest reliable values representing the maximums were manually chosen for the two types of stresses.

height of the skirt. The temperature profile through the skirt changes in accordance to its change in height, which is caused by lower insulation thickness. Considering that the thermal loads have the greatest impact on the structure, it may be presumed that shorter the skirt results in greater stresses. Based on this statement alone it can be concluded that the higher the support system, the better. However, since the buckling analysis has not been accounted for in this study, the aforementioned conclusion may not be 100 % reliable.

In Subsections 8.3.1 and 8.3.2 it has been concluded from the simulation results, that the stresses acting on the skirt are higher than or close to the strength limits of AISI 316. Considering that singularity may not be a problem in this case, possible improvements must be discussed. The simplest solutions would either be to change the material of the skirt or increase its thickness. However both options are causing an increase in the heat leakage, unless the new material has a poorer capability of conducting heat. Another solution would be to change the shape of the regions where the stresses are extremely high, or maybe change the shape and position of the entire system. In this particular case, the region where the stresses come close to, or exceed the limits of the material is a very tight angle<sup>2</sup> between the leg of the skirt and the part which is fixated to the walls of the tank. A great amount of deformation may cause that area to break. Reducing or eliminating that angle may show positive results.

## 9.2 Possible uncertainties

Most of the simulations and the results gathered have been validated through theoretical computations and well-founded arguments. Despite all the verifications conducted, there are some factors which may cause uncertainties in the results.

### 9.2.1 ANSYS and other technical issues

Using an advanced simulation software like ANSYS requires a significant amount of knowledge regarding every single step in the setup of an analysis. Throughout the entire simulation process, many of the analysis conducted have shown different results from the ones presented; results which have been proven to be unreliable. A list with some factors which may have caused such values are:

- **Improper design:** A poor designed model may include unconnected or overlapped segments affecting the contact regions between components. This has proven to be an issue mainly in the thermal analyses where the contact regions between the different surfaces had to be manually edited to avoid overestimated values. The automatic connection setup created by the software, resulted in some unwanted connections between surfaces which gave higher heat flow rate values than expected. This issue has been fixed for each modeled system in all the simulations conducted.
- **Poor quality mesh setup:** Despite the effort of trying to create fitting mesh to avoid results caused by singularities, the maximum values obtained from the steady state structural analysis of P1 may serve as a clear proof that the quality of the mesh has a significant effect on the outcome.
- **Placement of the corresponding boundary conditions:** Because the boundary conditions must be set on well defined bodies, surfaces, lines or points the external skirt in the A2 design had to be segmented. The reason is that the boundary temperature of 313 K is meant to be applied only on the surface which is in direct contact with the air. Having the support element formed of a single piece implies that the entire surface of the skirt must have the temperature of 313 K, including the one covered by PUF. For a correct distribution of the temperature, the support has been divided into two segments. This may have caused slightly higher stresses in that specific area. However this has not been verified as the results are not high enough to be of interest.

---

<sup>2</sup>For a clearer image it is recommended to check the figures in Appendix H

A technical aspect which has been proven to be a challenge is the lack of computer resources and the impossibility of simulating an entire system. Simulating a real case scenario of a storage tank on a ship in motion has been difficult to realize since not all the wave-induced loads could be applied. Therefore from a structural analysis point of view, the resulted values may give misleading information regarding the strength of the system at sea.

The one simulation conducted on the  $\frac{1}{2}$  of a P1-Design required a long waiting time and has been also conducted through the one-time use of a slightly stronger computer. Therefore, at the risk of excluding the transverse and longitudinal accelerations from the simulations of system A1 and A2 as well as the PS3, the 3D analyses have been conducted only on a  $\frac{1}{4}$  of the different models.

### 9.2.2 Chosen loads and boundary conditions

The main objective of the thermal and structural simulations has been to illustrate the behaviour of a large scale liquid hydrogen storage tanks in a close to reality environment. In spite this, due to the complexity of study some assumptions regarding the chosen loads have to be considered. Comparing to a real-life system, this may result in uncertainties which from different points of view can be more or less significant.

As already described in the previous section, the longitudinal and transverse wave-induced accelerations have been excluded most of the time, especially from the simulation of the alternative models. This is a unfavourable choice, but considering the aforementioned circumstances, it had to be considered. However, the decision is based on the differences between the results from the PS1 and PS2 simulations discussed in Section 6.3.2. With the deformation of only 1.85 mm greater than the deformation of PS1, and with resulting stresses well under the strength limits of the material, excluding the two wave-induced accelerations is relatively acceptable.

One other aspect creating uncertain results with respect to the loads present for a system at sea is that most of them are considered dynamic loads. Therefore the wave-induced accelerations may have different values if other sources of information are used.

As briefly described in Subsection 6.1.3 sloshing is considered negligible due to the low density of LH<sub>2</sub>, but also because the sloshing loads are present only if the container is partially filled, which is not the case for the conducted simulations.

From a thermal perspective, placing the two boundary temperatures directly on the surface of the two walls of the storage tank excludes the presence of convection between the system and the air and LH<sub>2</sub> respectively. However, this only gives overestimated values as the convective resistances which reduce the thermal ingress are absent. This may compensate for uncertainties regarding the choices of material and their ability to conduct heat.

### 9.2.3 Chosen materials and their material properties

The most significant aspect which causes uncertainties in the obtained results in this study is the applied materials and their physical and thermal properties.

Finding well defined materials has presented to be a challenging task, since similar types presented by different sources have different properties. For instance, the stainless steel 316 presented in Table 5.5 shows different tensile and yield strengths compared to AISI 316 from ANSYS Granta Design database from Section D.2 in the Appendix.

Despite the warning provided by ANSYS Inc. that it does not provide any warranty for the data provided by Granta, both stainless steel and low carbon steel have been used from the same database due to the detailed and complexity of the data provided. Not only that all the required information to run the simulation is provided, but most of the properties such as the thermal conductivity and coefficient thermal expansion are temperature dependent. From the perspective of this study it is a necessary requirement since the temperature through the support system for

instance is unevenly distributed.

The data gathered from the simulations may be under-evaluated as the material behaviour under cryogenic temperatures and when in contact with hydrogen molecules is not fully accounted for. Without having well-founded knowledge background concerning different materials and their properties under specific conditions, the concluded outcomes can easily be inaccurate.

Some decisions made regarding the best solutions for suitable materials to be used in the simulation are based on data gathered from the LNG industry and for smaller scale cryogenic containers such as the NASA liquid hydrogen storage tanks. Despite the augmentation given in Chapter 5, better suited materials may exist.

As for the evacuated insulation material, the evacuated glass microspheres 3M type B37/2000 - type is been used. With the two most important material properties defined by A. Hofmann [31] 3M type B37/2000 is chosen due to the possibility of calculating the apparent thermal conductivity based on the temperature difference and because of the density equal to  $225 \text{ kg/m}^3$ . Since the apparent thermal conductivity and the overall density of the material varies with the average diameter of the microspheres, these values may not be very accurate. Nonetheless, the material with the exact same properties has been used to represent a worst-case scenario as the density is relatively high. However, there are other types of glass microspheres with better properties which may equally be used.

#### 9.2.4 Use of apparent thermal conductivity

Choosing the correct heat transfer mechanism through all the system-components is a delicate topic regarding uncertainties, as it directly effect on concluding if the goal of under 0.2 % boil-off rate per day can be achieved or not.

As it has been proven challenging to account for all three heat transfer mechanisms for every material used, a more practical solution has been decided to be the use of apparent thermal conductivity which accounts for conduction, convection and radiation.

Another reason of using the apparent thermal conductivity is to be able to facilitate the setup of the steady-state thermal analysis. The only two material properties which can be attributed to be able to conduct a steady-state thermal analysis are the isotropic and orthotropic thermal conductivities. Including convection and radiation separately implies more boundary condition to the setup which can be confusing and difficult to keep track of.

However, the apparent thermal conductivities found in literature, especially for cryogenic insulation systems, are mostly based on experimental research using small containment systems. Their values are usually defined by boundary temperatures between 293 K and 77.4 K which is the normal boiling point of  $\text{LN}_2$ , as it is used as the evaporation liquid.

For liquid hydrogen and especially for large scale containment systems, values as low as  $0.001 \text{ W/(m}\cdot\text{K)}$  may not be reliable for several reasons. The three heat transfer mechanisms act differently under different boundary temperatures. At low temperatures, heat radiation has proven more effective, while the conductivity decreases. Therefore is difficult to assume a correct and reliable value as no concrete references were found. The only source which may come close to a promising solution is A.Hofmann's paper on "The thermal conductivity of cryogenic insulation materials and its temperature dependence" [31].

On the other hand, there is the evacuation level on which the apparent thermal conductivity of a cryogenic insulation material is highly dependable. What may be achievable in terms of evacuating large containment systems is uncertain and therefor the value of the apparent thermal conductivity becomes a great uncertainty for the thermal results of this study.

As can be concluded from the thermal simulations of the two alternative systems, an increase of only  $0.0022 \text{ W/(m}\cdot\text{K)}$  may gives a higher BOR despite the external PUF layer and greater internal

insulation thickness in A2.

### 9.2.5 Simplicity of the model

The simplicity of the modeled designs has several times been referred as a possible cause of underestimated results throughout the thesis. Two main components which are included in the LNG system, but are not designed in the simulated models have an increasing effect both on the stresses of the tank and in the heat leakage. These are the pipe tower and the tank dome. Some supportive elements may also be present which of course may negatively affect the overall boil-off rate. On top of that how the different components are welded to each other may affect both the structural and thermal results. The simplified design does not account for this aspect.

Therefore, in spite that the results of the simplified designs may seem favourable, a safety margin must be taken into account; such as an acceptable BOR maximum limit of 0.10-0.12 %/day for the simulated outcomes.

---

# Chapter 10

## Conclusion

The purpose of this study has been to investigate possible tank concepts for large scale liquid hydrogen storage having as goal the achievement of a boil-off rate of under 0.2 % per day, with respect to structural stress consideration and other thermal aspects.

From the analysis using the finite element method on three different models designed based on LNG and other cryogenic storage tanks, several key findings have been concluded:

- Using the finite element method is a convenient solution to simulate the thermal and structural behaviour of a liquid hydrogen storage tank, under different loading and boundary conditions. However, for best results, the computer should have the capacity of running simulations of an entire 3D system.
- The results show that a boil-off rate of under 0.2 % per day is possible to achieve, but at the cost of great amounts of materials with high quality insulation efficiency. To reach an acceptable LH<sub>2</sub> loss of under 0.2 % per day, an evacuated bulk insulation material is preferable. With a minimum insulation thickness of 0.4 to 0.5 m, the apparent thermal conductivity of the insulation may have a maximum value around 0.003 to 0.0035 W/(m·K); considering that a concept which reduces the surface temperature of the external tank is used.
- The LNG Moss Rosenberg design is a good starting point for analysing a large scale LH<sub>2</sub> storage tank model. Some of the dimensions as well as some materials used to construct a LNG spherical container with a capacity of 40 000 m<sup>3</sup> are also applicable for storing liquid hydrogen.
- Using unevacuated insulations as a main insulation material similar to the case of LNG, does not satisfy the goal of under 0.2 % BOR for insulation thicknesses lower than ca. 4.0 meters or probably higher.
- As an evacuated insulation system is required to achieve low BOR, the double-walled tank design is necessary. The preliminary model shows favourable results both structural and thermal. However, such a system may be difficult to achieve in real life.
- Despite the use of heavier materials and possible higher dimension to design a liquid hydrogen storage tank, when 100 % filled with cargo, the total weight of the system resulted in a lower value than for a LNG Moss Rosenberg tank with the same capacity. This is due to the density of the liquid natural gas which is ca. 6 times greater than the density of LH<sub>2</sub>.
- For a large scale hydrogen storage tank of 40 000 m<sup>3</sup>, the thermal loading seems to have the greatest impact in terms of plastic deformation, compared to other mechanical loads. Based on the results from the simulations under different loading conditions, the greatest deformation took place when the two temperatures of 313 K and 20.3 K were applied. From maximum results of a few mm, the maximum deformation became 11 times greater, when the thermal loading was applied.

- 
- The material properties are a major uncertainty with respect to the results, as different sources offer different values for the same material types. The properties applied must correspond with the conditions to which the system is subjected to, such as temperature and pressure levels. The apparent thermal conductivity is the most sensible to such factors as it is highly dependant on the boundary temperatures and evacuation degrees.



---

## Chapter 11

# Proposal for further work

The complexity of the topic at hand requires time and knowledge from several fields of study to fully cover all the possible aspects concerning the storage and transportation of liquid hydrogen. Some proposed topics for further work are described as follow:

**Improve the alternative design models:** The alternative designs result in possible structural failure. However, they show promising results in terms of achieving the goal of under 0.2 % boil-off rate per day. Slightly improvement could be done to the design which can result in an overall positive outcome, after a detailed analysis.

**Improved structural analysis:** A transient-state structural analysis is recommended for further work. This type of analysis can account for the dynamic loads defined in Table 5.1, and may give the possibility to further investigate fatigue failure and crack propagation.

**Buckling analysis:** Buckling is one of the ultimate limit state designs which are not analysed in the thesis at hand. From the analysed designs, there are two segments in particular which requires a rigorous buckling analysis to exactly conclude the structural strength of the system. The two segments are the external tank and the internal support element.

The results show that a longer skirt presents a better behaviour under plastic deformation. When it comes to buckling, the outcome may differ.

The outer tank is subjected to external overpressure. The steady-state structural analysis shows no significant deformation caused by this load, but at high levels of external overpressure buckling may occur. This issue may however be solved by reinforcing the external tank as it has negligible effect on the thermal intake if it is done on the exterior of the wall. Such reinforcements may have the form of stiffened panels as depicted in Figure 11.1.

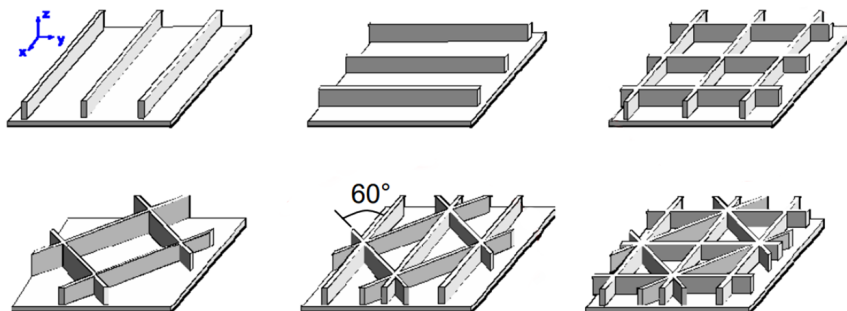


**Figure 11.1:** Possible grid stiffened panels for the structural reinforcement of the external tank [14]

**Application of shield refrigeration:** The concept of shield refrigeration serves the purpose of reducing the surface temperature of the cryogenic container so that less heat ingress may occur.

---

The topic of shield refrigeration is superficially touched in the present thesis in the shape of LNG external polyurethane insulation layer of the A2 design. However, in practice, the concept may complicate the process of maintaining and inspecting the external tank. Solution would be to move the PUR layer to the insulation of the ship hull to maintain a lower temperature on the surface of the outer tank than the outside ambient of 40 °C. The concept may be further developed by cooling of the shield space, e.g. by utilising the cold temperature of the evaporated liquid hydrogen cargo.

**Hanging internal tank:** On page 54, in the "Design Manual for Structural Stainless Steel" written by Euro Inox and The Steel Construction Institute, two interesting sentences are written: "Members subject to tension only do not suffer any instability due to buckling. (...) Members in compression are susceptible to a number of possible buckling models." [37, p. 54]. Based on this assessment, and considering that a buckling analysis has not been conducted in the present study, designs where the inner tank is hanging by supportive elements instead of sitting on it are possible better solutions. Therefore a proposed topic for future work is to validate if such models are better solutions. A good starting point are designs with hanging internal tanks either by thin columns or a suspended skirts similar to the one used in the P1 model. Such designs are depicted in Figures 11.2a and 11.2b.

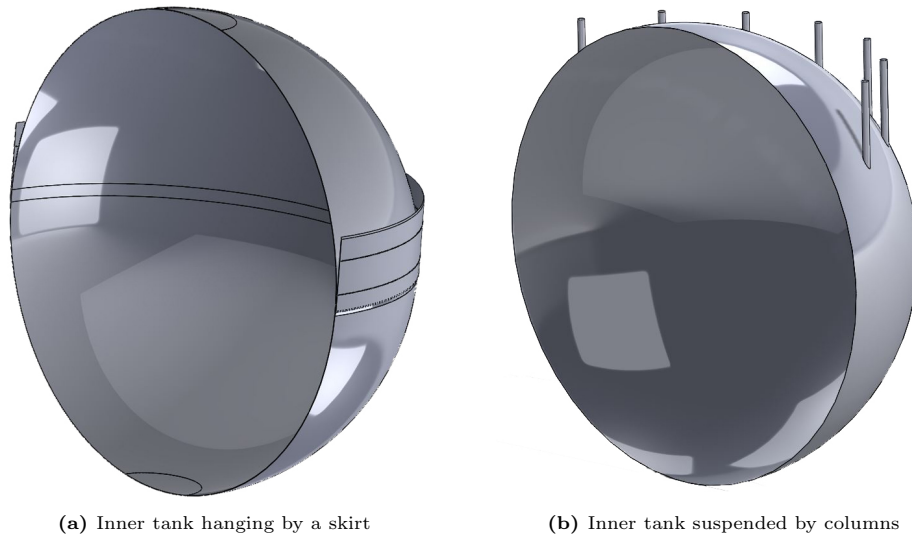


**Figure 11.2:** A1 system: von-Mises and maximum shear stress probes

Since the entire surface of the external tank is in direct contact with the external temperature, if possible deformation on it is caused by the weight of the inner system, the surface can be reinforced. Therefore, hanging the inner tank may not present an issue from this perspective.

**Plastic deformation causing increased thermal leakage:** The possible deformation may also have a negative effect on the thermal efficiency of the insulation. Since bulk fill insulation is used, the thermal contraction and expansion of the inner tank can cause movement in the particles of the insulation material. Through time, the distribution of the material between the tanks will be uneven. In areas where the density of the materials will increase, the thermal conduction through solids will increase as well. In the areas with reduced amount of particles, the thermal radiation may increase. All these changes will result in a higher ingress. Therefore the topic is highly important and further investigations are required.

**Construction proposition:** Having a design which passes both the thermal and structural analysis, but presents difficulties or may be impossible to construct does not fulfill the purpose of the study. Therefore this topic requires more attention, as in this study it has been rarely brought up. Probably a step by step method on how to construct a specific large scale LH<sub>2</sub> storage tank design can be in order.

# Bibliography

- [1] Emirates Classification Society (Tasneef). *Guide for the Design and Operation of Liquefied Natural Gas (LNG) Carriers*. 2016. URL: [http://tasneefmaritime.ae/sites/default/files/pdf\\_guide/Guide\\_for\\_the\\_design\\_and\\_operation\\_of\\_liquefied\\_natural\\_gas\\_\(LNG\)\\_carriers\\_\(2016\).pdf](http://tasneefmaritime.ae/sites/default/files/pdf_guide/Guide_for_the_design_and_operation_of_liquefied_natural_gas_(LNG)_carriers_(2016).pdf).
- [2] Gaztransport & Technigaz 2019. *Mark III systems*. Accessed: 05.11.2019. URL: <https://www.gtt.fr/en/technologies/markiii-systems>.
- [3] Gaztransport & Technigaz 2019. *NO96 systems*. Accessed: 05.11.2019. URL: <https://www.gtt.fr/en/technologies/no96-systems>.
- [4] I. Abt et al. "The GERmanium Detector Array for the search of neutrinoless decays of  $^{76}\text{Ge}$  at LNGS". In: (Mar. 2020).
- [5] J.M. Allen et al. *Advances in microsphere insulation systems*. Technical Report. Presented at the Cryogenic Engineering Conference in 2003. 2003. URL: [https://www.techapps.com/hs-fs/hub/165629/file-18312577-pdf/documents/cec\\_c2-c-03\\_advances\\_in\\_microsphere\\_insulation\\_systems.pdf](https://www.techapps.com/hs-fs/hub/165629/file-18312577-pdf/documents/cec_c2-c-03_advances_in_microsphere_insulation_systems.pdf).
- [6] Inc. ANSYS. *3-D 20-Node Structural Solid - SOLID186*. Accessed: 27.01.2020. 2018. URL: [http://www.mm.bme.hu/~gyebro/files/ans\\_help\\_v182/ans\\_elem/Hlp\\_E\\_SOLID186.html](http://www.mm.bme.hu/~gyebro/files/ans_help_v182/ans_elem/Hlp_E_SOLID186.html).
- [7] Inc. ANSYS. *3-D 20-Node Thermal Solid - SOLID90*. Accessed: 02.02.2020. 2018. URL: [http://www.mm.bme.hu/~gyebro/files/ans\\_help\\_v182/ans\\_elem/Hlp\\_E\\_SOLID90.html](http://www.mm.bme.hu/~gyebro/files/ans_help_v182/ans_elem/Hlp_E_SOLID90.html).
- [8] Inc. ANSYS. *3-D 8-Node Structural Solid Shell - SOLSH190*. Accessed: 27.01.2020. 2018. URL: [http://www.mm.bme.hu/~gyebro/files/ans\\_help\\_v182/ans\\_elem/Hlp\\_E\\_SOLSH190.html](http://www.mm.bme.hu/~gyebro/files/ans_help_v182/ans_elem/Hlp_E_SOLSH190.html).
- [9] Inc. ANSYS. *3-D 8-Node Surface-to-Surface Contact - CONTA174*. Accessed: 27.01.2020. 2018. URL: [http://www.mm.bme.hu/~gyebro/files/ans\\_help\\_v182/ans\\_elem/Hlp\\_E\\_CONTA174.html](http://www.mm.bme.hu/~gyebro/files/ans_help_v182/ans_elem/Hlp_E_CONTA174.html).
- [10] Inc. ANSYS. *3-D Target Segment - TARGE170*. Accessed: 27.01.2020. 2018. URL: [http://www.mm.bme.hu/~gyebro/files/ans\\_help\\_v182/ans\\_elem/Hlp\\_E\\_TARGE170.html](http://www.mm.bme.hu/~gyebro/files/ans_help_v182/ans_elem/Hlp_E_TARGE170.html).
- [11] Inc. ANSYS. *3-D Thermal Solid - SOLID70*. Accessed: 02.02.2020. 2018. URL: [http://www.mm.bme.hu/~gyebro/files/ans\\_help\\_v182/ans\\_elem/Hlp\\_E\\_SOLID70.html](http://www.mm.bme.hu/~gyebro/files/ans_help_v182/ans_elem/Hlp_E_SOLID70.html).
- [12] Inc. ANSYS. *Mechanical APDL 2020 R1: Theory reference - Structural fundamentals*. Accessed: 20.01.2020. 2020. URL: [https://ansyshelp.ansys.com/account/secured?returnurl=/Views/Secured/corp/v201/en/ans\\_thry/thy\\_heat.html](https://ansyshelp.ansys.com/account/secured?returnurl=/Views/Secured/corp/v201/en/ans_thry/thy_heat.html).
- [13] Makoto Arai et al. "Sloshing and swirling behavior of liquid in a spherical LNG tank". In: *Proceedings of PRADS2016 4* (2016), 8th.
- [14] Steven Arnold et al. "Spherical cryogenic hydrogen tank preliminary design trade studies". In: *48th AIAA/ASME/ASCE/AHS/ASC Structures, Structural Dynamics, and Materials Conference*. 2007, p. 2290.
- [15] DNV GL AS. *Class guideline: Liquefied gas carriers with spherical tanks of type B*. 2019. URL: <http://rules.dnvgl.com/docs/pdf/DNVGL/CG/2018-10/DNVGL-CG-0134.pdf>.
- [16] DNV GL AS. *Rules for classification of Ships/High Speed, Light Craft and Naval Surface Craft: Metallic materials*. 2016. URL: <http://rules.dnvgl.com/docs/pdf/dnv/rulesship/2016-01/ts202.pdf>.

- 
- [17] DNV GL AS. *Rules for classification ships: Part 5 Ship types - Chapter 7 Liquefied gas tankers*. 2017. URL: <https://rules.dnvgl.com/docs/pdf/dnvg1/ru-ship/2017-01/DNVGL-RU-SHIP-Pt5Ch7.pdf>.
- [18] Y. Bia et al. *Marine structural design - Chapter 4: LNG Carrier*. eng. 2nd ed. Amsterdam, Netherlands: Butterworth-Heinemann, 2016. ISBN: 0-08-100007-3.
- [19] Thomas D. Bostock and Ralph G. Scurlock. *Low-Loss Storage and Handling of Cryogenic Liquids : The Application of Cryogenic Fluid Dynamics*. eng. 2nd ed. 2019. International Cryogenics Monograph Series. Cham: Springer International Publishing : Imprint: Springer, 2019. ISBN: 3-030-10641-1. DOI: 10.1007/978-3-030-10641-6.
- [20] Liquefied Gas Carrier.com. *LNG vessel construction -Advantages of Moss Rosenberg technology*. Accessed: 27.09.2019. URL: <http://www.liquefiedgascarrier.com/moss-rosenberg-containment-system.html>.
- [21] X. Chen and Y. Liu. *Finite element modeling and simulation with ANSYS Workbench*. CRC press, 2014.
- [22] P. Christiansen. “A New Generation Moss Carrier”. In: *The 19th International LNG, LPG & Natural Gas Conference & Exhibition*. 2000. URL: <http://www.ivt.ntnu.no/ept/fag/tep4215/innhold/LNG%5C%20Conferences/2000/Data/Papers/Christiansen.pdf>.
- [23] Vlad Cristea. *Solution for transport and storage of liquefied hydrogen*. Tech. rep. Norwegian University of Science and Technology (NTNU), Department of Energy and Process Engineering (EPT), 2018.
- [24] JE Fesmire and SD Augustynowicz. “Thermal performance testing of glass microspheres under cryogenic vacuum conditions”. In: *AIP Conference Proceedings*. Vol. 710. 1. American Institute of Physics. 2004, pp. 612–618.
- [25] Amandine Gay et al. “Fatigue of aluminum/glass fiber reinforced polymer composite assembly joined by self-piercing riveting”. In: *Procedia Engineering* 133 (2015), pp. 501–507.
- [26] Matmatch GmbH. *Polyamide 6 Reinforced with 50% Glass Fibers (PA6+GF50)*. URL: <https://matmatch.com/materials/mbas132-polyamide-6-reinforced-with-50-glass-fibers-pa6-gf50>.
- [27] Agata Godula-Jopek, Walter Jehle, and Jörg Wellnitz. *Hydrogen Storage Technologies: New Materials, Transport and Infrastructure*. eng. 2nd ed. Weinheim, Germany: Wiley-VCH Verlag GmbH & Co. KGaA, 2012. ISBN: 3-527-64994-8.
- [28] Material Grades. *Stainless Steel 304 Vs 316*. Accessed: 03.12.2019. 2019. URL: <https://www.materialgrades.com/stainless-steel-304-vs-316-1975.html>.
- [29] Ram Gupta. *Compendium of Hydrogen Energy : Hydrogen Storage, Distribution and Infrastructure*. eng. Vol. 2. Woodhead Publishing Series in Energy. Burlington: Elsevier Science, 2015. ISBN: 1-78242-384-2.
- [30] Anne Marie Helmenstine. *Normal Boiling Point Definition (Chemistry)*. Published by: ThoughtCo, Accessed: 26.03.2020. 2020. URL: <https://www.thoughtco.com/definition-of-normal-boiling-point-605416>.
- [31] A Hofmann. “The thermal conductivity of cryogenic insulation materials and its temperature dependence”. In: *Cryogenics* 46.11 (2006), pp. 815–824.
- [32] IGU. *2019 World LNG Report*. 2019.
- [33] IGU. *Life Cycle Assessment of LNG*. 2015. URL: [http://www.igu.org/sites/default/files/node-page-field\\_file/LNGLifeCycleAssessment.pdf](http://www.igu.org/sites/default/files/node-page-field_file/LNGLifeCycleAssessment.pdf).
- [34] 2020 SlidePlayer.com Inc. *Material Used Shipbuling*. Accessed: 17.01.2020. 2016. URL: <https://slideplayer.com/slide/5275061/>.
- [35] ANSYS. Inc. *Mechanical APDL 2020 R1: Theory reference - Heat flow fundamentals*. Accessed: 20.01.2020. 2020. URL: [https://ansyshelp.ansys.com/account/secured?returnurl=/Views/Secured/corp/v201/en/ans\\_thry/thy\\_heat1.html](https://ansyshelp.ansys.com/account/secured?returnurl=/Views/Secured/corp/v201/en/ans_thry/thy_heat1.html).
- [36] Frank P. Incropera et al. *Incropera’s Principles of heat and mass transfer*. Wiley, 2017.
- [37] The Steel Construction Institute and 2006 Euro Inox. *Design manual for structural stainless steel*. he Steel Construction Institute, 2006. URL: <http://www.steel-stainless.org/media/1036/english.pdf>.
-

- 
- [38] Hyeonwon Jeong and W Jaewoo Shim. “Calculation of boil-off gas (BOG) generation OF KC-1 membrane LNG tank with high density rigid polyurethane foam by numerical analysis”. In: *Polish Maritime Research* 24.1 (2017), pp. 100–114.
- [39] Verfondern Karl. *Safety Considerations on Liquid Hydrogen*. Tech. rep. Forschungszentrum Jülich, Institute for Energy Research, 2008.
- [40] Piaras Kelly. “Solid Mechanics”. In: *Part I, Lecture notes: 7.3 The Thin-walled Pressure Vessel Theory, The University of Auckland* (2013).
- [41] Tae-Wook Kim et al. “Design of independent type-B LNG fuel tank: Comparative study between finite element analysis and international guidance”. In: *Advances in Materials Science and Engineering* 2018 (2018).
- [42] LE Klebanoff, JW Pratt, and CB LaFleur. “Comparison of the safety-related physical and combustion properties of liquid hydrogen and liquid natural gas in the context of the SF-BREEZE high-speed fuel-cell ferry”. In: *International Journal of Hydrogen Energy* 42.1 (2017), pp. 757–774.
- [43] Konecranes. *Lifting the ship-building process for over 50 years*. 2010. URL: <https://pdf.nauticexpo.com/pdf/konecranes/shipyard-cranes/30447-73579.html>.
- [44] A.G. Krenn and D.W. Desenberg. “Return to Service of a Liquid Hydrogen Storage Sphere”. In: (2019). URL: <https://ntrs.nasa.gov/archive/nasa/casi.ntrs.nasa.gov/20190028305.pdf>.
- [45] Rolf S. Kvamsdal. “Factors Influencing Design and Operation of LNG Ship, Viewed With Respect to Safety and Overall Economy”. In: *Proceedings of the Tenth World Petroleum Congress*. Heyden & Son. 1980, p. 99.
- [46] Huei-Huang Lee. *Finite element simulations with ANSYS Workbench 18*. SDC publications, 2018.
- [47] Linde. *Cryogenic tanks*. Accessed: 20.11.2019. 2019. URL: [https://www.linde-engineering.com/en/plant\\_components/cryogenic\\_tanks/index.html](https://www.linde-engineering.com/en/plant_components/cryogenic_tanks/index.html).
- [48] IndiaMART InterMESH Ltd. *Automatic Cryogenic Tanks, Capacity: 200 To 50, 000 Litres*. Accessed: 5.10.2019. 1996-2019. URL: <https://www.indiamart.com/proddetail/cryogenic-tanks-7116335630.html>.
- [49] NWSSSC Pty Ltd. *Moss Rosenberg*. Accessed: 27.09.2019. URL: <http://www.nwsssc.com/fleet/technical-information/moss-rosenberg/>.
- [50] Witherby Publishing Group Ltd. *Global LNG - LNG Competency*. Accessed: 05.11.2019. URL: <https://www.witherbyseamanship.com/media/lng-02.jpg>.
- [51] Key to Metals AG. *Properties of Aluminum Alloys at Cryogenic and Elevated Temperatures*. Accessed: 08.01.2020. 2001. URL: [totalmateria.com/page.aspx?ID=CheckArticle%5C&LN=EN%5C&site=KTN%5C&NM=23](http://totalmateria.com/page.aspx?ID=CheckArticle%5C&LN=EN%5C&site=KTN%5C&NM=23).
- [52] Key to Metals AG. *Stainless Steels for Cryogenic Applications*. Accessed: 08.01.2020. 2010. URL: <https://totalmateria.com/page.aspx?ID=CheckArticle%5C&site=kts%5C&NM=270>.
- [53] Le Thanh Hung Nguyen et al. “Charpy impact properties of hydrogen-exposed 316L stainless steel at ambient and cryogenic temperatures”. In: *Metals* 9.6 (2019), p. 625.
- [54] IHI Offshore Group Ship & Offshore Engineering Department. *SPB Tank Insulation*. Accessed: 09.10.2019. 2000. URL: [https://www.ihl.co.jp/offshore/insulation\\_e.htm](https://www.ihl.co.jp/offshore/insulation_e.htm).
- [55] IHI Offshore Group Ship & Offshore Engineering Department. *SPB Technology*. Accessed: 09.10.2019. 2000. URL: [https://www.ihl.co.jp/offshore/spbmenu\\_e.htm](https://www.ihl.co.jp/offshore/spbmenu_e.htm).
- [56] Naoki Oiwa et al. “Structure and welding technologies for SPB LNG aluminum tank”. In: *Light metal welding* 49.1 (2011), pp. 2–6.
- [57] U Petersen, G Würsig, and R Krapp. “Design and safety considerations for large-scale sea-borne hydrogen transport”. In: *International journal of hydrogen energy* 19.7 (1994), pp. 597–604.
- [58] Radovan Petrović et al. “Analytical, numerical and experimental stress assessment of the spherical tank with large volume”. In: *Tehnički vjesnik* 22.5 (2015), pp. 1135–1140.
-

- 
- [59] SL Robinson, BP Somerday, and NR Moody. “Hydrogen embrittlement of stainless steel”. In: *Proc. of the 11th Internat. Conf. on Fracture (Turin, Italy, March 20–25, 2005)*. 2005, p. 6.
- [60] W. S. Rogers and D. J. and Cox. *INCREASED CARGO TANK FILLING LIMITS ON LNG CARRIERS — THE LR APPROACH*. URL: <http://www.ivt.ntnu.no/ept/fag/tep4215/innhold/LNG%5C%20Conferences/1998/Papers/6-3-Rogers.PDF>.
- [61] Andreas Sanne. *Buckling of Non-spherical Moss-LNG tank*. Tech. rep. Norwegian University of Science and Technology (NTNU), Department of Marine Technology, 2018.
- [62] BE Scholtens et al. “Cryogenic thermal performance testing of bulk-fill and aerogel insulation materials”. In: *AIP conference proceedings*. Vol. 985. 1. American Institute of Physics. 2008, pp. 152–159. URL: <https://aip.scitation.org/doi/abs/10.1063/1.2908517>.
- [63] © 2019 United Nations Climate Change Secretariat. *Climate action and support trends*. 2019. URL: [https://unfccc.int/sites/default/files/resource/Climate\\_Action\\_Support\\_Trends\\_2019.pdf](https://unfccc.int/sites/default/files/resource/Climate_Action_Support_Trends_2019.pdf).
- [64] S.-H. Shin. “A Study on Simplified Analysis for the Initial Tank Design of Spherical Type LNG Carriers”. In: *Journal of the Society of Naval Architects of Korea* 52.2 (2015), pp. 125–134. URL: <http://dx.doi.org/10.3744/NAK.2015.52.2.125>.
- [65] SP Shipbase. *Arctic Princess K131005*. Accessed: 02.10.2019. URL: <http://www.skipslistene.no/samples-filer/Arctic%5C%20Princess%5C%20-%5C%20K131005.htm>.
- [66] Bonnie J. M. Swoger. *Types of Scientific Literature*. Accessed: 10.09.2019. 2011. URL: <https://undergraduatesciencelibrarian.org/a-very-brief-introduction-to-the-scientific-literature/types-of-scientific-literature/>.
- [67] A. Tamilarasan. *Numerical modelling of heat transfer and evaporation characteristics of cryogenic liquid propellant*. Tech. rep. University of Washington, 2015.
- [68] CL Tien and GR Cunningham. “Glass microsphere cryogenic insulation”. In: *Cryogenics* 16.10 (1976), pp. 583–586.
- [69] Klaus D Timmerhaus and Richard P Reed. *Cryogenic engineering: fifty years of progress*. Springer Science & Business Media, 2007.
- [70] Arne Tonnessen. “SPHERICAL LNG TANKS ON CONTINUOUS CYLINDRICAL SKIRTS. A SHIPBUILDER AND LICENCEE’S EXPERIENCE”. In: (1977).
- [71] Engineering ToolBox. *Vacuum Pressure - Units Converter*. Accessed: 02.03.2020. 2003. URL: [https://www.engineeringtoolbox.com/vacuum-converter-d\\_460.html](https://www.engineeringtoolbox.com/vacuum-converter-d_460.html).
- [72] Wikipedia contributors. *Hydrogen embrittlement — Wikipedia, The Free Encyclopedia*. [Accessed: 13.01.2020]. 2019. URL: [https://en.wikipedia.org/wiki/Hydrogen\\_embrittlement](https://en.wikipedia.org/wiki/Hydrogen_embrittlement).
- [73] Wikipedia contributors. *Liquid helium — Wikipedia, The Free Encyclopedia*. [Accessed: 02.12.2019]. 2019. URL: [https://en.wikipedia.org/wiki/Liquid\\_helium](https://en.wikipedia.org/wiki/Liquid_helium).
- [74] Wikipedia contributors. *LNG carrier — Wikipedia, The Free Encyclopedia*. [Accessed: 27.09.2010]. 2019. URL: [https://en.wikipedia.org/wiki/LNG\\_carrier#Moss\\_tanks\\_\(Spherical\\_IMO\\_type\\_B\\_LNG\\_tanks\)](https://en.wikipedia.org/wiki/LNG_carrier#Moss_tanks_(Spherical_IMO_type_B_LNG_tanks)).
- [75] Wikipedia contributors. *Pump — Wikipedia, The Free Encyclopedia*. [Accessed: 02.03.2020]. 2019. URL: <https://en.wikipedia.org/wiki/Pump>.
- [76] Wikipedia contributors. *Surface-area-to-volume ratio — Wikipedia, The Free Encyclopedia*. [Accessed: 21.11.2019]. 2019. URL: [https://en.wikipedia.org/w/index.php?title=Surface-area-to-volume\\_ratio%5C&oldid=943853222](https://en.wikipedia.org/w/index.php?title=Surface-area-to-volume_ratio%5C&oldid=943853222).
- [77] Wikipedia contributors. *Turbomolecular pump — Wikipedia, The Free Encyclopedia*. [Accessed: 02.03.2020]. 2019. URL: [https://en.wikipedia.org/wiki/Turbomolecular\\_pump](https://en.wikipedia.org/wiki/Turbomolecular_pump).
- [78] M. R. Zoolfakar. “Holistic modelling of LNG carrier systems”. In: 2012.

---

# Appendix A

## About cryogenic insulations

Insulation type	Advantages	Disadvantages
Fiberglass paper-aluminum foil combination	<ul style="list-style-type: none"><li>• Very low thermal conductivity</li><li>• Easily applied to cylindrical shapes</li><li>• Thermal conductivity increases with compression, but less than for other layered insulants</li><li>• Can be heated sufficiently for outgassing</li><li>• Not flammable in oxygen</li></ul>	<ul style="list-style-type: none"><li>• Needs high vacuum for best performance</li><li>• Paper relatively weak and easily torn</li><li>• Will not resist appreciable vibration</li><li>• Difficult to apply to complex configuration</li><li>• Difficult to evacuate</li></ul>
Synthetic fiber net-aluminum foil combination	<ul style="list-style-type: none"><li>• Very low thermal conductivity</li><li>• Organic fiber strong and easily handled</li><li>• Dimensionally stable</li><li>• Resists vibration</li><li>• Can be heated sufficiently for outgassing</li><li>• Organic nets give comparable performance to fiberglass but require fewer reflecting layers</li><li>• Readily obtained from many suppliers</li></ul>	<ul style="list-style-type: none"><li>• Needs high vacuum for best performance</li><li>• Difficult to apply to complex geometries</li><li>• Upper temperature limit of 425-475 K</li><li>• Application skill required for best performance</li><li>• Flammable</li><li>• Restricted to non-oxidizing materials</li><li>• Difficult to evacuate</li></ul>
Crinkled aluminized Mylar	<ul style="list-style-type: none"><li>• Only single layer for shield and spacer</li><li>• Very low thermal conductivity</li><li>• Installation easier than for combination layered insulation</li><li>• Easily handled</li><li>• Low lateral heat flow</li><li>• Easily evacuated, outgassing completed during aluminizing step</li><li>• Expensive</li></ul>	<ul style="list-style-type: none"><li>• Does not resist compression</li><li>• Has greatest increase of conductivity with compression for layered insulation</li><li>• Needs high vacuum for best performance</li><li>• Flammable</li><li>• Restricted to non-oxidizing materials</li><li>• Non-flammable material is available but more expensive</li></ul>
Fiberglass	<ul style="list-style-type: none"><li>• Acceptable thermal conductivity</li><li>• Fine fibers comparatively easy to handle</li><li>• Dimensionally stable</li><li>• Elastic in compression; allows for contraction and expansion</li><li>• Not hygroscopic</li><li>• Recoverable after water contact</li><li>• Readily available</li></ul>	<ul style="list-style-type: none"><li>• Requires careful packing for best performance</li><li>• Difficult to install in vacuum-insulated vessels</li><li>• Needs protection from atmosphere</li></ul>

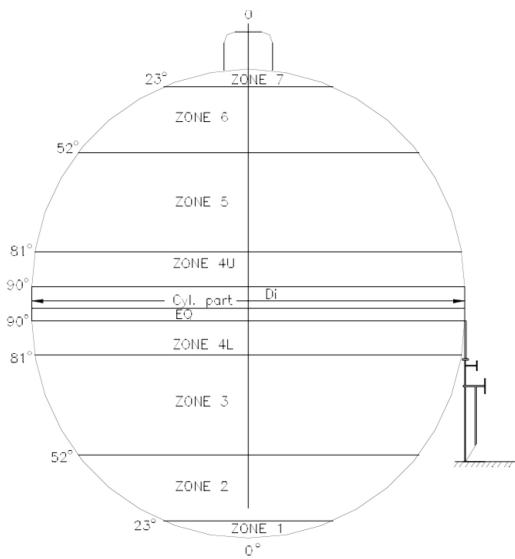
Expanded perlite	<ul style="list-style-type: none"> <li>• Acceptable thermal conductivity</li> <li>• Low density and low cost</li> <li>• Readily available</li> <li>• Non-inflammable</li> <li>• Not toxic or hygroscopic</li> <li>• Easy to install in insulation space</li> <li>• Flows readily when new</li> <li>• Easily conveyed pneumatically</li> <li>• Recoverable even after water contact</li> <li>• Does not cake in use</li> <li>• Can be produced on site</li> <li>• Useful in vacuum insulation</li> <li>• Easy to evacuate</li> </ul>	<ul style="list-style-type: none"> <li>• Easily damaged during handling with increase in bulk density</li> <li>• Dusty and abrasive</li> <li>• Cannot be used to insulate moving parts</li> <li>• Maintenance may require complete removal of insulant</li> <li>• Limited transformability</li> <li>• Non-elastic in compression and may have insulation gap after pressure release</li> </ul>
Silica aerogel	<ul style="list-style-type: none"> <li>• Acceptable thermal conductivity</li> <li>• Lightweight and easy flowing</li> <li>• Dimensionally stable when dry</li> <li>• Does not shrink when larger particles are broken</li> <li>• Slight elastic compressibility</li> <li>• Will not settle due to vibration after initial compaction</li> <li>• Not hygroscopic</li> <li>• Easy to evacuate</li> </ul>	<ul style="list-style-type: none"> <li>• Price is about 10 times that of expanded perlite</li> <li>• After water contact forms silica gel on drying with an increase in bulk density by a factor of 10 and decreased insulation properties</li> <li>• Needs protection from atmosphere</li> </ul>
Foamglass	<ul style="list-style-type: none"> <li>• Strong structure</li> <li>• Readily available</li> <li>• Closed pores, not permeable to water</li> <li>• Useful as a support for inner vessel</li> <li>• Dimensionally stable</li> <li>• Not hygroscopic</li> <li>• Non-inflammable</li> </ul>	<ul style="list-style-type: none"> <li>• Expensive</li> <li>• Needs skilled labor for proper installation</li> <li>• Needs vapor barrier between insulation blocks</li> <li>• Rather high thermal conductivity</li> </ul>
Foamed plastics	<ul style="list-style-type: none"> <li>• Lightweight</li> <li>• Acceptable thermal conductivity</li> <li>• Relatively available in many grades</li> <li>• Useful as a support for inner vessel</li> <li>• Available with closed pores, not permeable to water</li> <li>• Can be foamed in site, simplifying installation</li> </ul>	<ul style="list-style-type: none"> <li>• Needs skilled labor for proper installation</li> <li>• Has large contraction and expansion</li> <li>• Upper temperature limit can be as low as 350 K</li> <li>• Foaming materials generally flammable</li> <li>• Unusable in an oxygen-enriched atmosphere</li> <li>• Requires nitrogen purge if used below 90 K</li> </ul>

Table is taken from the book entitled "Cryogenic Engineering: Fifty Years of Progress" written by K.D. Timmerhaus and R.P. Reed [69, p.130].

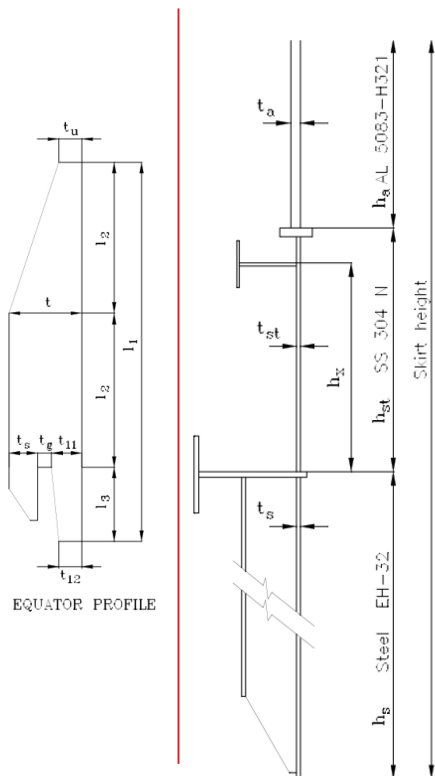


# Appendix B

## LNG tank - scantlings



SPHERE	HEIGHT mm	THICK. mm
Zone no. 7	1610	30
Zone no. 6	6160	29
Zone no. 5	9290	42
Zone no. 4U	2560	47
Cyl. part	2000	60
EO	1200	169
Zone no. 4L	2560	57
Zone no. 3	9290	50
Zone no. 2	6160	44
Zone no. 1	1610	45



		DIMENSIONS mm	
EQUATOR PROFILE	$l_1$	1200	
	$l_2$		
	$l_3$		
	$t$	169	
	$t_s$	65	
	$t_g$		
	$t_{11}$	47	
	$t_{12}$	57	
SKIRT	$h_x$	2300	
	Aluminium	$h_a$	2100
		$t_a$	65
	Stainless st. Stiffener	$h_{st}$	2500
		$t_{st}$	56
	Low temp. steel Ring Stiffener	$h_s$	7930
$t_s$		35	
	Vert. Stiffener	T 600x200x20x30 Spacing 3965 HP 370x15 Spacing 1140	

Scantlings taken from [22, p.9].

---

# Appendix C

## Email from Moss Maritime AS

**From:** Skogan Tor <Tor.Skogan@mosswww.com>  
**Sent:** Thursday, January 16, 2020 1:40 PM  
**To:** Vlad Cristea <vladc@stud.ntnu.no>  
**Cc:** Andersen Thormod <Thormod.Andersen@mosswww.com>  
**Subject:** RE: Questions regarding LNG Moss Rosenberg tank design

Hi,

See our replies inside your e-mail below.

Best regards  
Tor Skogan  
VP LNG, Moss Maritime AS  
Mobile [REDACTED]

---

**From:** Svien Toril <Toril.Svien@mosswww.com> **On Behalf Of** Moss Maritime Mailbox  
**Sent:** Thursday, January 16, 2020 13:01  
**To:** Skogan Tor <Tor.Skogan@mosswww.com>  
**Cc:** Andersen Thormod <Thormod.Andersen@mosswww.com>  
**Subject:** FW: Questions regarding LNG Moss Rosenberg tank design

**From:** Vlad Cristea <vladc@stud.ntnu.no>  
**Sent:** torsdag 16. januar 2020 12:51  
**To:** Moss Maritime Mailbox <mossmaritime@mosswww.com>  
**Subject:** Questions regarding LNG Moss Rosenberg tank design

My name is Vlad Cristea, and I am a student at NTNU. I am writing my Master Thesis about transport of liquid hydrogen on sea, and one of the task is to study models of LNG carriers. I am sending this mail, according to the telephonic discussion we had earlier today, describing my request. There are some general questions I have, and I would really appreciate an answer followed probably by some illustrations/articles describing the design. The questions are as follows:

1. What type of materials are used for the tank cover of the LNG Moss Rosenberg design? I found out that it is usually steel. However, I would like the exact type of steel used (f. eks Steel A588 Grande 50) so that it is possible for me to find the mechanical and physical properties of the material.  
**Moss:** Normal shipbuilding carbon steel (mild steel), NV-A grade with yield strength 235 MPa.
2. What is a typical thickness of the cylindrical skirt which supports the inner spherical tank, and again what are the exact materials used to construct this component? Some illustrations would be highly appreciated. **Moss:** The upper part of the skirt is aluminium (maybe 2 meters high, thickness 65mm), then follows a middle part of 304 stainless steel (maybe 2.5 meters high, thickness 45mm) and the lower part which is welded to the ship double bottom is high strength carbon steel (maybe 7-8 meters high, thickness 30mm). Note that dimensions and thickness of the plates in the skirt depend on tank dimensions and weight, so will be designed for each size/design of the tank.




---

## Appendix D

# Material Properties

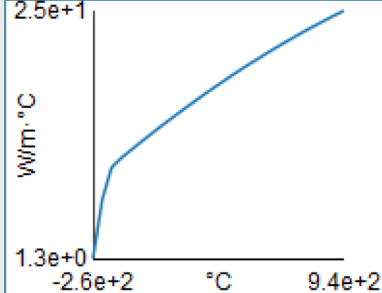
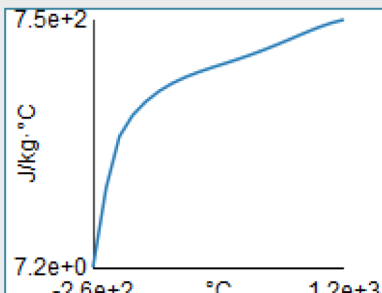
All the data of the materials is taken directly from the the simulation program, ANSYS Workbench.

### D.1 Low carbon steel

Density	7850 kg/m <sup>3</sup>
<b>Structural</b> 	
▼ Isotropic Elasticity	
Derive from	Young's Modulus and Poisson's Ratio
Young's Modulus	2.1e+11 Pa
Poisson's Ratio	0.29
Bulk Modulus	1.6667e+11 Pa
Shear Modulus	8.1395e+10 Pa
Isotropic Secant Coefficient of Thermal Expansion	1.22e-05 1/°C
Tensile Ultimate Strength	3.65e+08 Pa
Tensile Yield Strength	2.33e+08 Pa
<b>Thermal</b> 	
Isotropic Thermal Conductivity	52 W/m·°C
Specific Heat Constant Pressure	485 J/kg·°C
<b>Electric</b> 	
Isotropic Resistivity	1.44e-07 ohm·m

## D.2 AISI 316

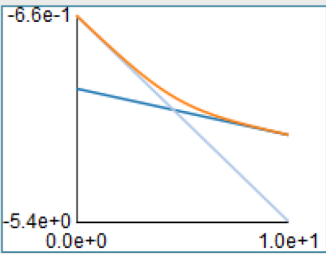
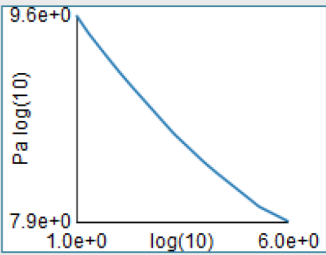
Density	7969 kg/m <sup>3</sup>
<b>Structural</b> <span style="float: right;">▼</span>	
Isotropic Elasticity	
Multilinear Isotropic Hardening	
▼ Isotropic Secant Coefficient of Thermal Expansion	
Coefficient of Thermal Expansion	
Zero-Thermal-Strain Reference Temperature	20 °C
S-N Curve	
Tensile Ultimate Strength	5.651e+08 Pa
Tensile Yield Strength	2.521e+08 Pa

Thermal	
Isotropic Thermal Conductivity	
Specific Heat Constant Pressure	
Electric	
Isotropic Resistivity	7.476e-07 ohm·m

### D.3 Type of polyurethane foam used on the external insulation in design A2

Density	39,800 kg/m <sup>3</sup>
<b>Structural</b> <span style="float: right;">▼</span>	
▼ Isotropic Elasticity	
Derive from	Young's Modulus and Poisson's Ratio
Young's Modulus	2,583e+07 Pa
Poisson's Ratio	0,29980
Bulk Modulus	2,1503e+07 Pa
Shear Modulus	9,9361e+06 Pa
Isotropic Secant Coefficient of Thermal Expansion	2,191e-05 1/°C
Tensile Ultimate Strength	5,399e+05 Pa
Tensile Yield Strength	3,989e+05 Pa
<b>Thermal</b> <span style="float: right;">▼</span>	
Isotropic Thermal Conductivity	0,028980 W/m·°C
Specific Heat Constant Pressure	1127,0 J/kg·°C
<b>Electric</b> <span style="float: right;">▼</span>	
Isotropic Resistivity	1e+12 ohm·m

## D.4 Structural Steel

Density	7850,0 kg/m <sup>3</sup>
<b>Structural</b> <span style="float: right;">▼</span>	
▼ Isotropic Elasticity	
Derive from	Young's Modulus and Poisson's Ratio
Young's Modulus	2e+11 Pa
Poisson's Ratio	0,30000
Bulk Modulus	1,6667e+11 Pa
Shear Modulus	7,6923e+10 Pa
Isotropic Secant Coefficient of Thermal Expansion	1,2e-05 1/°C
Compressive Ultimate Strength	0 Pa
Compressive Yield Strength	2,5e+08 Pa
Strain-Life Parameters	
S-N Curve	
Tensile Ultimate Strength	4,6e+08 Pa
Tensile Yield Strength	2,5e+08 Pa
<b>Thermal</b> <span style="float: right;">▼</span>	
Isotropic Thermal Conductivity	60,500 W/m·°C
Specific Heat Constant Pressure	434,00 J/kg·°C
<b>Electric</b> <span style="float: right;">▼</span>	
Isotropic Resistivity	1,7e-07 ohm·m
<b>Magnetic</b> <span style="float: right;">▼</span>	
Isotropic Relative Permeability	10000

---

# Appendix E

## Dimensions of the designs

### E.1 Preliminary design (P1)

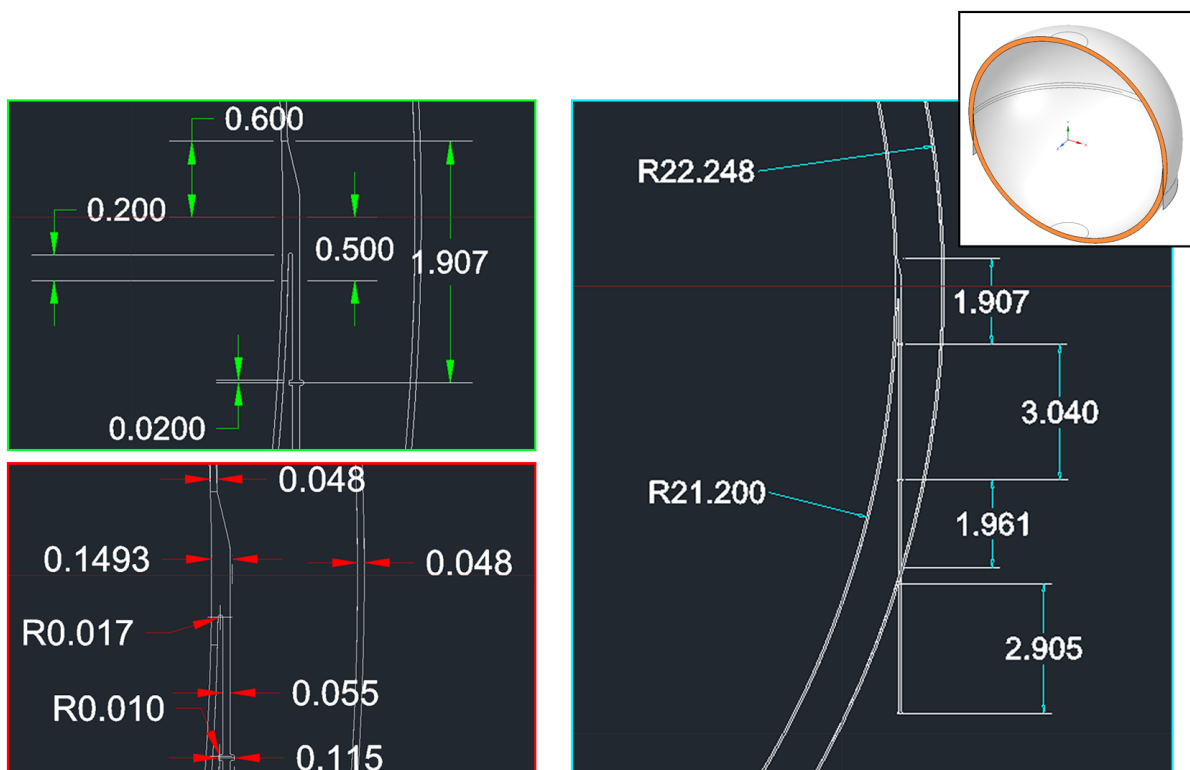


Figure E.1: Dimensions of the preliminary design P1 [m]



## E.2 Alternative design (A1)

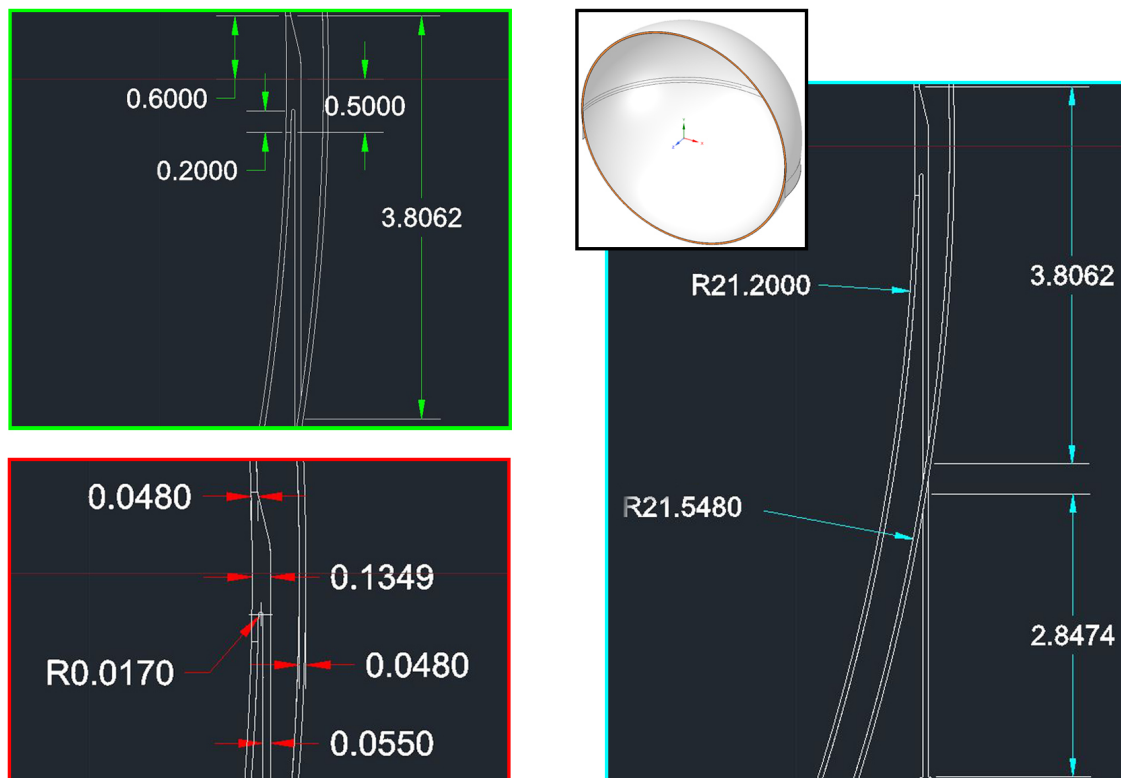


Figure E.2: Dimensions of the alternative design A1 [m]

### E.3 Alternative design (A2)

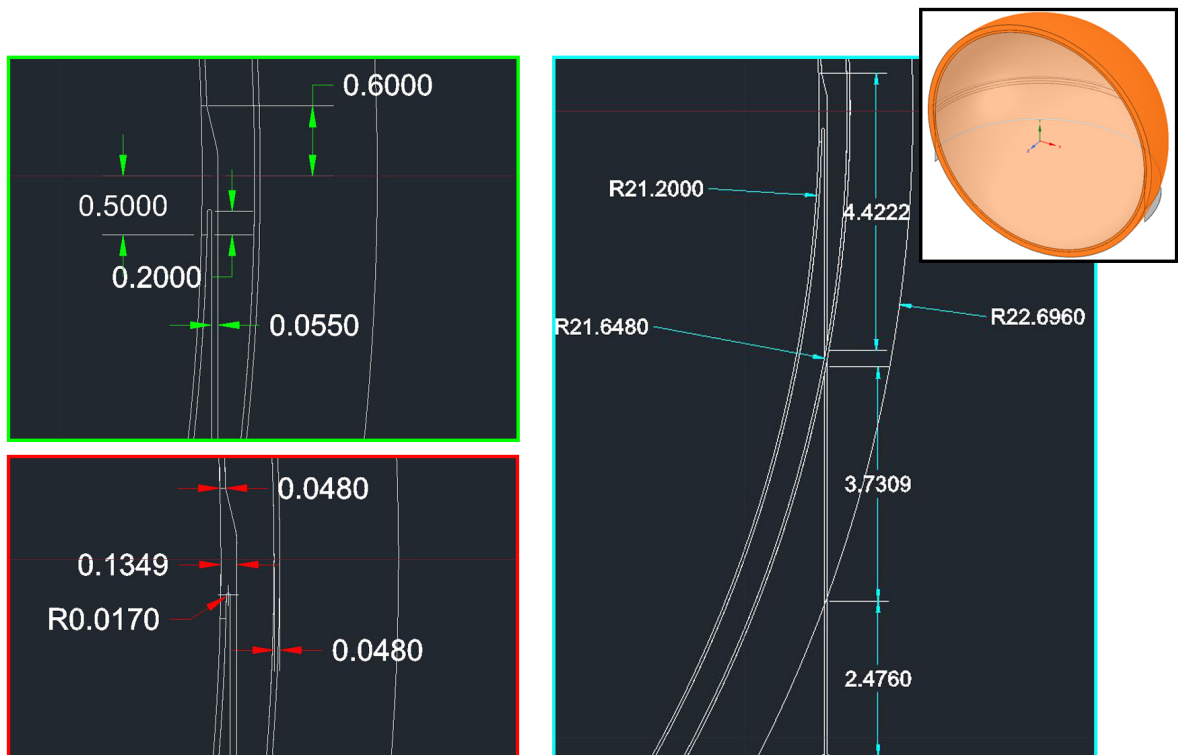


Figure E.3: Dimensions of the alternative design A2 [m]

---

## Appendix F

# Results from validatory simulations

### F.1 Results from simulations with different mesh patterns and symmetry setups

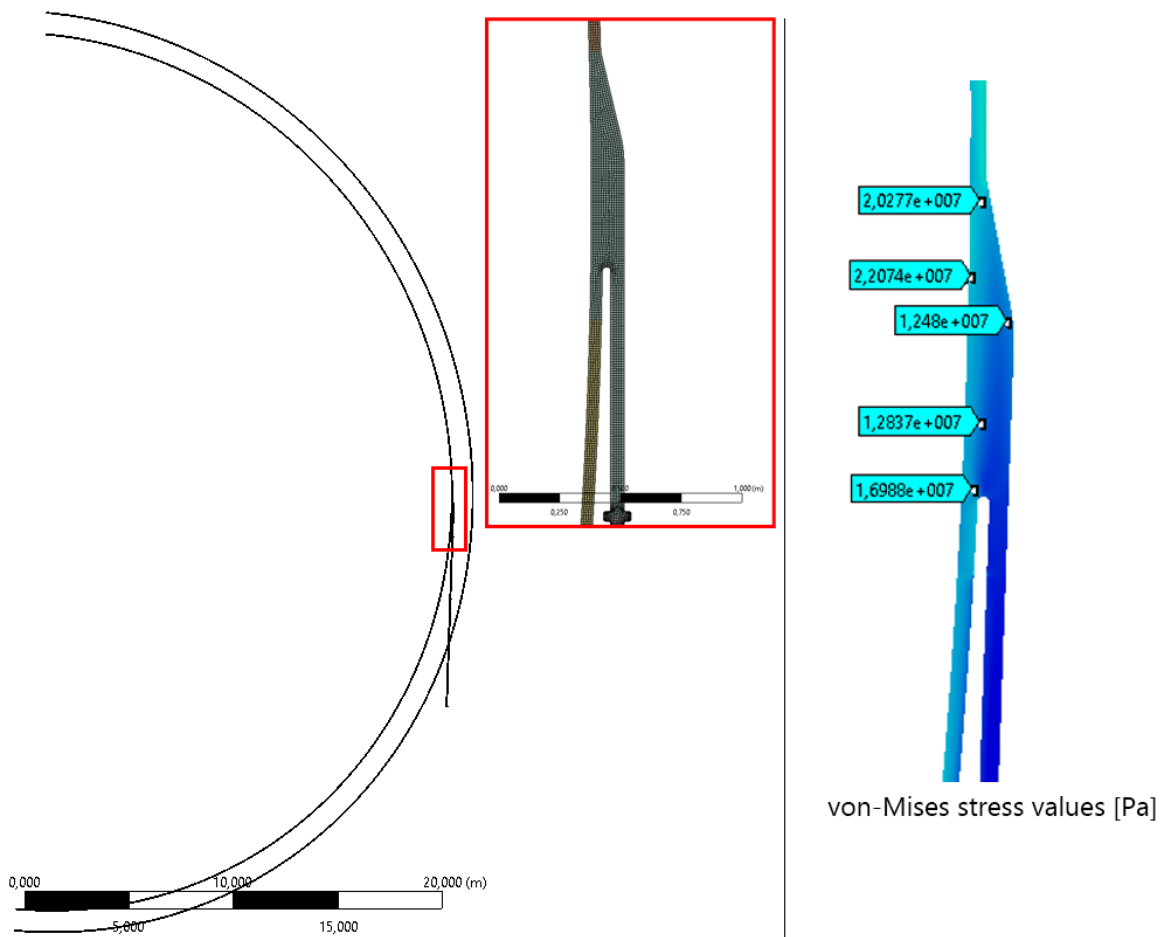


Figure F.1: Setup 1 (2D-axisymmetry): mesh representation and results

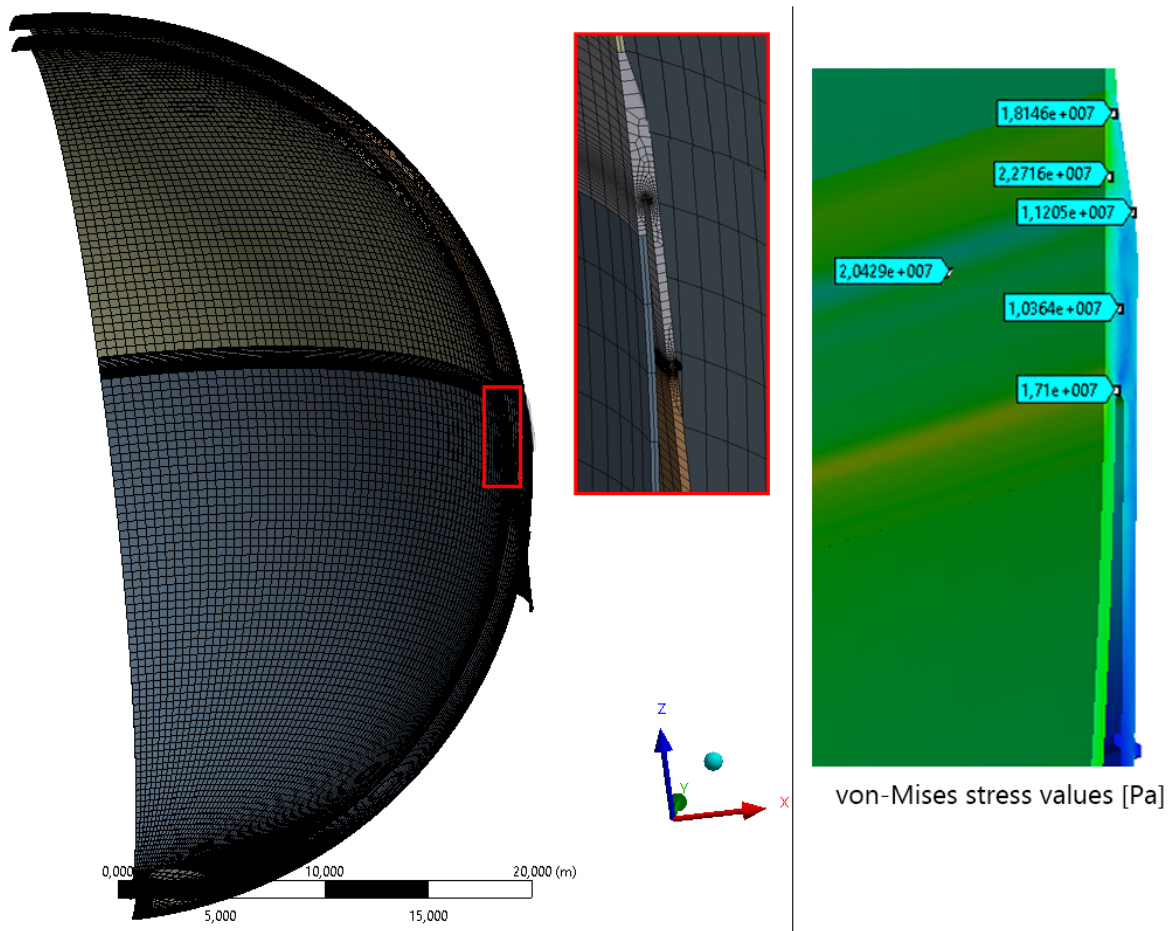


Figure F.2: Setup 2 (Cyclic-symmetry): mesh representation and results

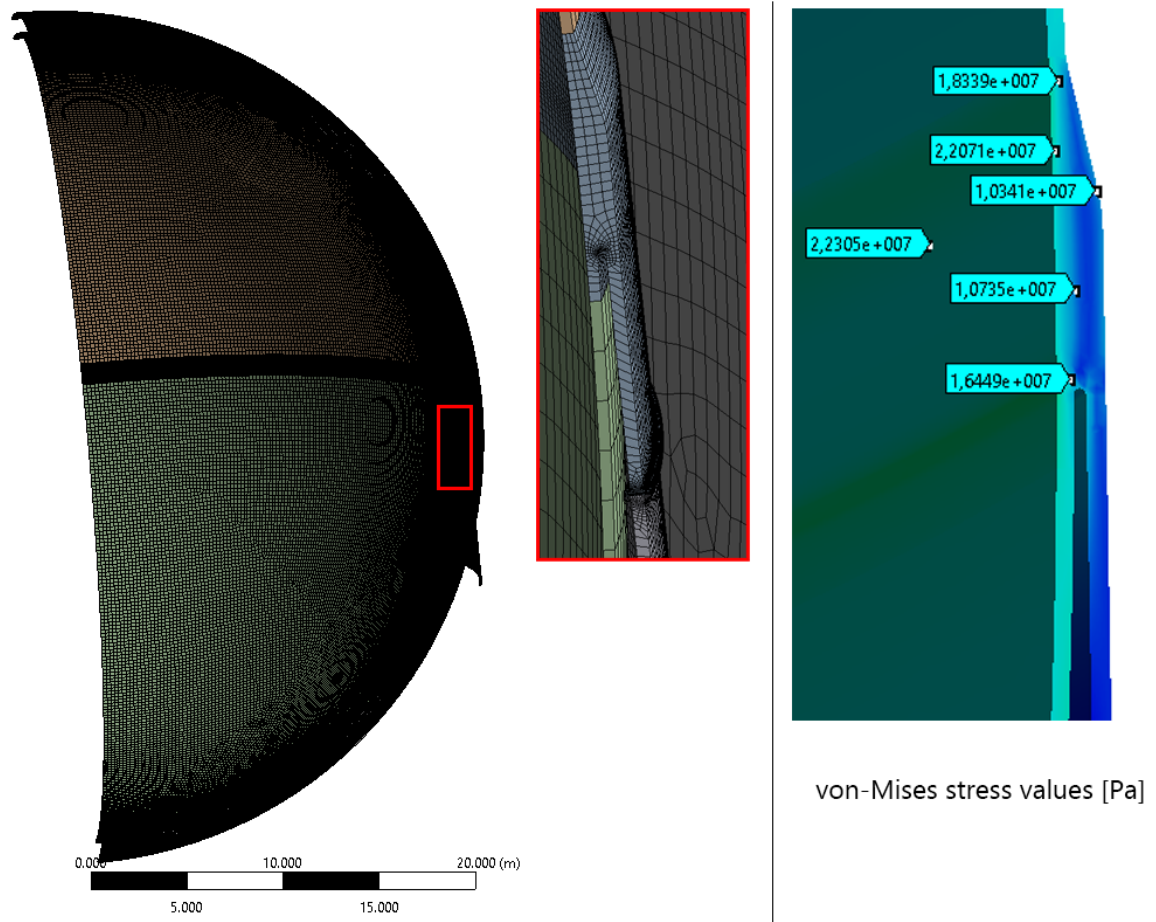


Figure F.3: Setup 3 (High quality mesh): mesh representation and results

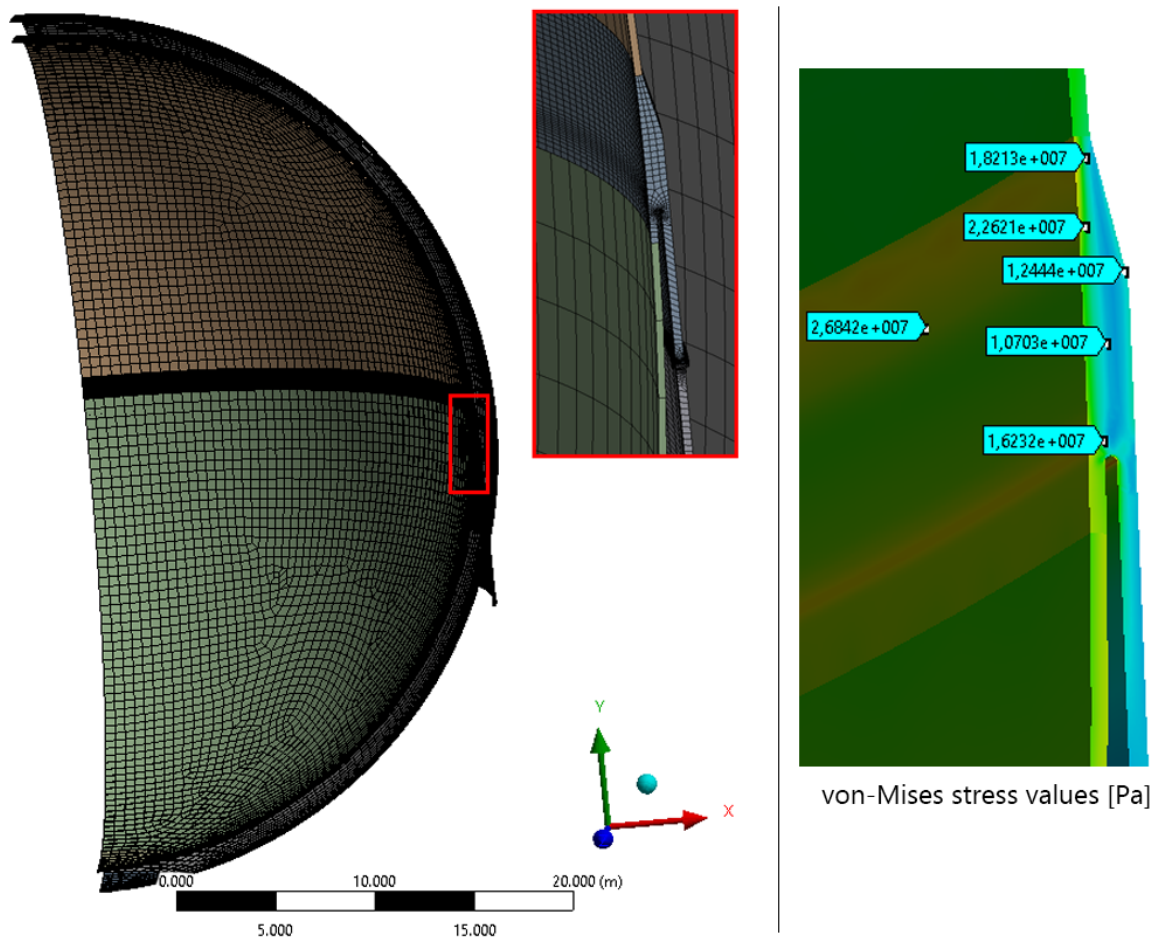


Figure F.4: Setup 4 (Most favourable option): mesh representation and results

## F.2 Results from Simulation C1

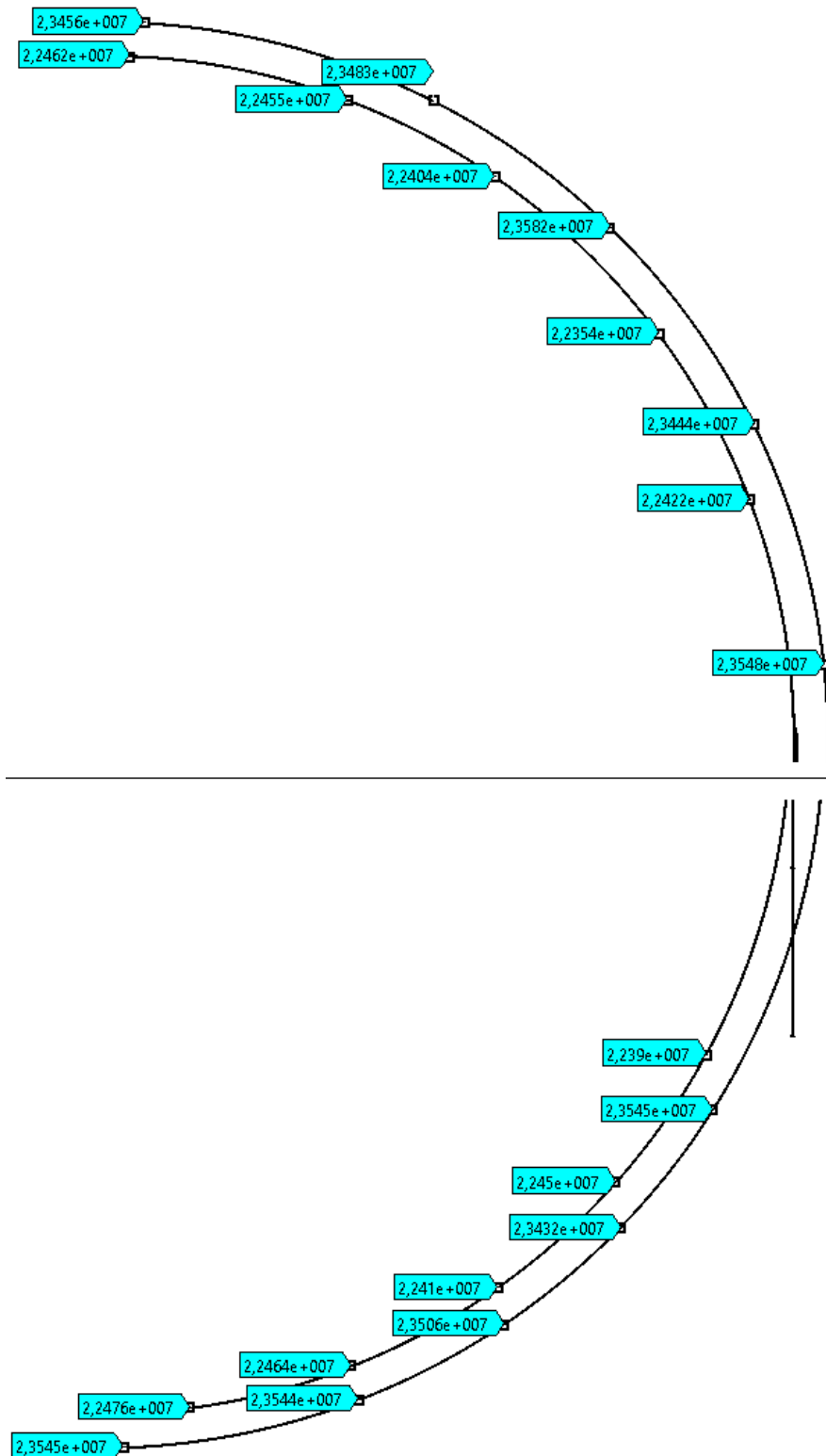


Figure F.5: Results from Simulation C1 for 3D-design [Pa]

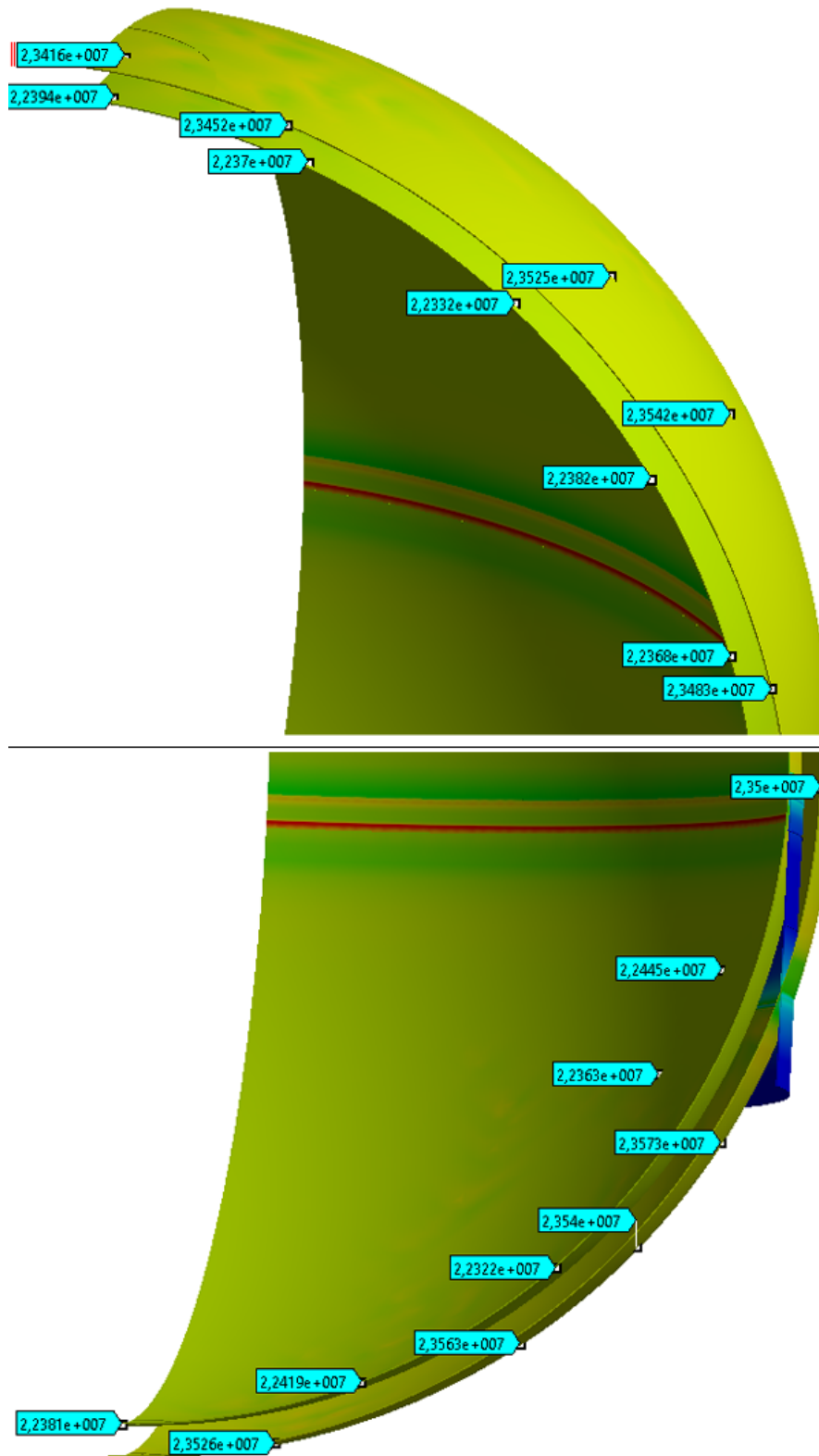


Figure F.6: Results from Simulation C1 for 3D-design [Pa]



### F.3 Results from Simulation C2

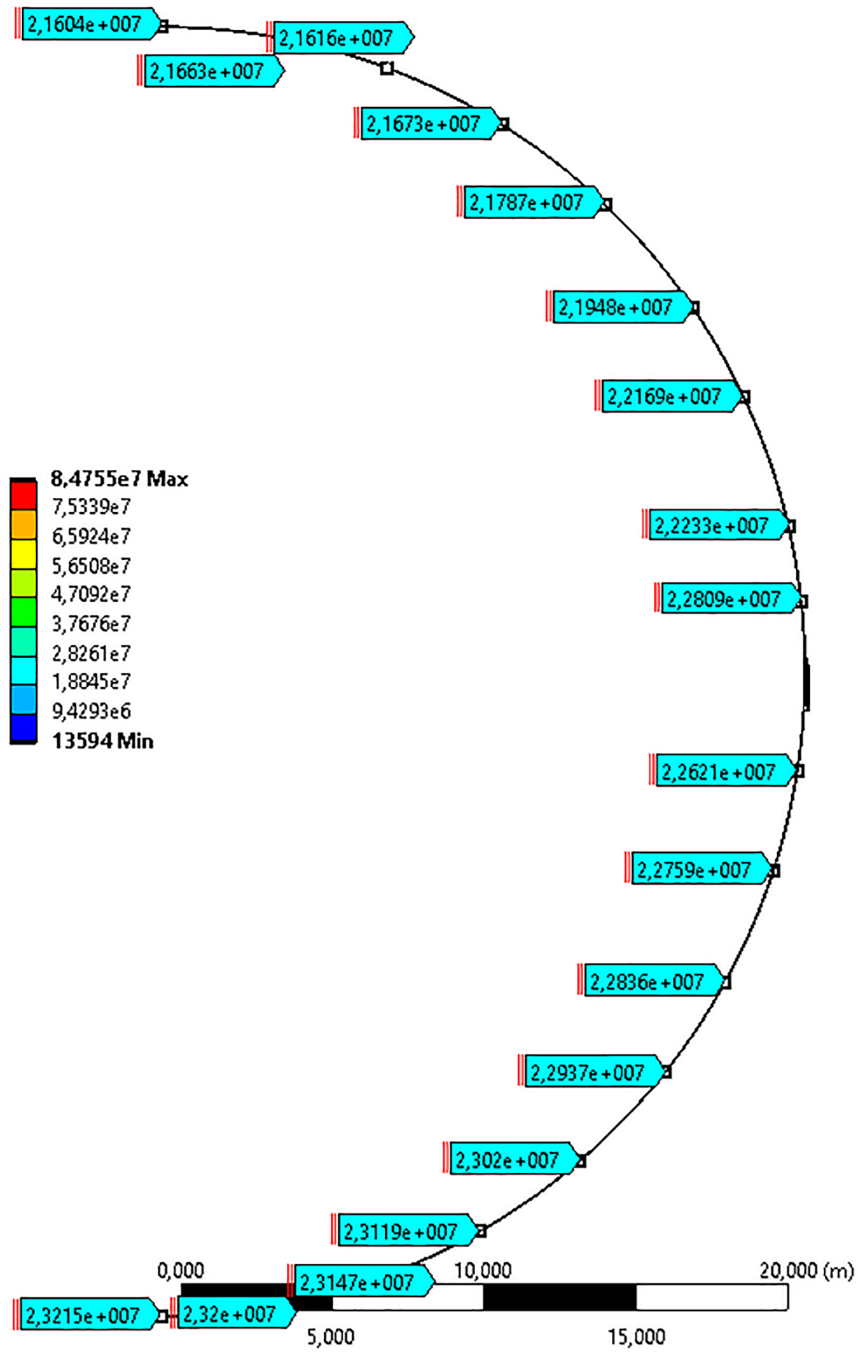


Figure F.7: Results from Simulation C2 for 2D-design [Pa]

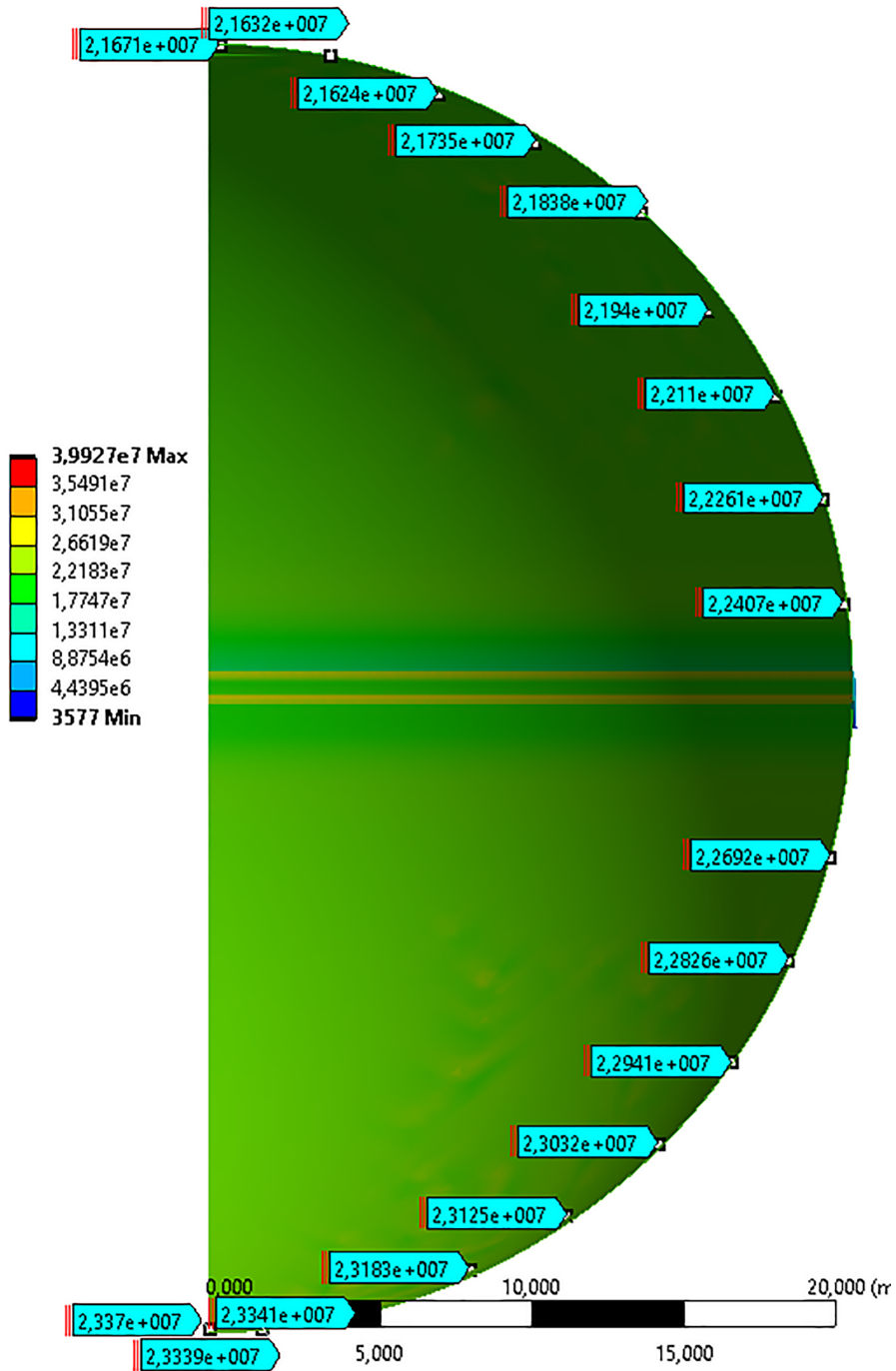


Figure F.8: Results from Simulation C2 for 3D-design [Pa]

### F.4 Results from Simulation C3

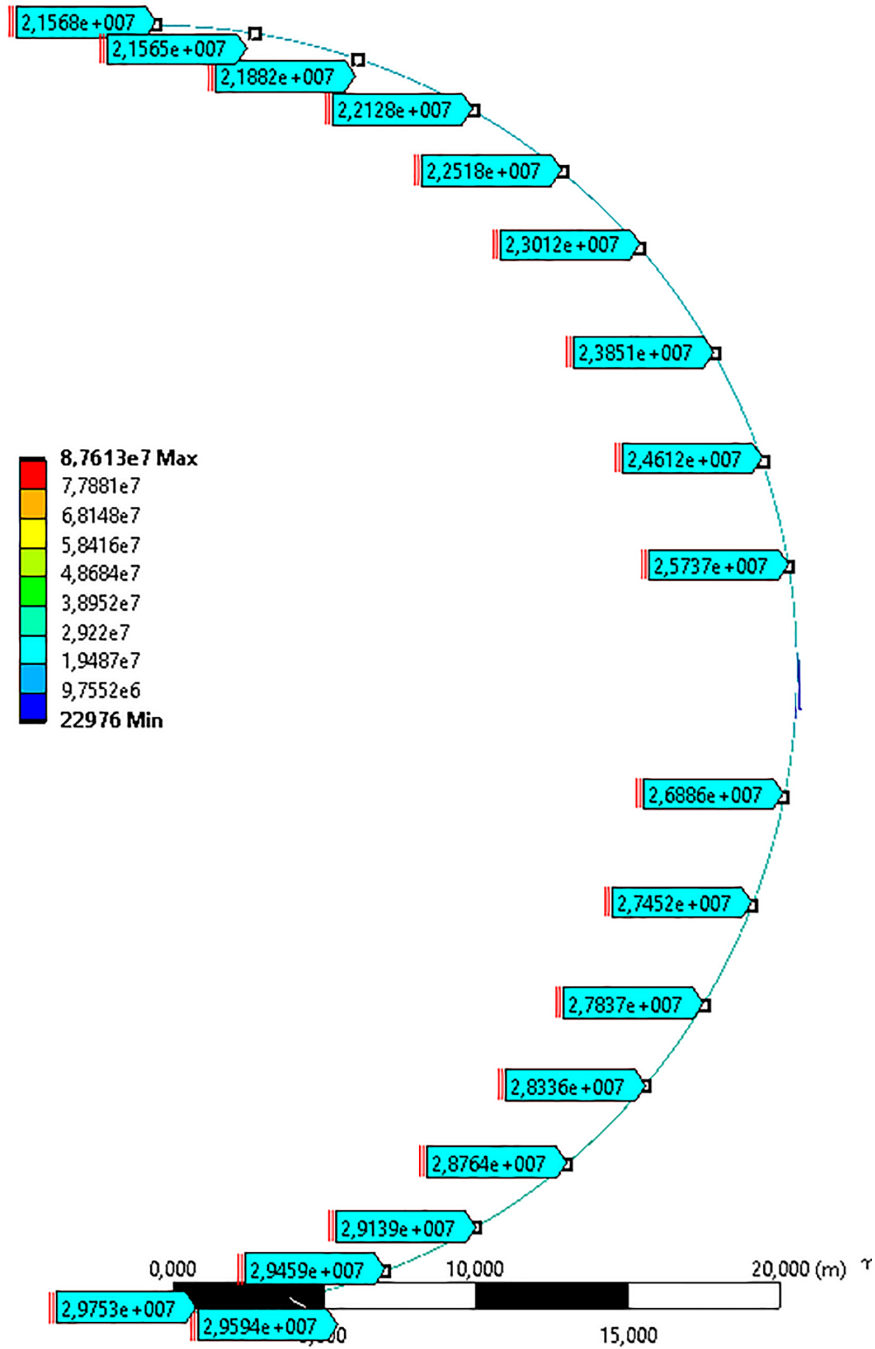


Figure F.9: Results from Simulation C3 for 2D-design [Pa]

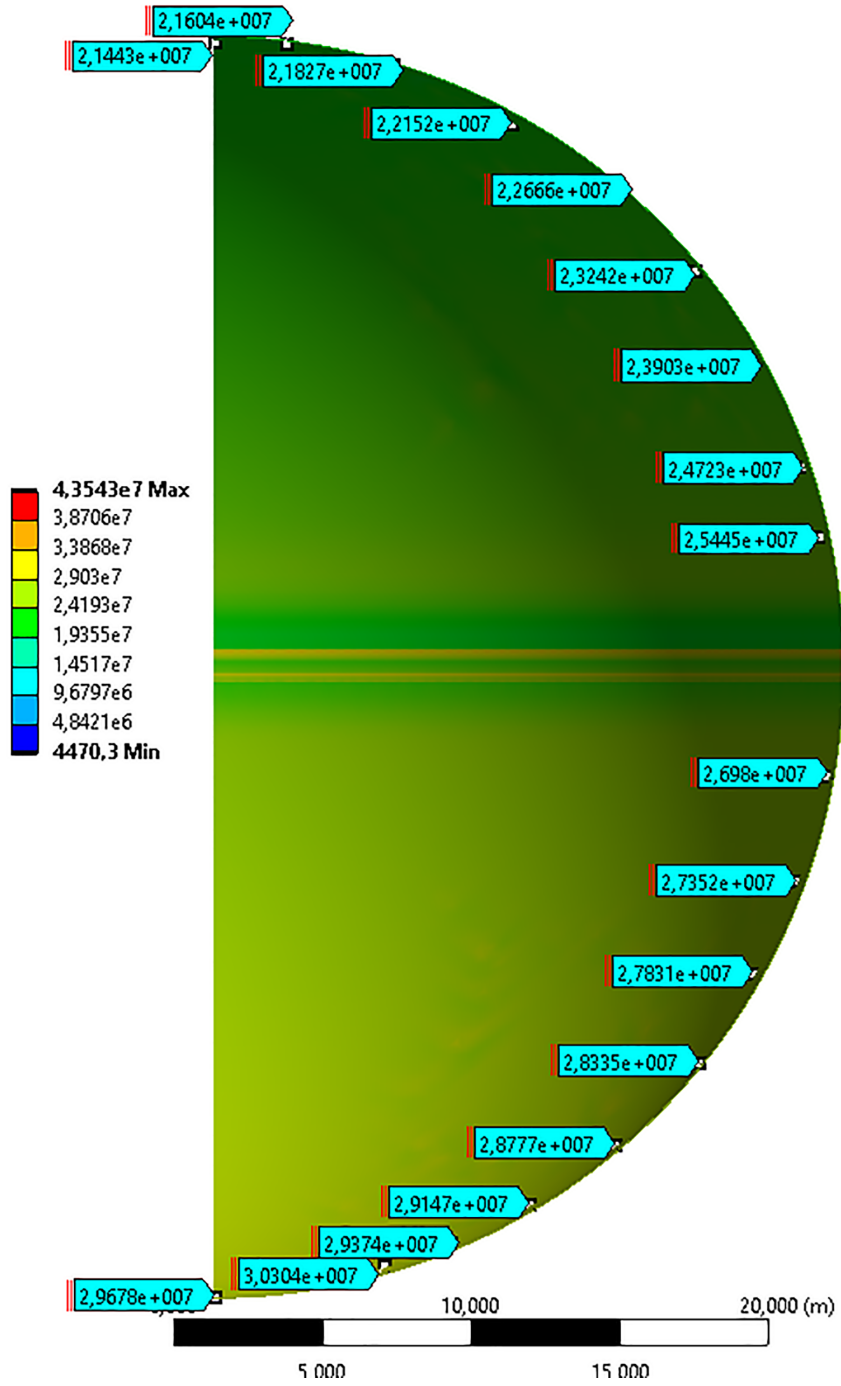


Figure F.10: Results from Simulation C3 for 3D-design [Pa]

---

## Appendix G

# Resulted stresses from simulation of the preliminary design

### G.1 Results from PS1

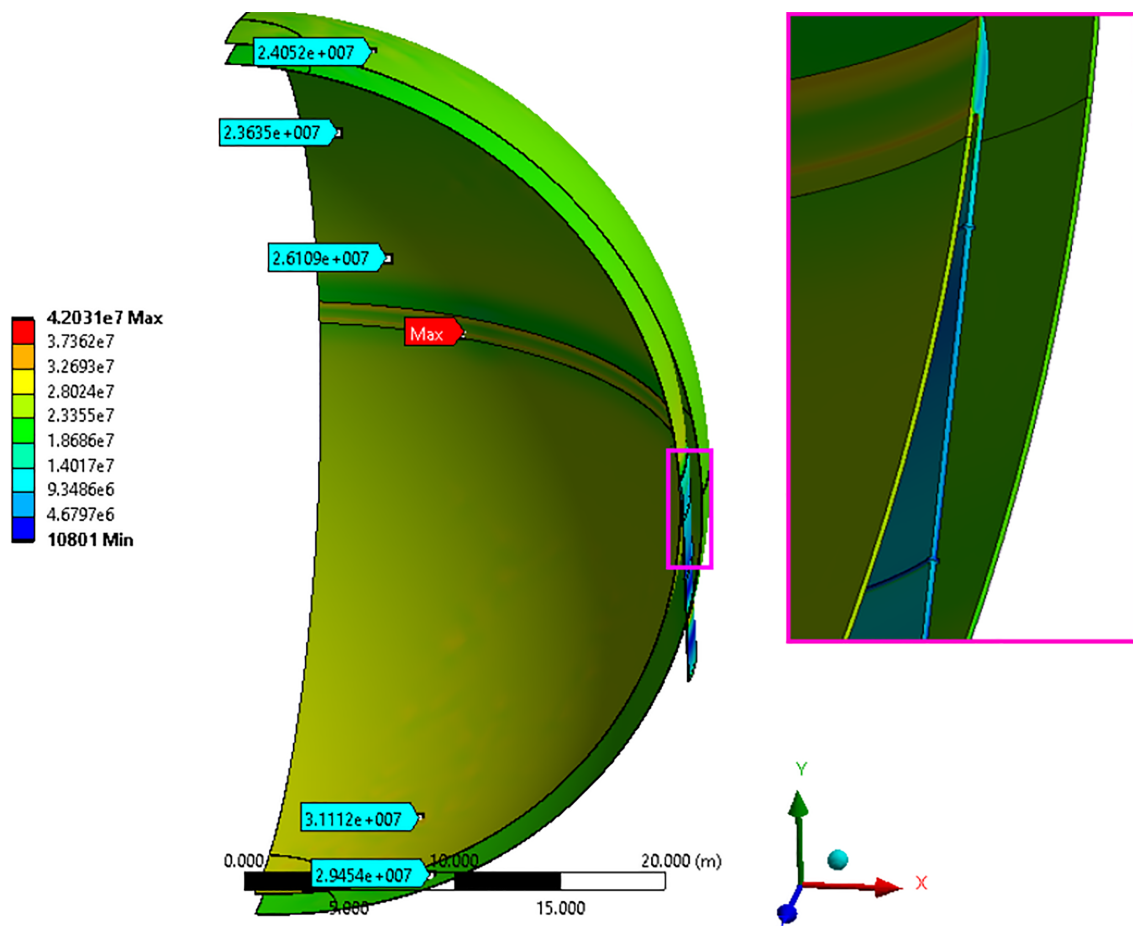


Figure G.1: PS1: von-Mises Stress [Pa]

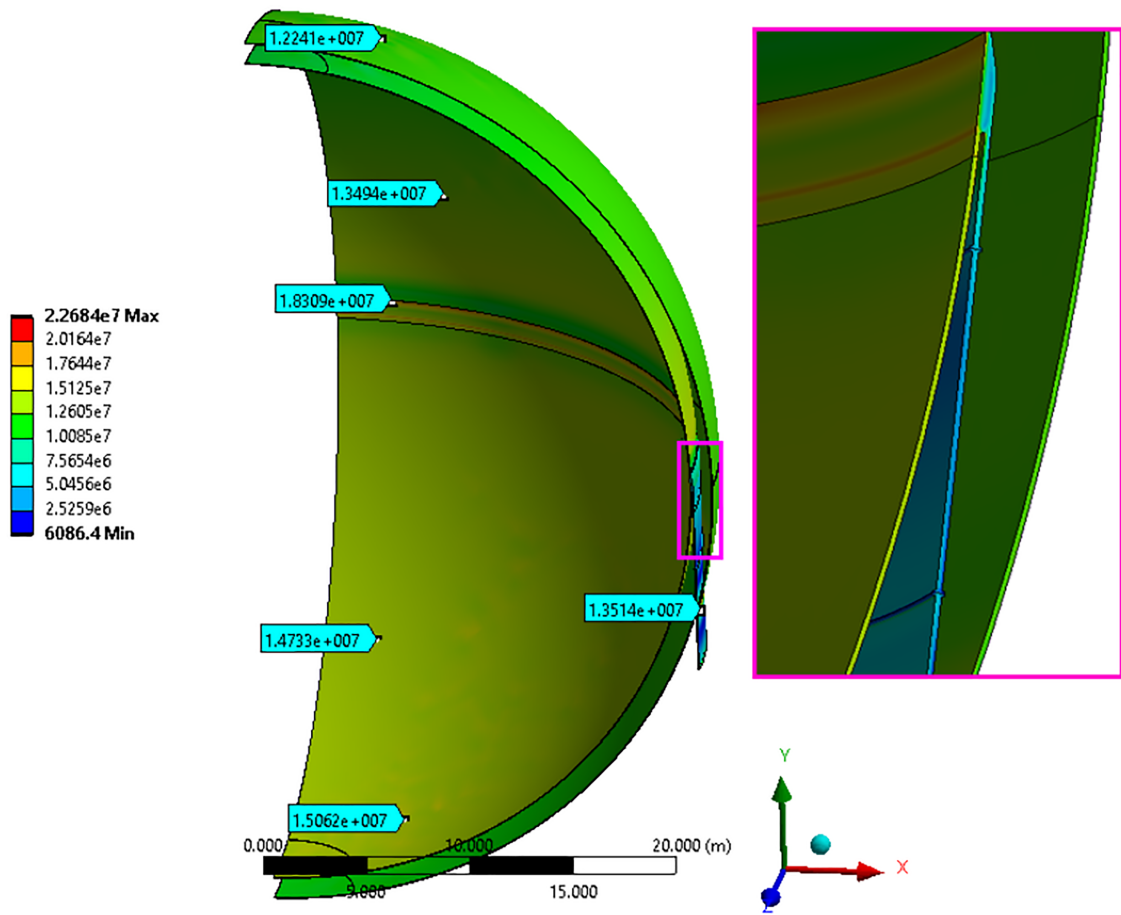


Figure G.2: PS1: Maximum Shear stress [Pa]

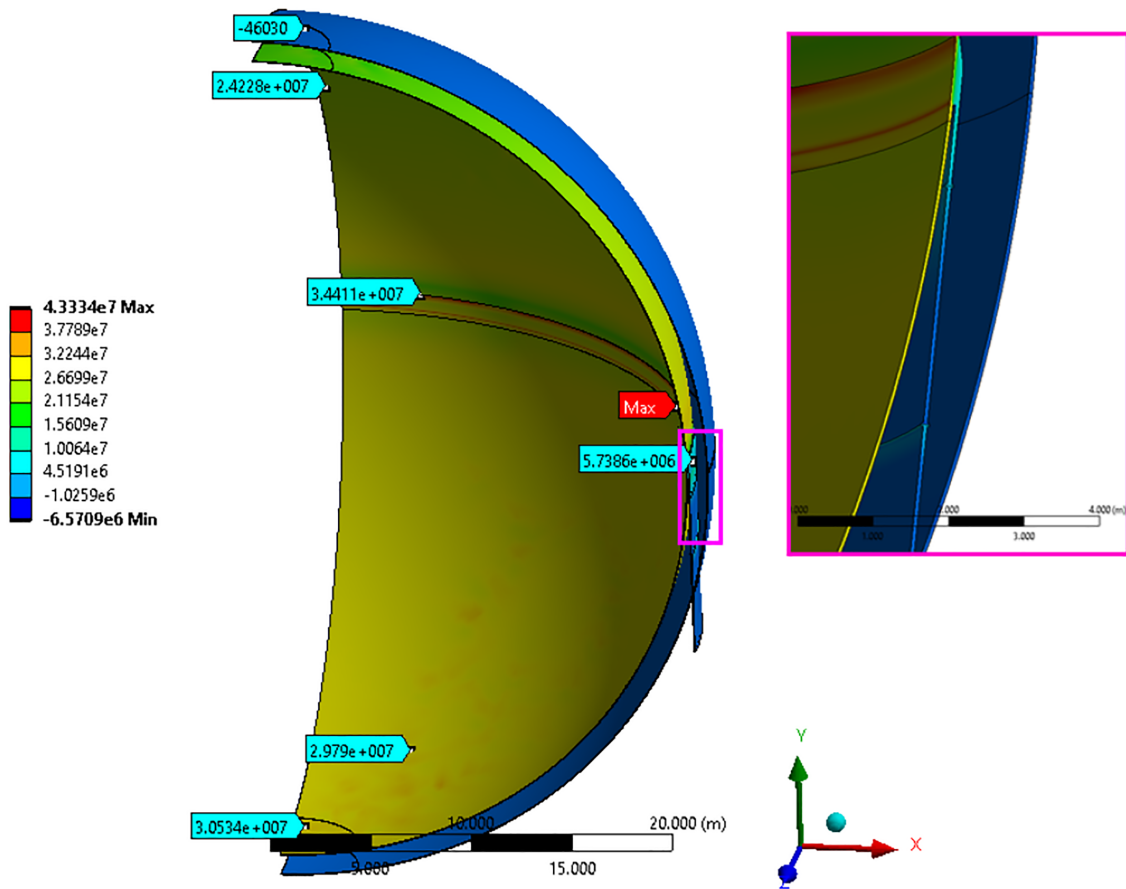


Figure G.3: PS1: Maximum Principal stress [Pa]

## G.2 Results from PS2

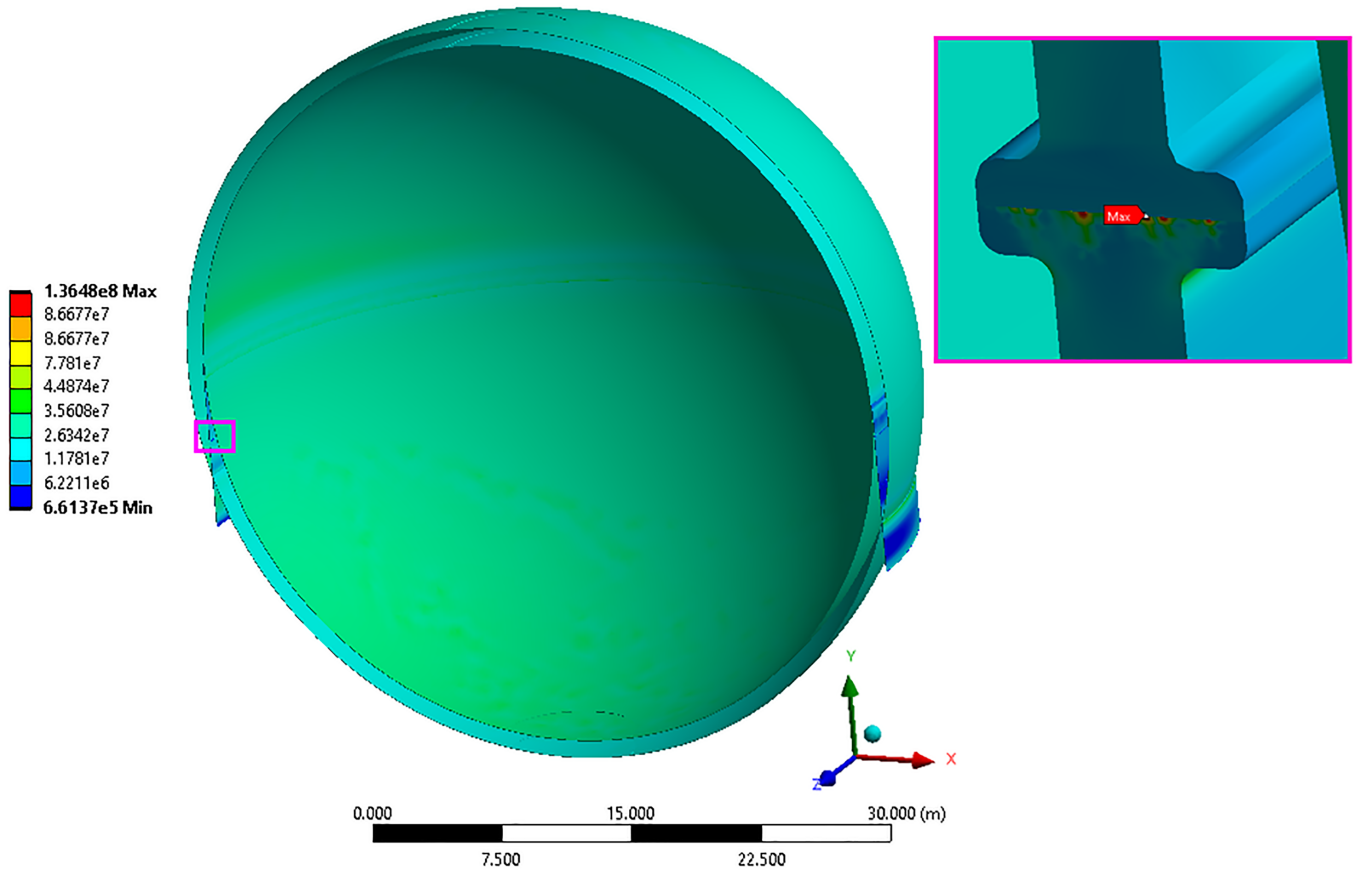


Figure G.4: PS2: von-Mises Stress [Pa]



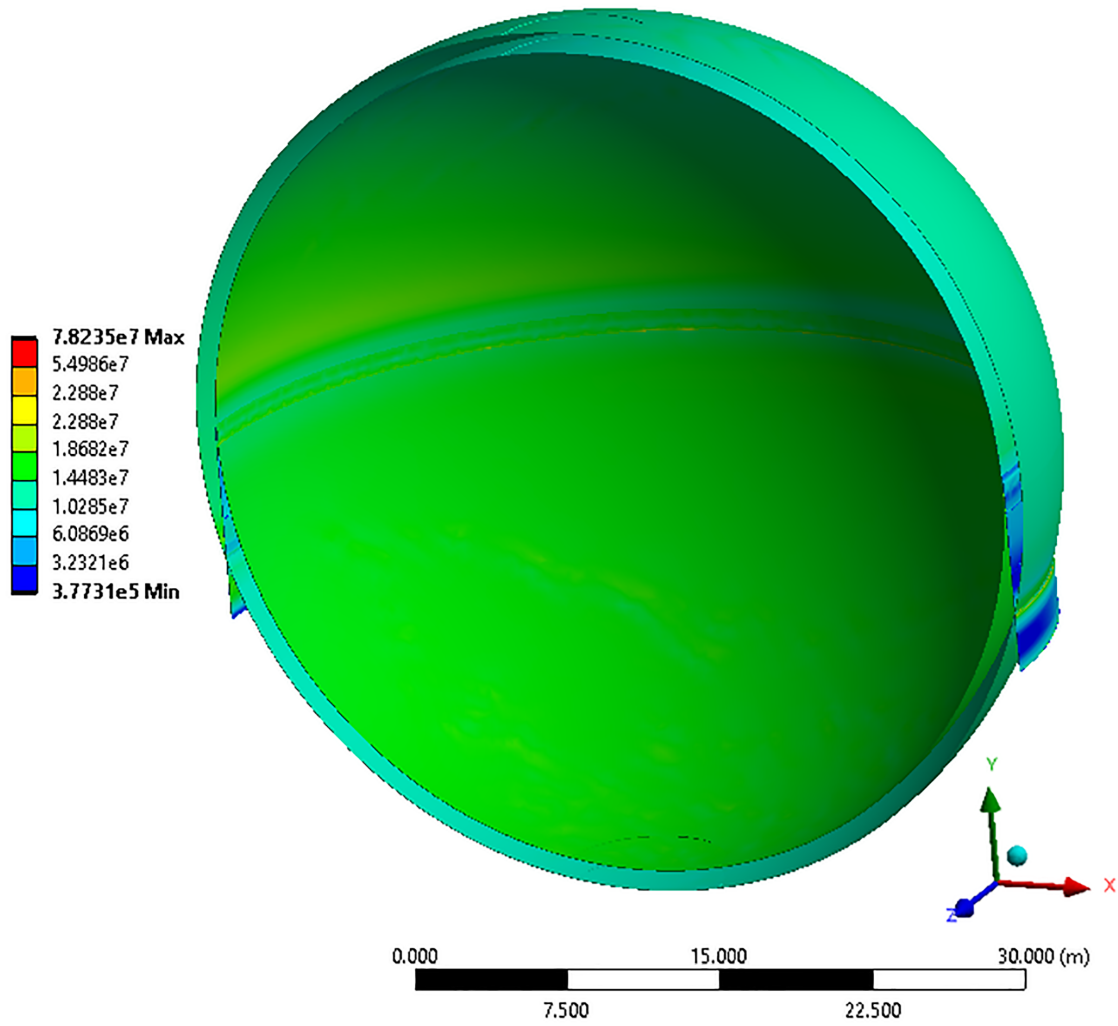


Figure G.5: PS2: Maximum Shear stress [Pa]

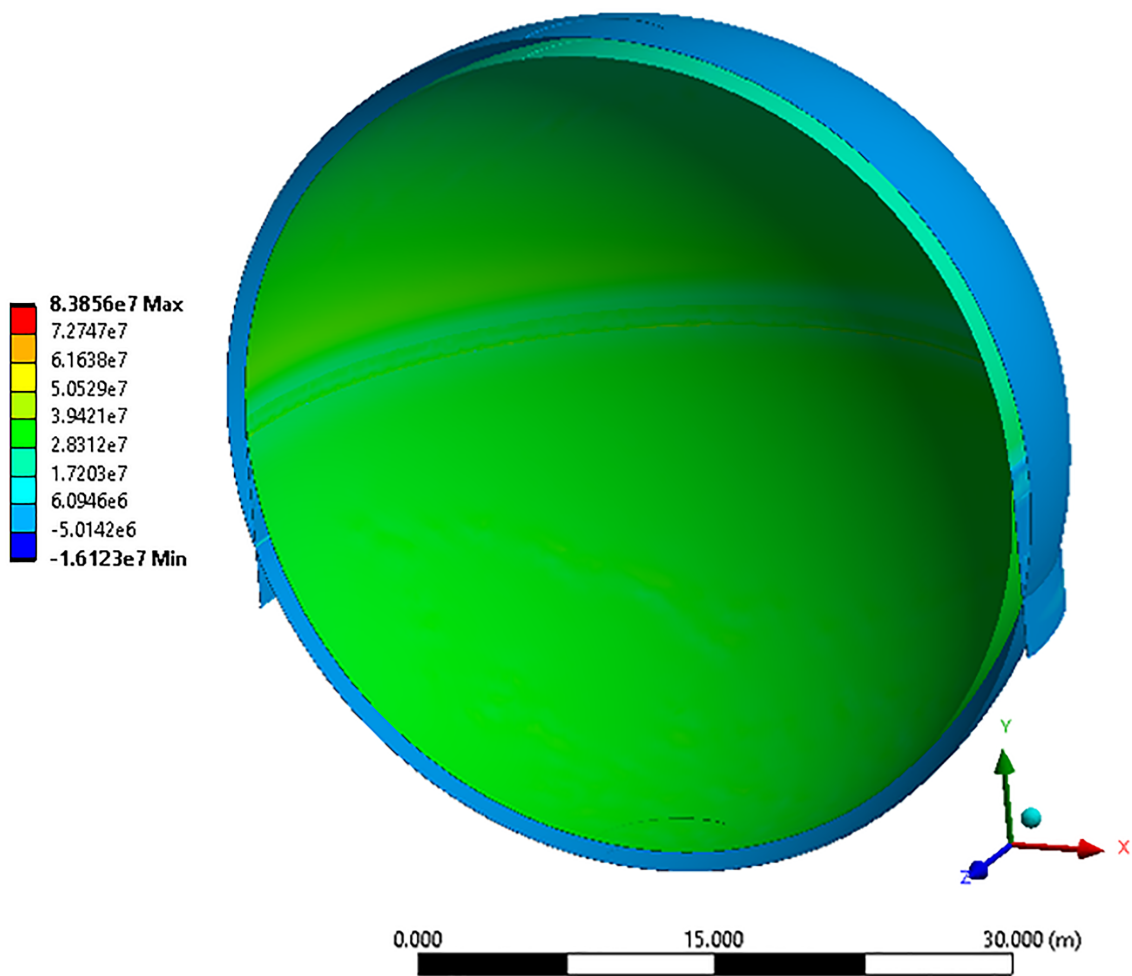


Figure G.6: PS2: Maximum Principal stress [Pa]

### G.3 Results from PS3

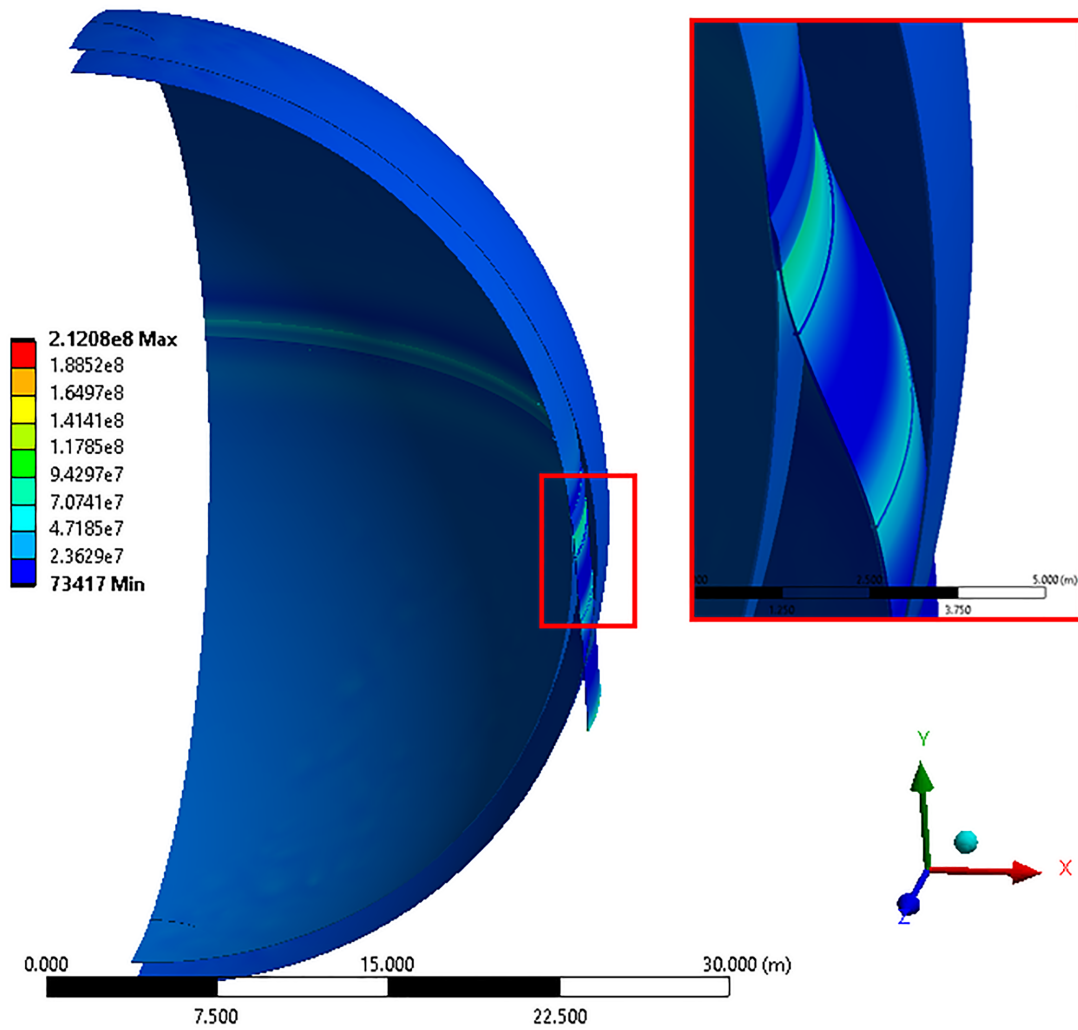


Figure G.7: PS3: von-Mises Stress [Pa]

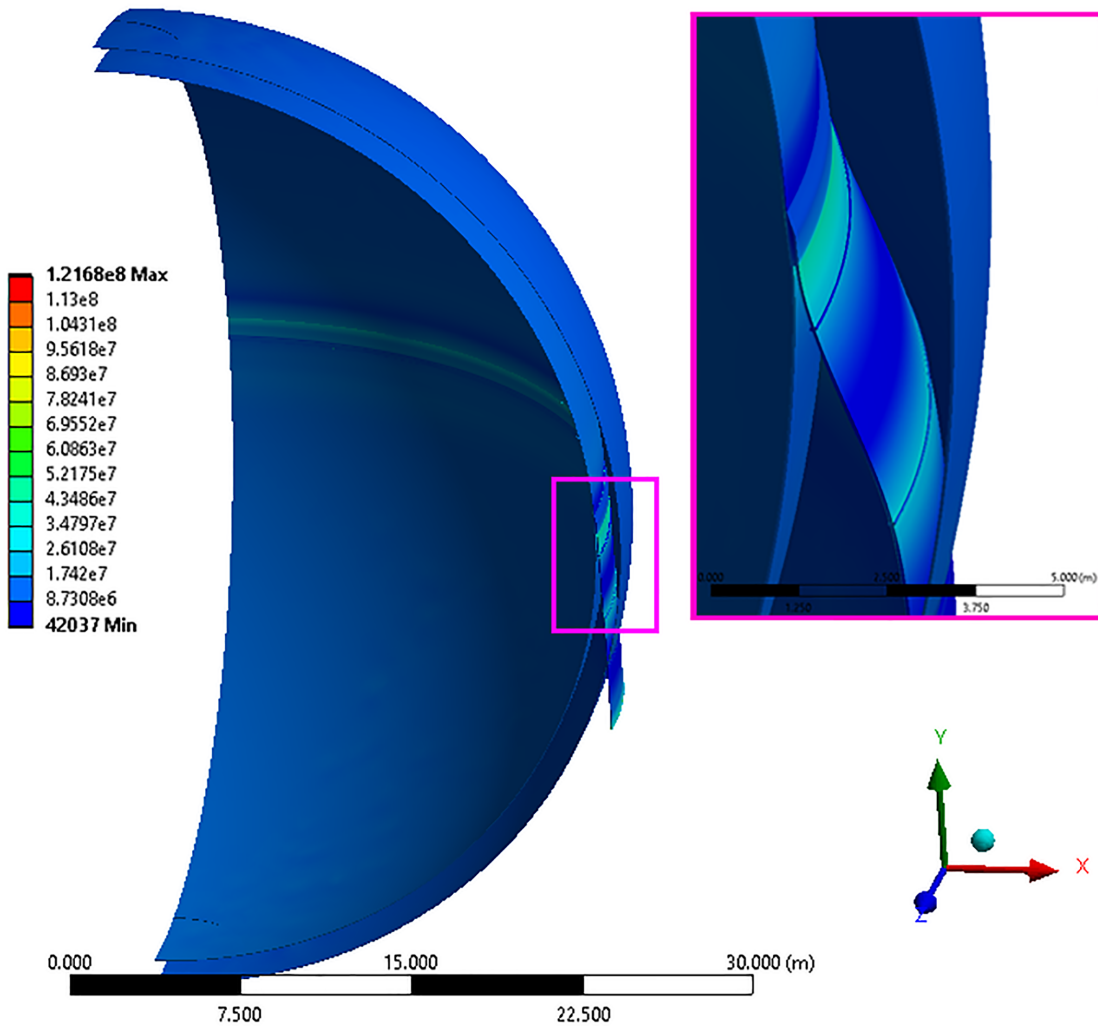


Figure G.8: PS3: Maximum Shear stress [Pa]

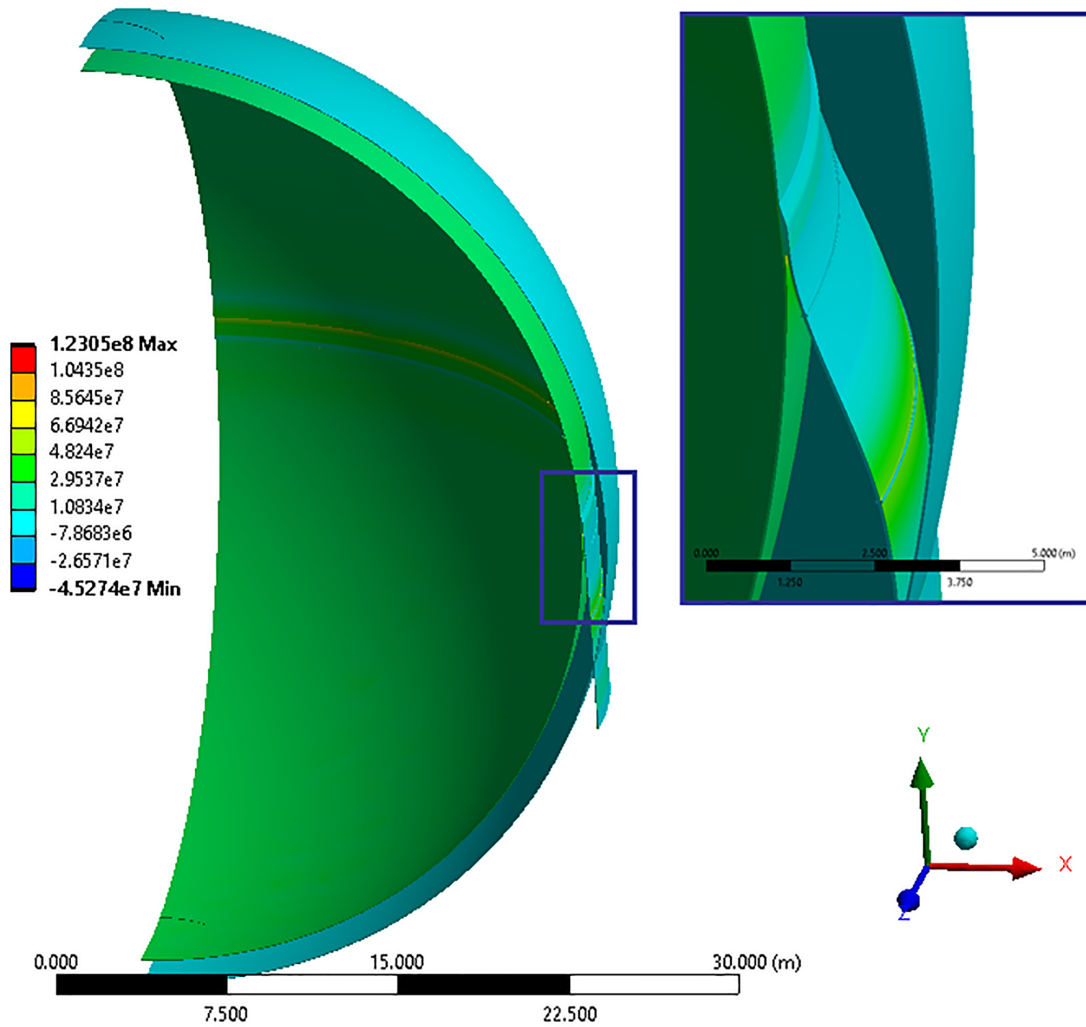


Figure G.9: PS3: Maximum Principal stress [Pa]

---

## Appendix H

# Resulted stresses from simulation of the alternative designs

### H.1 Results from A1

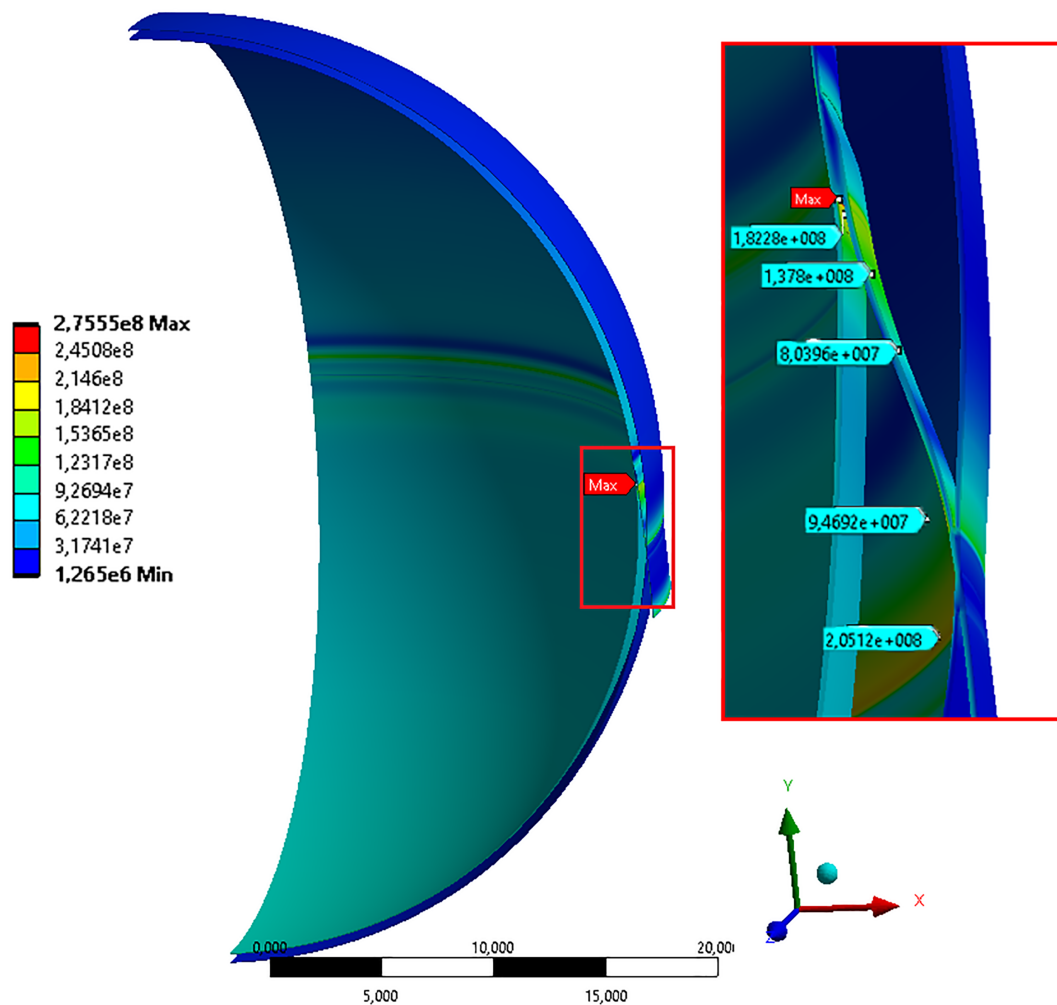


Figure H.1: A1: von-Mises Stress [Pa]

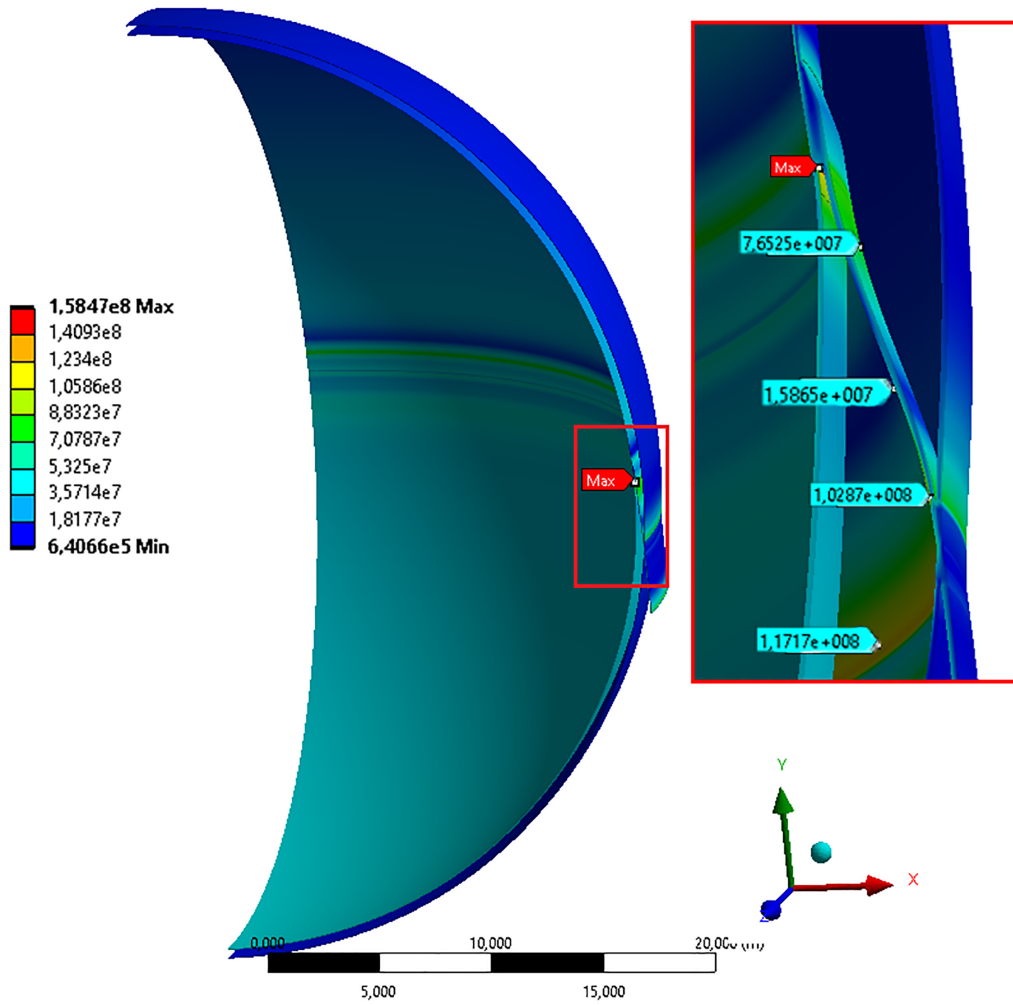


Figure H.2: A1: Maximum Shear stress [Pa]

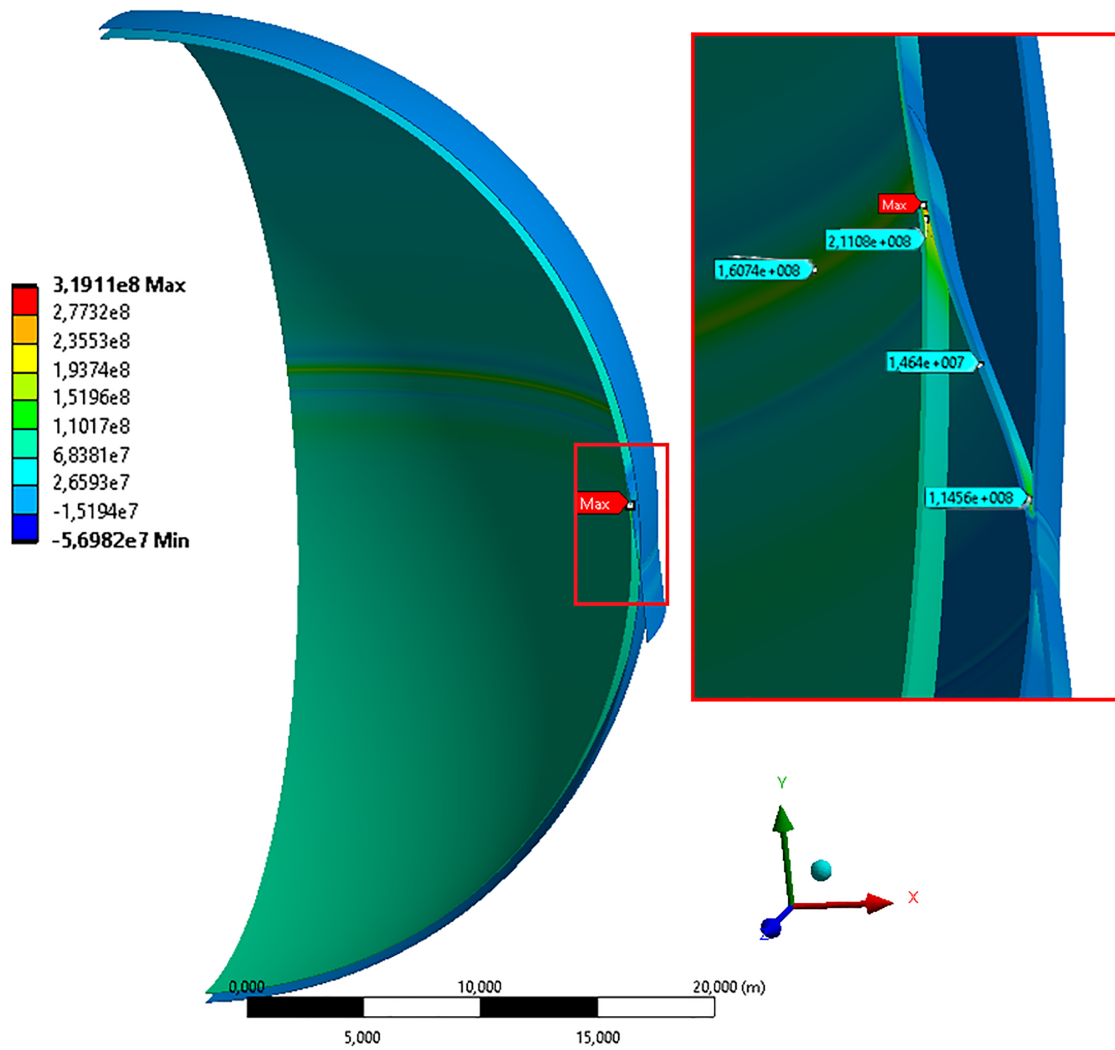


Figure H.3: A1: Maximum Principal stress [Pa]



## H.2 Results from A2

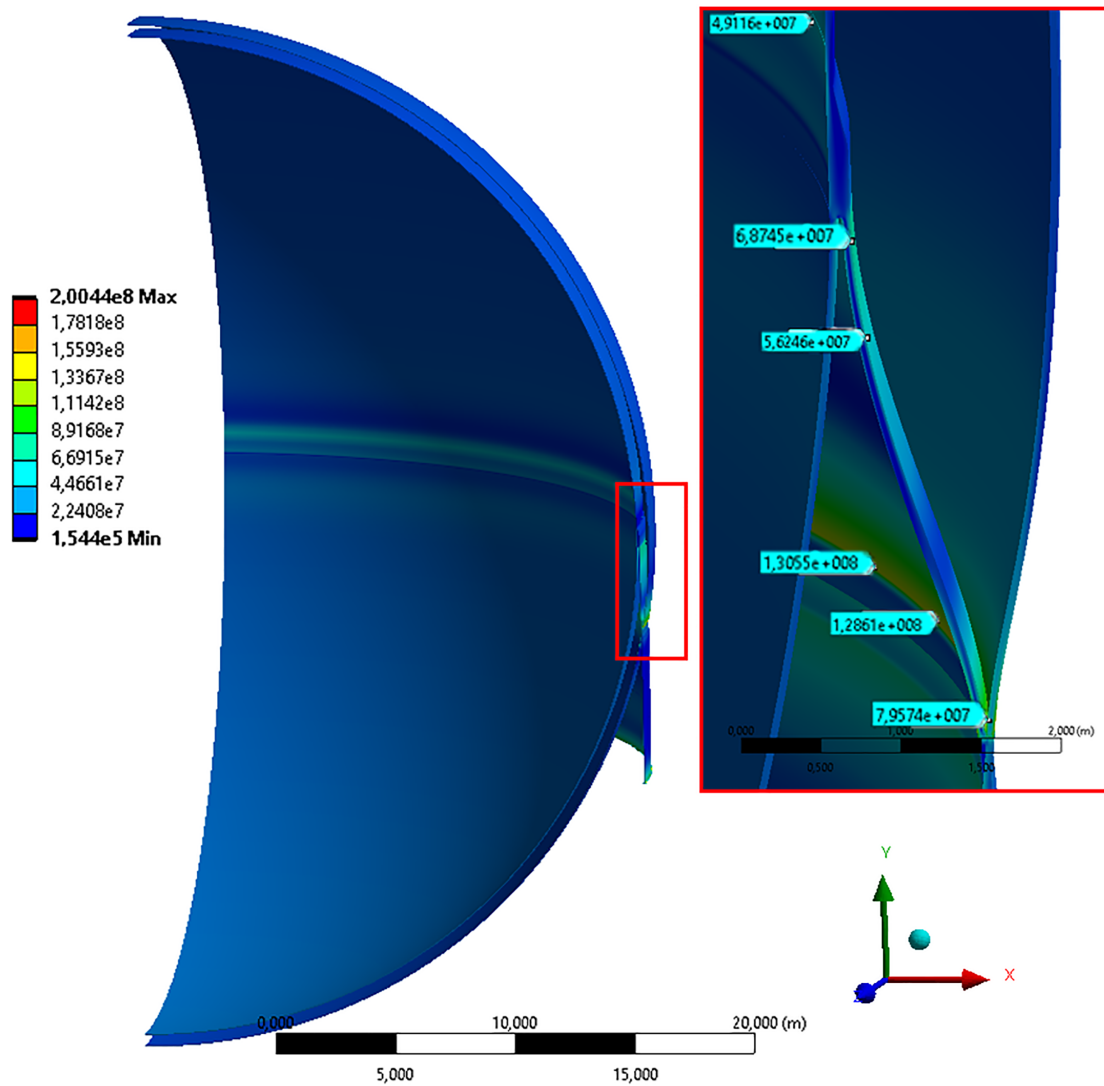


Figure H.4: A2: von-Mises Stress [Pa]

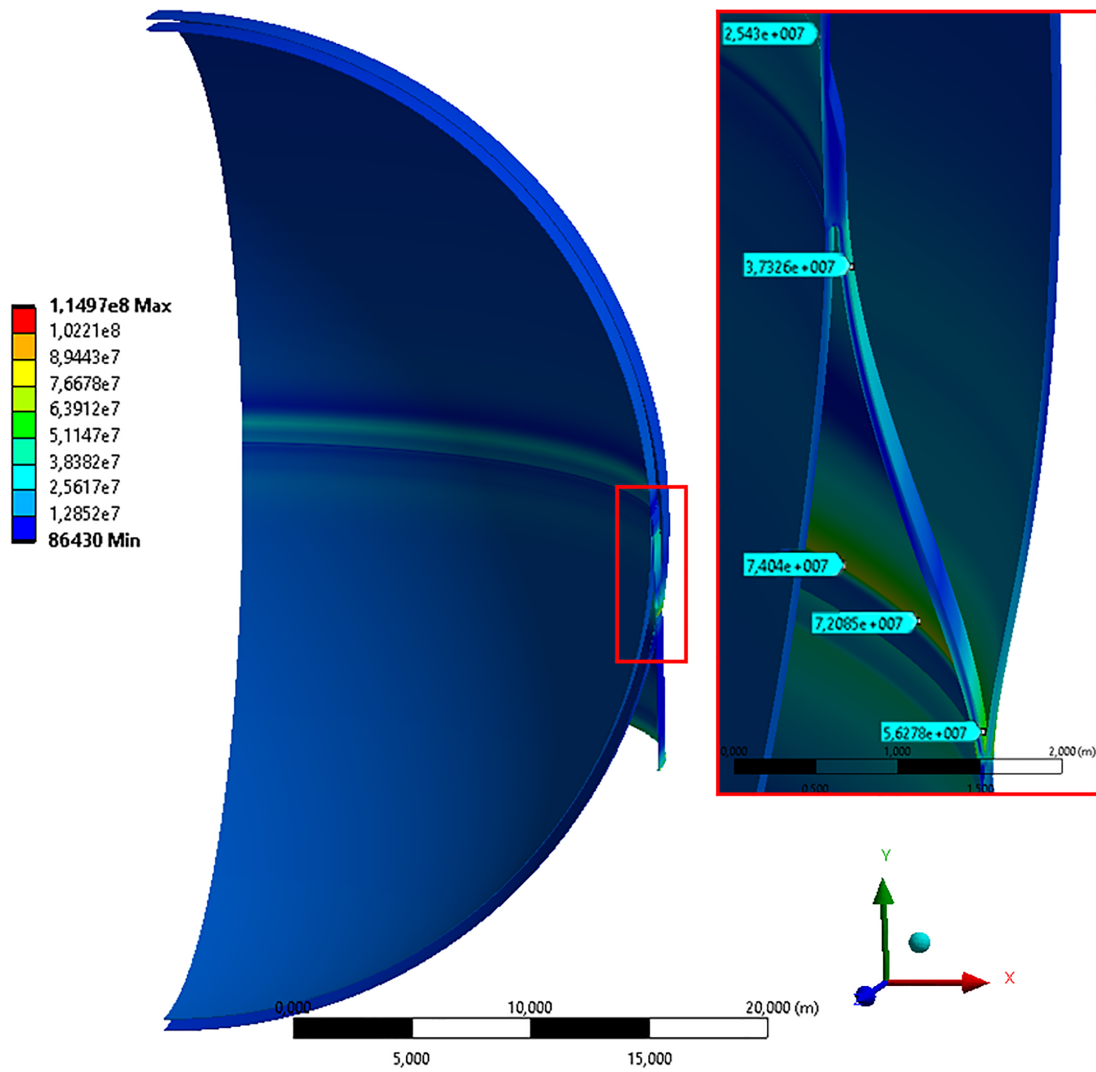


Figure H.5: A2: Maximum Shear stress [Pa]

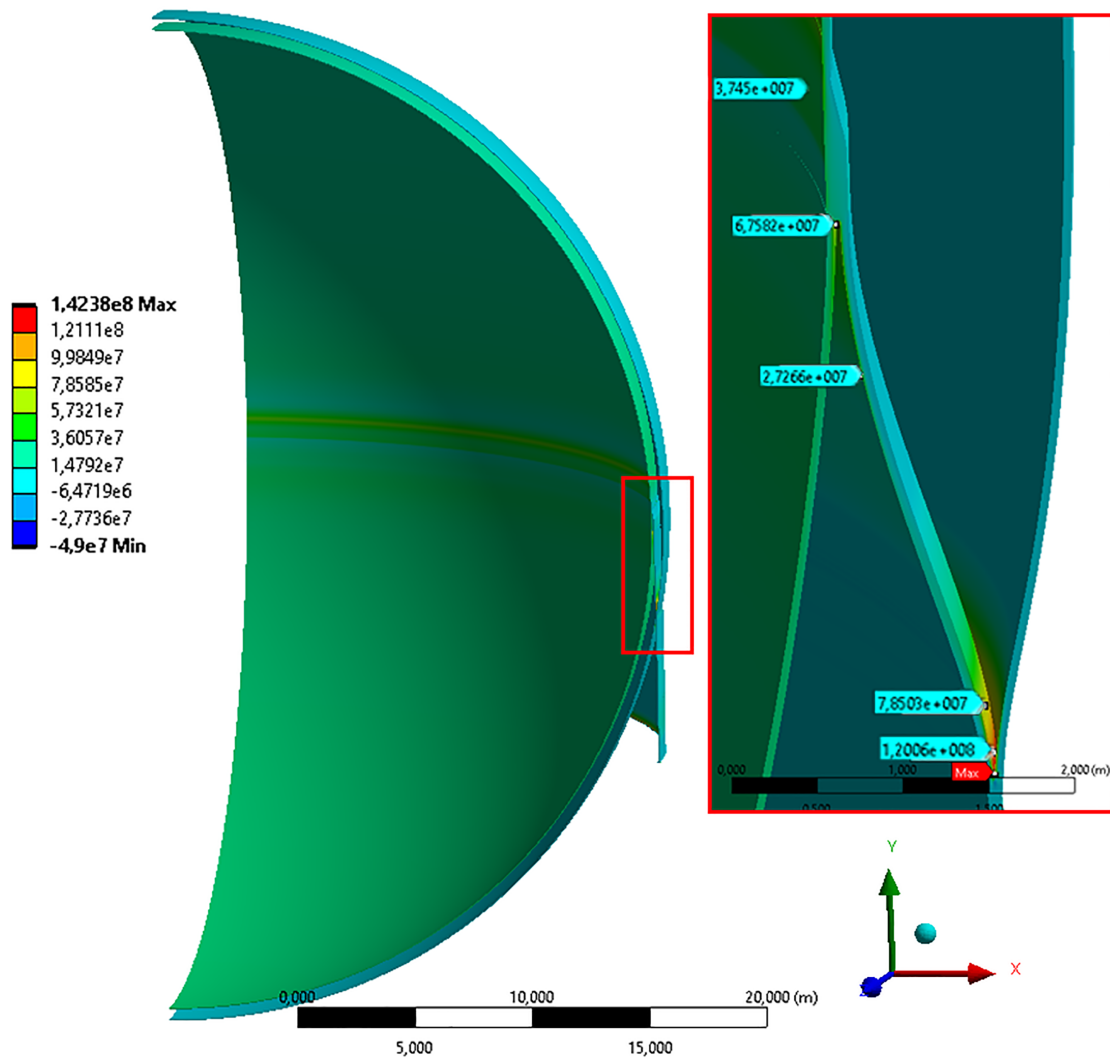


Figure H.6: A2: Maximum Principal stress [Pa]

